International Journal of Navigation and Observation

# Integrating Radio Positioning and Communications: New Synergies

Guest Editors: Ronald Raulefs, Simon Plass, and Marco Luise

# Integrating Radio Positioning and Communications: New Synergies

International Journal of Navigation and Observation

# Integrating Radio Positioning and Communications: New Synergies

Guest Editors: Ronald Raulefs, Simon Plass, and Marco Luise

This is a special issue published in volume 2010 of "International Journal of Navigation and Observation." 

# Contents

Hindawi Publishing Corporation
International Journal of Navigation and Observation
Volume 2010, Article ID 802842, 2 pages
doi:10.1155/2010/802842

*Editorial*

# Integrating Radio Positioning and Communications: New Synergies

**Ronald Raulefs,[1] Simon Plass,[1] and Marco Luise[2]**

[1] *German Aerospace Center (DLR), Institute of Communications and Navigation, Oberpfaffenhofen, 82234 Wessling, Germany*
[2] *Dipartimento di Ingegneria dell'Informazione, Università degli Studi di Pisa, 56100 Pisa, Italy*

Correspondence should be addressed to Ronald Raulefs, ronald.raulefs@dlr.de

Received 14 November 2010; Accepted 14 November 2010



## Integrating Radio Positioning and Communications: New Synergies

Wireless communications and positioning systems and services, although often coexisting into the same terminal and sharing to some extent signal formats, have different constraints to cope with. Communications systems usually target high spectral efficiency (in terms of data rate per occupied bandwidth) with specific requirements such as low latency, low bit error rate, and low power consumption. Positioning terminals either base their functionality on very accurate synchronization with the received signals for acquisition and tracking, or they derive location information from previous knowledge of the wireless system or even obtain their position from knowledge of the radio propagation channel. The two technologies have different goals and, therefore, achieve different solutions.

However, communications and localization have a high potential to benefit from each other and appear more and more to be intertwined. This holds for physical (PHY) and medium access control (MAC) layer issues as well as for the application layer. The convergence of communications and positioning in the PHY and MAC layers have gradually attracted research interest and represent the enabling factor for the application layer. In fact, positioning information is an emerging "must-have" for numerous applications in smart phones (location-based applications), and companies are developing their business models on the ubiquitous access of data *and* of position information. Mobile radio services are already using nowadays positioning information for intelligent transport systems, location sensitive billing, and location-based advertising, just to mention a few.

The papers in this special issue represent a valid snapshot of current research in the field, showing the new synergies of integrated radio positioning and wireless communications.

The papers are grouped into three clusters: (i) practical investigations in real networks to show the performance gains based on fingerprinting techniques, (ii) focusing on the coexistence of different communications systems and global navigation satellite systems (GNSS), and (iii) underlay cognitive radio system using positioning information to support the secondary user.

In the first group of papers, the studies are carried out by practical investigations focusing on trials and realisation effort.

*I. Ahriz* et al. study handset localization with high accuracies by using 2G cellular mobile radio systems. The paper focuses on an indoor environment—urban apartments—to support health care applications. All GSM carriers are used as fingerprints. Even by reducing the numbers of GSM carriers that are exploited for received signal strength (RSS) fingerprinting to less than 10% of the full set, the performances were still in a reasonable range.

*S. Spinella* et al. focus on the indoor environment as well and show an example of combining WLAN and RFID to aid one another. WLAN is employed to build a fingerprinting signal map to position the device. The RFID tags allow splitting the area into zones that support the fingerprinting algorithm to further gain in speed and accuracy. The theoretical results were evaluated and confirmed in a measurement campaign.

The second group of papers investigates systems that use GNSS as part of their evaluation. *B. Motella* et al. assess the impact of interference due to communications

systems transmitting in close bandwidths to GNSS signals. The impact on GNSS is quantified by using *interference error envelopes* which measure the correlation of the distortion versus the characteristic of the interferer.

The next paper by *C. Mensing* et al. explores GNSS critical environments. The ubiquitous available cellular mobile radio systems are capitalized to improve acquisition and tracking of the position of the mobile phone. In addition, the mobility of the user is used to track the mobile phone and help to overcome the signal loss of GNSS in GNSS denied environments (e.g., urban canyons). The performance evaluation for the mobile radio differs between the different areas in a cellular radio system, for instance, proximity of the base station or cell edge.

The hybridization of multiple signal sources through nonlinear filters is studied by *C. Fritsche* and *A. Klein*. The authors apply their data-fusion algorithms to (raw) measurements in terms of time and received signal strength (RSS) from 2G mobile radio systems as well as to partial information (pseudoranges) coming from GNSS systems. The baseline assumption is that the radio base stations are all synchronized (based on GNSS timing information). They show that hybridization improves the localization method by increasing the accuracy of the global positioning system (GPS) in severe scenarios.

*S. Sergi* et al. discuss a ranging technique based on RSS for indoor scenarios by clustering mobile phones. The mobile phones perform ranging by using multiple measurement links (multiple base stations), and clustering is the enabling factor to attain reasonably accurate positioning.

Finally, *N. Yi* et al. investigate the concept of underlay cognitive radios (UCRs) which allows a secondary user to enter a primary user's spectrum. A location-aided UCR physical-layer model is established and analyzed. The positioning information is linked to the channel quality, and the knowledge of the terminal position is used to study new spectrum and power allocation techniques to optimize the capacity of the secondary user as well as the capacity penalty of the first user.

We would like to thank all authors and reviewers for their contributions. We do hope that this special issue may serve to promote further research in this new and exciting area. Finally, we would like to acknowledge the EU Research Projects WHERE (Contract no. 217033) and NEWCOM++ (Contract no. 216715) which aim at inspiring the development of new position-aware procedures to enhance the efficiency of communications networks and of new positioning algorithms based both on (outdoor or indoor) wireless communications and on satellite navigation systems.

*Ronald Raulefs*
*Simon Plass*
*Marco Luise*

Hindawi Publishing Corporation
International Journal of Navigation and Observation
Volume 2010, Article ID 497829, 7 pages
doi:10.1155/2010/497829

*Research Article*

# Full-Band GSM Fingerprints for Indoor Localization Using a Machine Learning Approach

**Iness Ahriz,[1] Yacine Oussar,[1] Bruce Denby,[2,1] and Gérard Dreyfus[1]**

[1] *Signal Processing and Machine Learning (SIGMA) Laboratory, ESPCI—ParisTech, 10 rue Vauquelin, 75005 Paris, France*
[2] *Université Pierre et Marie Curie—Paris VI, 4 place Jussieu, 75005 Paris, France*

Correspondence should be addressed to Bruce Denby, denby@ieee.org

Received 1 October 2009; Accepted 25 March 2010

Academic Editor: Simon Plass



Indoor handset localization in an urban apartment setting is studied using GSM trace mobile measurements. Nearest-neighbor, Support Vector Machine, Multilayer Perceptron, and Gaussian Process classifiers are compared. The linear Support Vector Machine provides mean room classification accuracy of almost 98% when all GSM carriers are used. To our knowledge, ours is the first study to use fingerprints containing all GSM carriers, as well as the first to suggest that GSM can be useful for localization of very high performance.

## 1. Introduction

Location-based services for cellular telephone networks are today very much in the public eye [1]. Global Positioning System, or GPS, receivers integrated into cellular handsets can provide very accurate positioning information; however, few mobiles are so equipped at present, and GPS furthermore performs poorly in the indoor and urban canyon environments which are prevalent in wireless networks. For these reasons, the study of localization techniques based upon the radio networks themselves is also a very active area. Most commercially installed systems still rely on cell-ID, in which the mobile station's position is reported as that of the serving base station. Although improvement is possible using triangulation, time of arrival, and the like, the accuracy of such methods is in practice compromised by the path loss and multipath characteristics inherent in the radio channel [2].

The database correlation method [3] allows to overcome channel effects to a certain extent. In this method, a mobile is localized by comparing one of the regularly emitted Received Signal Strength (RSS) measurements to a position-labelled database of such measurements, which are often called fingerprints. Existing localization services implemented in some GSM networks rely on Network Measurement Reports (NMR), which are a part of the GSM norm and contain the RSS and Base Station Identity Code (BSIC) of the serving cell and six strongest neighboring cells. The resulting 7-component vector allows a localization precision of some tens of meters in outdoor environments (see, e.g., [4, 5]).

As for indoor radio-based localization, most studies which have appeared in the literature have involved WiFi networks, describing "corridor waveguide" scenarios in the workplace, and obtaining performance which, though interesting, can still be improved [6–8]. Another approach, using the household power lines as an antenna, appears in [9]. The notion of using GSM or CDMA networks for localization in indoor environments, particularly in domestic settings, is still somewhat new (see, e.g., [10, 11]). The basic idea is that inside a building, the RSS of the external base stations will be strongly correlated with a mobile's exact position, due to for example the varying absorption of electromagnetic energy by different building materials, and the exact placement of doors and windows. There has also been evidence that including more than the standard 7-carriers of the NMR fingerprint is advantageous in indoor GSM localization [10, 12].

In this article, we present tests of indoor GSM localization using scans containing large numbers of carriers—up to the full GSM band. In order to keep working with such large numbers of carriers tractable, we propose to create a mathematical model mapping fingerprints to position using machine-learning techniques, in this case Support Vector

Machines (SVM), and Multilayer Perceptrons (MLP), often also referred to as neural networks. We demonstrate the superiority of the machine learning approach, for problems with such high input dimensionality, over more traditional classifiers based on Euclidean (K-Nearest Neighbor) and Mahalanobis (Gaussian process) distances. Our results show that in an urban apartment setting, the room in which a handset is located can be identified with nearly 98% accuracy when the full set of GSM carriers is included. To our knowledge, this study, which is an extension of that described in [12], is the first to use fingerprints of all carriers in the GSM band, and the first to demonstrate very good performance on indoor localization using GSM.

The structure of the article is as follows. The data sets used in our study are presented in Section 2, while a discussion of preprocessing and the classifiers tested are given in Section 3. Our results are discussed in Section 4, while our conclusion, as well as some perspectives for the future is outlined in the final section.

## 2. Data Sets

The TEMS [14] trace mobile system was used to take twice-daily scans of the entire set of 498 GSM carriers in 5 rooms of a 5th floor apartment (top floor) in Paris, France. Both the RSS and the BSIC, where readable, were requested for each carrier in the scans. The layout of the apartment is shown in Figure 1. Acquisitions could be made anywhere within a room; however, in practice, the scans were recorded in those areas where the necessary laptop and cellphone could be conveniently set down and accessed. An exhaustive coverage of all rooms was thus not assured.

## 3. Data Analysis

*3.1. Preprocessing.* Ten of the carriers were found to contain no energy and were removed from the study. As the BSICs of the remaining 488 proved unreadable in many instances, a decision was made to exclude the BSICs entirely from the subsequent analysis, despite the possibility this engenders of confusing carriers at the same frequency in separate cellular motifs. The data set contained a total of 241 scans—approximately 48 scans per class, where a class is defined here simply as the index of the room within the apartment, indicated in Figure 1. To obtain a measure of the statistical significance of our classification results, cross-validation was performed with ten independent randomly selected splits of our data, each one containing 169 training examples and 72 validation examples. In a given split, the training and validation examples were uniformly distributed over time during the one-month acquisition period.

*3.2. Dimensionality Reduction and Fingerprint Types.* The relatively small size of our dataset is a reflection of the difficult, time-consuming nature of obtaining labeled scan data—a point to which we will return later. Its high dimensionality (488 carriers) also limits the complexity of the classifiers which may be applied. To deal with these issues, signal strength-based carrier selection was initially carried out so as to define the four fingerprint types defined below. Further dimensionality reduction of any fingerprint can be obtained by a subsequent application of Principal Component Analysis (PCA).

Three vectors are used in defining the fingerprints:

$$\mathbf{g}_j^7 = \left\{ i = 1 \cdots 488, \sum_k \mathbf{1}_{\mathrm{RSS}(i,j) < RSS(k,j)} \leq 6 \right\},$$

$$\mathbf{G}^7 = \bigcup_j \mathbf{g}_j^7, \tag{1}$$

$$\mathbf{G}^{35} = \left\{ i = 1 \cdots 488, \sum_k \mathbf{1}_{\langle \mathrm{RSS}(i,j) \rangle_j < \langle \mathrm{RSS}(k,j) \rangle_j} \leq 34 \right\},$$

where $\mathbf{1}$ is the so-called indicator function, and $\langle\rangle_j$ represents the mean over the index $j$. The first, $\mathbf{g}_j^7$, contains the indices of the 7 strongest carriers, $i$, in example $j$. The vector $\mathbf{G^7}$, composed of the indices of the carriers which were among the strongest 7 in at least one scan of the training set, contains between 36 and 40 of such "good" carriers, depending upon the random split used. The third vector, $\mathbf{G^{35}}$, consists of the indices of the 35 carriers which were the strongest on average, over the whole training set. The fingerprints may then be defined as follows.

(1) *Current Top 7.* These seven carrier fingerprints, $\mathrm{RSS}(\mathbf{g}_j^7)$, are meant to mimic standard "top 7" NMRs, which were not present in our scans. Indeed, NMRs are only logged during a communication, while our scans were obtained in idle mode. Validation set fingerprints can in fact contain less than 7 elements if certain carriers were not represented in the training set. For classifiers requiring fixed labeling of input vectors, such as KNN, SVM, and MLP, the seven $\mathrm{RSS}(\mathbf{g}_j^7)$, values are entered at the corresponding positions in a vector of length $\|\mathbf{G}^7\|$, and the rest of the elements are set to zero.

(2) *Top 7 with Memory.* This fingerprint, defined as $\mathrm{RSS}(\mathbf{G}^7)$, includes the values of all of the 36–40 "good" carriers; they are thus "wider" than the *Current Top 7* fingerprint defined above.

(3) *35 Best Overall.* The *35 Best Overall* fingerprint, of length 35, is defined as $\mathrm{RSS}(\mathbf{G}^{35})$. It thus gives another way of assessing the "goodness" of a carrier, by the size of its average RSS value over the whole training set.

(4) *All 488.* All of the active carriers' RSS values are included in the fingerprint, that is, no selection is in fact made.

*3.3. Classifiers.* Four types of classifier were tested:

(1) *Support Vector Machines (SVM).* A 2-class SVM classifier [15] finds the separating surface which maximizes the distance (or "margin") between that surface and the data points on either side of it. The SVM can be linear and operate

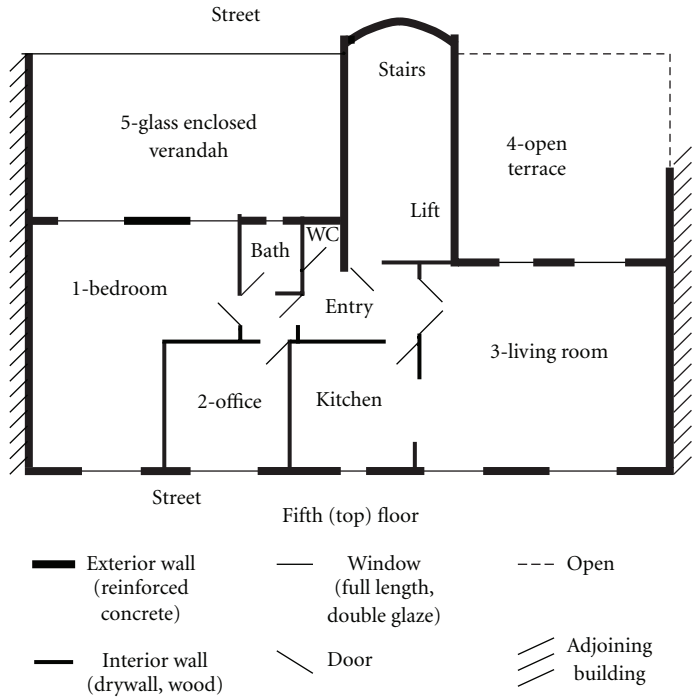


Figure 1: Schematic of apartment layout.

directly upon the data, or first map the data onto a higher-dimensional space using a non-linear transformation, before finding the maximum margin surface. The SVM decision rule takes the sign of

$$f(\mathbf{x}) = \sum_{i=1}^{N_s} \alpha_i y_i K(\mathbf{s}_i, \mathbf{x}) + b \tag{2}$$

with $\mathbf{x}$ the RSS vector to be localized, $N_s$ the number of support vectors $\mathbf{s}_i$ (training vectors which are on the boundary of the optimal margin), and $y_i = \pm 1$ the class label of the vector $\mathbf{s}_i$. $K(\cdot)$ here is the selected kernel, and $b$ as well as the $\alpha_i$ are parameters determined in the search for the optimal separating surface. For large, well-behaved data sets, the SVM rule approximates the Bayes decision rule [15].

In the case of a linear SVM, the kernel function is just the scalar product $K(\mathbf{s}_i, \mathbf{x}) = \mathbf{s}_i \cdot \mathbf{x}$. The standard Gaussian kernel was adopted in our tests of non-linear SVMs,

$$K(\mathbf{s}_i, \mathbf{x}) = e^{-|\mathbf{s}_i - \mathbf{x}|^2/\sigma^2}, \tag{3}$$

where the variance, $\sigma^2$, is optimized in the cross-validation stage. Since a "soft margin" approach was used (i.e., some training examples were allowed to lie within the margin), a regularization parameter controlling the complexity of the separating surface [15] was also estimated by cross-validation. For $m$ classes, it is traditional, using the "conventional recipe" [16], to construct $m$ binary, one-versus-rest classifiers, and take as the output class that of the classifier having the largest output value before thresholding. This procedure is illustrated for the case of $m = 5$ in Figure 2. The Spider SVM package [17] was used in all of our analyses.

(2) *Multilayer Perceptron (MLP).* A multilayer Perceptron is a multivariate, nonlinear, scalar or vector function, which is a combination of parameterized elementary nonlinear functions called neurons [18]. A neuron is usually a function of the form $f = \tanh(\boldsymbol{\theta} \cdot \mathbf{x})$ where $\boldsymbol{\theta}$ is the vector of parameters of the neuron and $\mathbf{x}$ is the vector of variables. A single-output "multilayer Perceptron" $g(\mathbf{x})$ is a combination of $N_h$ "hidden" neurons $f_i (i = 1 \text{ to } N_h)$ and of a constant equal to 1. Denoting by $\Theta_1$ the vector of parameters of the linear combination (of size $N_h + 1$), by $\Theta_2$ the $(N + 1, N_h)$ matrix whose elements are the parameters of the "hidden" neurons, and by $\mathbf{f}$ the vector (of size $N_h$+1) of functions computed by the $N_h$ hidden neurons with an additional component equal to 1, the multilayer Perceptron function is of the form

$$g(\mathbf{x}) = h(\Theta_1 \cdot \mathbf{f}(\Theta_2 \mathbf{x})). \tag{4}$$

Multilayer Perceptrons are frequently described pictorially as shown in Figure 3.

The parameters of the multilayer Perceptron are estimated from the available training data by minimizing the least squared cost function

$$J(\Theta_1, \Theta_2) = \sum_{k=1}^{n} (y_k - g(\mathbf{x}_k))^2 \tag{5}$$

with respect to all parameters, where $\mathbf{x}_k$ is the vector of variables pertaining to example $k$ and $y_k$ is the measured value of the quantity of interest for example $k$. In the present study, the gradient of the cost function was computed by a computationally efficient algorithm known as "backpropagation", and the optimization of the cost function was

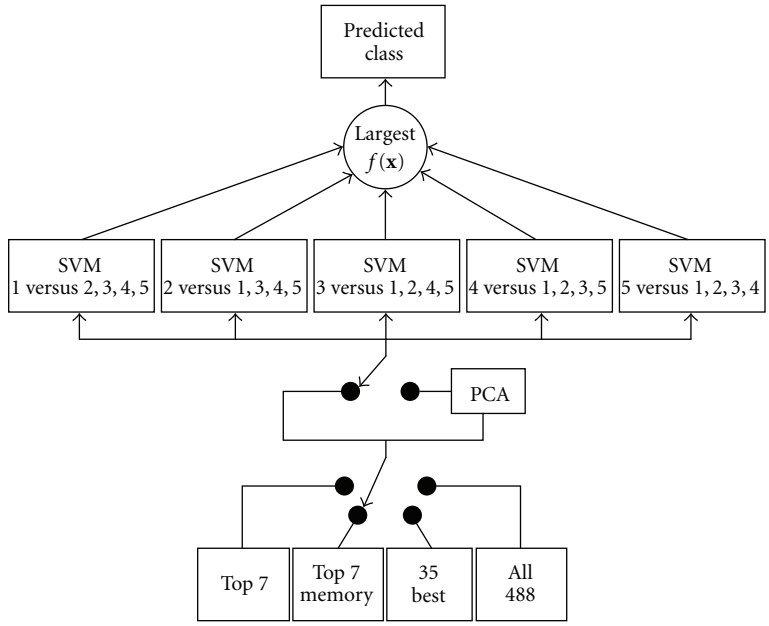


Figure 2: Architecture combining five one-versus-rest SVM classifiers to predict the class of an RSS vector from one of the carrier sets.

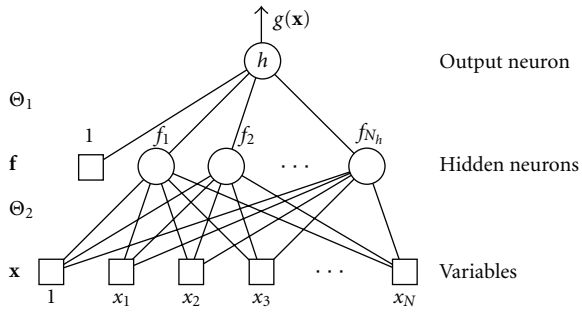


Figure 3: A multilayer Perceptron with a single output.

performed by the conjugate gradient algorithm with Powell-Beale restarts [19].

In a two-class ($A$, $B$) classification problem, $y_k = +1$ for all examples of class $A$ and $y_k = -1$ for all examples of the other class. After training, an unknown example described by vector $\mathbf{x}$ is assigned to class $A$ if $\text{sgn}(g(\mathbf{x})) = +1$, and to class $B$ otherwise. In the present study, function $h$ was taken identical to function $f$. For a $c$-class problem, example $k$, belonging to class $i$ ($1 \le i \le c$), is assigned a vector $\mathbf{y}_k$, of dimension $c$, that encodes the class in a 1-out-of-$c$ code: all components are equal to $-1$, except component $i$, which is equal to $+1$. The number of output neurons is equal to the number of classes, so that the output of the multilayer Perceptron is a vector $\mathbf{g}(\mathbf{x})$ of dimension $c$. The cost function that is optimized during training is

$$J(\Theta_1, \Theta_2) = \sum_{k=1}^{n} \left\| \mathbf{y_k} - \mathbf{g}(\mathbf{x}_k) \right\|^2. \tag{6}$$

In the present study, two strategies were compared for multiclass classification with multilayer Perceptrons.

(i) All functions $h$ were taken identical to $f$ (sigmoid functions), so that the output vector of the multilayer Perceptron was

$$\mathbf{g}(\mathbf{x}) = \mathbf{h}(\Theta_1 \mathbf{f}(\Theta_2 \mathbf{x})), \tag{7}$$

where $\Theta_1$ is the $(c, N_h+1)$ matrix of the parameters of the output neurons.

(ii) Output $i$ ($1 \le i \le c$) of the multilayer Perceptron was computed as

$$g_i(\mathbf{x}) = \frac{\exp[(\Theta_1 \mathbf{f}(\Theta_2 \mathbf{x}))_i]}{\sum_{j=1}^{c} \exp\left[(\Theta_1 \mathbf{f}(\Theta_2 \mathbf{x}))_j\right]} \quad \text{(softmax function)}. \tag{8}$$

In either case, and example described by $\mathbf{x}$ was assigned to the class $j$ such that

$$j = \text{argmax}_{1 \le i \le c}(g_i(\mathbf{x})). \tag{9}$$

In the second case, the components of vector $\mathbf{g}$ belong to $[0, 1]$ and sum to 1, so that they can be interpreted safely as estimates of the posterior probability of class $c$ given the observed vector $\mathbf{x}$.

(3) *K-Nearest Neighbor (K-NN).* As a first step, *K-NN* ranks the training vectors according to their RSS-space Euclidean distances from a test vector to be localized. The predicted class of this test vector is then the class most often represented in the $K$ "nearest" vectors according to the defined metric. The $K$ parameter is chosen empirically, to optimize performance. When a single best neighbor is used, $K = 1$, and the classifier is called *1-NN*.

Table 1: Percentage of correct radio fingerprint classifications on the 4 carrier sets described in the text. Figures quoted are averages and standard deviations over 10 randomly selected validation sets. All classifiers achieve their best performance when all 488 carriers are included. The most effective classifier for this case is the linear SVM.

| Classifier | | Fingerprint Type: Current Top 7 (≤7 carriers)[1] | Top 7/Memory (36–40 carriers) | 35 Best Overall (35 carriers) | All 488 (488 carriers) |
|---|---|---|---|---|---|
| Linear SVM | | 71.3 ± 7.2 | 84.6 ± 3.6 | 90.4 ± 3.5 | **97.8 ± 1.5** |
| Gauss. SVM | w/o PCA | 72.2 ± 3.6 | 89.2 ± 2.9 | 93.2 ± 3.4 | —[2] |
| | w/PCA[3] | 71.8 ± 3.2 | 85.6 ± 5.3 | 92.0 ± 3.0 | 96.4 ± 1.5 |
| Linear Perceptron | | 66.9 ± 4.1 | 73.2 ± 5.1 | 79.7 ± 5.1 | 94.4 ± 2.6 |
| MLP (one versus all) | w/o PCA | 66.9 ± 7.1 | 87.2 ± 3.3 | 91.8 ± 3.4 | —[2] |
| | w/PCA[3] | 68.1 ± 3.4 | 87.5 ± 4.5 | 89.6 ± 2.5 | 95.7 ± 2.1 |
| MLP (multiclass) sigmoids | w/o PCA | 56.8 ± 7.1 | 80.4 ± 12.9 | 92.6 ± 3.2 | —[2] |
| | w/PCA[3] | 66.4 ± 5.7 | 85.1 ± 9.5 | 89.4 ± 3.6 | 96.1 ± 1.1 |
| MLP (multiclass) softmax | w/o PCA | 64.3 ± 7.5 | 85.7 ± 15.8 | 91.2 ± 4.2 | —[2] |
| | w/PCA[3] | 67.7 ± 5.7 | 88.2 ± 3.9 | 90.4 ± 3.1 | 96.6 ± 2.4 |
| $K_{best}$ K-NN | | 5 59.3±3.5 | 26 85.1±3.0 | 20 93.3±2.1 | 20 94.9±1.9 |
| 1-NN | | 58.1 ± 5.2 | 74.7 ± 3.7 | 86.0 ± 2.9 | 87.2 ± 2.8 |
| GP ($\sigma = 5$ dB) | | 78.8 ± 3.7 | | —[4] | |

[1]SVM and K-NN can have < 7 carriers if some did not show up in the training set.
[2]Small training set size precludes training a nonlinear classifier due to Cover's theorem [13].
[3]Best result obtained using the first 4 principal components.
[4]Gaussian process is equivalent to 1-NN for fixed input vector length.

(4) *Gaussian Process (GP)*. As in the case of $K$-NN, GP starts by comparing the test RSS vector to be localized to every vector in the training set. The probability, $P_1$, that the compared vectors correspond to measurements at the same geographical position is assumed to be Gaussian in the Euclidean RSS distance between the two vectors, using a fixed variance $\sigma^2$ which is determined empirically. If a carrier appears in one of the compared vectors, but not in the other, GP presumes that the missing value was below the reception threshold in the vector lacking it. A penalty term probability, $P_p$, is introduced, in which the missing RSS value is replaced by an estimate of the reception threshold, taken to be the smallest RSS in the vector which is missing the carrier. The overall GP probability, $P$, is the product of $P_1$ and $P_p$.

To be more precise, let $A$ and $B$ be sets of indices of carriers contained in a training set vector, and a test set vector, respectively. We define the set of common carriers as $C = A \cap B$, and the noncommon carrier sets as $D = A - C$ and $E = B - C$, for the train and test sets, respectively. We then have

$$
\begin{aligned}
P_1 &= \sqrt[|C|]{\prod_{i\in C} e^{-\left|\mathrm{RSS}_i^A - \mathrm{RSS}_i^B\right|^2/\sigma^2}}, \\
P_p &= \sqrt[|D|]{\prod_{j\in D} e^{-\left|\mathrm{RSS}_j^D - \min_B\left(\mathrm{RSS}^B\right)\right|^2/\sigma^2}} \\
&\quad \times \sqrt[|E|]{\prod_{k\in E} e^{-\left|\mathrm{RSS}_k^E - \min_A\left(\mathrm{RSS}^A\right)\right|^2/\sigma^2}}, \\
P &= P_1 \cdot P_p,
\end{aligned}
\tag{10}
$$

where $\mathrm{RSS}_i^A$ is the signal strength of the $i$th carrier of set $A$, and the order of each root normalizes the probability to the number of carriers in the corresponding term. GP is actually the only classifier tested which is able to handle missing carriers in a natural way. When input vectors are of fixed length—a requirement for SVM, MLP, and KNN—and all variables must be represented, GP is equivalent to a 1-NN classifier. As a caveat, however, as we do not use the BSIC information, in some cases, carriers with the same index can belong to different cellular motifs, which would penalize the GP method.

## 4. Results

We define the localization performance of a given classifier as the average of the validation scores obtained over our ten random splits, expressed as a percentage of correctly identified locations. The standard deviation over the ten splits is also calculated. The results are shown in Table 1.

A few preliminary remarks about the table are in order. First, when the *All 488* fingerprint is used, it is not meaningful to apply a non-linear classifier to the data. This is because of Cover's theorem [13], which states that the examples of a training set are always linearly separable when the number of input variables exceeds the number of examples. The corresponding table entries are thus left blank (footnote 2 in the table). Secondly, on the other hand, dimensionality reduction by principal component analysis is known to often make examples nonlinearly separable, giving poor performance (nonlinear separability of the training examples was verified using the Ho-Kashyap algorithm [20]).

Table 2: Confusion Matrices for 35 Best Overall and All 488 carrier sets, using a Linear SVM classifier. Figures quoted are in percent. Using the full number of carriers tightens up the diagonal to give individual room classification efficiencies near 100%.

(a)

| Confusion Matrix | True class 35 Best overall | | | | |
|---|---|---|---|---|---|
| Pred. Class | 1 | 2 | 3 | 4 | 5 |
| 1 | 95 | 5.3 | | | 3.3 |
| 2 | 1.4 | 93.3 | 3.6 | | |
| 3 | 0.7 | 1.3 | 77.9 | 11.4 | |
| 4 | | | 16.4 | 87.9 | 0.7 |
| 5 | 2.9 | | 2.1 | 0.7 | 96 |

(b)

| Confusion Matrix | True class All 488 | | | | |
|---|---|---|---|---|---|
| Pred. Class | 1 | 2 | 3 | 4 | 5 |
| 1 | 100 | | 0.7 | | |
| 2 | | 100 | | | |
| 3 | | | 91.4 | 1.4 | 1.3 |
| 4 | | | 5.7 | 98.6 | |
| 5 | | | 2.2 | | 98.7 |

For this reason, linear classifiers are not applied in those cases where PCA is used. A few further details are explained in the remaining footnotes of Table 1.

The table shows that the performance of all classifiers tested improves as more carriers are added to the fingerprint, but that very good performance—for example, our best result of 97.8% in the case of the linear SVM—is only obtained on the *All 488* carrier fingerprint. The implication is that indoor position can indeed be deduced from the RSS of GSM cell towers, but that commonly used 7-carrier NMRs and even "wide" fingerprints are insufficient: high performance requires fingerprints of very high dimensionality. It is reassuring to see that this conclusion is supported by all the classifiers tested, including a simple *K-NN*, even if the best results are obtained with SVM and MLP machine learning techniques. MLP performance appears slightly worse than that of linear SVMs, within the statistics of our sample, with the best MLP performance, 96.6%, obtained on a multiclass MLP with the softmax output function applied to *All 488* carriers, after an input dimensionality reduction.

A more detailed look at our conclusion is given in Table 2, where the confusion matrices for the linear SVM classifier on the *35 Best Overall* and *All 488* fingerprints appear. The table shows once again that the ability to sharply discriminate between rooms comes only with the inclusion of the full GSM carrier set. The deviation of our global result from 100% is in fact dominated by the confusion between class 3 and class 4, which appears to be the most difficult case.

## 5. Conclusions and Perspectives

We believe this study, which is an extension of that presented in [12], to be the first to include the full set of GSM carriers in RSS fingerprints for localization. Although confirmation with more extensive databases will be required, our results strongly suggest that high-performance room-level localization is possible through the use of such fingerprints. The fact that good performance is obtained irrespective of the machine learning technique used (MLPs or SVMs,) is a further confirmation that the useful information for localization is obtained by taking into account many GSM carriers, including those which may be rather weak. Finally, it is interesting to note that our result is robust against time-dependent effects—network modifications, propagation channel changes, meteorological effects, and so forth, as our dataset was acquired over a period of one month.

Acquiring datasets and labeling scans is a tedious and time-consuming activity. To address this issue, two independent solutions are currently being investigated. First, experiments with semisupervised classification techniques using kernel methods (see, e.g., [21]) are being carried out, which will permit to take advantage of the unlabeled scans during the training procedure. The second approach entails the design and construction, in our laboratory, of a set of ten autonomous scanning devices which will allow the acquisition of large datasets simultaneously in different rooms, labeled with very little human intervention. These devices will also enable to test the efficiency of our approach when implemented using mixed datasets of scans acquired both indoors and in nearby outdoor areas. For larger outdoor areas, preliminary results indicate that a regression approach using $x$-$y$ coordinates seems more suitable than the room-by-room classification used here for indoor localization.

## References

[1] A. Küpper, *Location-Based Services: Fundamentals and Operation*, John Wiley & Sons, New York, NY, USA, 2005.

[2] H. Laitinen, et al., "CELLO: cellular network optimization based on mobile location," Internal Report IST-2000-25382-CELLO, EU IST Project, October 2001, http://www.telecom.ntua.gr/cello/documents/CELLO-WP2-VTT-D03-007-Int.pdf.

[3] D. Zimmermann, J. Baumann, M. Layh, F. Landstorfer, R. Hoppe, and G. Wölfle, "Database correlation for positioning of mobile terminals in cellular networks using wave propagation models," *Proceedings of the 60th IEEE Vehicular Technology Conference*, vol. 7, pp. 4682–4686, September 2004.

[4] M. Chen, T. Sohn, D. Chmelev, et al., "Practical metropolitan-scale positioning for GSM phones," in *Proceedings of the 8th International Conference on Ubiquitous Computing*, P. Dourish and A. Friday, Eds., vol. 4206 of *Lecture Notes in Computer Science*, pp. 225–242, Springer, Orange County, Calif, USA, September 2006.

[5] B. Denby, Y. Oussar, and I. Ahriz, "Geolocalisation in cellular telephone networks," in *Proceedings of the NATO Advanced Study Institute on Mining Massive Data Sets for Security*, F. Fogelman-Soulié, D. Perrotta, J. Piskorski, and R. Steinberger, Eds., IOS Press, Amsterdam, The Netherlands, 2007.

[6] M. Brunato and R. Battiti, "Statistical learning theory for location fingerprinting in wireless LANs," *Computer Networks and ISDN Systems*, vol. 47, no. 6, pp. 825–845, 2005.
[7] A. M. Ladd, K. E. Bekris, A. P. Rudys, D. S. Wallach, and L. E. Kavraki, "On the feasibility of using wireless ethernet for indoor localization," *IEEE Transactions on Robotics and Automation*, vol. 20, no. 3, pp. 555–559, 2004.
[8] Q. Yang, S. J. Pan, and V. W. Zheng, "Estimating location using Wi-Fi," *IEEE Intelligent Systems*, vol. 23, no. 1, pp. 8–9, 2008.
[9] S. N. Patel, K. N. Truong, and G. D. Abowd, "Powerline positioning: a practical sub-room-level indoor location system for domestic use," in *Proceedings of the 8th International Conference on Ubiquitous Computing (UbiComp '06)*, Orange County, Calif, USA, September 2006.
[10] V. Otsason, A. Varshavsky, A. LaMarca, and E. de Lara, "Accurate GSM indoor localization," in *Proceedings of the International Conference on Ubiquitous Computing (UbiComp '05)*, M. Beigl, et al., Ed., pp. 141–158, Springer, Berlin, Germany, 2005.
[11] W. ur Rehman, E. De Lara, and S. Saroiu, "CILoS: a CDMA indoor localization system," in *Proceedings of the 10th International Conference on Ubiquitous Computing (UbiComp '08)*, pp. 104–113, Seoul, Korea, 2008.
[12] B. Denby, Y. Oussar, I. Ahriz, and G. Dreyfus, "High-performance indoor localization with full-band GSM fingerprints," in *Proceedings of the IEEE International Conference on Communications Workshops (ICC '09)*, Dresden, Germany, June 2009.
[13] T. M. Cover, "Geometrical and statistical properties of systems of linear inequalities with applications in pattern recognition," *IEEE Transactions on Electronic Computers*, vol. 14, pp. 326–334, 1965.
[14] Test Mobile System, http://www1.ericsson.com/solutions/tems.
[15] N. Cristianini and J. Shawe-Taylor, *Support Vector Machines and Other Kernel-Based Learning Methods*, Cambridge University Press, Cambridge, UK, 2000.
[16] Y. Lee, Y. Lin, and G. Wahba, "Multicategory support vector machines: theory and application to the classification of microarray data and satellite radiance data," *Journal of the American Statistical Association*, vol. 99, no. 465, pp. 67–81, 2004.
[17] The Spider, http://www.kyb.tuebingen.mpg.de/bs/people/spider.
[18] G. Dreyfus, *Neural Networks: Methodology and Applications*, Springer, New York, NY, USA, 2005.
[19] M. J. D. Powell, "Restart procedures for the conjugate gradient method," *Mathematical Programming*, vol. 12, no. 1, pp. 241–254, 1977.
[20] Y.-C. Ho and R. L. Kashyap, "An algorithm for linear inequalities and its applications," *IEEE Transactions on Electronic Computers*, vol. 14, no. 5, pp. 683–688, 1965.
[21] O. Chapelle, B. Schölkopf, and A. Zien, *Semi-Supervised Learning*, MIT Press, Cambridge, Mass, USA, 2006.

Hindawi Publishing Corporation
International Journal of Navigation and Observation
Volume 2010, Article ID 397467, 11 pages
doi:10.1155/2010/397467

*Research Article*

# On Potentials and Limitations of a Hybrid WLAN-RFID Indoor Positioning Technique

**Silverio C. Spinella, Antonio Iera, and Antonella Molinaro**

*Department DIMET, Laboratory of A.R.T.S., University Mediterranea of Reggio Calabria, Loc. Feo di Vito, 89100 Reggio Calabria, Italy*

Correspondence should be addressed to Antonio Iera, antonio.iera@unirc.it

Received 15 November 2009; Accepted 25 March 2010

Academic Editor: Simon Plass



This paper addresses the important issue of position estimation in indoor environments. Starting point of the research is positioning techniques that exploit the knowledge of power levels of RF signals from multiple 802.11 WLAN APs (Access Points). In particular, the key idea in this paper is to enhance the performance of a WLAN fingerprinting approach by coupling it to a RFID-based procedure. WLAN and RFID technologies are synergistically used to provide a platform for a more performing positioning process, in which the very strong identification capabilities of the RFID technology allow to increase the accuracy of positioning systems via WLAN fingerprinting. The algorithm performance is assessed through general and repeatable experimental campaigns, during which the main algorithm parameters are dimensioned. The results testify both to the feasibility of the solution and to its higher accuracy (attainable at very reduced costs) compared to traditional positioning techniques.

## 1. Introduction

Recently, the wireless telecommunications market has increased its interest towards so-called "location-based" applications, which are proposed to the end-user attention as the most promising response to their need of personalized communications in fields such as Infomobility, mobile entertainment and gaming, Intelligent Transportation Systems, assisted driving, and so forth. This phenomenon has been fostered both by the availability of mobile terminals equipped with multiple radio network interfaces, and by extensive research efforts undertaken by Industries and Research Institutions to develop platforms for efficient indoor and outdoor positioning solutions.

While the availability of low-cost GPS (Global Positioning System) [1] receivers, built in the mobile terminals, promoted the development of location-based applications in outdoor scenarios, still barriers to the spread of location-based services are present in indoor scenarios. Therein, in fact, the GPS technology (which relies on satellite signals) cannot be exploited, and no other technology has shown to be ready to play a leadership role. In order to achieve accurate position estimation inside the buildings, several solutions have been proposed, which differ from each other in the used technology, positioning accuracy, offered coverage, frequency of updates, and costs of installation and maintenance. As it will be shown in the following, several comparative studies on competing positioning systems are available from the literature; most of them are based on Radio Frequency (RF) technologies (e.g., Wi-Fi, Bluetooth) [2–7].

The technology that has gained the greatest success, thanks to its low cost, widespread diffusion, and robust communication capabilities, even in non Line of Sight (nLOS) conditions, is definitely the WLAN (Wireless Local Area Network) technology. According to WLAN-based techniques, it is possible to locate Wi-Fi card equipped devices, with an accuracy of some meters, by means of two-phase positioning algorithms. During the *offline* training phase, the Received Signal Strength Indicator (RSSI) distributions, collected from Wi-Fi Access Points (APs) situated in predefined reference positions within the interest area, are tabulated

together with their physical real-world coordinates. This originates a so-called *radio map* (or fingerprint database), in which any single dataset is called *fingerprint*. During the subsequent *online* location determination phase, RSSI samples received from a subset of APs are used to search for similar patterns in the radio map. The best match is chosen, and its physical coordinates are returned as the position estimate. Although a fingerprinting technique avoids the complicated computation of path loss, since fingerprint data are already affected by multipath and by signal attenuation phenomena, still the position estimation may not be accurate enough, thus owing to *false positives*.

On the other hand, solutions are appearing that exploit the Radio Frequency IDentification (RFID) technology, which was originally introduced as a key technology only applied to item identification in fields, such as asset tracking, manufacturing, supply chain management, retailing, electronic payment, security and access control, and so forth. RFID-based positioning solutions can be split into two main categories: *tag-oriented* and *reader-oriented*. The former aims at locating RFID tags, while the latter tries to find the position of portable RFID readers. Both approaches are likely to be employed as a basis to implement location-based services.

The idea behind the proposal in the present paper is to use both Wi-Fi and RFID technologies synergistically, to design a platform for more performing location sensing services. The very strong identification capability of RFID technology can indeed be very useful for increasing the accuracy of positioning systems based on WLAN fingerprinting techniques. The purpose of RFID components is to allow a reduction in the number of iterations when searching for the best fingerprint match in the database of the Wi-Fi positioning system. As it will become clearer in the following sections, a performing behaviour is achieved by splitting (thanks to the RFID technology) the fingerprint database into "zones" (during the *offline* phase) and, later (during the *online* phase) by introducing a "zone matching" process. The resulting technique shows the following points of strength: (a) significant reduction of false positives, (b) low additional costs compared to traditional Wi-Fi based detection systems, and (c) ability to take advantage of tags that in the future will be largely present in indoor environments (in the view of the Internet of Things). Furthermore, compared to other mechanisms, our solution is easily and quickly deployable and does not require a high tag density.

Potentials and limitations of the proposed hybrid WLAN-RFID positioning technique will be highlighted, and its effectiveness validated by a comprehensive measurement campaign. This latter will testify that the emerging synergies between a typical *communication system* (like Wi-Fi) and a typical *identification technology* (like RFID) are able to implement low complexity solutions to enhance performance of location sensing mechanism.

The rest of the paper is organised as follows. In Section 2, we survey related work in the area of location tracking in indoor environments. Section 3 reports the rationale of the proposed WLAN-RFID hybrid positioning solution and describes its operational behaviour. Section 4 focuses on experimental results obtained in different scenarios through field tests, that aim at comparing our approach with alternative location sensing solutions and at evaluating the impact of design parameters on the location accuracy. Section 5 concludes the paper.

## 2. Related Works

In [4, 8–10] WLAN-based location systems have been proposed, based on empirical signal strength measurements as well as on simple signal propagation models. RADAR [4] is an RF-based system for locating and tracking users inside the buildings. It uses standard IEEE 802.11 network adapters to measure signal strengths at multiple base stations, positioned to provide overlapping coverage in a given area. The system combines empirical measurements and signal propagation modeling to determine the user position. Other approaches use a Bayesian algorithm [11] or Delaunay triangulation with lines of constant signal strength [12]. The use of Delaunay triangulation and interpolation allows building a radio map with low density of calibration points and reduces the training phase delay. *WhereNet* [13] uses timing signals transmitted from tags to a network of receivers. It is based on the same 2.4 GHz band as the 802.11 and Bluetooth systems, but uses a dedicated standard protocol optimized for low power spread-spectrum position determination. The Ekahau [3] Wi-Fi positioning system computes the location of a client device by applying a probabilistic model to the signal strengths measured at the Wi-Fi client device (*Ekahau device*). The indoor environment must be calibrated a priori to provide the positioning engine with a signal strength map of the room. Ekahau devices continually send their signal strength vectors to the positioning engine, which keeps track of each device location.

In the last few years, besides *WLAN-based location*, also the *location through RFID* has been investigated from several application perspectives. Two location approaches exist: *tag-oriented* and *reader-oriented*. Earlier work on the former class of solutions is well synthesized by LANDMARC [14], which proposes to locate an active RFID tag through RF-power distances with respect to *reference* RFID tags in fixed and known locations. Power levels of the reference tags are stored in a database. Tags in unknown positions are sensed by the reader antennas and their power levels are compared to those of the reference tags. The reference tags with the most similar power readings are assumed to be the closest to the target tag and used to predict the unknown tag position by using the Nearest Neighbor Algorithm. In [15] results of a wide campaign are reported to evaluate the performance of LANDMARC under general experimental conditions, especially in indoor environments. The authors concludes that such tag-oriented algorithm may require highly expensive infrastructures, composed of many RFID tags and readers/antennas, if satisfactory position accuracy is required.

As for reader-oriented location solutions, [16] proposes a tagged environment with numerous reference tags over the area of interest, thus creating a so-called *Super-distributed*

*RFID tag infrastructure*. In this solution, location targets are equipped with mobile readers, thus, reversing the traditional approach in employing readers and tags. A portable reader position is discovered through either the identification of the closest reference tag surrounding it or, in case of multiple tags identification, by averaging the positions of the identified tags. Reader-oriented location solutions have also been studied in the field of assistance to blind people [17–19] and in robot localization [20], where statistical filters are exploited to enhance odometer information by means of RFID tag identification. Researches in [17, 18] are focalized on navigation rather than environment disclosure; instead, Ubibus [21] has been proposed to help blind people in public transportation scenarios.

Particle filters have also been applied in absolute location systems. Most notable works are in [22, 23], according to which the location of a user is based on measurements received from a variety of sensor systems. As already addressed, the proposal in the present paper differs from the literature in that it is an hybrid algorithm that jointly uses WLAN and RFID technologies to achieve improved location accuracy, similar to other sensor fusion approaches. The main aim is to select, by means of the RFID technology, the WLAN RSSI points that are actually close to the target WLAN device location and, then, to average their positions getting a final position estimate.

## 3. Proposed WLAN-RFID Hybrid Positioning Technique

In the present section the basic features of the proposed hybrid approach to positioning via a joint exploitation of WLAN fingerprinting and RFID technologies are introduced. As already addressed, the proposed location algorithm could be considered as an evolution of WLAN fingerprinting techniques; in fact, the "two phases" approach is maintained, while the RFID integration is used to overcome some inherent drawbacks of such an approach. Our proposal requires that the mobile target, whose location must be determined, is equipped with both a WLAN card and a RFID reader. Besides, a set of reference tags is associated to any given "zone" in the observation area.

*Phase 1* (offline: building the fingerprinting database). Still the presence of reference points for RSSI measurements from the WLAN Access Point (APs) is required. WLAN reference points are carefully selected to populate the database and, through an accurate measurement campaign, each of them is characterized in terms of a set of RSSI values, one for each available AP. The main weakness of the described measurement phase is, undoubtedly, the possibility of measuring very similar power levels in different (and often distant) areas. This phenomenon may occur quite often in indoor environments.

In order not to stray too far from traditional WLAN fingerprinting techniques, we thought to maintain a traditional approach and merely increase the information related to each reference point. Specifically, according to the proposed approach, the observed area is split into *zones* and each reference point, besides a position $(x, y)$, has also a "belonging zone" associated. Zones are individuated by RFID tags, positioned within the area of interest. This hopefully counters the possible ambiguity in the choice of the right area.

To take into account the variability of the propagated WLAN signal (affected by phenomena of reflection, diffraction, and scattering) measurements at one WLAN reference point need to be repeated $n_o$ times (*number of observations*) and suitably selected. A preliminary study has shown that an acceptable number of RSSI observations, which gives a robust characterization of each reference point, is $n_o = 40$, relevant to each of the available APs. For each AP, the most frequent value of RSSI is selected among 40 available values. This might seem a too simplistic assumption, but optimization of reference point characterization is not an issue we are interested into, because the aim of the algorithm presented in this paper is to improve the positioning accuracy through the synergic action of two technologies. In the literature, more effective ways to characterize the reference points are available; whatever the choice, still the effectiveness of our approach is granted.

*Phase 2* (online: positioning the mobile unit). During the online position determination phase, different from the traditional approach, our proposal exploit two kinds of measurement to identify the unknown position of a Mobile Unit (MU). Both the WLAN interface and the RFID mobile reader (plugged into the MU) measure the RSSI values from APs and RFID tags, respectively. The actual advantages of the proposal emerge during this phase. In fact, the mobile device can take its decision about its estimated position by counting on RFID RSSI measurements, in addition to the traditional WLAN RSSI values to be compared with the fingerprints in the database. More specifically, the envisaged algorithm applies a two-step approach.

First, it identifies the "zone" in the observed area where the MU is likely located, by basing its decision on RSSI values received from the RFID tags scattered across the environment and associated to each zone. During the zone identification phase, the RFID reader in the MU generates a sequence of interrogations, that is, it broadcasts *scan* messages that wake up the reachable tags and query their IDs, and associates to each identified tag an RF power level. In any position, the reader will get signals from multiple tags under its coverage and select the strongest tag signals and, consequently, the associated zone. As a results, a "rough" MU position estimation is performed.

Second, the information relevant to the estimated zone is used to filter the WLAN RSSI entries in the database, over which the best matching algorithm must be executed. This drastically reduces ambiguities in associating measured RSSI values to fingerprinting values, thus enhancing the accuracy and effectiveness of the overall method. This second step is thus a sort of "refinement" of the localization estimation process. Figure 1 illustrates the whole process foreseen by the proposed approach.

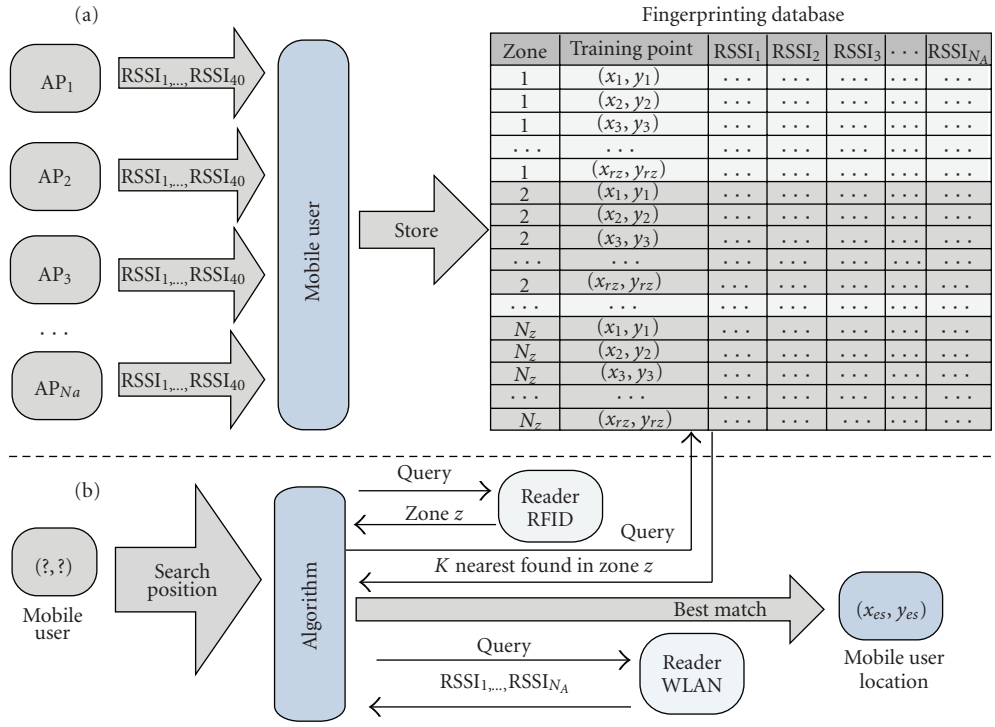


Figure 1: Online (a) and offline (b) phases of the proposed algorithm.

```
//zone determination: get the zone with the strongest RSSI value
for each zone in numZone
    for each tag in numTag
      maxTagRSSI [zone] = ValueRSSI (tag, zone);

selectedZone = zone with highest maxTagRSSI;

//for each AP, the most frequent value of RSSI is selected among the
numObservations available
for each ap in numAP
    for each obs in numObservations
      vectorRSSI [ap] = mostFrequentRSSI (ap, obs);

//search the k nearest reference points to vectorRSSI in zone subset of
database
selectedReferencePoints = searchDB (selectedZone, vectorRSSI, k);

userPosition = weightedFunction (selectedReferencePoints)
```

Algorithm 1: *Maximum RSSI mode:* pseudocode description.

During the zone determination phase, the RFID reader in the MU can act in two alternative ways. According to the first mode, named *maximum RSSI*, the reader generates a sequence of interrogations with increased transmission power. The Reader starts interrogating at the lowest admitted transmission power and stops when the first tag (likely the nearest) is reached. If more than one tag is detected, then only the one with the highest transmission power is considered as an indicator of the location zone. Algorithm 1 shows the pseudocode description of this approach. According to the alternative policy, named *average RSSI* instead, the Reader directly starts interrogating tags at the highest allowed transmission power, in order to detect the largest number of RFID tags is possible, and calculates an average RSSI value per zone, according to the pseudo-code in Algorithm 2. The higher computational load of the average RSSI approach when compared to the maximum RSSI approach, is counterbalanced by the lower cost of the former method in terms of positioning time; it, in fact, avoids the progressive augmentation of the transmitted power in 1dbm steps, until a RFID tag is detected.

```
//zone determination: get the zone with the strongest average RSSI value
for each zone in numZone
    for each tag in numTag
      averageTagRSSI [zone] = valueRSSI (tag, zone);

selectedZone = zone with max averageTagRSSI;

//for each AP, the most frequent value of RSSI is selected among the
numObservations available
for each ap in numAP
    for each obs in numObservations
      vectorRSSI [ap] = mostFrequentRSSI (ap, obs);

//search the k nearest reference points to vectorRSSI in zone subset of
database
selectedReferencePoints = searchDB (selectedZone, vectorRSSI, k);

userPosition = weightedFunction (selectedReferencePoints);
```

Algorithm 2: *Average RSSI mode:* pseudocode description.

## 4. Performance Analysis

In this section, a comprehensive performance evaluation campaign, which aims at assessing the behaviour of the proposed hybrid WLAN-RFID solution, is illustrated.

The first steps are the definition of a metric to quantify location errors, that is, the distance between estimated position and actual position, and the setting up of a test-bed to perform our evaluation campaign. With reference to a given zone of interest $z \in [1, N_Z]$ in which the best matching algorithm has to be run, and to a number $n$ of APs, let's define $S_{pz} = \{\text{RSSI}_{pzn}\}_{n=1,\ldots,N_A}$, a generic power vector for any $p$th reference point (with $p \in [1, r_z]$) belonging to the zone $z$. As addressed above, during the online position determination phase, the zone $z$ is individuated by scanning the closest RFID tags.

As a subsequent step, the algorithm scans and collects the RSSI values received from different APs. Let's define $\theta = \{\text{RSSI}_n\}_{n=1,\ldots,N_A}$ the *n-uple* of power values measured by the mobile device's WLAN card in the unknown position. Thus, a set of distances can be defined in the RSSI space, between the set of collected measures from the unknown position and each reference point of the generic zone $z$, $e_{pz} = d(\theta, S_{pz})$, $E = \{e_{pz}\}_{p=1,\ldots,r_z}$. The vector $E$ of distances is used to apply the *k-nearest neighbours* algorithm.

As regards the definition of distance $d$ in the space of RSSI measures and relevant weights $w$, we utilize the *Euclidean distance in signal strengths*, defined as

$$d_{pz} = \sqrt{\sum_{n=1}^{N_A} \left(\theta - S_{pz}\right)^2}, \tag{1}$$

and a *weight function,* referred to as *received power,* defined as

$$w_m = \frac{1/e_{pz_m}}{\sum_{m=1}^{k} 1/e_{pz_m}}. \tag{2}$$

To quantify the performance levels of our approach, the error distance is used as a metric of the accuracy of the system.

*4.1. Indoor Test-Bed Definition.* An indoor test-bed is deployed in an office floor of the University of Reggio Calabria, Italy, and measurements are taken in "non ideal" conditions, that is, usual environmental conditions during working hours (please refer to Figures 2(a) and 2(b) for the scenario layout—AP and Tag positions, as well as zone splitting, are *only for illustration purposes*). Experiments are carried out by using i-Q RFID tags produced by Identec Solutions and operating in the UHF range [24], capable of up to 100 m identification range; WLAN Access Point model is WL-537 produced by 3Com [25] while the portable RFID reader, is a low-cost Identec i-Card3 PCMCIA reader, mounted on a Acer laptop PC with wireless card Intel(R) PRO/Wireless 2200BG programmed to run the proposed algorithms. The i-Card3 reader generates interrogations at different RF transmission power values, ranging between −60 dbm and 10 dbm.

Design parameters considered during the evaluation campaign are: (i) *number of zones* ($N_Z$) discriminated by means of active RFID tags in the area of interest, (ii) *gap* ($\Delta$) in centimetres between reference points belonging to the WLAN RSSI grid, (iii) *number of access points* ($N_A$).

In the remaining part of the paper four different evaluation campaigns are illustrated to give the reader an accurate view of the algorithm potentials. Being the last set of experiments performed outdoor, an outdoor test-area, which will be better described later, has been exploited.

*4.2. First Campaign: "Max RSSI Values" Hybrid versus WLAN Fingerprinting.* The first set of measurement aims at comparing the performance of the Hybrid WLAN-RFID algorithm and of the well-know RADAR [4] technique, used as a reference in our test-bed. In the specific sample scenario

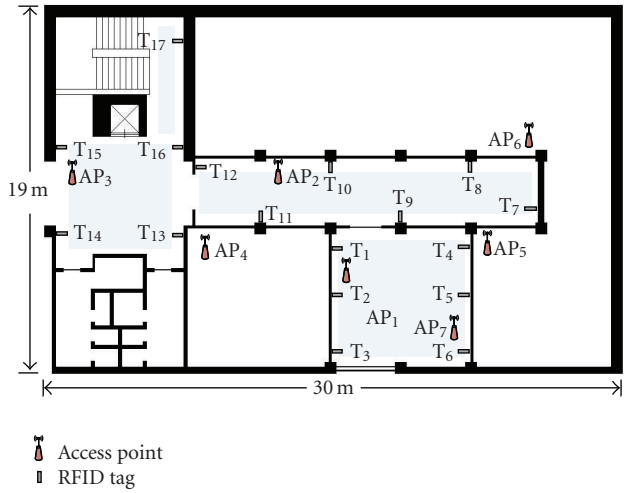


(a)

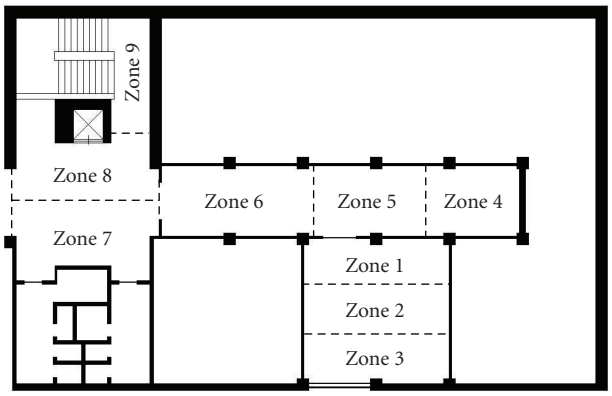


(b)

Figure 2: (a) Indoor area chosen for the experiments; (b) example of splitting into zones.

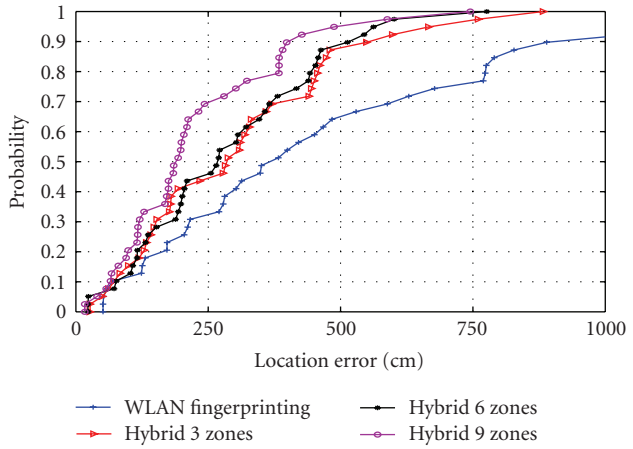


Figure 3: WLAN Fingerprinting versus Hybrid WLAN-RFID: location error; $N_Z = [3, 6, 9]$, $\Delta = 240$ cm, $N_A = 4$; "maximum RSSI" mode.

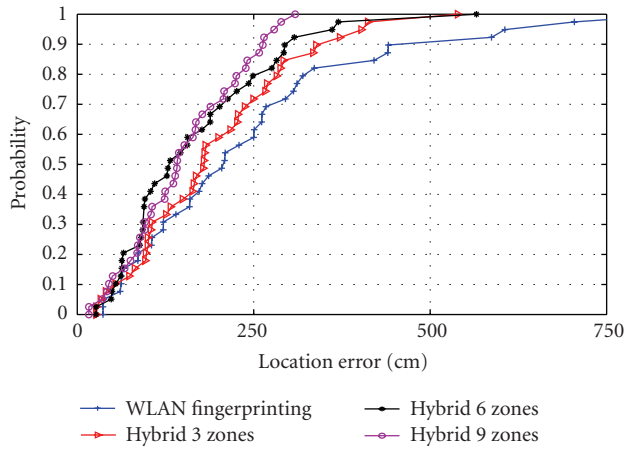


Figure 4: WLAN Fingerprinting versus Hybrid WLAN-RFID: location error; $N_Z = [3, 6, 9]$, $\Delta = 120$ cm, $N_A = 7$; "maximum RSSI" mode.

presented in this initial campaign, we set $N_Z = [0, 3, 6, 9]$, $\Delta = [240, 120]$, and $N_A = [4, 7]$. $N_Z = 0$ is the special case of WLAN fingerprinting approach only, without the presence of RFID tags; obviously, this corresponds to the standard RADAR algorithm.

Initial studies focuses on the *maximum RSSI approach*, with a RFID Reader transmission power progressively increasing in steps of 1 dbm at a time, until one (or more) RFID tag is detected. The main objective is the evaluation of the influence that system parameters have on the proposed approach. To this purpose, the performance of the positioning algorithm is evaluated by varying number of zones $N_Z$, gap between reference points $\Delta$, and number of access points $N_A$.

What is expected is a significant decrease in location errors consequent to denser grids of reference WLAN points (i.e., reduction of the $\Delta$ value). Also, an increase in the number of WLAN APs would favour a performance increase, due to the beneficial effect of the greater number of RSSI samples taken into consideration. Lastly, by increasing the number of zones identified through the RFID technology, the positioning errors are likely reduced, due to the more accurate matching among measures and entries in the fingerprinting database.

In Figure 3, a comparison between the *WLAN only* and the *hybrid WLAN-RFID* fingerprinting technique, for a variable number of zones, is shown. Curves illustrate the experimental cumulative distributions of the location errors of both fingerprinting algorithms, when $k = 3$ reference WLAN points are selected as *near WLAN points* and *received power* is used as the weight function among near WLAN points. The choice of the number of near WLAN points is the result of a tuning campaign that considered a trade-off between attainable location accuracy and computational load. In this sample configuration, the hybrid solution attains a lower location error when increasing the number of zones; this witnessing to the beneficial effects of the introduction of RFID technologies into WLAN positioning methods.

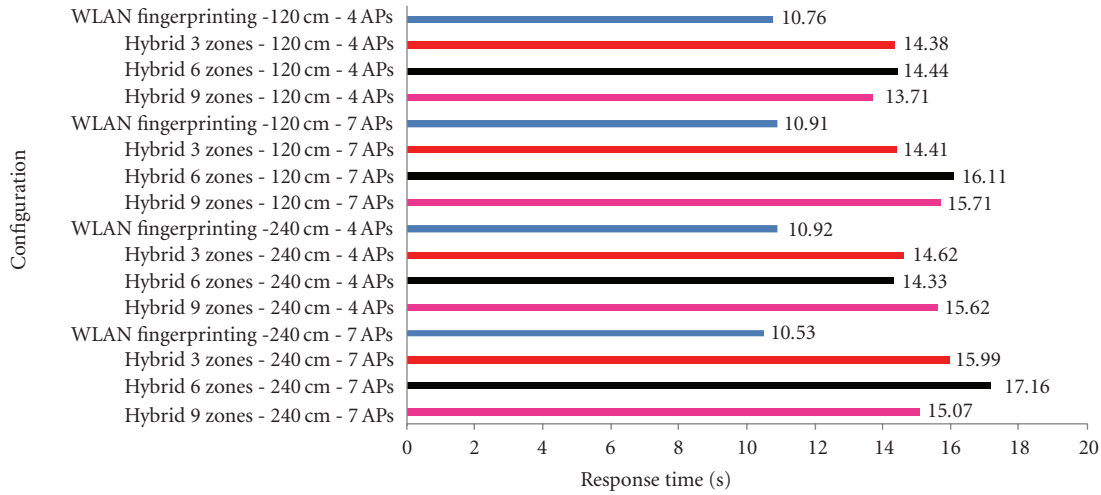


Figure 5: Response time in different configurations ("maximum RSSI" mode).

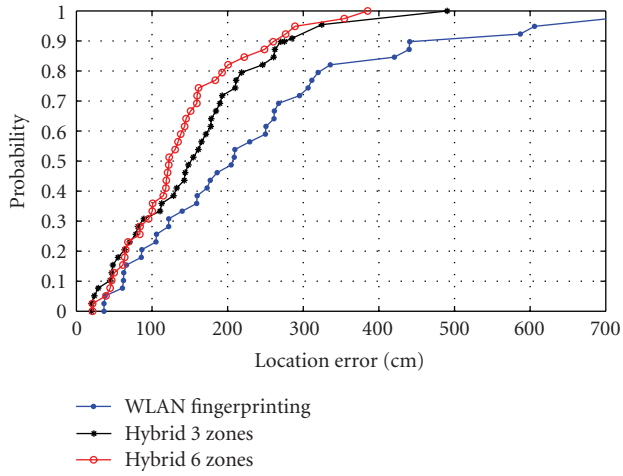


Figure 6: WLAN Fingerprinting versus Hybrid WLAN-RFID: location error; $N_Z = [3, 6]$, $\Delta = 120$ cm, $N_A = 7$; "average RSSI" mode.

Table 1: Location estimation error.

| $\Delta$ | $N_A$ | Algorithm | Average Error (cm) | $Error_{90\%}$ (cm) |
|---|---|---|---|---|
| 240 cm | 4 | *WLAN Fingerprinting* | 504 | 904 |
| | | Hybrid - 3 zones | 308 | 554 |
| | | Hybrid - 6 zones | 291 | 516 |
| | | Hybrid - 9 zones | 237 | 401 |
| | 7 | *WLAN Fingerprinting* | 350 | 732 |
| | | Hybrid - 3 zones | 270 | 509 |
| | | Hybrid - 6 zones | 221 | 416 |
| | | Hybrid - 9 zones | 180 | 295 |
| 120 cm | 4 | *WLAN Fingerprinting* | 441 | 952 |
| | | Hybrid - 3 zones | 250 | 461 |
| | | Hybrid - 6 zones | 198 | 380 |
| | | Hybrid - 9 zones | 171 | 289 |
| | 7 | *WLAN Fingerprinting* | 249 | 455 |
| | | Hybrid - 3 zones | 198 | 342 |
| | | Hybrid - 6 zones | 168 | 295 |
| | | Hybrid - 9 zones | 152 | 263 |

The good level of performance significantly improves when thickening the grid of reference points and increasing the number of WLAN APs, as Figure 4 shows.

Results are highly valuable, compared to what is available in the literature, if we consider the good trade-off among achieved performance, amount of used equipment, and low cost of the solution. Each probability value plotted in Figure 4 is computed with a 95% confidence interval.

In Table 1 location estimation errors obtained during different measurement campaign are reported. In the last column figures relevant to the location estimation error when considering 90% of the measurements, $Error_{90\%}$, are reported.

Parameter values considered are those that show a better trade-off between positioning accuracy, equipment costs, and processing time. This last aspect shall be better investigated if we recall that, differently from a RADAR-like fingerprinting approach, in a hybrid WLAN-RFID solution the number of iterations in the fingerprint database to search the best match is smaller, due to a reduced localization area. Notwithstanding, one might think that this advantage is invalidated by the lengthening of the computational time, due to the additional phase of zone identification.

In Figure 5, an increase in the average response time of the hybrid solution compared to traditional WLAN fingerprinting is confirmed. Fortunately, a small increase, ranging from 3 seconds to 4 seconds only, is observed; this demonstrates that the advantages in terms of achievable location accuracy overcome the disadvantages caused by the additional processing delay.

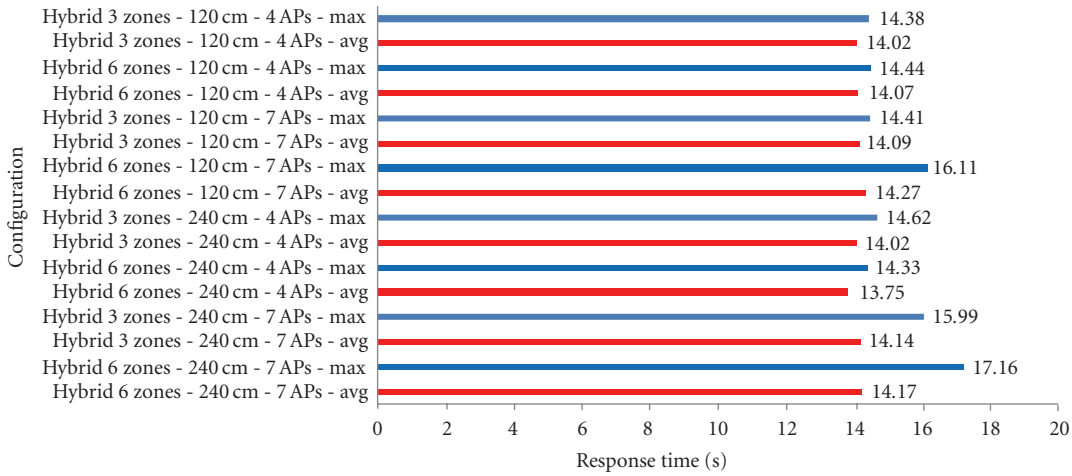


Figure 7: Response time: comparison of "average RSSI" (Avg) mode and "maximum RSSI" (Max) mode.

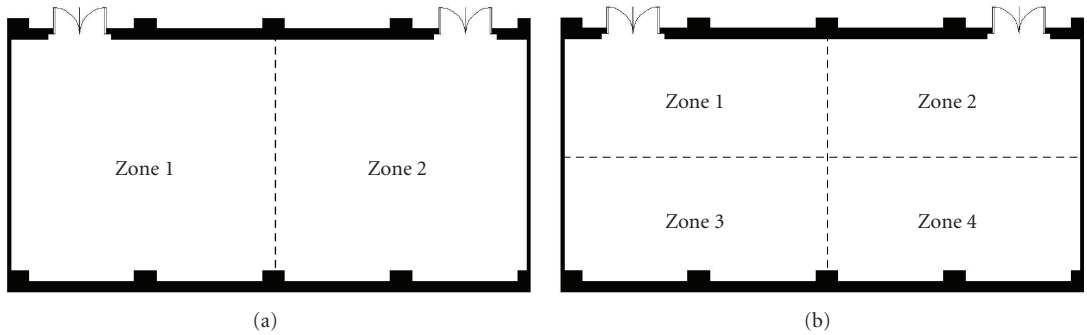


Figure 8: Area of localization split into (a) 2 and (b) 4 zones.

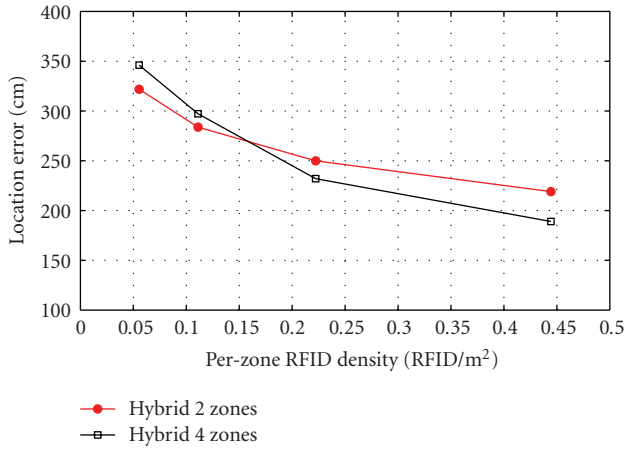


Figure 9: Comparison of location error: Hybrid with 2 zones versus Hybrid with 4 zones when varying per-zone RFID density.

*4.3. Second Campaign: "Maximum RSSI" versus "Average RSSI" Modes.* The test campaign illustrated in the present section aims at comparing two possible approaches to the zone selection: "maximum RSSI" and "average RSSI" modes. In Figure 6, sample curves of location error probability are reported, which show how the latter approach overcomes the former in terms of performance.

For a thorough comparison of the two approaches, the reader can refer to the output of sample test campaigns reported in Table 2. It is manifest that the "average RSSI" approach allows for an additional location accuracy with respect to the "maximum RSSI" mode.

The average performance increase is about 22,5% when considering the 90% measurement error (about 1 additional meter of accuracy achievable) and 17,3% (about 40 cm) when considering the average localization error. The response time also decreases (please refer to Figure 7). Specifically, under the same test conditions an average reduction of the response time equal to 7% (more that 1 second less) is observed.

The main reason of a better location accuracy is that the choice of considering average RSSI values of RFID tags better fits the radio propagation characteristics in indoor environments (such as, severe multipath, rare LOS path, absorption, diffraction, and reflection [26]). This reduces the number of zone errors and false positives. The variant based on the maximum RSSI values would, in fact, be deceived by the likely presence of spurious peaks of power in the RFID responses. In the average RSSI variant, during the estimation of the reference zone, any power peak in the zone is offset.

Table 2: Location estimation error for maximum RSSI and average RSSI techniques.

| Δ | $N_A$ | Algorithm | | Average Error (cm) | Error$_{90\%}$ (cm) |
|---|---|---|---|---|---|
| 240 cm | 4 | *WLAN Fingerprinting* | | 504 | 904 |
| | | Hybrid 3 zones | Max | 308 | 554 |
| | | | Average | 264 | 526 |
| | | Hybrid 6 zones | Max | 291 | 516 |
| | | | Average | 212 | 326 |
| | 7 | *WLAN Fingerprinting* | | 350 | 732 |
| | | Hybrid 3 zones | Max | 270 | 509 |
| | | | Average | 215 | 366 |
| | | Hybrid 6 zones | Max | 221 | 416 |
| | | | Average | 194 | 311 |
| 120 cm | 4 | *WLAN Fingerprinting* | | 441 | 952 |
| | | Hybrid 3 zones | Max | 250 | 461 |
| | | | Average | 213 | 337 |
| | | Hybrid 6 zones | Max | 198 | 380 |
| | | | Average | 168 | 284 |
| | 7 | *WLAN Fingerprinting* | | 249 | 455 |
| | | Hybrid 3 zones | Max | 198 | 342 |
| | | | Average | 158 | 270 |
| | | Hybrid 6 zones | Max | 168 | 295 |
| | | | Average | 143 | 260 |


Figure 10: Outdoor localization area.

Please notice that, besides the advantage in terms of accuracy, response time decreases: this situation is justified by the type of interrogation carried out by the RFID reader. In case of "maximum RSSI", the Reader runs a series of tag interrogations at increasing power, awaiting for tag response (with the consequent waste of time in case of unanswered questions); differently, in case of "average RSSI," the Reader interrogates tags only at its maximum power.

*4.4. Third Campaign: Dependence on the Density of RFID Tags.* So far, we have shown that the estimated location error of the Hybrid approach depends on the number of zones in the area of interest, the number of APs used, the gap among WLAN training points, and, finally, by the algorithm by which a zone is identified. Now we want to demonstrate that a further parameter to be considered, to a full discussion, is the density of RFID tags. The expected behaviour is that the location estimate accuracy increases by increasing the tag density because, once again, false positives are reduced. With the introduction of our hybrid approach we are able to distinguish two types of false positives: *intra-zone* and *inter-zone* false positives. Intra-zone false positives are typical of WLAN fingerprinting techniques. Inter-zone false positives are a peculiarity of our algorithm. Parameters $N_Z$, $N_A$, and Δ affect intra-zone false positives; while the area identification algorithm and the density of RFID tags are responsible for inter-zone false positives. The latter type of false positives affects tracking errors more than the previous one because, if the zone is wrongly identified, the portion of database considered by the usual fingerprinting technique does not include any combination [RSSI$_1$,...,RSSI$_{N_A}$] associated with the test point (or its surroundings); therefore, localization error certainly occurs.

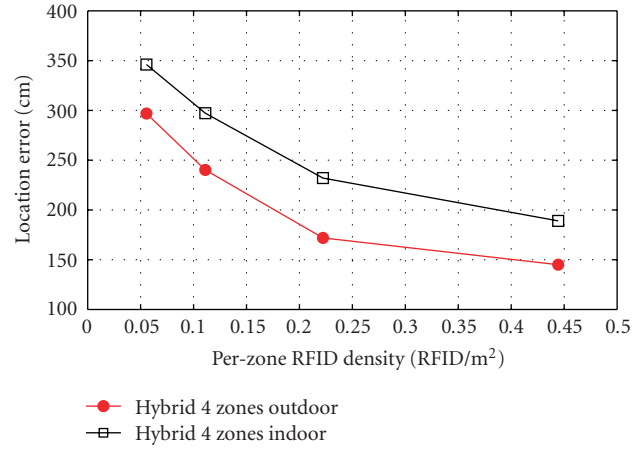


Figure 11: Comparison of location error between Hybrid 4 zones indoor and Hybrid 4 zones outdoor while varying the per-zone RFID density.

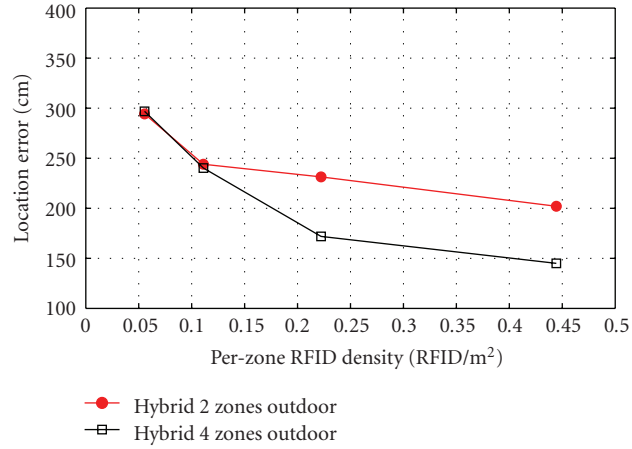


Figure 12: Comparison of location error between Hybrid 2 zones and Hybrid 4 zones while varying the per-zone RFID density.

A different test area is set up (due to the need for symmetrical conditions) to perform the analysis of the effects of tag density, as in Figures 8(a) and 8(b). In this scenario we consider constant parameters $N_A = 4$ and $\Delta = 150$, whereas the best algorithm of zone selection, that is, *average RSSI*, is used. Therefore, let us introduce a new parameter, the *per-zone RFID density* ($Pz_{Rd}$), which defines the RFID tag density used in each zone. The location accuracy performance will be evaluated in terms of per-zone RFID tag density (RFID/m$^2$), when considering the sample cases $N_Z = 2$ and $N_Z = 4$.

Figure 9 shows the location error vs. the density of RFID tags, both for the hybrid algorithm with 2 zones and for the hybrid algorithm with 4 zones. The figure shows that curves intersect for $Pz_{Rd} = 0.15$ RFID tags/m$^2$. In general, as shown in the first test campaign, the benefits in terms of location accuracy improve when increasing the number of zones. Actually, this rule is valid above a given RFID tag density $Pz_{Rd}$ threshold, here $Thr_{density}$. Below the threshold, in fact, the phenomenon of indoor interference (multipath fading) makes the Tag-to-Reader power response unstable and unreliable. Then, the zone selection algorithm, although working on average values, still shows a higher failure probability when the number of zones increases (for the same number of RFID tags), and commits a greater number of inter-zone mistakes. Specifically,

(i) when $Pz_{Rd} < Thr_{density}$, the inter-zone error is more frequent and, therefore, a limited zoning should be considered;

(ii) when $Pz_{Rd} \geq Thr_{density}$, the inter-zone error is uncommon, the intra-area error (due to WLAN) dominates, and then a more extensive zoning can be considered.

*4.5. Fourth Campaign: Outdoor Scenario.* Now let us consider an outdoor scenario (Figure 10), in order to highlight how the performance of the proposed algorithm changes. We consider an area in which barriers and electromagnetic phenomena are less manifest than in typical indoor environments.

It is expected that inter-zone errors, due to the RFID technology, and intra-zone errors, due to the WLAN technology, are less than in the indoor case. Furthermore, it is also important to analyze how the value of $Thr_{density}$ varies in certain conditions.

In order to compare indoor and outdoor scenarios, let us consider again $N_A = 4$, $\Delta = 150$, and the "*average RSSI*" algorithm for zone selection. Figure 11 shows the performance, in terms of location error, of the hybrid algorithm with 4 zones both indoor and outdoor, when varying the RFID tag density. It is also interesting to understand if the proposed positioning method can be exploited *with continuity* when passing from the inside out. As expected, the best performance is achieved outdoor, as less inter- and intra-zone errors are experienced. This is due to the fact that undesired interfering phenomena are contained, or at least reduced, compared to the indoor case. Similar behaviour can be demonstrated with any value of $N_Z$.

In the outdoor environment, errors of localization with varying density of RFID tags are illustrated in Figure 12, both for the case Hybrid 2 zones and for the case Hybrid 4 zones. It is observed that the value $Thr_{density}$ is now lower than indoor, about 0.08 RFID tags/m$^2$. This feature is a direct consequence of the lower interference conditions in which the Hybrid algorithm is operating. We can, therefore, state that, in outdoor environments, the proposed algorithm works well even for low RFID tag densities.

## 5. Conclusions

In this paper we investigated the feasibility of a new approach to positioning, which exploits *WLAN and RFID Integration* to enhance the performance of a localization algorithm in indoor scenarios. We started from the well-know fingerprinting approach, based on the evaluation of RF power levels from various WLAN 802.11 APs (Access Points). Besides, RFID technology has been introduced to split into zones the whole localization area. A first positive effect has been the severe reduction of the number of search iterations in the fingerprints database (by forcing the algorithm to search the best match only within the actual area of interest). A further effect of the joint use of the two technologies has been the more accurate estimates of the client device position and a manifest reduction in the localization error. A thorough measurement campaign is conducted in indoor and outdoor environments to study the impact of main project parameters affecting the final location accuracy, in order to determine the best operational conditions. The results testified both to the feasibility of the proposed solution and to its higher accuracy when compared to a traditional WLAN-based reference positioning technique.

## References

[1] E. Kaplan and C. Hegarty, *Understanding GPS: Principles and Applications*, Artech House, Boston, Mass, USA, 2nd edition, 2005.

[2] Aerocut, http://www.aeroscout.com/.

[3] Ekahau Positioning System, http://www.ekahau.com/.

[4] P. Bahl and V. N. Padmanabhan, "RADAR: an in-building RF-based user location and tracking system," in *Proceedings of the 19th Annual Joint Conference of the IEEE Computer and Communications Societies (INFOCOM '00)*, vol. 2, pp. 775–784, Tel-Aviv, Israel, March 2000.

[5] J. Small, A. Smailagic, and D. Siewiorek, "Determining user location for context aware computing through the use of a wireless LAN infrastructure," December 2000.

[6] M. Youssef, A. Agrawala, and A. U. Shankar, "WLAN location determination via clustering and probability distributions," in *Proceedings of the 1st IEEE International Conference on Pervasive Computing and Communication (PerCom '03)*, Fort Worth, Tex, USA, March 2003.

[7] Bluelon, http://www.bluelon.com/.

[8] Y. Gwon, R. Jain, and T. Kawahara, "Robust indoor location estimation of stationary and mobile users," in *Proceedings of the 23rd Annual Joint Conference of the IEEE Computer and Communications Societies (INFOCOM '04)*, vol. 2, pp. 1032–1043, March 2004.

[9] S. Ganu, A. S. Krishnakumar, and P. Krishnan, "Infrastructure-based location estimation in WLAN networks," in *Proceedings of IEEE Wireless Communications and Networking Conference (WCNC '04)*, vol. 1, pp. 465–470, March 2004.

[10] D. Madigan, E. Elnahrawy, R. P. Martin, W.-H. Ju, P. Krishnan, and A. S. Krishnakumar, "Bayesian indoor positioning systems," in *Proceedings of the 24th Annual Joint Conference of the IEEE Computer and Communications Societies (INFOCOM '05)*, vol. 2, pp. 1217–1227, March 2005.

[11] A. M. Ladd, K. E. Bekris, A. Rudys, D. S. Wallach, and L. E. Kavraki, "On the feasibility of using wireless Ethernet for indoor localization," *IEEE Transactions on Robotics and Automation*, vol. 20, no. 3, pp. 555–559, 2004.

[12] U. Großmann, C. Röhrig, S. Hakobyan, T. Domin, and M. Dalhaus, "WLAN indoor positioning based on Euclidian distance and interpolation (Isobars)," in *Proceedings of the 8th Wireless Technologies Kongress*, pp. 296–305, Dortmund, Germany, September 2006.

[13] "WhereNet location tracking systems," http://www.wherenet.com/.

[14] L. M. Ni, Y. Liu, Y. C. Lau, and A. P. Patil, "LANDMARC: indoor location sensing using active RFID," *Wireless Networks*, vol. 10, no. 6, pp. 701–710, 2004.

[15] S. Polito, D. Biondo, A. Iera, M. Mattei, and A. Molinaro, "Performance evaluation of active RFID location systems based on RF power measures," in *Proceedings of IEEE International Symposium on Personal, Indoor and Mobile Radio Communications (PIMRC '07)*, Athens, Greece, September 2007.

[16] J. Bohn, "Prototypical implementation of location-aware services based on super-distributed RFID tags," in *Proceedings of the 19th International Conference on Architecture of Computing Systems (ARCS '06)*, vol. 3894 of *Lecture Notes in Computer Science*, pp. 69–83, Springer, Frankfurt, Germany, 2006.

[17] M. Hirose and T. Amemiya, "Wearable finger-braille interface for navigation of deaf-blind in ubiquitous barrier-free space," in *Proceedings of the 10th International Conference on Human-Computer Interaction (HCI '03)*, Crete, Greece, June 2003.

[18] S. Willis and S. Helal, "RFID information grid for blind navigation and wayfinding," in *Proceedings of the 9th International Symposium on Wearable Computers (ISWC '05)*, pp. 34–37, IEEE Computer Society, Washington, DC, USA, 2005.

[19] G. Ghiani, B. Leporini, and F. Paternò, "Vibrotactile feedback as an orientation aid for blind users of mobile guides," in *Proceedings of the 10th International Conference on Human-Computer Interaction with Mobile Devices and Services (MobileHCI '08)*, pp. 431–434, Amsterdam, The Netherlands, 2008.

[20] D. Hähnel, W. Burgard, D. Fox, K. Fishkin, and M. Philipose, "Mapping and localization with RFID technology," in *Proceedings of IEEE International Conference on Robotics and Automation (ICAR '04)*, pp. 1015–1020, 2004.

[21] M. Banâtre, M. Becus, P. Couderc, and J. Pauty, "Ubibus: ubiquitous computing to help blind people in public transport," in *Proceedings of the 6th International Symposium on Mobile Human-Computer Interaction (MobileHCI '04)*, vol. 3160 of *Lecture Notes in Computer Science*, pp. 310–314, 2004.

[22] J. Hightower, *The Location stack*, Ph.D. thesis, Department of Computer Science & Engineering, University of Washington, Seattle, Wash, USA, 2004.

[23] A. LaMarca, Y. Chawathe, S. Consolvo, et al., "Place lab: device positioning using radio beacons in the wild," in *Proceedings of the 3rd IEEE International Conference on Pervasive Computing and Communication (Pervasive '05)*, vol. 3468, pp. 116–133, 2005.

[24] Identec solutions, http://www.identecsolutions.com/.

[25] 3Com, http://www.3com.com/.

[26] T. Rappaport, *Wireless Communications: Principles and Practice*, Prentice Hall, Upper Saddle River, NJ, USA, 2001.

Hindawi Publishing Corporation
International Journal of Navigation and Observation
Volume 2010, Article ID 294525, 8 pages
doi:10.1155/2010/294525

*Research Article*

# A Method to Assess Robustness of GPS C/A Code in Presence of CW Interferences

**Beatrice Motella,[1] Simone Savasta,[2] Davide Margaria,[2] and Fabio Dovis[2]**

[1] *Navigation Lab, Istituto Superiore Mario Boella, via P.C. Boggio 61, 10138 Torino, Italy*
[2] *Dipartimento di Elettronica, Politecnico di Torino, C.so Duca degli Abruzzi 24, 10129 Torino, Italy*

Correspondence should be addressed to Davide Margaria, davide.margaria@polito.it

Received 1 October 2009; Revised 9 March 2010; Accepted 1 June 2010

Academic Editor: Marco Luise



Navigation/positioning platforms integrated with wireless communication systems are being used in a rapidly growing number of new applications. The mutual benefits they can obtain from each other are intrinsically related to the interoperability level and to a properly designed coexistence. In this paper a new family of curves, called Interference Error Envelope (IEE), is used to assess the impact of possible interference due to other systems (e.g., communications) transmitting in close bandwidths to Global Navigation Satellite System (GNSS) signals. The focus is on the analysis of the GPS C/A code robustness against Continuous Wave (CW) interference.

## 1. Introduction

In the last years navigation technology is becoming essential for several civil applications, some of them even unthinkable at the time of the satellite navigation starting. Alongside the wide use in the transports fields (e.g., aviation, maritime, rail, and road), the range of civil uses is constantly increasing. Surveying, precision agriculture, environmental protection, scientific research (e.g., monitoring geological change, wildlife behaviour, atmospheric modelling, oceanic studies, space exploration), time-based applications (e.g., line power or telecommunications network synchronization and management) are examples of the most various applications based on the estimation of the user Position, Velocity, and Time (PVT).

This kind of applications, especially those devoted to safety, requires the coexistence of different communication systems and GNSS. The use of receivers able to provide multiple services, such as user position estimation and data transmission, embeds the problem of managing different systems with different specifications.

Despite Wireless Communication Systems (WCSs) use of different carrier frequencies with respect to GNSS bands, they could likewise represent potential threats for GNSS modules integrated in personal devices and communication units. This is due to the low-received GNSS signal power [1, 2], which makes the systems vulnerable to potential dangerous effects caused by undesired and unintentional interfering signals that might appear in the GNSS bandwidths. These interferences could compromise the correct functioning of the main blocks of the GNSS receiver chain, such as acquisition and tracking stages.

This fact would affect also the service based on the integrated communication/positioning system and might result in dangerous failures for those applications oriented to safety of life or as the ones involving financial transactions. For this reason, the development of strategies devoted to analyze and mitigate the impact of undesired signals that could compromise the correct integration of WCSs and GNSS receivers becomes crucial.

In this paper a tool for the evaluation of the potential receiver performance in presence of interfering signals is proposed. The strategy is based on a class of curves named Interference Error Envelope (IEE) and the derived Interference Running Average (IRA), able to assess the error made in the user position estimation due to the presence of an interference signal generated by some WCSs.

The paper is structured as follows. Section 2 gives an overview of real cases of GNSS malfunctioning due to presence of WCSs interference in GNSS bands. Sections 3 and 4 are dedicated to present the concepts of Interference Error Envelope and Interference Running Average and to explore the use of the IEE for assessing the GPS C/A code robustness. At the end some conclusions on the use of the proposed tools will be drawn.

## 2. Interference Impact on GNSS

It is well known that a GNSS receiver can be vulnerable to many classes of undesired signals. These disturbances can lead to a complete misbehaviour of the operational blocks in the receiver chain with consequences such as erroneous user position estimations or up to a full outage. This weakness is due to the low-power level of the Signal in Space (SIS) from which the pseudorange information is extracted (e.g., −158.5 dBW for GPS L1 C/A civil code [1] and −157 dBW expected for Galileo E1 [2]).

As a demonstration of interference vulnerability and jamming impact on GPS equipments, some trials have been recently conducted by the General Lighthouse Authorities of the United Kingdom and Ireland (GLA), in collaboration with the UK Ministry of Defence (MOD), Defence Science and Technology Laboratory (DSTL), aiming at assessing the effects of GPS jamming on safe navigation [3]. These trials demonstrated that when a GPS-equipped vessel enters in a jamming zone (area covered by an intentional jamming unit), numerous failures occur to systems based on GPS signals.

Every kind of communication system operating by frequencies near to the GNSS bands or with a high-power level with respect to GNSS, due to implementation imperfections, or to an inaccurate matching of the specifications, can affect the correct receiver functionalities. The presence of growing wireless communication infrastructures significantly increases the probability of spurious emissions in GNSS bands in some geographical area. An example of unintentional interference signal emissions is the malfunctioning of electronic devices (e.g.,: nonlinear amplifiers in TV transmitters) that might generate harmonics or intermodulation products.

In [4], the Digital Video Broadcasting—Terrestrial (DVB-T) system is analyzed as potential interference signal for both Galileo and GPS signals. Due to the high power transmitted, the harmonics of Orthogonal Frequency Division Multiplexing (OFDM) signal used in the DVB-T transmission have been analyzed, showing a degradation of the Carrier to density Noise ratio ($C/N_0$) up to 90 Km from the emitting sources.

In [5], an analysis of real interference sources in VHF and UHF bands is reported, highlighting how such kind of signals can partially or completely corrupt the GPS signal. Systems working at frequencies relatively far away from L1 band are explored as potential emitters in band by secondary harmonics.

Even if nonintentional Radio Frequency Interference (RFI) is not a priori predictable, several cases have been experienced in the past and reported in literature [6].

(i) In 1994, in Germany, Digital Repeater transmissions at 1200 MHz degraded the $C/N_0$ in L2 band denying a correct acquisition of GPS signal [7].

(ii) In 1995, both in Nice (France) and Vicenza (Italy), interferences related to secondary harmonics emitted by TV transmissions and microwave interference have been detected in GPS bands [7].

(iii) In 1995 at the Edinburg Airport (Germany), an interference due to a Distance Measuring Equipment (DME) transmitter caused a $C/N_0$ degradation [7].

(iv) In 1993, in the metropolitan Boston area (USA) an interference generated by TV emitters (Channel 10 and Channel 66) affected the quality of GPS signal forcing low $C/N_0$ with consequent tracking loss [7].

(v) In April 2006, DVB spurious emission of TV transmitters located in Torino (Italy) degraded the performance in the acquisition stage of a GPS receiver operating in the area, with consequently loss of the GPS signal tracking [8]. The interference was the same that ESA researchers detected using the Galileo Experimental Tracking Receiver (GETR) with the GIOVE-A E1 signals at INRIM (Torino) [9].

(vi) In July 2006, UHF harmonics have been detected in Sidney around TV antennas. The undesired signal in the L1 band corrupted the correct performance of the receiver chain observing significant variations in the AGC/ADC block and in the final user positioning [10].

In several cases, due to the nature of emitted signals with respect to the GNSS bands, the interference can be modelled as pure Continuous Wave (CW), i.e. sinusoidal signals. This kind of RFI might saturate the first stage of receiver chain, such as the Low Noise Amplifier (LNA) or the Automatic Gain Control (AGC) for the Analog to Digital Conversion (ADC), or might lead to erroneous position estimations. Due to its spectral characteristics, as it will be shown in Section 4, this kind of interference is considered one of the most critical for the GPS C/A code [11].

It must be noticed that the choice of using the CW interference as a model for WCSs do not prevent from drawing general conclusions on the interference vulnerability due to other interference sources. In fact, as already noticed by the authors in [12] and [13], IEE curves obtained with a CW interference can be easily used to predict the behaviour of the receiver in presence of different interfering sources (e.g., wideband interferences, applying a moving average on the CW IEE).

Next Section is then devoted to the introduction of the concepts of IEE and IRA curves.

## 3. Interference Impact Assessment Tools

Although the impact of CW interferences on GNSS receivers is a topic already approached in different publications, only in some cases theoretical and/or simulative models for the interference impact have been derived. In [14], a theoretical formula for the code tracking bias due to Continuous Wave interference has been introduced. In order to take into account also the receiver front-end filtering effect, in assessing the interference impact on receiver performance, a novel method (intended as both an analytical and simulative framework) has been recently defined by the authors in [12, 13].

A new family of curves, named Interference Error Envelope (IEE), is introduced as a reliable tool for evaluating the potential GNSS receiver performance in terms of potential positioning error due to the presence of interfering signals, varying one or more parameters of the interference (e.g., the carrier frequency for a CW signal) and/or the receiver setup (e.g., integration time, bandwidth, discriminator type, correlator spacing).

The IEE curves are based on a concept similar to that used for the well-known Multipath Error Envelopes (MEE, see [15]): the idea is to measure the worst-case distortion of the discrimination function when the useful SIS is affected by a specific type of interference.

Figure 1 shows a qualitative example of how the presence of an interference might distort a coherent discrimination function obtained with a GPS L1 (Binary Phase Shift Keying—BPSK modulation) signal. In this case the interferer is modelled as a CW signal, with the carrier frequency centred at 0.5 MHz from the GPS L1 carrier. Due to the CW, the code discrimination function in Figure 1 is distorted and a bias can be noticed in the zero-crossing (Delay Look Loop tracking point), leading to a ranging error.

A detailed theoretical analysis of the interference impact on GNSS receivers can be found in [13]. In general, assuming a received signal affected by a generic interference signal $i(t)$ at a frequency shift $f_i$ with respect to signal carrier frequency, the maximum bias ($b_{\max}$) on the zero-crossing point of the discrimination function can be computed as

$$b_{\max}(f_i) = \alpha \cdot \frac{2}{\mathrm{ML}} \int_{-\infty}^{\infty} |I(f)|\,|W(f)|\,|C(f)| \sin(\pi f \Delta) df, \tag{1}$$

where

(i) $\alpha = -(c \cdot T_C \cdot \Delta)/2$, being $c$ is the speed of light, $T_C$ the code chip duration, and $\Delta$ the Early-Late spacing;

(ii) $L$ is the length of a code period in samples and $M$ is the number of integration periods in the coherent integration time for computing the correlation values;

(iii) $I(f)$ is the Discrete Time Fourier Transform (DTFT) of the interference signal $i(t)$: $I(f) = \mathrm{DTFT}\{i(nT_s)\}$;

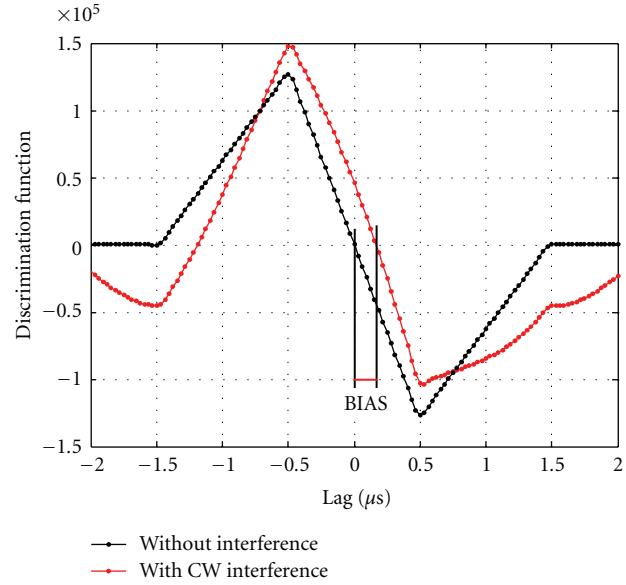


Figure 1: GPS L1 signal (BPSK) discrimination function distortion due to the presence of a CW interference (coherent Early-Late discriminator with 1 chip spacing, integration time equal to 4 ms).

(iv) $W(f) = \mathrm{DTFT}\{w(nT_s)\}$, being $w(nT_s)$ the discrete time impulse response modeling the receiver front end;

(v) $C(f) = \mathrm{DTFT}\{c(nT_s)\}$, being $c(t)$ the code chip sequence, including also the SIS modulation.

In case of a CW interference at a frequency shift $f_i$, $|I(f)|$ can be modeled as

$$|I(f)| = A \cdot \delta(f - f_i) \tag{2}$$

where $A$ is the amplitude of the CW interference.

Substituting (2) in (1), the maximum bias $b_{\max}^{\mathrm{CW}}$ in presence of a CW interference can then be expressed as

$$b_{\max}^{\mathrm{CW}}(f_i) = \alpha \cdot \frac{2A}{\mathrm{ML}} |W(f_i)|\,|C(f_i)| \sin(\pi f_i \Delta). \tag{3}$$

It is important to remark that in (1) and (3) the maximum distortion of the discrimination function depends not only on the features of the interference and the received signals, but also on the receiver setup (integration time, front-end filter, correlator spacing). For the complete derivation and validation of previous equations please refer to [13], where the generalization in case of wideband interferences is also presented.

The IEE is then defined as a measure of the maximum distortion of the discriminator function with respect to one (or more) parameter of the interfering signal: the worst cases corresponding to the maximum and minimum ranging error values (expressed in meters) are plotted versus one of the variable interference characteristics being considered (e.g., the carrier frequency for a continuous wave interferer) [12, 13].

The main innovation of the IEE and IRA curves with respect to other interference assessment methods is that they

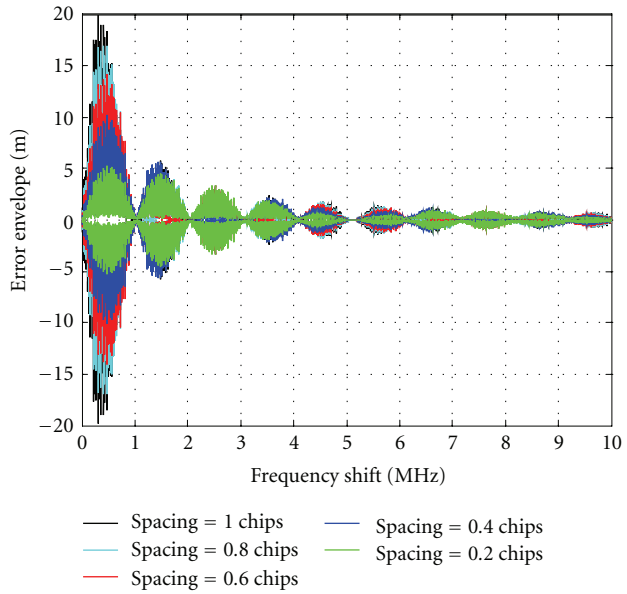


Figure 2: Interference Error Envelope comparison in presence of a CW interference obtained for a coherent Early-Late discriminator with different correlator spacings (from 0.2 to 1 chip) with a BPSK (GPS L1) signal.

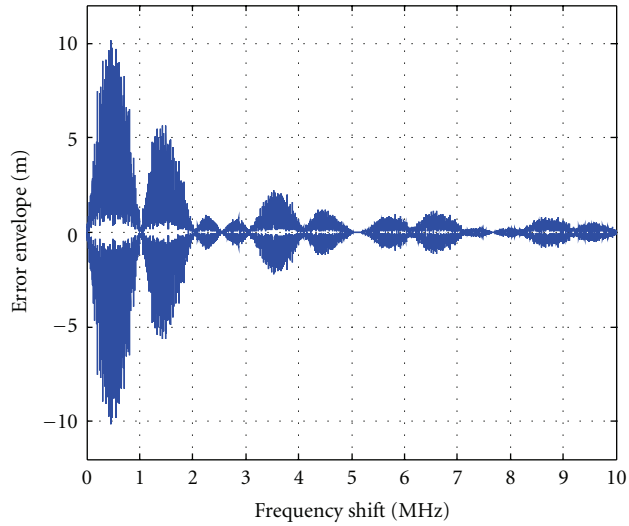


Figure 3: Interference Error Envelope in presence of a CW interference obtained for a coherent Early-Late discriminator with a correlator spacing of 0.4 chip with a BPSK signal.

are not limited to the analysis of the received signal features, allowing detailed analysis on specific interference parameters also taking into account the receiver setup.

As an example, in order to better understand the idea the method is based on, some IEE curves are depicted in Figure 2. In this case the effect of a CW interference on the GPS L1 signal (Binary Phase Shift Keying—BPSK modulation) is assessed, considering a coherent Early-Late discriminator with different correlator spacings (from 1 to 0.2 chips).

This plot has been obtained simulating a carrier to interference power ratio equal to 0 dB (same power for the useful SIS and the CW interference). The carrier frequency of the CW sweeps from 0 to 10 MHz with respect to the GPS L1 carrier frequency and its phase has been varied from 0 to $2\pi$.

The IEE curves in Figure 2 have then been obtained considering the maximum and the minimum values (over all the possible phases) of the ranging errors versus the CW carrier frequency (the $x$ axis represents the offset between the CW and the GPS carrier frequency). In this way a useful tool for assessing the worst-case errors (maximum and minimum) for each CW carrier frequency is provided.

From this kind of analysis and plots the ranging errors due to a specific interference can be easily evaluated. Observing Figure 2, the error envelopes present symmetry between positive and negative values with a shape similar to the BPSK spectrum. It is possible to notice that for large values of the correlator spacing the IEE curves present high-ranging errors while they decrease with the reduced Early-Late distance. But in all the cases the CW interference is more harmful if its carrier frequency is around 0.5 MHz (corresponding to the half of the main lobe of the spectrum) and then its impact decreases moving away from the central frequency.

The shape of the IEE and the resulting performance also depend on the characteristics of the specific PRN code being considered, as it will be discussed in Section 4. The zeros of Figure 2 depend on the modulation of two different contributes of (3) the following:

(i) The code elementary function, contained in the DTFT $C(f)$. In case of a BPSK signal the contribute is a sinc function with zeros defined by the inverse of the chip period $T_c$. Notice that in case of a BOC(1,1) modulation, the zeros position is different from the BPSK case since the chip shaping is defined by the combination of a sinc and a sine profile with period $1/T_c$ [13].

(ii) The sine function (dependent on the spacing $\Delta$). It introduces zeros accordingly to its period.

To show the modulation effect on the zeros placement due to the two contributes, the IEE of a CW in case of spacing $\Delta = 0.4$ is reported in Figure 3. In this case two zeros at 2.5 MHz and 7.5 MHz are added to the zeros observed at entire multiple of 1.023 MHz.

An alternative way to show the described results is the Interference Running Average (IRA) curves, obtained averaging the IEE and representing the potential average impact of an interference whose carrier frequency is uniformly distributed in a chosen frequency range [13]. The IRA curves do not add information to the analysis performed using the IEE, but provide a simplified representation of the receiver performance, allowing an easy comparison of interference vulnerability for different receiver configurations.

The IEE curves, together with the corresponding IRA curves, are a reliable quantitative method that can be used in order to assess and compare the interference robustness

level of different GNSS signals. Some examples of analysis already performed by means of IEE are provided in [12, 13], where the impacts of both continuous wave and wide band interference are assessed, performing a full comparison between different GNSS modulations (BPSK, BOC, CBOC, and TMBOC) and considering different receiver configurations. Referring to the concepts introduced in this Section, the paper focuses the attention on the GPS C/A code.

While in [12, 13] the IEE is used to compare the interference robustness among different modulation types and vary the receiver configuration, here the performed analysis is focused on comparing the robustness among the GPS C/A PRN codes by varying the CW carrier frequency.

The final goal is to identify the worst case (i.e., the most dangerous CW carrier frequency) for each specific GPS satellite signal.

## 4. Impact on IEE of the GPS C/A Code Lines

The GPS C/A code signal is based on the Gold code characteristics [1]. Such signal has a line spectrum (neglecting the navigation data) with lines at 1 kHz from each other. Moreover, depending on the code, there are some lines that are stronger [11]. This means that a CW jammer might mix with a strong C/A code line and leak through the correlator, affecting the receiver performance or even preventing the correct functioning of the receiver. Three facts must be pointed out:

(i) Because of the C/A code signal structure, CWs might be very harmful sources of interference [11];

(ii) Such a harmfulness is strictly related with the relative position between the CW carrier frequency and the code strongest line [16];

(iii) Also the relative carrier phase can have an impact.

From [17], the Power Spectral Density (PSD) of the C/A code signal spectrum can be expressed as

$$S_{C/A} = \frac{T_b}{(NT_C)^2} |C(f)|^2 \sum_{l=-\infty}^{\infty} \operatorname{sinc}^2\left[T_b\left(f - \frac{l}{NT_C}\right)\right], \tag{4}$$

where

(i) $|C(f)|^2 = T_C^2 N \cdot \operatorname{sinc}^2(fT_C) \cdot |X_{\text{code}}(f)|^2$;

(ii) $X_{\text{code}}(f)$ is the Discrete Time Fourier Transform of $x_n$: $X_{\text{code}}(f) = \sum_{n=0}^{N-1} x_n e^{j2\pi f n T_C}$;

(iii) $\{x_n\}_{n=0}^{N-1}$ is the binary Gold code sequence;

(iv) $T_C = 0.976\,\mu s$ is the code chip duration;

(v) $N = 1023$ is the number of chips in 1 code period;

(vi) $T_b = 20 \cdot N \cdot T_C = 20$ ms is the data bit duration.

It must be remarked that $S_{C/A}$ in (4) is composed by three functions in the frequency domain:

(i) $\operatorname{sinc}^2(fT_C)$, due to the rectangular code chip;

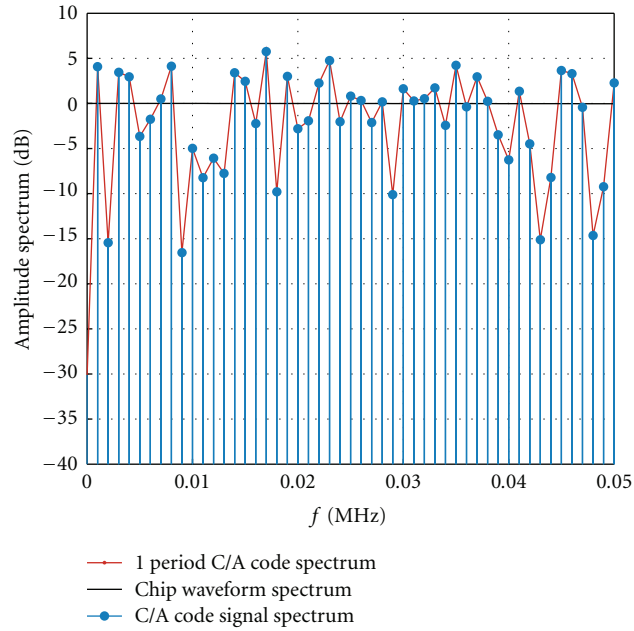


Figure 4: Spectrum of 1 period of the PRN 23 C/A code (orange line), chip waveform spectrum (solid black line), and PRN 23 C/A code signal spectrum (solid cyan line).

(ii) $X_{\text{code}}(f)$ which is the DTFT of the Gold code;

(iii) The third term is due to the code repetition and consists of a comb of sinc functions, at 1 kHz from each other.

All these three components are clearly depicted in Figure 4.

It is also possible to appreciate the three frequency functions by changing the resolution bandwidth to a spectrum analyzer linked with a RF GPS signal generator. The effect is shown in Figure 5, where the GPS C/A code spectrum is depicted tuning the resolution bandwidth at 100 kHz, 1 kHz, and 100 Hz, respectively.

The difference in terms of energy carried by each line can be noticed in Figure 6, where the spectrum of the C/A code signal is depicted for two different codes (PRN 7 and 23).

In terms of interference robustness, the strongest line for each C/A code can be called *worst line*, since it is more susceptible to interference. Table 1 lists all the PRN codes worst lines [11].

One of the tests that has been performed using the IEE tool (see Section 3) verifies that, after fixing the CW frequency shift and evaluating the IEE for each PRN code, the maximum IEE is obtained for the PRN having the strongest line coincident with the CW shift, as reported in Table 2.

The double check between Table 1 and Table 2 confirm the test. All the PRN worst line combinations correspond. Only two facts have to be remarked:

(i) For CW at 151 kHz, the maximum IEE corresponds to PRN 9, instead of PRN 25. This is because the strongest line of PRN 25 and the sixth strongest line of PRN 9 have practically the same amplitude (−23.78 and −23.81 dB);

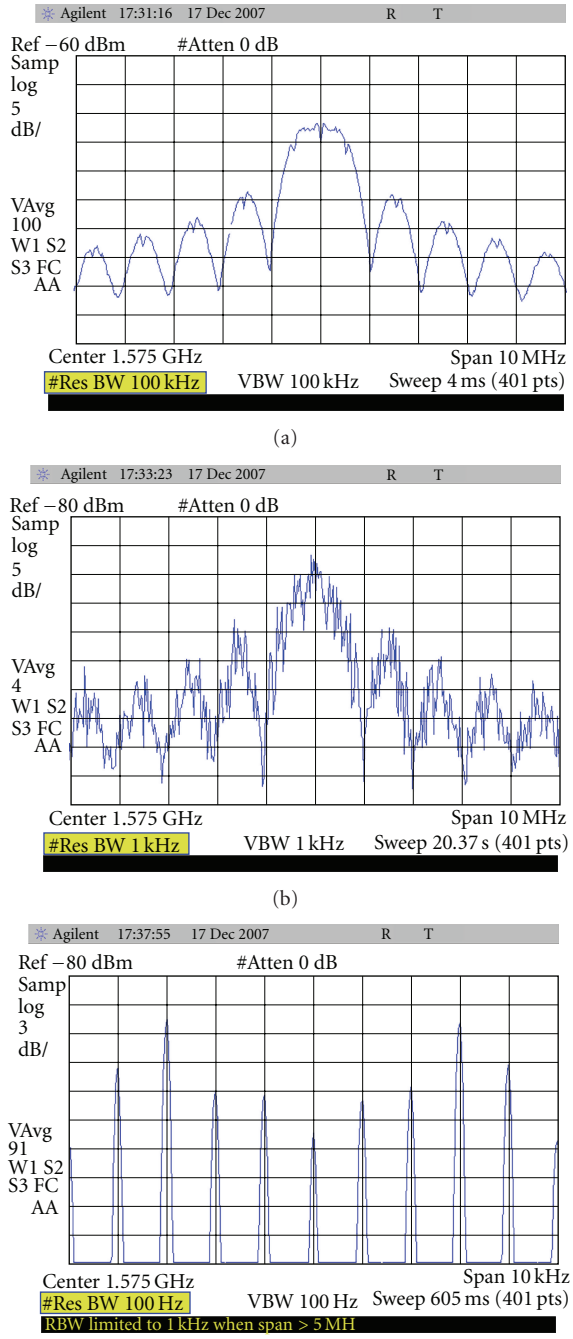


Figure 5: PSD evaluated by the ESA-E series Agilent 4402B spectrum analyzer, with a resolution bandwidth of 100 kHz, 1 kHz and 100 Hz, respectively.

(ii) Both the PRN 4 and PRN 11 have the strongest line at 122 kHz. The maximum IEE at this frequency corresponds to PRN 11. This fact is confirmed by the two line amplitudes: −22.98 dB for the PRN 4 and −22.64 dB for PRN 11.

Using the IEE curves, it is possible to define *new worst lines* for the specific receiver configuration (taking into account the discriminator setting, the front end filter type and bandwidth).

Table 1: GPS C/A Code Worst Lines for Prn 1 to 32.

| C/A code PRN # | Worst Line Frequency [kHz] | C/A code PRN # | Worst Line Frequency [kHz] |
|---|---|---|---|
| 1 | 42 | 17 | 138 |
| 2 | 263 | 18 | 183 |
| 3 | 108 | 19 | 211 |
| 4 | 122 | 20 | 30 |
| 5 | 23 | 21 | 55 |
| 6 | 227 | 22 | 12 |
| 7 | 78 | 23 | 127 |
| 8 | 66 | 24 | 123 |
| 9 | 173 | 25 | 151 |
| 10 | 16 | 26 | 102 |
| 11 | 122 | 27 | 132 |
| 12 | 199 | 28 | 203 |
| 13 | 214 | 29 | 176 |
| 14 | 120 | 30 | 63 |
| 15 | 69 | 31 | 72 |
| 16 | 154 | 32 | 74 |

Table 2: Analysis of Code Lines from IEE Maximum.

| CW frequency shift [kHz] | PRN (IEE max) | CW frequency shift [kHz] | PRN (IEE max) |
|---|---|---|---|
| 12 | 22 | 122 | 11 |
| 16 | 10 | 123 | 24 |
| 23 | 5 | 127 | 23 |
| 30 | 20 | 132 | 27 |
| 42 | 1 | 138 | 17 |
| 55 | 21 | 151 | 9 |
| 63 | 30 | 154 | 16 |
| 66 | 8 | 173 | 9 |
| 69 | 15 | 176 | 29 |
| 72 | 31 | 183 | 18 |
| 74 | 32 | 199 | 12 |
| 78 | 7 | 203 | 28 |
| 102 | 26 | 214 | 13 |
| 108 | 3 | 221 | 19 |
| 120 | 14 | 227 | 6 |
| | | 263 | 2 |

The new worst-case frequencies lines are listed in Table 3. They have been obtained simulating an infinite bandwidth signal with a coherent discriminator (Early-Late with spacing 1 chip).

Referring to first line in Table 3, Figure 7 provides an example of the procedure followed for the definition of the new worst line on the IEE obtained simulating the PRN 1.

It is important to point out that the definition of *"new" worst lines* changes the point of view in assessing the interference impact. This definition points out that the strongest code line can also not be the worst one.

In fact the new definition is receiver dependent, since the impact of a CW interferer is related to several factors:

(i) CW characteristics, that is, power, carrier frequency, phase;

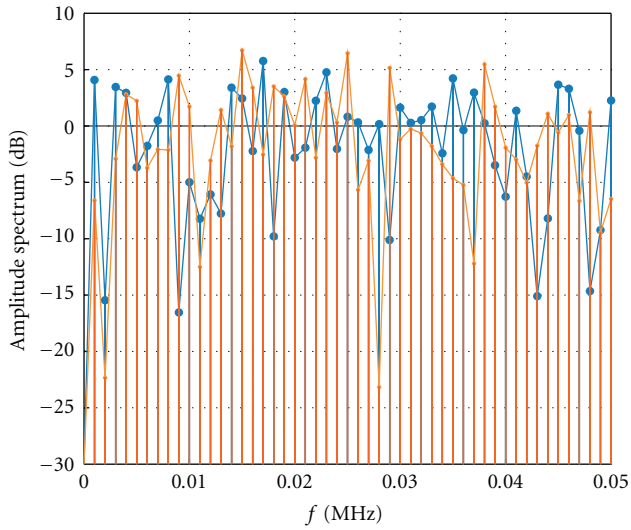


Figure 6: PRN 7 (orange) and PRN 23 (cyan) C/A code signal spectra.

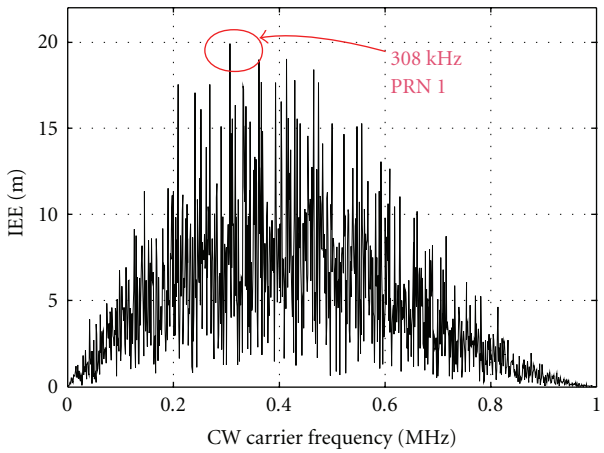


Figure 7: Definition of the new GPS C/A code worst line on the IEE for the PRN 1.

(ii) Specific code features (PRN number);

(iii) Receiver characteristics, that is, discriminator spacing, and front end parameters (filter, ADC, AGC, etc.).

As an example of the dependence of the IEE on the receiver setup, an additional analysis has been carried out in order to assess the impact of the discriminator spacing on the new worst lines. In detail the GPS C/A PRN 1 signal has been simulated with infinite bandwidth and processed by using a coherent Early-Late discriminator with different correlator spacings (from 0.2 to 1 chip). Figure 8 shows a zoom on Figure 2, aiming at investigating the impact of the spacing on the worst case error in presence of CW interference. The obtained results in terms of worst lines are summarized in Table 4. As already remarked in Section 3, these results confirm that a reduction of the spacing decreases the magnitude of the envelope errors.

Table 3: "New" GPS C/A Code Worst Lines.

| C/A code PRN # | Worst Line Frequency (kHz) | C/A code PRN # | Worst Line Frequency (kHz) |
|---|---|---|---|
| 1 | 308 | 17 | 434 |
| 2 | 402 | 18 | 456 |
| 3 | 447 | 19 | 394 |
| 4 | 456 | 20 | 461 |
| 5 | 381 | 21 | 453 |
| 6 | 347 | 22 | 364 |
| 7 | 376 | 23 | 438 |
| 8 | 435 | 24 | 384 |
| 9 | 354 | 25 | 257 |
| 10 | 443 | 26 | 417 |
| 11 | 397 | 27 | 441 |
| 12 | 410 | 28 | 355 |
| 13 | 412 | 29 | 433 |
| 14 | 369 | 30 | 426 |
| 15 | 338 | 31 | 423 |
| 16 | 423 | 32 | 376 |

Table 4: Worst Lines for GPS C/A PRN no. 1 varying the Discriminator Spacing.

| Coherent Early-Late Discriminator Spacing (chips) | Worst Line Frequency (kHz) | IEE max (m) |
|---|---|---|
| 1 | 308 | 19.91 |
| 0.8 | 466 | 16.94 |
| 0.6 | 466 | 14.13 |
| 0.4 | 466 | 10.16 |
| 0.2 | 466 | 5.30 |

In addition, it is possible to notice that, by varying the spacing, the worst lines can match different frequencies. In detail, the worst line is at 308 kHz only for a spacing of 1 chip, whereas other spacings lead to a different interference vulnerability, showing a worst line at 466 kHz. It must be remarked that these results have been obtained simulating a BPSK modulated signal (GPS C/A code). Obviously different results are expected considering other signals (e.g., BOC modulated), featuring a larger spectral occupation, or different PRN codes, leading to different worst lines.

Finally, it must be remarked that, as noted in [12, 13], CW analysis is the base for predicting results also in presence of larger bandwidth interference (wideband signals), that might affect more than one line at the time.

## 5. Conclusions

The increasing number of application based on the integration of wireless communications and navigation/localization techniques leads to the need to verify their interoperability. Within this scenario, the assessment of the GNSS interference robustness is one of the most sensitive issues.

An innovative quantitative method to measure the interference impact for GNSS signals has been described in the paper. It consists in evaluating the distortion of the discrimination function produced by the presence of

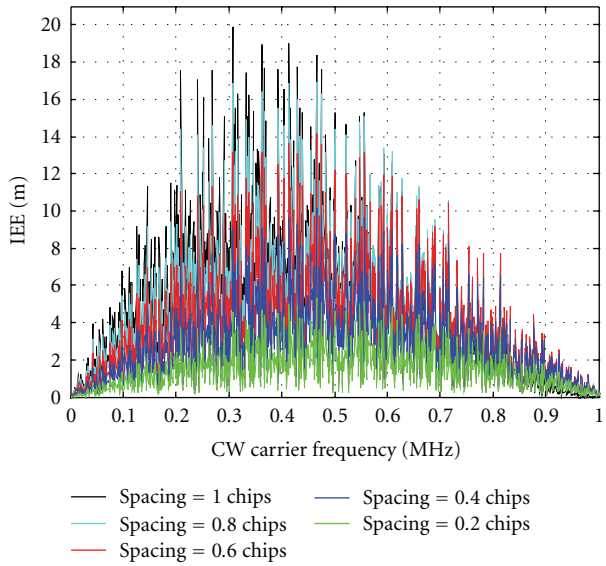


FIGURE 8: Comparison of IEE curves obtained varying the coherent Early-Late discriminator spacing (zoom on Figure 2).

the interference and can be customized for each type of disturbance. A new family of curves, the *Interference Error Envelope*, has been introduced. Each IEE measures the maximum correlation distortion versus the specific interferer characteristic being considered (e.g., the carrier frequency for a continuous wave interferer), for a specific receiver setting.

Moreover the paper presented a detailed analysis on the effect of CW interference on the different GPS C/A codes. Starting from the concept of worst line (the strongest line for each code), and exploiting the IEE tool, *new worst lines*, that also take into account the receiver architecture, have been found.

## References

[1] Interface Specification, IS-GPS-200 Rev.D, IRN-200D-001, 7 March 2006.

[2] Galileo Signal In Space Interface Control Document (OS SIS ICD), Draft 1, February 2008, http://www.gsa.europa.eu.

[3] A. Grant, P. Williams, N. Ward, and S. Basker, "GPS jamming and the impact on maritime navigation," *Journal of Navigation*, vol. 62, no. 2, pp. 173–187, 2009.

[4] D. Borio, S. Savasta, and L. L. Presti, "On the DVB-T coexistence with Galileo and GPS systems," in *Proceedings of the 3rd ESA Workshop on Satellite Navigation User Equipment Technologies (NAVITEC '06)*, ESA/ESTEC, Noordwijk, The Netherlands, December 2006.

[5] R. J. Landry and A. Renard, "Analysis of potential interference sources and assessment of present solutions for GPS/GNSS receivers," in *Proceedings of the 4th International Conference on Integrated Navigation Systems*, pp. 1–13, 1997.

[6] John A. Volpe National Transportation Systems Centre, "Vulnerability assessment of the transportation infrastructure relying on the global positioning system," Final Report, US Department of Transportation, Washington, DC, USA, August 2001.

[7] E. Backer, D. Van Willigen, and R. Rawlings, "Technical and operational assessment of the suitability of GPS to meet the BRNAV requirements," Tech. Rep., Delft University of Technology Telecommunications and Traffic Control Systems Group, Delft, The Netherlands, August 1997.

[8] B. Motella, M. Pini, and F. Dovis, "Investigation on the effect of strong out-of-band signals on global navigation satellite systems receivers," *GPS Solutions*, vol. 12, no. 2, pp. 77–86, 2008.

[9] P. F. De Bakker, J. Samson, P. Joosten, M. Spelat, M. Hollreiser, and B. Ambrosius, "Effect of radio frequency interference on GNSS receiver output," in *Proceedings of the 3rd ESA Workshop on Satellite Navigation User Equipment Technologies (NAVITEC '06)*, Noordwijk, The Netherlands, December 2006.

[10] A. T. Balaei, B. Motella, and A. G. Dempster, "GPS interference detected in Sydney-Australia," in *Proceedings of the International Global Navigation Satellite Systems Society conference (IGNSS '07)*, Sydney, Australia, December 2007.

[11] E. D. Kaplan and C. J. Hegarty, *Understanding GPS: Principles and Applications*, Artech House, Norwood, Mass, USA, 2nd edition, 2006.

[12] B. Motella, S. Savasta, D. Margaria, and F. Dovis, "An interference impact assessment model for GNSS signals," in *Proceedings of the 21st International Technical Meeting of the Satellite Division of the Institute of Navigation (ION GNSS '08)*, vol. 4, pp. 900–908, Savannah, Ga, USA, September 2008.

[13] B. Motella, S. Savasta, D. Margaria, and F. Dovis, "A method for assessing the interference impact on GNSS receivers," *IEEE Transactions on Aerospace and Electronic Systems*. In press.

[14] A. Martineau, *Performance of receiver autonomous integrity monitoring (RAIM) for vertically guided approaches*, Ph.D. thesis, 2008.

[15] M. Irsigler, J. A. Avila-Rodriguez, and G. W. Hein, "Criteria for GNSS multipath performance assessment," in *Proceedings of the 18th International Technical Meeting of the Satellite Division of The Institute of Navigation (ION GNSS '05)*, Long Beach, Calif, USA, September 2005.

[16] A. T. Balaei, B. Motella, and A. Dempster, "A preventative approach to mitigating CW interference in GPS receivers," *GPS Solutions*, vol. 12, no. 3, pp. 199–209, 2008.

[17] P. Misra and P. Enge, *Global Positioning System. Signal Measurements and Performance*, Ganga-Jamuna Press, Lincoln, Mass, USA, 2nd edition, 2006.

Hindawi Publishing Corporation
International Journal of Navigation and Observation
Volume 2010, Article ID 812945, 12 pages
doi:10.1155/2010/812945

*Research Article*

# Hybrid Data Fusion and Tracking for Positioning with GNSS and 3GPP-LTE

**Christian Mensing, Stephan Sand, and Armin Dammann**

*German Aerospace Center (DLR), Institute of Communications and Navigation, Oberpfaffenhofen, 82234 Wessling, Germany*

Correspondence should be addressed to Christian Mensing, christian.mensing@dlr.de

Received 13 November 2009; Revised 1 April 2010; Accepted 1 June 2010

Academic Editor: Marco Luise



Global navigation satellite systems (GNSSs) can provide reliable positioning information under optimum conditions, where at least four satellites can be accessed with sufficient quality. In critical situations, for example, urban canyons or indoor, due to blocking of satellites by buildings and severe multipath effects, the GNSS performance can be decreased substantially. To overcome this limitation, we propose to exploit additionally information from communications systems for positioning purposes, for example, by using time difference of arrival (TDOA) information. To optimize the performance, hybrid data fusion and tracking algorithms can combine both types of sources and further exploit the mobility of the user. Simulation results for different filter types show the ability of this approach to compensate the lack of satellites by additional TDOA measurements from a future 3GPP-LTE communications system. This paper analyzes the performance in a fairly realistic manner by taking into account ray-tracing simulations to generate a coherent environment for GNSS and 3GPP-LTE.

## 1. Introduction

Position information of mobile stations (MSs) in a communications system has become a very important feature in recent years. Services and applications based on very accurate location knowledge will play a fundamental role in future wireless systems [1]. Besides the well-known location-based services it is stated by the United States Federal Communications Commission (FCC) that wireless service providers have to deliver the locations of all enhanced 911 (E911) emergency callers with specified accuracy [2]. To meet this requirement, global navigation satellite systems (GNSSs) [3]—like the current Global Positioning System (GPS) and the future European Galileo system—can deliver very good position estimates under optimum conditions. However, especially in critical positioning scenarios with severe multipath propagation and blocking of several satellites by buildings the performance loss can be very high [4]. For instance, in urban canyons the number of visible satellites can be below the required four. In these situations, we propose to include timing measurements from a communications system to compensate the lack of satellites.

As a supplement to GNSS or as stand-alone solution, already available communications systems can be included in the MS localization process. Generally, measurements in terms of time of arrival (TOA), time difference of arrival (TDOA), angle of arrival, or received signal strength, provided by the base stations (BSs) or the MS, can be used [1]. Of very high interest is TDOA positioning as it is already included in several systems (e.g., GSM, UMTS, CDMA2000) [5, 6], in the standardization process for 3GPP-LTE (cf. [7–9]), and also under discussion for positioning in future systems (cf. [10, 11]).

The hybrid data fusion (HDF) of measurements from GNSS and communications systems is important for seamless positioning and navigation in critical environments [12]. The additional utilization of tracking algorithms will further improve the performance for mobile users [13]. In this paper, we investigate a joint HDF and tracking based on different filter types, where we focus on Positioning Kalman filter (PKF), extended Kalman filter (EKF) [14], and particle filter (PF) [15], that combine GNSS measurements with TDOA measurements from a future 3GPP-LTE communications system. Contrary to state-of-the-art work (e.g., [13]), this

paper analyzes the performance in a fairly realistic manner, especially by taking into account ray-tracing simulations and mobility models for the pedestrian use-case. Since combined channel models for GNSS and communications systems are not yet available, this procedure allows to generate a coherent and correlated environment for both considered systems.

Section 2 starts with a description of the system models for GNSS and the communications system, including also an overview of positioning methods in current and future systems. Section 3 discusses the HDF and tracking algorithms that are employed for this investigation. Finally, simulation results in Section 4 show the performance for the developed approaches in coherent environments for pedestrian positioning in urban canyons.

## 2. System Model

*2.1. Global Navigation Satellite Systems.* GPS and the future European Galileo system will be considered in our investigations [3]. The distances between the $N_{\text{Sat}} = N_{\text{GPS}} + N_{\text{Galileo}}$ visible satellites located at the positions $x_\mu = [x_\mu, y_\mu, z_\mu]^{\text{T}}, \mu \in \{1, 2, \ldots, N_{\text{Sat}}\}$, which are assumed to be under line-of-sight (LOS) conditions, and the MS at position $x = [x, y, z]^{\text{T}}$ are given by

$$r_\mu(x) = \sqrt{(x_\mu - x)^2 + (y_\mu - \text{y})^2 + \left(z_\mu - \text{z}\right)^2}. \quad (1)$$

The resulting pseudoranges between the satellites and MS can then be modeled as

$$\hat{r}_\mu = r_\mu(x) + b_{\text{clock}} + b_{\text{multipath},\mu} + n_\mu, \quad (2)$$

where $b_{\text{clock}}$ is the clock bias coming from the time-offset of the receiver with respect to the satellite clocks, and $n_\mu$ is the elevation depending residual error chosen according to user-equivalent range error (UERE) models for single-band GNSS receivers and effects like tropospheric errors and receiver noise [3]. The multipath error is included in terms of $b_{\text{multipath},\mu}$. It will be calculated for each channel impulse response (CIR), assuming noncoherent integration and a state-of-the-art narrow early-minus-late correlator with correlator spacing of 0.1 chips, where one chip corresponds to around 300 m for GPS.

A LOS visibility analysis for GPS and GPS+Galileo created by ray-tracing simulations is shown in Figure 1. It shows the number of LOS-visible satellites in an urban scenario located in Munich, Germany, where the average building height is around 26 m. We see that especially inside the urban canyons there occur several situations, where only less than four satellites are visible. Hence, only limited performance of GNSSs can be expected. Additionally, the impact of multipath propagation to the overall error is comparably high in these situations. Therefore, supplementation from communications systems is of high interest and importance in these GNSS-critical environments.

*2.2. Communications Systems.* Besides GNSS, also communications systems have the ability to provide positioning information about one or several MSs. Especially in environments with limited GNSS-performance, for example, urban canyons or indoor, communications systems usually have a good coverage. Different principles for obtaining positioning information can be used by communications systems. For instance, measurements in terms of TOA, TDOA, angle of arrival, or received signal strength can be exploited [1]. However, most of the communications systems—already deployed, standardized, or under research—were not foreseen for positioning applications in advance. Hence, the positioning capabilities are usually restricted.

The best performance can be obtained with timing measurements (e.g., [6]), where the key implementation is based on TDOA. They can easily be extracted from system-inherent measurements. The basic idea is to extract the arriving times of signals from several BSs at the MS. To do so, the MS listens to appropriate synchronization channels depending on the system. Then, the TDOAs can be obtained from that. Nevertheless, many challenges have to be overcome in real systems. For instance, for positioning it is assumed that the BSs are fully time and frequency synchronized which is not foreseen in all systems or only an optional feature. However, so-called location measurement units (LMUs) can be used to compute the misalignment of the BSs and provide this information to the network or MS. Furthermore, mobile radio systems are designed in a way that only one strong serving BS should be heard due to spectral efficiency reasons. From a positioning point of view, we need at least three BSs with sufficient signal-to-interference-and-noise ratios (SINRs) for two-dimensional location estimation. This is usually only given at the cell edge. Close to a BS the interference of the serving BS can be too high for detection of the out-of-cell BSs with a reasonable good quality.

Considering deployed systems, in the GSM EDGE radio access network (GERAN), three location principles are specified (cf. [5]): besides the cell identity procedure a TDOA-based method called enhanced observed time difference (E-OTD) is standardized. However, due to large cells in GSM the positioning accuracy can be in the order of several hundred meters. Another specified method is assisted GPS (A-GPS). In assisted solutions, parts of the navigation data—which traditionally is included in the GNSS satellite signals—can be communicated much faster to the MS by the network. This can help to reduce the time-to-first-fix in the acquisition process and to increase the sensitivity in the tracking stage since longer integration times are possible. In CDMA-based systems (e.g., UMTS, W-CDMA, CDMA2000) similar positioning principles as in GSM have been implemented [6]. However, the technical realization is different due to the CDMA properties of the system. On the one hand long integration times can be realized, on the other hand the well-known near-far problem is hard to overcome. However, also here TDOA-based positioning techniques are used to determine the MS position without GNSS support. Additionally, A-GPS approaches are standardized.

The deployment of CDMA-based mobile radio systems is still on-going; nevertheless, the successors are completing the standardization process, where in this paper we focus on

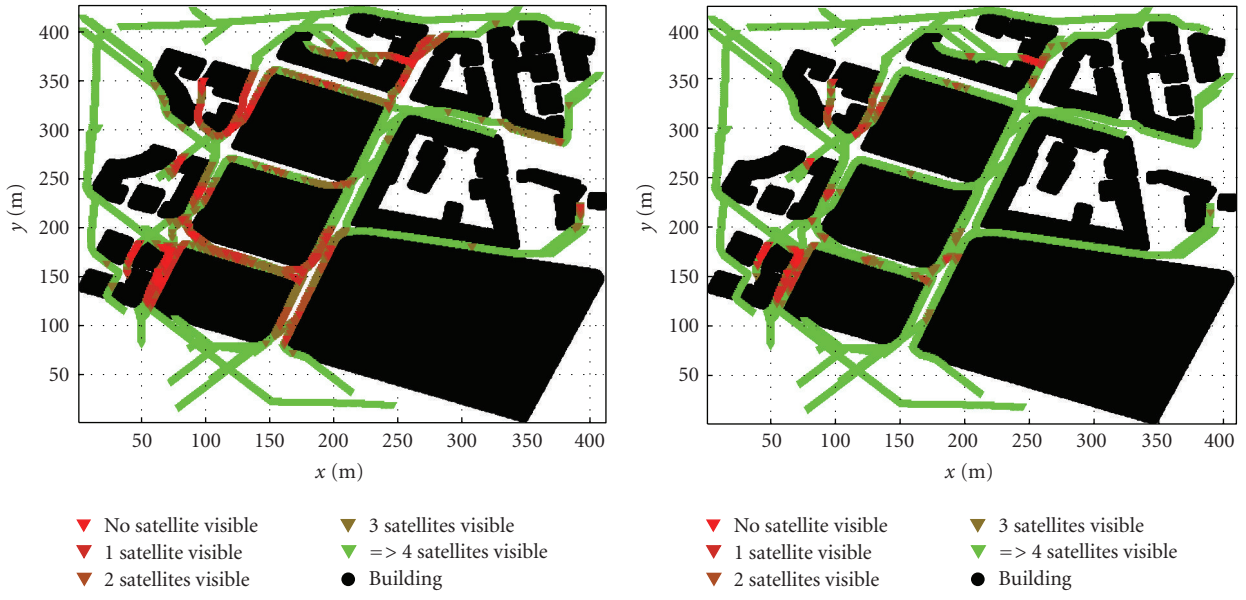


(a) GPS (b) GPS+Galileo

Figure 1: Number of visible GNSS satellites.

3GPP-LTE [7]. 3GPP-LTE will be an orthogonal frequency division multiplexing (OFDM) system with bandwidths up to 20 MHz. For timing-based positioning the synchronization and reference channels can be used to determine the TDOAs at the receiver side (e.g., [8, 9]). Generally, timing-based positioning relies on known sequences in the signals. In 3GPP-LTE the primary and secondary synchronization channels (P-SCH, S-SCH) as well as the downlink reference signal (DL-RS) could be used [16] (cf. Figure 2 for the frame structure of 3GPP-LTE, P-SCH in blue, S-SCH in green, DL-RS in black). For the detection of the different sectors (we assume three sectors per BS) a searching algorithm is applied, which builds replicas of the known synchronization sequences and correlates them with the received signals from all surrounding sectors in time domain to determine the arrival time of the sequences and, thus, to determine finally the TDOAs (e.g., [17]). For our investigations, we simulate a FDD system with 20 MHz bandwidth, directional antennas, and transmit powers of 43 dBm (cf. [17]); however, as specified in the standard, the synchronization sequences only occupy 1 MHz bandwidth.

It can be expected that also the generation of mobile radio systems after 3GPP-LTE will be OFDM based, where the occupied bandwidth will further increase. However, it is questionable if a target bandwidth of 100 MHz (as proposed in [10]) can be realized in spectrum as a whole or only by sophisticated overlay systems. The further integration of local communications systems for hot spot situations will also be challenging from a positioning point of view. On the one hand, the coverage can be really high since an overlap of these hot spots is naturally given. On the other hand, the exact location of these plug-and-play devices is not a priori known which encounters new difficulties in the location determination process. Another concept under discussion is relay enhanced cells, especially in urban environments.

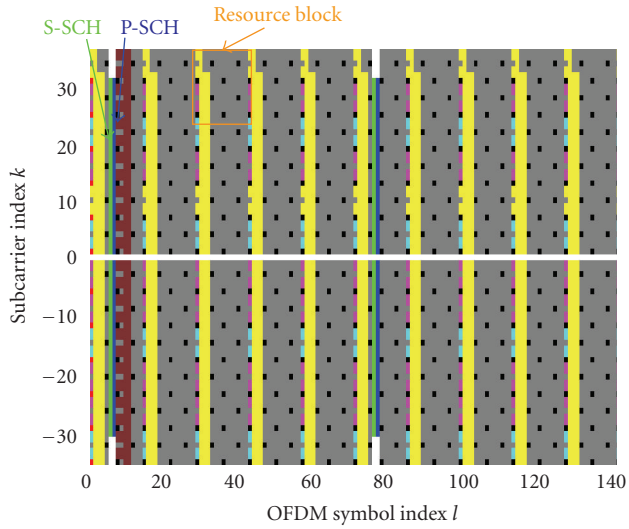


Figure 2: 3GPP-LTE frame structure.

As discussed before, for the measurements from the communications part we use TDOAs. In TDOA only time-differences from several BSs are used; thus, the receiver time-offset with respect to the synchronized BSs is compensated inherently. Hence, we obtain

$$d_{\nu,1}(x) = r_\nu(x) - r_1(x), \quad \nu \in \{2, 3, \ldots, N_{\mathrm{BS}}\}, \tag{3}$$

where we chose BS 1 as reference BS which gives $N_{\mathrm{BS}} - 1$ linear independent TDOAs. The TDOA measurement model is determined as

$$\hat{d}_{\nu,1} = d_{\nu,1}(x) + n_{\nu,1}. \tag{4}$$

Each error contribution $n_{\nu,1} = n_\nu - n_1$ depends on two measurements which results in strong correlations, especially

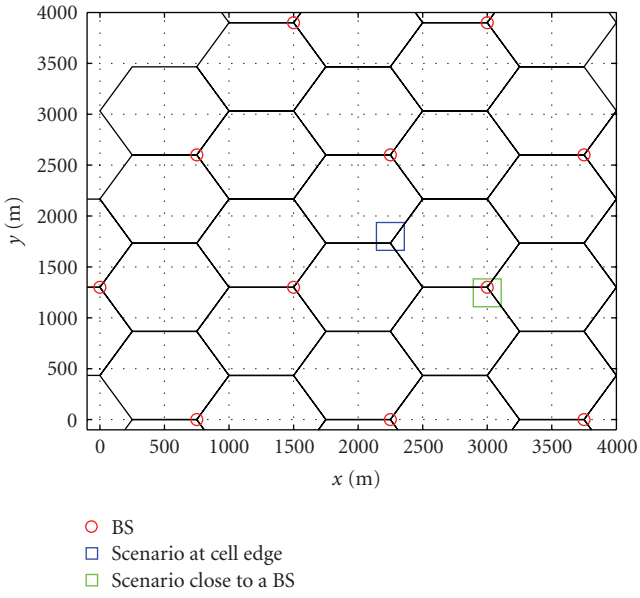


Figure 3: Cell layout and simulated scenarios.

with respect to the reference BS. The timing information is extracted from the synchronization algorithms between the MS and several BSs at the same time, where—similar as for GNSS—also here coherent channel conditions are generated (cf. Section 2.3). Note that both multipath and NLOS propagation are considered in the TDOA measurements. However, as multipath is not exploited or mitigated, the multipath effects are not explicitly denoted in this equation; that is, all effects are included in the noise. As pointed out before, we have used a 3GPP-LTE system to provide the TDOAs (e.g., [17]). The cellular network structure is shown in Figure 3, where the urban canyon scenario (cf. Figure 1) is located at two different positions: at the cell edge or close to a BS.

*2.3. Channel and Mobility Models.* To assess the performance of HDF and tracking algorithms, realistic channel models for GNSSs and communications systems are required, where strong system-, spatial-, and time-correlations occur. No current models meet these requirements in an adequate manner so far. Thus, we created realistic models by using ray-tracing simulations in an urban canyon scenario to generate CIRs for satellites and BSs at several points. This allows a coherent simulation for the HDF and tracking algorithms. Further, we have adapted and implemented a mobility model that is based on gas diffusion [18]. This model generates realistic path tracks of the MS especially for slow moving pedestrian users. Some of these tracks were already shown in Figure 1. Typical CIRs for such a track assuming a GPS satellite and a BS are depicted in Figure 4. We observe, for example, the high number of reflections and also the clear LOS situations at time-steps 80–170 and 320–350 for the GPS satellites. Note that for each simulated track the CIRs from all satellites and all BSs are calculated to obtain a coherent and correlated environment.

## 3. Hybrid Data Fusion and Tracking Algorithms

The MS positions are usually correlated over time. For instance—considering a pedestrian—certain information about the position can be derived using the history of past estimates and suitable movement or mobility models. For instance, a pedestrian cannot jump from one position to another in limited time. This behavior can be used as side-information for position tracking algorithms.

We assume a hidden Markov model with unknown states $s_k \in \mathbb{R}^{N_s}$ that have to be estimated in each time-step $k \in \mathbb{N}$. The estimation process takes into account the measurements $y_k \in \mathbb{R}^{N_y}$ in each time-step $k$ in addition to the model parameters. The measurements $y_k$ depend only on the state vector $s_k$ at the current time-step. This dependence is defined by the so-called measurement model:

$$y_k = g_k(s_k, n_k). \tag{5}$$

The function $g_k$ is a possibly nonlinear function of the state $s_k$ and the measurement noise $n_k \in \mathbb{R}^{N_n}$. The properties of the measurement noise $n_k$ define the measurement uncertainties. Another equivalent representation of the measurement model is based on the conditioned probability density function (PDF) of the measurements given the states, that is, $p(y_k \mid s_k)$.

The state model defines a relation between the previous state $s_{k-1}$ and the current state $s_k$. It is given as

$$s_k = f_{k-1}(s_{k-1}, v_{k-1}), \tag{6}$$

where the function $f_{k-1}$ is a possibly nonlinear function of the state $s_{k-1}$ and the state process noise $v_{k-1} \in \mathbb{R}^{N_v}$. The properties of the state process noise $v_{k-1}$ define how random the state changes can be. The equivalent representation of the state model is based on the conditioned PDF $p(s_k \mid s_{k-1})$. In the positioning context the state vector can include information about the MS position or its velocity. The corresponding state model includes information about the mobility or movement of the MS. Therefore, it is often denoted as mobility model.

Following the Bayesian approach (e.g., [14, 19]), it is required that the PDF of the current state is estimated by considering all previous and the current measurements, that is, the PDF $p(s_k \mid y_1, y_2, \ldots, y_k)$ has to be constructed. This is done recursively by assuming that the prior distribution of the state $s_0$ is known.

In the first step of Bayesian estimation, the state model is used to obtain the prior PDF of the state at time-step $k$ by

$$p(s_k \mid y_1, y_2, \ldots, y_{k-1}) = \int p\left(s_k \mid s_{k-1}\right) p\left(s_{k-1} \mid y_1, y_2, \ldots, y_{k-1}\right) ds_{k-1}. \tag{7}$$

The PDF $p(s_k s_{k-1})$ is defined by the state equation and the known statistics of the state noise $v_{k-1}$. This step is denoted as prediction step since the new state is estimated as a prediction of the old state.

For the second step, it is required that at time-step $k$ the measurements $y_k$ become available. They can be used

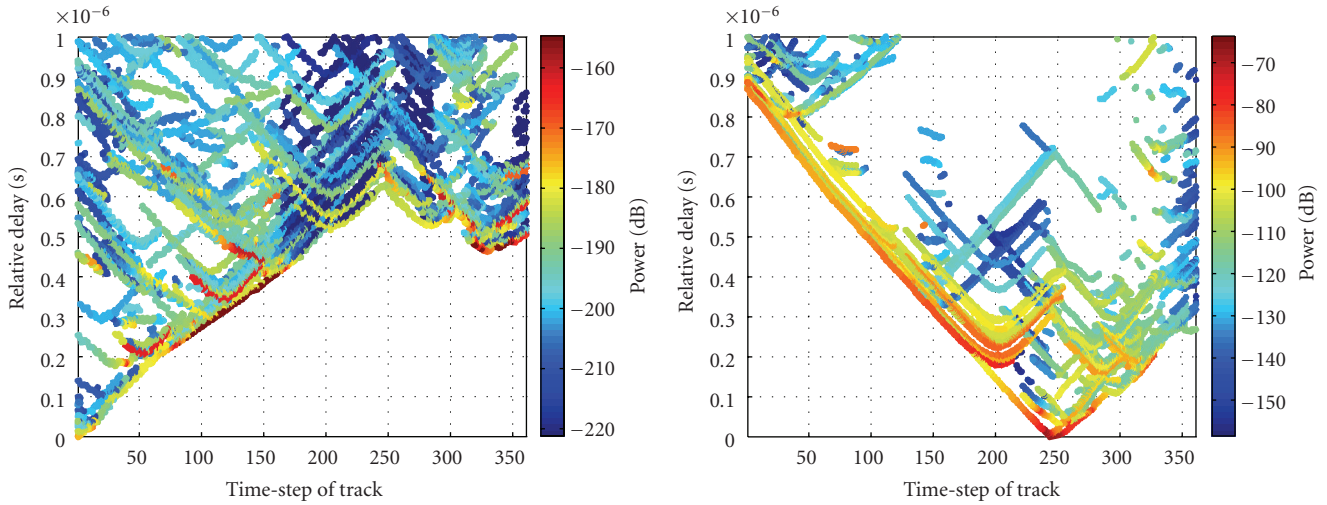


(a) GPS satellite (b) BS

Figure 4: CIRs for one track realization.

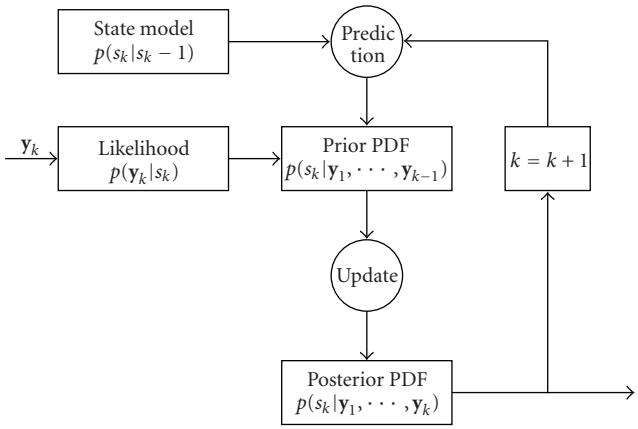


Figure 5: Recursive Bayesian estimation.

to update the prior PDF by the Bayes' rule resulting in a normalized product of the likelihood $p(y_k \mid s_k)$ and the prior PDF, that is,

$$p(s_k \mid y_1, y_2, \ldots, y_k) = \frac{p(y_k \mid s_k)\, p(s_k \mid y_1, y_2, \ldots, y_{k-1})}{p(y_k \mid y_1, y_2, \ldots, y_{k-1})}, \tag{8}$$

with normalization constant $p(y_k \mid y_1, y_2, \ldots, y_{k-1})$. Therefore, the posterior PDF can be calculated by using the measurement model and the known statistics of the measurement noise $n_k$. Since the measurements of time-step $k$ are used to modify the prior PDF for obtaining the posterior PDF, this step is called update step. The complete principle of the recursive Bayesian estimator is shown in Figure 5 (cf. [20]).

Finally, the solution that maximizes the posterior PDF is nothing else than the maximum-a-posteriori (MAP) estimator:

$$\hat{s}_{\mathrm{MAP},k} = \underset{s_k}{\operatorname{argmax}}\, p(s_k \mid y_1, y_2, \ldots, y_k). \tag{9}$$

Contrary to that, the minimum mean square error (MMSE) estimator calculates the expectation over the PDF, that is,

$$\hat{s}_{\mathrm{MMSE},k} = \int s_k\, p(s_k \mid y_1, y_2, \ldots, y_k)\, ds_k, \tag{10}$$

where for Gaussian noise distributions both estimators yield the same result.

Usually there are no closed-form solutions for the general integrals in Bayes estimation [15]. One option to handle these integrals is certain assumptions for the models or approximations: the classical Kalman filter (KF) approach (Section 3.1) presumes linear models and Gaussian noise distributions. The EKF approximates non-linear models in a linearization step which will be shown in Section 3.2. Another option to handle the integrals is numerical integration. An approximate solution by Monte-Carlo methods is the PF being described in Section 3.3.

*3.1. Kalman Filter.* The KF (cf. [14]) is one of the most widely used implementation of Bayesian filters. One of the main advantages of KFs is the computational efficiency in the implementation using only matrix and vector operations on the mean and covariances of Gaussian processes.

To perform optimum, it must hold for the system model in (6) and the measurement model in (5) that the system process noise $v_k \sim \mathcal{N}(0_{N_s}, Q_k)$ and measurement noise $n_k \sim \mathcal{N}(0_{N_y}, C_k)$ are drawn from zero-mean Gaussian distributions with known covariances. For GNSS the covariance matrix of the measurement noise is based on the error model for each satellite (which is, e.g., elevation dependent);

for the 3GPP-LTE TDOA measurements it is based on the SINRs. Note that for a general derivation it is not necessarily required that the noise is zero-mean (e.g., [14]) which is assumed here for simplicity. Furthermore, $f_{k-1}$ and $g_k$ have to be known linear functions.

Then, we can rewrite (6) and (5) as

$$s_k = A_{k-1}s_{k-1} + v_{k-1}, \tag{11}$$

$$y_k = H_k s_k + n_k. \tag{12}$$

The matrix $A \in \mathbb{R}^{N_s \times N_s}$ is the state matrix and includes the linear dependencies between the states of time-steps $k$ and $k-1$. The measurement matrix $H \in \mathbb{R}^{N_y \times N_s}$ reflects the linear relation between the measurements and the state at time-step $k$. In general, all matrices can be time-variant. In the context of positioning applications this could reflect, for example, changing mobility models over time. The optimum filter equations can then be written as follows.

In a first step (prediction) the state of the current time-step is calculated taking into account the state of the previous time-step and the knowledge of the state matrix given by $A_k$. Then, the estimate of the state after prediction is

$$\hat{s}_{k|k-1} = A_{k-1}\hat{s}_{k-1|k-1}, \tag{13}$$

with the estimate of the previous time-step $\hat{s}_{k-1k-1}$. Additionally, the corresponding MMSE or covariance matrix after that prediction step can be calculated as

$$M_{k|k-1} = A_{k-1}M_{k-1|k-1}A_{k-1}^{T} + Q_k, \tag{14}$$

where $M_{k-1|k-1}$ is the MMSE matrix of the previous time-step. From the Bayesian PDF point of view, the prior PDF can be represented as a Gaussian distribution according to

$$p(s_k \mid y_1, y_2, \ldots, y_{k-1}) \sim \mathcal{N}(\hat{s}_{k|k-1}, M_{k|k-1}). \tag{15}$$

The Kalman gain matrix includes a weighting between the predicted estimate (already calculated) and the current measurements. It is given by

$$K_k = M_{k|k-1}H_k^{\mathrm{T}}\left(C_k + H_k M_{k|k-1}H_k^{\mathrm{T}}\right)^{-1}. \tag{16}$$

Finally, the correction step combines the predicted estimates with the current measurements weighted with the Kalman gain matrix. This results in the final estimate of the state vector:

$$\hat{s}_{k|k} = \hat{s}_{k|k-1} + K_k(y_k - H_k\hat{s}_{k|k-1}). \tag{17}$$

The corresponding MMSE or covariance matrix after the correction step is obtained as

$$M_{k|k} = (\mathbf{I}_{N_s} - K_k H_k)M_{k|k-1}. \tag{18}$$

The resulting posterior PDF can then be written as Gaussian distribution according to

$$p(s_k \mid y_1, y_2, \ldots, y_k) \sim \mathcal{N}(\hat{s}_{k|k}, M_{k|k}). \tag{19}$$

The KF is initialized with $s_{0|0}$ and $M_{0|0}$ determined by the prior distribution of the initial state.

In the context of position tracking applications, we assume that the state vector consists of position and velocity, that is,

$$s_k = [x_k, y_k, z_k, v_{x,k}, v_{y,k}, v_{z,k}]^{\mathrm{T}}. \tag{20}$$

For the mobility model, we choose a very simple model corresponding to the principle of random walk. For that, the resulting time-invariant system matrix is given by

$$A = \begin{bmatrix} 1 & 0 & 0 & T & 0 & 0 \\ 0 & 1 & 0 & 0 & T & 0 \\ 0 & 0 & 1 & 0 & 0 & T \\ 0 & 0 & 0 & 1 & 0 & 0 \\ 0 & 0 & 0 & 0 & 1 & 0 \\ 0 & 0 & 0 & 0 & 0 & 1 \end{bmatrix}. \tag{21}$$

The sampling time $T$ depends on the application. For instance, for pedestrian positioning sampling times of around 1 s are usually sufficient. The covariance matrix of the process noise is a diagonal matrix including the variance of the mobility (process drift) in all directions for position and velocity. This model implies that the change of the MS position is controlled by process noise of a certain variance.

For the measurement model, we assume that in every time-step a static position estimate is available. The static solution (cf. [12]) results in a weighted non-linear least squares estimation problem. As an analytic solution is not possible, an iterative procedure based on the Gauss-Newton algorithm is applied. Hence, for the Kalman equations the measurements are given in terms of position measurements and have a linear dependency with the state vector which is reflected in the time-invariant measurement matrix:

$$H = \begin{bmatrix} 1 & 0 & 0 & 0 & 0 & 0 \\ 0 & 1 & 0 & 0 & 0 & 0 \\ 0 & 0 & 1 & 0 & 0 & 0 \end{bmatrix}. \tag{22}$$

We do not consider any velocity estimates which are available from the position estimation entity. Thus, the velocity is handled as hidden state and estimated implicitly in the filter equations. The resulting filter in the positioning context is denoted as positioning KF (PKF).

*3.2. Extended Kalman Filter.* The performance of the PKF is optimum if the conditions on Gaussianity and linearity are fulfilled completely. Further, the KF requires that the underlying entity which provides the static solutions performs optimum; that is, in each time-step enough sources (here, at least three) have to be available and the static position estimation errors have further to fulfill the Gaussian assumption. Especially in critical positioning situations like urban canyons or indoor, it may happen quite often that only less than the required number of sources are available for a certain time. Then, the PKF would totally fail since the static solution cannot provide any estimates.

The EKF (e.g., [14, 21]) is a much more flexible tool being able to handle directly non-linear models. We assume that the state model is given by

$$s_k = a_{k-1}(s_{k-1}) + v_{k-1} \tag{23}$$

and the measurement model can be written as

$$y_k = h_k(s_k) + n_k. \tag{24}$$

Basic idea of the EKF is a linearization of $a_{k-1}(s_{k-1})$ about the estimate of $s_{k-1}$. We obtain

$$a_{k-1}(s_{k-1}) \approx a_{k-1}(\hat{s}_{k-1|k-1}) + A_{k-1}(s_{k-1} - \hat{s}_{k-1|k-1}) \tag{25}$$

with the Jacobian matrix:

$$A_{k-1} = \left.\frac{\partial a_{k-1}(s_{k-1})}{\partial s_{k-1}}\right|_{s_{k-1}=\hat{s}_{k-1|k-1}}. \tag{26}$$

Equivalently, we linearize $h_k(s_k)$ about the estimate of $s_k$, that is,

$$h_k(s_k) \approx h_k(\hat{s}_{k|k-1}) + H_k(s_k - \hat{s}_{k|k-1}) \tag{27}$$

with the Jacobian matrix:

$$H_k = \left.\frac{\partial h_k(s_k)}{\partial s_k}\right|_{s_k=\hat{s}_{k|k-1}}. \tag{28}$$

Obviously, the Jacobians have to be recalculated in every time-step since they depend on the estimates of the previous time-steps. However, the resulting structure of the EKF as pointed out in the following is very similar to the PKF solution.

It starts with the prediction, where knowledge of the MS movement model is applied to obtain

$$\hat{s}_{k|k-1} = a_k(\hat{s}_{k|k-1}), \tag{29}$$

with the estimate of the previous time-step $\hat{s}_{k-1|k-1}$. Similarly, the corresponding MMSE or covariance matrix after that prediction step is

$$M_{k|k-1} = A_{k-1}M_{k-1|k-1}A_{k-1}^T + Q_k. \tag{30}$$

$$H_k = \begin{bmatrix} \frac{x_k^{(\mathrm{Sat})} - x_1}{r_{1,k}^{(\mathrm{Sat})}(s_k)} & \frac{y_k^{(\mathrm{Sat})} - y_1}{r_{1,k}^{(\mathrm{Sat})}(s_k)} & \frac{z_k^{(\mathrm{Sat})} - z_1}{r_{1,k}^{(\mathrm{Sat})}(s_k)} & 1 \\ \vdots & \vdots & \vdots & \vdots \\ \frac{x_k^{(\mathrm{Sat})} - x_{N_{\mathrm{BS}}}}{r_{N_{\mathrm{Sat}},k}^{(\mathrm{Sat})}(s_k)} & \frac{y_k^{(\mathrm{Sat})} - y_{N_{\mathrm{BS}}}}{r_{N_{\mathrm{Sat}},k}^{(\mathrm{BS})}(s_k)} & \frac{z_k^{(\mathrm{Sat})} - z_{N_{\mathrm{BS}}}}{r_{N_{\mathrm{BS}},k}^{(\mathrm{Sat})}(s_k)} & 1 \\ \frac{x_k^{(\mathrm{BS})} - x_2}{r_{2,k}^{(\mathrm{BS})}(s_k)} - \frac{x_k^{(\mathrm{BS})} - x_1}{r_{1,k}^{(\mathrm{BS})}(s_k)} & \frac{y_k^{(\mathrm{BS})} - y_2}{r_{2,k}^{(\mathrm{BS})}(s_k)} - \frac{y_k^{(\mathrm{BS})} - y_1}{r_{1,k}^{(\mathrm{BS})}(s_k)} & \frac{z_k^{(\mathrm{BS})} - z_2}{r_{2,k}^{(\mathrm{BS})}(s_k)} - \frac{z_k^{(\mathrm{BS})} - z_1}{r_{1,k}^{(\mathrm{BS})}(s_k)} & 0 \\ \vdots & \vdots & \vdots & \vdots \\ \frac{x_k^{(\mathrm{BS})} - x_{N_{\mathrm{BS}}}}{r_{N_{\mathrm{BS}},k}^{(\mathrm{BS})}(s_k)} - \frac{x_k^{(\mathrm{BS})} - x_1}{r_{1,k}^{(\mathrm{BS})}(s_k)} & \frac{y_k^{(\mathrm{BS})} - y_{N_{\mathrm{BS}}}}{r_{N_{\mathrm{BS}},k}^{(\mathrm{BS})}(s_k)} - \frac{y_k^{(\mathrm{BS})} - y_1}{r_{1,k}^{(\mathrm{BS})}(s_k)} & \frac{z_k^{(\mathrm{BS})} - z_{N_{\mathrm{BS}}}}{r_{N_{\mathrm{BS}},k}^{(\mathrm{BS})}(s_k)} - \frac{z_k^{(\mathrm{BS})} - z_1}{r_{1,k}^{(\mathrm{BS})}(s_k)} & 0 \end{bmatrix}. \tag{31}$$

Due to the linearization step the resulting estimated prior PDF in the Bayesian sense is a Gaussian approximation of the true prior PDF. Hence, the estimated prior PDF is given as

$$p(s_k \mid y_1, y_2, \ldots, y_{k-1}) \sim \mathcal{N}(\hat{s}_{k|k-1}, M_{k|k-1}). \tag{32}$$

The Kalman gain matrix can be obtained by

$$K_k = M_{k|k-1}H_k^T\left(C_k + H_kM_{k|k-1}H_k^T\right)^{-1}, \tag{33}$$

Finally, the correction step combines the predicted estimates with the current measurements weighted with the Kalman gain matrix. This results in the final estimate of the state vector being calculated as

$$\hat{s}_{k|k} = \hat{s}_{k|k-1} + K_k\left(y_k - h(\hat{s}_{k|k-1})\right). \tag{34}$$

The corresponding MMSE or covariance matrix after correction is obtained as

$$M_{k|k} = (\mathbf{I}_{N_s} - K_kH_k)M_{k|k-1}. \tag{35}$$

Also the resulting posterior PDF is a Gaussian distribution of the true posterior PDF. It is given as

$$p\ (s_k \mid y_1, y_2, \ldots, y_k) \sim \mathcal{N}(\hat{s}_{k|k}, M_{k|k})\ . \tag{36}$$

Compared to the PKF, the EKF has no optimality properties, where its accuracy depends on the accuracy of the linearization. Nevertheless, the EKF turns out to be a flexible and robust approach widely used for position tracking applications.

Considering position tracking (as shown for the PKF in Section 3.1), the state vector $s_k$ is only extended by

the unknown clock offset between GNSS satellites and MS, that is, by $b_{\text{clock}}$. However, in principle we assume the same state model, that is, a linearization of the state equation is not necessary. Therefore, the prediction step is similar for EKF and PKF. As measurements we process directly the pseudorange measurements from GNSS and the TDOA measurements from the communications system—in contradiction to the PKF, where the measurements were processed beforehand by a static position estimation. Since the measurements are non-linear with respect to position, for the update step a linearization of the measurement model is necessary. For that, the Jacobian matrix including the derivatives of the measurement model with respect to the state vector has to be available. For the considered set-up, $H_k$ is shown in (31) with the corresponding indices for satellites (Sat) and BSs (BS).

*3.3. Particle Filter.* Another important class of Bayesian filters is based on approximation of integrals by numerical integration. These methods are commonly denoted as PFs ([15, 19, 22]) and became quite popular for position tracking applications (e.g., [23]). PFs are based on a sequential Monte-Carlo methodology (cf. [24]) and calculate recursively the relevant PDFs by importance sampling and approximation of PDFs with discrete random measures. Compared to KFs the PFs have usually a much higher complexity depending on the number of particles that have to be generated to model the required PDFs. In addition, they can suffer from phenomena like sample degeneracy or sample impoverishment causing unstable behavior.

In PFs, the posterior PDF is represented as the weighted sum:

$$p(s_k \mid y_1, y_2, \ldots, y_k) = \sum_{i=1}^{N_p} w_k^i \delta\left(s_k - s_k^i\right), \tag{37}$$

where each particle consists of a state $s_k^i$ and a weight $w_k^i$, and $\delta(\cdot)$ is the Dirac delta measure. The particles are drawn according to the principle of importance sampling from a proposal density $q(s_k \mid s_k^i, y_k)$. The corresponding weights can then be calculated by

$$w_k^i \sim w_k^{i-1} \frac{p\left(y_k \mid s_k^i\right)\, p\left(s_k^i \mid s_k^{i-1}\right)}{q\left(s_k \mid s_k^i, y_k\right)}. \tag{38}$$

The generic PF applies the optimum proposal density which in practice is difficult to use. Therefore, often the so-called sampling importance resampling PF (SIR-PF) is implemented (cf. [15, 19, 25]). It only requires that the state and measurement functions $f_k$ and $g_k$ are known and that sampling of realizations from the state noise distribution of $v_{k-1}$ as well as the prior distribution is possible. In addition, the likelihood function $p(s_k| y_k)$ has to be available for pointwise evaluation.

In the first step of SIR-PF, for each particle $i = 1, 2, \ldots, N_p$, a sample from the proposal density has to be drawn, that is,

$$s_k^i \sim p\left(s_k \mid s_{k-1}^i\right). \tag{39}$$

This can be realized by generating a state noise sample $v_{k-1}^i$ with the corresponding PDF $p_v(v_{k-1})$ and setting

$$s_k^i = f_{k-1}\left(s_{k-1}^i, v_{k-1}^i\right). \tag{40}$$

In a second step, for each particle the weights have to be calculated. With the chosen proposal density, this step reduces to

$$w_k^i = p\left(y_k \mid s_k^i\right). \tag{41}$$

Finally, all weights have to be normalized by

$$w_k^i = \frac{w_k^i}{W}, \tag{42}$$

using

$$W = \sum_{i=1}^{N_p} w_k^i. \tag{43}$$

A crucial problem of the PF is the degeneracy phenomenon ([15, 19]). It points out that after a few iterations, all but one particle will have weights very close to zero. Simply using a very large number of particles is often too inefficient from a computational complexity point of view. A much better method is the application of resampling where degeneracy can be reduced remarkably. The idea is an elimination of particles with low weights to concentrate on particles having large weights. In this manner, a new set of states $\tilde{s}_k^i, i = 1, 2, \ldots, N_p$ is created by resampling $N_p$ times from an approximate discrete representation of

$$p(s_k \mid y_1, y_2, \ldots, y_k) \approx \sum_{i=1}^{N_p} w_k^i \delta\left(s_k - s_k^i\right). \tag{44}$$

Given

$$P\left(\tilde{s}_k^j = s_k^i\right) = w_k^j, \tag{45}$$

the resulting sample is an i.i.d. sample from the discrete density. Even though the degeneracy can be reduced by resampling, another effect denoted as sample impoverishment is introduced in practical implementations. Besides the problem of limited parallelization due to the fact that the particles have to be combined, particles with large weights are statistically selected much more often than the other particles. So the diversity among the particles is reduced since the resulting sample will contain many repeated points. Especially for systems with small state noise the sample impoverishment can be a serious problem and all particles can be concentrated to a single state after a few iterations.

In addition to the SIR-PF, there exist several other PF approaches in the literature. Briefly mentioned at this point should be the auxiliary sampling importance resampling PF [26] or the regularized PF [27].

Note that in this paper, the PF is not used as an object of research but solely as lower bound for our positioning algorithms. For that we have used the SIR-PF implementation using 10000 particles.

## 4. Simulation Results

We assume a fixed GNSS constellation during one track and two different BS constellations. The first scenario is close to a BS, and the second scenario is at the cell edge (cf. Figure 3). We assume a cellular network with inter-BS distance of 1500 m, three sectors for each BS, and 3GPP-LTE parameters following the on-going standardization process [16].

We start with simulation results for positioning with GNSS. Figure 6 shows the performance of different GNSS systems averaged over several noise realizations and several generated tracks. The cumulative distribution function (CDF) shows the probability that the position estimation error is below a certain value $x$. In particular, all simulations are performed for the 50 tracks shown in Figure 1 of 290 time-steps each. For each track 100 noise realizations were generated. All in all this results in 1450000 simulated estimates for creating the CDFs. As comparison, the curves for an optimum free space situation are shown in this plot as well. We observe very high performance losses in the urban canyon scenario compared to the free space situation, which comes from lack of satellites and high multipath impacts. However, we can also see that the EKF clearly outperforms the static solution for this situation. Furthermore, the large benefit of additional Galileo satellites with respect to GPS-only positioning becomes obvious.

Figure 7 compares the performance in the urban canyon scenario for different tracking filter types using GPS+Galileo. We observe that with the static solution an accuracy of better than 40 m can be achieved in 90% of the cases. With the PKF this can be improved to around 27 m. Using an EKF implementation, we can achieve around 9 m which comes very close to the performance bound of the PF. For this GNSS-only scenario this is not surprising as the requirement on Gaussianity is met and the nonlinearities are not severe.

Next, the quality of the TDOA measurements is analyzed in detail. Figure 8 shows the investigation for the urban canyon scenario at the cell edge using different filter types when processing two TDOA measurements (i.e., three BSs). As expected, the accuracy as well as the availability is worse compared to GNSS positioning. Nevertheless, using the PF a 90%-accuracy of around 40 m can be achieved. The EKF provides a slightly worse performance in terms of availability; with static solution and PKF no precise positioning is possible. Note that if the scenario is close to a BS (not shown here), the performance becomes even worse. In that situation also EKF and PF cannot provide a reliable position estimates. Reason for this behavior is that close to a BS usually out-of-cell BSs cannot be received with sufficient quality due to the strong interference of the serving BS. In these situations either a change in the standard is necessary (e.g., 3GPP-LTE proposes a positioning reference mode with idle periods and extended pilot grid [28]) or advanced receiver techniques have to be applied (e.g., [17] proposes to use interference cancellation to increase hearability of out-of-cell BSs). From Figures 7 and 8 it can be concluded that the EKF is a sufficiently good estimator for the considered scenario and the—much more complex—PF gives no fundamental additional performance gains. Hence, in the following we focus on HDF approaches using EKF tracking.

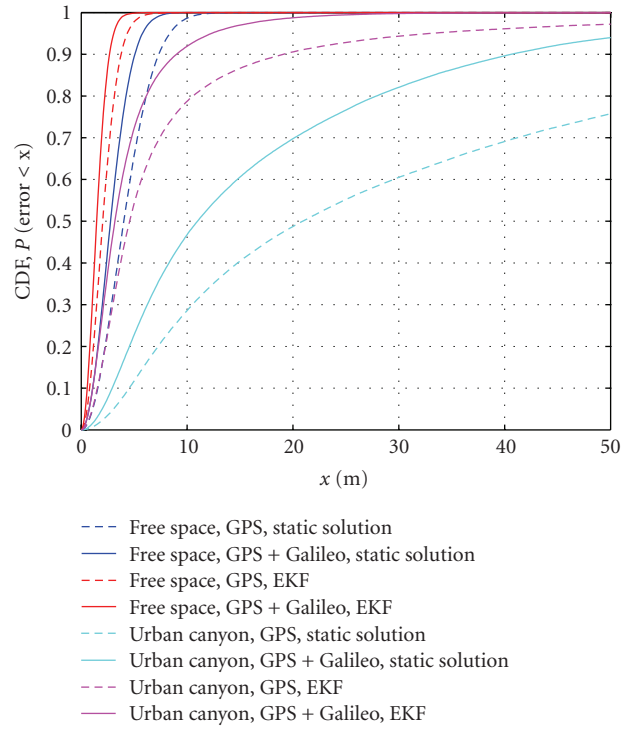


Figure 6: GNSS positioning, different scenarios.

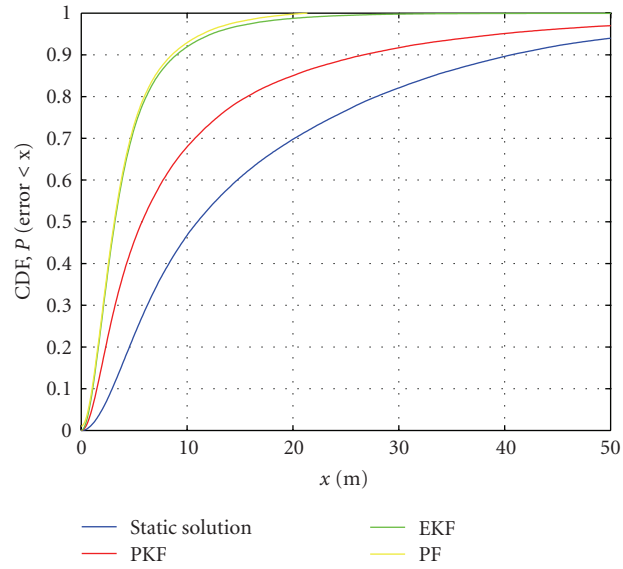


Figure 7: GNSS positioning in urban canyon, different tracking filters.

When using stand-alone TDOA positioning it is reasonable to use two TDOAs (i.e., three BSs) for position estimation since this is the minimum number of required measurements. However, when we fuse GNSS with TDOA measurements, simulations have shown that an adaptive algorithm can help to improve the performance. Since the

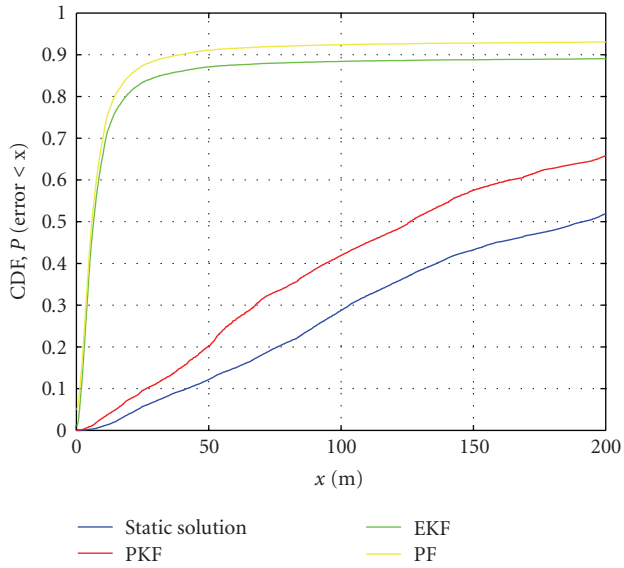


Figure 8: TDOA positioning in urban canyon, cell edge, different tracking filters.

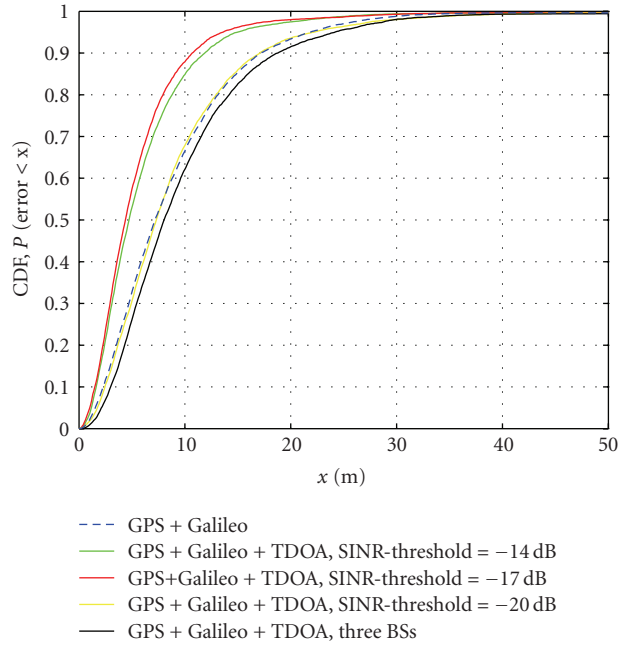


Figure 9: HDF in critical situations, cell edge, EKF tracking, different SINR-thresholds.

tracking filters allow a flexible number of measurements in each time-step, we can adapt the number according to the received SINR levels. Therefore, we define an SINR-threshold, where we drop all measurements that are below this threshold. Hence, unreliable TDOA estimates are not used for the HDF process. Note that the weighting is only based on the SINRs; however, also multipath and especially NLOS propagation have a high impact on the TDOA estimates which are not completely reflected by the SINRs. As we do not assume to know the CIRs or do not consider

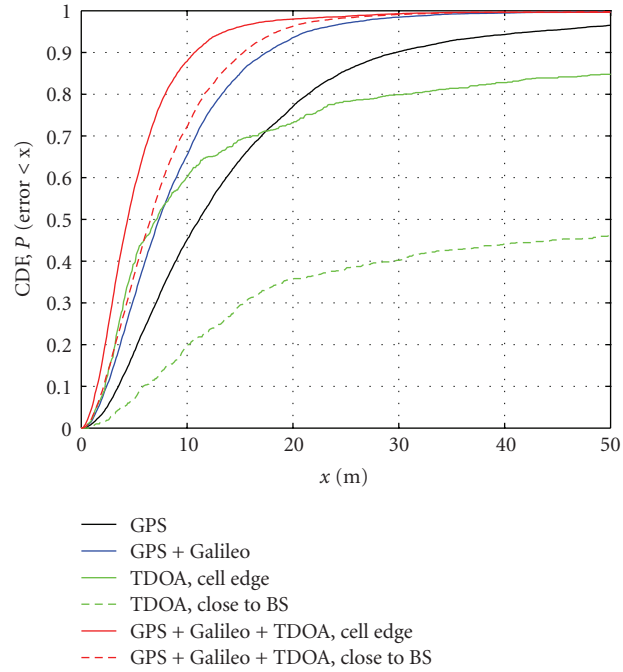


Figure 10: Different positioning systems in critical situations, EKF tracking.

any multipath mitigation, the SINR-thresholding results in different performances. The simulation results in Figure 9 show that an SINR-threshold of −17 dB is a good choice for the considered scenarios, achieving nearly 10 m for the 90%-accuracy in this scenario using GPS+Galileo+TDOA compared to around 17 m for only GPS+Galileo. The adaptive approach which uses the SINR-thresholding also clearly outperforms the classical approach that uses a fixed number of three BSs.

Figure 10 shows the location estimation performance for the GNSS critical situations, where only less than four satellites are available. In these situations, cellular support is particular beneficial. Nevertheless, for stand-alone cellular positioning we observe the high dependency on the MS position in the scenario. At the cell edge a reasonable performance can be achieved, whereas close to the BS the accuracy is very low. Investigating the classical GNSS-based navigation, we observe the advantage of the additional Galileo satellites compared to GPS-stand-alone positioning. The 90%-accuracy can be reduced from 30 m to around 18 m using both systems. When we further include TDOA measurements from the communications system, the performance can be improved to around 15 m if we are close to the BS and to below 11 m for the cell edge situation.

In Figure 11, the LOS visibility of all GNSS satellites is plotted over time for one characteristic MS track realization. We see that in several situations the number of LOS-visible and, hence, detectable satellites is below four; that is, we have a critical scenario. Figure 12 shows the corresponding root mean square errors (RMSEs) over time for GPS+Galileo and the TDOA supplements. It can be observed that in critical GNSS situations the RMSE increases as expected.

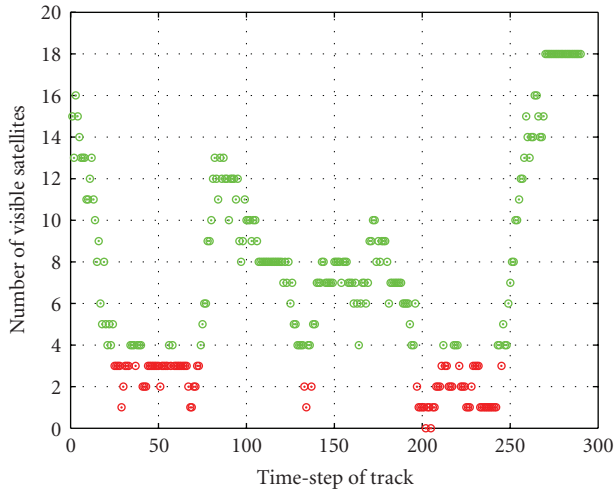


Figure 11: Number of visible satellites versus time for one track.

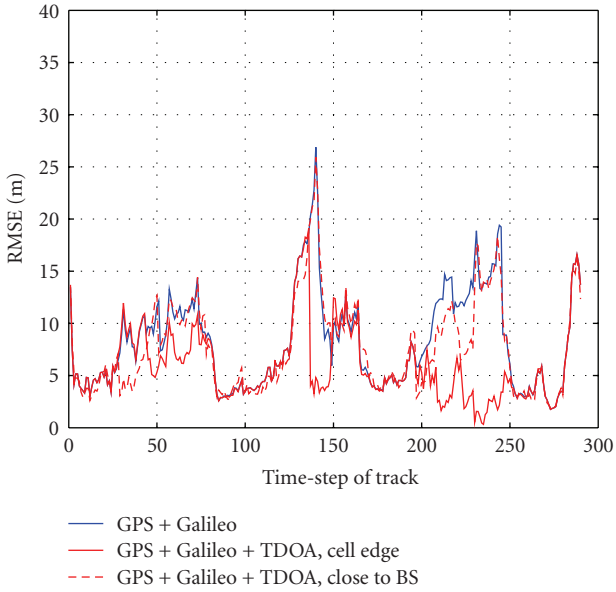


Figure 12: RMSE versus time with different positioning systems for one track, EKF tracking.

This comes on the one hand from the limited number of visible satellites. On the other hand, these satellites are affected by severe multipath contributions that cause additional biases in the timing measurements. Furthermore, the geometric constellation of these satellites is usually bad as satellites are only visible above the MS. In this situation the TDOA measurements can compensate the lack of satellites and further improve the geometric conditions. However, if the scenario is close to a BS, the performance gain is restricted and no fundamental improvement to satellite-only positioning can be achieved. For the cell edge situation, the RMSE can be reduced remarkably in the considered critical situations.

## 5. Conclusions

In this paper we have analyzed hybrid positioning methods that combine measurements from GNSS and future 3GPP-LTE communications systems. As expected, the performance depends strongly on the location in the network, that is, cell edge or close to a BS, where TDOA measurements are exploited for stand-alone positioning and to support GNSS in critical urban canyon scenarios. The simulations were performed in a fairly realistic manner. The urban environment was reflected by CIRs from the satellites and BSs, which were obtained by ray-tracing. Simulation results in this coherent and correlated scenario have shown that in situations where several satellites are blocked, it is very beneficial to have additional TDOA measurements to compensate the missing satellites. Besides the static solution, different tracking filters were investigated, in particular PKF, EKF, and PF. The simulations showed that the EKF provides the best trade-off between accuracy and complexity for the considered scenarios.

## Acknowledgments

This work has been performed in the projects WHERE (Grant Agreement no. 217033) and GRAMMAR (Grant Agreement no. 227890), which are partly funded by the European Union under the European Community's Seventh Framework Programme (FP7/2007-2013), and the DLR-internal project Galileo Advanced Applications. The material in this paper was partly presented at the International Workshop on Synergies in Communications and Localization (SyCoLo), Dresden, Germany, June 2009.

## References

[1] A. H. Sayed, A. Tarighat, and N. Khajehnouri, "Network-based wireless location," *IEEE Signal Processing Magazine*, vol. 22, no. 4, pp. 24–40, 2005.

[2] "FCC 99-245: third report and order," Tech. Rep., Federal Communications Commission (FCC), Rickey Davis, Ala, USA, October 1999, http://www.fcc.gov/911/enhanced/.

[3] P. Misra and P. Enge, *Global Positioning System: Signals, Measurements and Performance*, Ganga-Jamuna Press, Lincoln, Mass, USA, 2004.

[4] R. Ercek, P. De Doncker, and F. Grenez, "Study of pseudo-range error due to non-line-of-sight-multipath in urban canyons," in *Proceedings of the 18th International Technical Meeting of the Satellite Division of The Institute of Navigation (ION GNSS '05)*, pp. 1083–1094, September 2005.

[5] Y. Zhao, "Mobile phone location determination and its impact on intelligent transportation systems," *IEEE Transactions on Intelligent Transportation Systems*, vol. 1, no. 1, pp. 55–64, 2000.

[6] Y. Zhao, "Standardization of mobile phone positioning for 3G systems," *IEEE Communications Magazine*, vol. 40, no. 7, pp. 108–116, 2002.

[7] Third Generation Partnership Project (3GPP), 2009, http://www.3gpp.org.

[8] 3GPP, Qualcomm Europe, "R1-090353: On OTDOA in LTE," 3GPP TSG-RAN WG1 #55bis, January 2009.

[9] 3GPP, Nortel, "R1-090765: LTE Neighbor Cell Hearability," 3GPP TSGRAN WG1 #56, February 2009.

[10] Wireless World Initiative New Radio (WINNER) Project, September 2008, https://www.ist-winner.org.

[11] IST-2003-507581, "WINNER Deliverable D4.8.1: WINNER II Intramode and Intermode Cooperation Schemes Definition," June 2006, https://www.ist-winner.org.

[12] F. Dovis, P. Mulassano, and D. Orgiazzi, "Assessment study of navigation and communication terminal-based hybrid positioning," in *Proceedings of the International Technical Meeting of the Satellite Division of The Institute of Navigation (ION/GNSS '02)*, May 2002.

[13] T. Perälä and R. Piché, "Robust extended Kalman filtering in hybrid positioning applications," in *Proceedings of the 4th Workshop on Positioning, Navigation and Communication (WPNC '07)*, pp. 55–63, March 2007.

[14] S. M. Kay, *Fundamentals of Statistical Signal Processing: Estimation Theory*, Prentice Hall, New York, NY, USA, 1993.

[15] M. S. Arulampalam, S. Maskell, N. Gordon, and T. Clapp, "A tutorial on particle filters for online nonlinear/non-Gaussian Bayesian tracking," *IEEE Transactions on Signal Processing*, vol. 50, no. 2, pp. 174–188, 2002.

[16] 3GPP TS 36.211, "Evolved Universal Terrestrial Radio Access (E-UTRA)—Physical Channels and Modulation, V8.8.0," September 2009, http://www.3gpp.org.

[17] C. Mensing, S. Sand, A. Dammann, and W. Utschick, "Interference-aware location estimation in cellular OFDM communications systems," in *Proceedings of the IEEE International Conference on Communications (ICC '09)*, June 2009.

[18] J. Kammann, M. Angermann, and B. Lami, "A new mobility model based on maps," in *Proceedings of the IEEE 58th Vehicular Technology Conference (VTC '03)*, pp. 3045–3049, October 2003.

[19] B. Ristic, S. Arulampalam, and N. Gordon, *Beyond the Kalman Filter—Particle Filters for Tracking Applications*, Artech House, Norwood, Mass, USA, 2004.

[20] B. Krach, M. Lentmaier, and P. Robertson, "Bayesian detection and tracking for joint positioning and multipath mitigation in GNSS," in *Proceedings of the 5th Workshop on Positioning, Navigation and Communication (WPNC '08)*, pp. 173–180, March 2008.

[21] P. Maybeck, *Stochastic Models, Estimation and Control*, vol. 1, Academic Press, New York, NY, USA, 1979.

[22] P. M. Djurić, J. H. Kotecha, J. Zhang et al., "Particle filtering," *IEEE Signal Processing Magazine*, vol. 20, no. 5, pp. 19–38, 2003.

[23] F. Gustafsson, F. Gunnarsson, N. Bergman et al., "Particle filters for positioning, navigation, and tracking," *IEEE Transactions on Signal Processing*, vol. 50, no. 2, pp. 425–437, 2002.

[24] A. Doucet, J. F. G. de Freitas, and N. J. Gordon, "An introduction to sequential Monte Carlo methods," in *Sequential Monte Carlo Methods in Practice*, A. Doucet, J. F. G. de Freitas, and N. J. Gordon, Eds., Springer, New York, NY, USA, 2001.

[25] N. J. Gordon, D. J. Salmond, and A. F. M. Smith, "Novel approach to nonlinear/non-Gaussian Bayesian state estimation," *Proceedings the IEE*, vol. 140, no. 2, pp. 107–113, 1993.

[26] M. K. Pitt and N. Shephard, "Filtering via simulation: auxiliary particle filters," *Journal of the American Statistical Association*, vol. 94, no. 446, pp. 590–599, 1999.

[27] C. Musso, N. Oudjane, and F. LeGland, "Improving regularized particle filters," in *Sequential Monte Carlo Methods in Practice*, A. Doucet, J. F. G. de Freitas, and N. J. Gordon, Eds., Springer, New York, NY, USA, 2001.

[28] 3GPP, Ericsson, ST-Ericsson, Qualcomm, "R4-093400: OTDOA positioning studies in RAN4: Updated Proposal on System Simulation Assumptions," 3GPP TSG-RAN WG4 #52, August 2009.

Hindawi Publishing Corporation
International Journal of Navigation and Observation
Volume 2010, Article ID 149065, 17 pages
doi:10.1155/2010/149065

*Research Article*

# Nonlinear Filtering for Hybrid GPS/GSM Mobile Terminal Tracking

**Carsten Fritsche and Anja Klein**

*Communications Engineering Lab, Technische Universität Darmstadt, Merckstraße. 25, 64283 Darmstadt, Germany*

Correspondence should be addressed to Carsten Fritsche, c.fritsche@nt.tu-darmstadt.de

Received 30 September 2009; Revised 16 March 2010; Accepted 1 June 2010

Academic Editor: Ronald Raulefs



The Global Positioning System (GPS) has become one of the state-of-the-art location systems that offers reliable mobile terminal (MT) location estimates. However, there exist situations where GPS is not available, for example, when the MT is used indoors or when the MT is located close to high buildings. In these scenarios, a promising approach is to combine the GPS-measured values with measured values from the Global System for Mobile Communication (GSM), which is known as hybrid localization method. In this paper, three nonlinear filters, namely, an extended Kalman filter, a Rao-Blackwellized unscented Kalman filter, and a modified version of the recently proposed cubature Kalman filter, are proposed that combine pseudoranges from GPS with timing advance and received signal strengths from GSM. The three filters are compared with each other in terms of performance and computational complexity. Posterior Cramér-Rao lower bounds are evaluated in order to assess the theoretical performance. Furthermore, it is investigated how additional GPS reference time information available from GSM influences the performance of the hybrid localization method. Simulation and experimental results show that the proposed hybrid method outperforms the GSM method.

## 1. Introduction

In the past few years, there is an increased interest in wireless location systems offering reliable mobile terminal (MT) location estimates. On the one hand, this is due to upcoming and already available commercial services (aka Location Based Services) such as intelligent transport systems, fraud detection, yellow page services, location sensitive billing, and other promising services that rely on accurate MT location estimates [1]. On the other hand, the United States Federal Communications Commission (FCC) issued an order, in which all wireless service providers are required to report the location of an E-911 caller within a specified accuracy [2]. This FCC mandate together with the emerging Location-Based Services has pushed further the research and standardization activities in the field of MT localization.

Until now, several localization methods have been proposed to solve the problem of locating an MT in a wireless network [3, 4]. The global navigation satellite systems (GNSSs), such as the Global Positioning System (GPS) and the prospective European counterpart Galileo, are promising candidates to fulfill the FCC requirements [5]. In the GNSS, the MT location is estimated from the propagation time; the satellite (SAT) signals need to propagate to the MT, which is known as time of arrival (ToA) method. If the MT receives satellite signals from at least four different satellites, a three-dimensional (3D) MT location estimate can be found, where the fourth satellite signal is needed to resolve the unknown bias between the MT and satellite clock [5]. In a similar manner, one can obtain a 2D MT location estimate if the MT receives signals from at least three different satellites. However, there exist situations where the GNSS signals are blocked, for example, when the MT is located indoors or in urban canyons. In these scenarios, the number of satellites in view is often not sufficient to obtain a 3D or even 2D MT location estimate.

An alternative to the GNSS is the exploitation of communication signals of the cellular radio network, in order to obtain MT location estimates. In the Global System for Mobile Communication (GSM), for example, measurements

such as the received signal strength (RSS), timing advance (TA), angle of arrival (AoA), or enhanced observed time difference (E-OTD) exist that give information on the MT location. An appealing advantage of these measurements is that they are almost everywhere available. However, the corresponding localization methods that are based on these measurements cannot offer the same accuracy as their GNSS-based counterpart. The combination of measured values from the GNSS and the cellular radio network is, thus, a promising approach in order to obtain MT location estimates even if less than four or three satellites are in view [6–13]. The resulting hybrid localization methods are expected to improve the accuracy and availability of MT location estimates.

In [6, 7], a hybrid localization method combining pseudorange- (PR-) measured values from GPS and E-OTD-measured values from GSM is investigated. In [8], a hybrid method is presented that is based on the fusion of PR-measured values from GPS and round trip delay-measured values from a cellular radio network that is, perfectly synchronized to GPS time. However, [6–8] only provide general descriptions of their hybrid methods and no algorithms or theoretical performance bounds are given. In [9], a hybrid method based on the combination of PR measured values from GPS and time difference of arrival (TDoA) measured values from a cellular radio network using a least squares approach is introduced. In [11], a hybrid data fusion approach is presented that combines pseudoranges from the GNSS with TDoA measurements from future 3GPP-LTE communication systems using an extended Kalman filter (EKF). In [12, 13], we have developed an extended Kalman filter- (EKF-) based and Rao-Blackwellized unscented Kalman filter- (RBUKF-) based MT tracking algorithm that fuses TA- and RSS-measured values from GSM- and PR-measured values from GPS.

This paper deals with the combination of RSS-, TA-, and PR-measured values from GSM and GPS, as they can be easily obtained from off-the-shelf mobile handsets and conventional GPS receivers. The underlying hybrid mobile terminal tracking problem is then solved using the EKF, RBUKF, and the recently proposed cubature Kalman filter (CKF) [14]. Here, a novel extension of the CKF is introduced, accounting for the linear process model structure, which is called the modified cubature Kalman filter (MCKF). Furthermore, it is investigated in this paper how GPS reference time information from the GSM network, which is available from the Radio Resource Location Services Protocol (RRLP) [15], can help to improve the performance of the hybrid localization methods. The different filtering approaches are then compared to each other, the expected computational complexity is evaluated, and their achievable performance is compared in a realistic simulation study with the posterior Cramér-Rao lower bound (PCRLB). The PCRLB gives the theoretical best achievable performance of nonlinear filters [16] and serves here as an important tool for the design of a hybrid MT tracking system. Finally, the three different algorithms are tested on "real world" GSM measurements together with synthetic GPS-measured values, and their enhanced performance compared to the GSM-based localization method is demonstrated.

The remainder of this paper is organized as follows. In Section 2, the hybrid localization problem is formulated as a nonlinear filtering problem where the optimal solution is given, at least conceptually, by the Bayesian filter. In Section 3, the MT process model and the measurement models for the PR, TA, RSS, and GPS reference time uncertainty are presented that are required to use the different filters. In Section 4, three different nonlinear filters, namely, the EKF, RBUKF, and MCKF are introduced for the hybrid localization problem as well as the PCRLB. The main differences between the different filters are highlighted and the computational complexity is analyzed. In Sections 5 and 6, simulation and experimental results are presented, where the proposed algorithms are compared to each other, and where the advantage of the proposed hybrid method is demonstrated. Finally, Section 7 concludes the work.

## 2. Problem Statement

In this paper, the MT tracking problem is formulated as a nonlinear filtering problem, where a sequence of measurements available from GSM and GPS is used to estimate the actual state of the MT. Consider the following discrete-time state-space model with additive noise:

$$\begin{aligned} &\text{Process Model}: \quad \mathbf{x}(k) = \mathbf{f}(\mathbf{x}(k-1)) + \mathbf{v}(k-1), \\ &\text{Measurement Model}: \quad \mathbf{y}(k) = \mathbf{h}(\mathbf{x}(k)) + \mathbf{w}(k), \end{aligned} \tag{1}$$

where $k$ denotes the discrete-time index, $\mathbf{x}(k) \in \mathbb{R}^{n_x}$ denotes the state vector, $\mathbf{y}(k) \in \mathbb{R}^{n_y}$ denotes the measurement vector, and $\mathbf{f}(\cdot)$ and $\mathbf{h}(\cdot)$ are some known vector-valued, possibly nonlinear, mapping functions. Here, it is worth noting that the function $\mathbf{f}(\cdot)$ models the deterministic relationship between $\mathbf{x}(k)$ and $\mathbf{x}(k-1)$. Similarly, the function $\mathbf{h}(\cdot)$ models the deterministic relationship between the state vector $\mathbf{x}(k)$ and the corresponding measurements $\mathbf{y}(k)$ available from GPS and GSM. The process and measurement noise $\mathbf{v}(k-1)$ and $\mathbf{w}(k)$ are assumed to be mutually independent zero-mean white Gaussian noise sequences with covariances $\mathbf{Q}(k-1)$ and $\mathbf{R}(k)$, respectively.

The aim in nonlinear filtering is to recursively compute estimates of the state $\mathbf{x}(k)$ using the sequence of all available measurements $\mathbf{Y}(k) = \{\mathbf{y}(l), l = 1, \ldots, k\}$ up to and including time $k$. From a Bayesian point of view, the aim is to recursively compute the posterior probability density function (pdf) $p(\mathbf{x}(k) \mid \mathbf{Y}(k))$, since it provides a complete statistical description of the state $\mathbf{x}(k)$ at that time. The optimal Bayesian solution is given by the following recursions:

Time Update:

$$\begin{aligned} p(\mathbf{x}(k) \mid \mathbf{Y}(k-1)) = \int_{\mathbb{R}^{n_x}} & p(\mathbf{x}(k) \mid \mathbf{x}(k-1)) \\ & \times \; p(\mathbf{x}(k-1) \mid \mathbf{Y}(k-1)) \mathrm{d}\mathbf{x}(k-1). \end{aligned} \tag{2}$$

Measurement Update:

$$p(\mathbf{x}(k) \mid \mathbf{Y}(k)) = \frac{p(\mathbf{y}(k) \mid \mathbf{x}(k))\, p(\mathbf{x}(k) \mid \mathbf{Y}(k-1))}{p(\mathbf{y}(k) \mid \mathbf{Y}(k-1))}, \quad (3)$$

where $p(\mathbf{y}(k) \mid \mathbf{Y}(k-1))$ is a normalizing constant given by

$$p(\mathbf{y}(k) \mid \mathbf{Y}(k-1)) = \int_{\mathbb{R}^{nx}} p(\mathbf{y}(k) \mid \mathbf{x}(k))\, p(\mathbf{x}(k) \mid \mathbf{Y}(k-1))\, \mathrm{d}\mathbf{x}(k), \quad (4)$$

and where the pdfs $p(\mathbf{x}(k) \mid \mathbf{x}(k-1))$ and $p(\mathbf{y}(k) \mid \mathbf{x}(k))$ can be determined from (1). The above recursions are initiated by $p(\mathbf{x}(0) \mid \mathbf{Y}(0)) = p(\mathbf{x}(0))$ [17]. It is well known that the nonlinear recursive filtering problem only allows analytical solutions in a few special cases, for example, for linear Gaussian models, where the Kalman filter provides the optimal solution [18]. However, for the general model (1), an analytical solution to the above recursions is intractable and, thus, one has to resort to suboptimal algorithms.

For the hybrid localization method three suboptimal nonlinear filters are investigated, namely, the extended Kalman filter, the Rao-Blackwellized unscented Kalman filter, and the modified cubature Kalman filter. But before these filters will be explained in more detail, it will be first shown how the process model and measurement models are chosen for the hybrid localization method.

## 3. Process and Measurement Model

*3.1. Introduction.* In the following, it is assumed that the MT location $\mathbf{x}_{\mathrm{MT}} = [x_{\mathrm{MT}}, y_{\mathrm{MT}}]^\top$ to be estimated and the known base station (BS) locations $\mathbf{x}_{\mathrm{BS}}^{(n)} = [x_{\mathrm{BS}}^{(n)}, y_{\mathrm{BS}}^{(n)}]^\top$, $n = 1, \ldots, N_{\mathrm{BS}}$, lie in the $xy$-plane, where $[\cdot]^\top$ denotes the transpose of a vector or matrix. The known satellite locations are given by $\mathbf{x}_{\mathrm{SAT}}^{(l)} = [x_{\mathrm{SAT}}^{(l)}, y_{\mathrm{SAT}}^{(l)}, z_{\mathrm{SAT}}^{(l)}]^\top$, $l = 1, \ldots, N_{\mathrm{SAT}}$. For the case of 3-D MT and BS locations, the process and measurement models can be obtained in a similar way. The measurements that are used for the hybrid localization method are the PR-measured values from GPS and TA, RSS, and GPS reference time uncertainty measured values from GSM. Here, it is worth noting that the hybridization takes place by combining different types of measurements from GPS and GSM rather than location estimates from GPS and GSM. That is, one first collects at every time step $k$ all the measurements from GPS and GSM and then these measurements are processed jointly in the filter in order to estimate the MT location. With this strategy, it is possible to obtain MT location estimates even if less than three satellites are visible to the MT.

*3.2. Process Model.* For the hybrid localization method, the states of the process model include the 2-D MT location and velocity, the MT clock bias, and clock drift, that is, $\mathbf{x} = [\, x_{\mathrm{MT}}, \dot{x}_{\mathrm{MT}}, y_{\mathrm{MT}}, \dot{y}_{\mathrm{MT}}, c_0 \cdot \delta t, c_0 \cdot \delta \dot{t}\, ]^\top$, where $c_0$ is the speed of light. The movement of the MT is approximated with a nearly constant velocity (CV) model and the receiver clock bias is modeled by a second-order Gauss-Markov process [19, 20]. The resulting linear process model for the hybrid localization method is, thus, given by

$$\mathbf{x}(k) = \mathbf{\Phi} \cdot \mathbf{x}(k-1) + \mathbf{\Gamma} \cdot \mathbf{v}(k-1) \quad (5)$$

with

$$\mathbf{\Phi} = \mathbf{I}_3 \otimes \begin{bmatrix} 1 & T_{\mathrm{S}} \\ 0 & 1 \end{bmatrix}, \qquad \mathbf{\Gamma} = \mathrm{diag}\left(\mathbf{I}_2 \otimes \begin{bmatrix} \frac{T_{\mathrm{S}}^2}{2}, T_{\mathrm{S}} \end{bmatrix}^\top, \mathbf{I}_2 \cdot c_0\right), \quad (6)$$

where $\mathbf{I}_q$ is the identity matrix of size $q$, $\otimes$ denotes the Kronecker product, and $T_{\mathrm{S}}$ is the sampling time. The process noise $\mathbf{v} = [v_x, v_y, v_{\delta t}, v_{\delta \dot{t}}]^\top$ is assumed to be a zero-mean white Gaussian noise sequence with block diagonal covariance matrix $\mathbf{Q} = \mathrm{diag}\,(\mathbf{Q}_{\mathrm{CV}}, \mathbf{Q}_{\delta t})$. The covariance matrix $\mathbf{Q}_{\mathrm{CV}}$ is given by $\mathbf{Q}_{\mathrm{CV}} = \mathrm{diag}(\sigma_x^2, \sigma_y^2)$, where $\sigma_x^2$ and $\sigma_y^2$ denote the noise variances in the $x$- and $y$-direction. The elements of the symmetric $2 \times 2$ matrix $\mathbf{Q}_{\delta t}$ are given by

$$\begin{aligned} Q_{11} &= h_0 \frac{T_{\mathrm{S}}}{2} + 2h_{-1} T_{\mathrm{S}}^2 + \frac{2}{3}\pi^2 h_{-2} T_{\mathrm{S}}^3, \\ Q_{12} &= Q_{21} = 2h_{-1} T_{\mathrm{S}} + \pi^2 h_{-2} T_{\mathrm{S}}^2, \\ Q_{22} &= \frac{h_0}{2T_{\mathrm{S}}} + 2h_{-1} + \frac{8}{3}\pi^2 h_{-2} T_{\mathrm{S}}, \end{aligned} \quad (7)$$

where the parameters $h_0, h_{-1}$, and $h_{-2}$ correspond to values of a typical quartz standard [19].

### 3.3. Measurement Model

*3.3.1. Pseudorange.* In GPS, the MT is measuring the time the satellite signal requires to travel from the satellite to the MT, which is known as ToA principle [5]. The corresponding ToA-measured values are affected by delays due to the transmission of the satellite signal through the ionosphere and the troposphere and due to other errors, for example, receiver noise or multipath propagation [5]. In addition to that, the MT's clock is generally not time-synchronized to the clocks of the GPS satellites, resulting in an unknown receiver clock bias $\delta t(k)$ that has to be estimated. The corresponding measured biased ranges or measured pseudoranges can be obtained from multiplying the biased ToA-measured values by $c_0$.

In the following, it is assumed that each measured pseudorange is corrected for the known errors that are available using parameter values in the navigation message from the satellite [5]. Let $\mathbf{y}_{\mathrm{PR}}(k)$ denote the vector of $N_{\mathrm{SAT}}$-corrected PR-measured values. Then, the PR measurement model can be written as

$$\mathbf{y}_{\mathrm{PR}}(k) = \mathbf{h}_{\mathrm{PR}}(\mathbf{x}_{\mathrm{MT}}(k), \delta t(k)) + \mathbf{w}_{\mathrm{PR}}(k) \quad (8)$$

with

$$\begin{aligned} &\mathbf{h}_{\mathrm{PR}}(\mathbf{x}_{\mathrm{MT}}(k), \delta t(k)) \\ &\quad = \left[ d_{\mathrm{SAT}}^{(1)}(\mathbf{x}_{\mathrm{MT}}(k)), \ldots, d_{\mathrm{SAT}}^{(N_{\mathrm{SAT}})}(\mathbf{x}_{\mathrm{MT}}(k)) \right]^\top \\ &\qquad + c_0 \cdot \delta t(k), \end{aligned} \quad (9)$$

where $d_{\mathrm{SAT}}^{(l)}(\mathbf{x}_{\mathrm{MT}}(k))$ denotes the Euclidean distance between the MT and the $l$th satellite. The random variable $\mathbf{w}_{\mathrm{PR}}(k)$ describes unmodeled effects, modeling errors, and measurement errors; each PR-measured value is affected by, for example, delays as the signal propagates through the atmosphere, receiver noise, as well as errors due to changing propagation conditions, that is, line-of-sight (LOS) or non-line-of-sight (NLOS) situations. It is assumed that $\mathbf{w}_{\mathrm{PR}}(k)$ is Gaussian distributed with mean vector $\boldsymbol{\mu}_{\mathrm{PR}} = [\mu_{\mathrm{PR}}^{(1)}, \ldots, \mu_{\mathrm{PR}}^{(N_{\mathrm{SAT}})}]^{\top}$ accounting for NLOS propagation and covariance matrix $\mathbf{R}_{\mathrm{PR}} = \mathrm{diag}((\sigma_{\mathrm{PR}}^{(1)})^2, \ldots, (\sigma_{\mathrm{PR}}^{(N_{\mathrm{SAT}})})^2)$, where $\mu_{\mathrm{PR}}^{(l)}$ and $\sigma_{\mathrm{PR}}^{(l)}$ denote the mean and standard deviation from the PR-measured value of the $l$th satellite.

*3.3.2. Timing Advance.* In GSM, the Timing Advance (TA) is a parameter that is used to synchronize the transmitted bursts of the MTs to the frame of the receiving BS [1]. In principle, the TA is a quantized value of the round trip time, that is, the time the radio signal requires to propagate from the BS to the MT and back. Let $\mathbf{y}_{\mathrm{TA}}(k)$ denote the vector of $N_{\mathrm{BS}}$ TA-measured values multiplied by $c_0/2$. Then, the TA-measurement model is given by

$$\mathbf{y}_{\mathrm{TA}}(k) = \mathbf{h}_{\mathrm{TA}}(\mathbf{x}_{\mathrm{MT}}(k)) + \mathbf{w}_{\mathrm{TA}}(k) \tag{10}$$

with

$$\mathbf{h}_{\mathrm{TA}}(\mathbf{x}_{\mathrm{MT}}(k)) = \left[d_{\mathrm{BS}}^{(1)}(\mathbf{x}_{\mathrm{MT}}(k)), \ldots, d_{\mathrm{BS}}^{(N_{\mathrm{BS}})}(\mathbf{x}_{\mathrm{MT}}(k))\right]^{\top}, \tag{11}$$

where $d_{\mathrm{BS}}^{(n)}(\mathbf{x}_{\mathrm{MT}}(k))$ denotes the Euclidean distance between the MT and the $n$th BS. The random variable $\mathbf{w}_{\mathrm{TA}}(k)$ accounts for the errors each TA-measured value is affected by, such as quantization, changing propagation conditions—LOS or NLOS situation—and measurement noise. These errors are assumed to be Gaussian distributed with mean vector $\boldsymbol{\mu}_{\mathrm{TA}} = [\mu_{\mathrm{TA}}^{(1)}, \ldots, \mu_{\mathrm{TA}}^{(N_{\mathrm{BS}})}]^{\top}$ accounting for NLOS propagation and covariance matrix $\mathbf{R}_{\mathrm{TA}} = \mathrm{diag}((\sigma_{\mathrm{TA}}^{(1)})^2, \ldots, (\sigma_{\mathrm{TA}}^{(N_{\mathrm{BS}})})^2)$, where $\mu_{\mathrm{TA}}^{(n)}$ and $\sigma_{\mathrm{TA}}^{(n)}$ denote the mean and standard deviation from the TA-measured value of the $n$th BS.

*3.3.3. Received Signal Strength.* In GSM, the RSS value is an averaged value of the strength of a radio signal received by the MT. The attenuation of the signal strength through a mobile radio channel is caused by three factors, namely, fast fading, slow fading, and path loss. Since, in GSM, the RSS-measured values are averaged over several time-consecutive measurements, the error due to fast fading can be neglected. The model for the path loss in dB is given by

$$L^{(n)}(\mathbf{x}_{\mathrm{MT}}(k)) = A^{(n)} + 10 \cdot B^{(n)} \cdot \log_{10}\left(\frac{d_{\mathrm{BS}}^{(n)}(\mathbf{x}_{\mathrm{MT}}(k))}{1\,\mathrm{km}}\right). \tag{12}$$

Reference[3], where $A^{(n)}$ denotes the reference path loss at a BS to MT distance of 1 km and $B^{(n)}$ is the path loss exponent of the $n$th BS. Both parameters $A^{(n)}$ and $B^{(n)}$ strongly depend on the propagation conditions and BS antenna settings and can be determined either empirically or from well-known path loss models as, for example, Hata [21] or COST 231 Walfisch-Ikegami [22].

In real systems, the BSs may be equipped with directional antennas in order to increase the cell's capacity. However, the employment of directional antennas at the BSs should be directly taken into account in the model for the RSS measured value, because otherwise the performance of the tracking algorithms will considerably degrade. In the following, it is assumed that antenna gain models are a priori available. Let $A_{\mathrm{m}}^{(n)}$ and $\varphi_{3\,\mathrm{dB}}^{(n)}$ denote the minimum gain and 3 dB beamwidth of the BS antenna. Let further $\varphi_{\mathrm{BS}}^{(n)}(\mathbf{x}_{\mathrm{MT}}(k))$ denote the azimuth angle between the MT and the $n$th BS antenna, counted counterclockwise from the boresight direction of the BS antenna. Then, a model for the normalized antenna gain in dB scale is given by

$$g\left(\varphi_{\mathrm{BS}}^{(n)}(\mathbf{x}_{\mathrm{MT}}(k))\right) = -\min\left\{12\left(\frac{\varphi_{\mathrm{BS}}^{(n)}(\mathbf{x}_{\mathrm{MT}}(k))}{\varphi_{3\,\mathrm{dB}}^{(n)}}\right)^2, A_{\mathrm{m}}^{(n)}\right\}. \tag{13}$$

Reference [10], where $\min\{a, b\}$ denotes the smallest value in the set $\{a, b\}$. Let $\mathbf{y}_{\mathrm{RSS}}(k)$ denote the vector of $N_{\mathrm{BS}}$ RSS-measured values. Then, the RSS measurement model in dB scale is given by

$$\mathbf{y}_{\mathrm{RSS}}(k) = \mathbf{h}_{\mathrm{RSS}}(\mathbf{x}_{\mathrm{MT}}(k)) + \mathbf{w}_{\mathrm{RSS}}(k) \tag{14}$$

with

$$\mathbf{h}_{\mathrm{RSS}}(\mathbf{x}_{\mathrm{MT}}(k)) = \left[h_{\mathrm{RSS}}^{(1)}(\mathbf{x}_{\mathrm{MT}}(k)), \ldots, h_{\mathrm{RSS}}^{(N_{\mathrm{BS}})}(\mathbf{x}_{\mathrm{MT}}(k))\right]^{\top},$$
$$h_{\mathrm{RSS}}^{(n)}(\mathbf{x}_{\mathrm{MT}}(k)) = P_{\mathrm{T}}^{(n)} - \left\{L^{(n)}(\mathbf{x}_{\mathrm{MT}}(k)) - g\left(\varphi_{\mathrm{BS}}^{(n)}(\mathbf{x}_{\mathrm{MT}}(k))\right)\right\}, \tag{15}$$

where $P_{\mathrm{T}}^{(n)}$ denotes the $n$th BS's equivalent isotropic radiated power. The random variable $\mathbf{w}_{\mathrm{RSS}}(k)$ accounts for errors, such as errors due to slow fading, quantization, and NLOS propagation. It is assumed that $\mathbf{w}_{\mathrm{RSS}}(k)$ is zero-mean Gaussian distributed with covariance matrix $\mathbf{R}_{\mathrm{RSS}} = \mathrm{diag}((\sigma_{\mathrm{RSS}}^{(1)})^2, \ldots, (\sigma_{\mathrm{RSS}}^{(N_{\mathrm{BS}})})^2)$, where $\sigma_{\mathrm{RSS}}^{(n)}$ denotes the standard deviation from the RSS-measured value of the $n$th BS.

*3.3.4. GPS Reference Time Uncertainty.* In GSM, there exists the possibility to obtain GPS reference time information that can be used to estimate the unknown clock bias $\delta t(k)$ in the pseudorange equations (cf. (9)) according to the available RRLP [15]. However, in [15] it is stated that this reference time can be provided only with a specified accuracy which is expressed by the so-called GPS reference time uncertainty. In the following, a model connecting the GPS reference time uncertainty to the unknown MT clock bias will be derived.

Since the satellite clocks can be assumed to be mutually synchronized [5], the MT clock bias can be written as $\delta t(k) = t_{\mathrm{GPS}}(k) - t_{\mathrm{MTC}}(k)$, where the difference describes the offset between the GPS reference time scale $t_{\mathrm{GPS}}(k)$, which is unknown to the MT, and the known MT clock time-scale $t_{\mathrm{MTC}}(k)$. Here, it is worth noting that the bias is not constant over time, since the MT clock experiences errors due to clock

drifts. Let $y_{\mathrm{RTU}}(k)$ denote the GPS reference time uncertainty measurement. Then, the GPS reference time uncertainty measurement model is given by

$$y_{\mathrm{RTU}}(k) = t_{\mathrm{GPS}}(k) + w_{\mathrm{RTU}}(k), \tag{16}$$

which can be directly converted into an MT clock bias measurement model:

$$y_{\mathrm{BIAS}}(k) = y_{\mathrm{RTU}}(k) - t_{\mathrm{MTC}}(k) = \delta t(k) + w_{\mathrm{RTU}}(k), \tag{17}$$

where the noise $w_{\mathrm{RTU}}(k)$ models the GPS reference time uncertainty which is assumed to be zero-mean Gaussian distributed with standard deviation $\sigma_{\mathrm{RTU}}$. Since we now have related the GPS reference time uncertainty measurement to the clock bias, the uncertainty of the MT clock is implicitly modelled with the process model (cf. (5)) where the MT clock bias evolves according to a second-order Gauss-Markov process.

*3.3.5. Combined.* In the following, the PR, TA, RSS, and MT clock bias-measured values are concatenated into a single measurement vector, yielding $\mathbf{y}(k) = [\, \mathbf{y}_{\mathrm{PR}}^{\top}(k), \mathbf{y}_{\mathrm{TA}}^{\top}(k), \mathbf{y}_{\mathrm{RSS}}^{\top}(k), y_{\mathrm{BIAS}}(k) \,]^{\top}$. Here, GPS reference time uncertainty-measured values are treated as MT clock bias-measured values according to (17). The corresponding combined nonlinear measurement model for the hybrid localization problem can be written as

$$\mathbf{y}(k) = \mathbf{h}(\mathbf{x}(k)) + \mathbf{w}(k), \tag{18}$$

where

$$\begin{aligned} \mathbf{h}(\mathbf{x}(k)) = \big[&\mathbf{h}_{\mathrm{PR}}^{\top}(\mathbf{x}_{\mathrm{MT}}(k), \delta t(k)), \mathbf{h}_{\mathrm{TA}}^{\top}(\mathbf{x}_{\mathrm{MT}}(k)), \\ &\mathbf{h}_{\mathrm{RSS}}^{\top}(\mathbf{x}_{\mathrm{MT}}(k)), \delta t(k)\big]^{\top}, \end{aligned} \tag{19}$$

$$\mathbf{w}(k) = \big[\mathbf{w}_{\mathrm{PR}}^{\top}(k), \mathbf{w}_{\mathrm{TA}}^{\top}(k), \mathbf{w}_{\mathrm{RSS}}^{\top}(k), w_{\mathrm{RTU}}(k)\big]^{\top}. \tag{20}$$

The random variable $\mathbf{w}(k)$ is Gaussian distributed with mean vector $\boldsymbol{\mu} = [\, \boldsymbol{\mu}_{\mathrm{PR}}^{\top}(k), \boldsymbol{\mu}_{\mathrm{TA}}^{\top}(k), \mathbf{0} \,]^{\top}$, where $\mathbf{0}$ denotes the zero vector of size $1 \times N_{\mathrm{BS}} + 1$, and block diagonal covariance matrix $\mathbf{R} = \mathrm{diag}(\mathbf{R}_{\mathrm{PR}}, \mathbf{R}_{\mathrm{TA}}, \mathbf{R}_{\mathrm{RSS}}, \sigma_{\mathrm{RTU}})$.

## 4. Nonlinear Filters for Hybrid Localization

*4.1. Introduction.* After having described the linear process model and the nonlinear relationship between the MT location and the PR-, TA-, and RSS-measured values, the problem at hand is how one can efficiently sequentially estimate the MT state from these measured values. The optimal Bayesian solution given by ((2), (3), and (4)) provides a unified approach for nonlinear filtering problems. However, due to the fact that the measurement model is nonlinear (cf. (18)) the multidimensional integral involved in (4) is intractable and, thus, one has to resort to suboptimal algorithms [14, 16, 23–25]. In this paper, three different suboptimal algorithms, namely, the extended Kalman filter, the Rao-Blackwellized unscented Kalman filter, and the modified cubature Kalman filter, are proposed in order to solve the underlying hybrid localization problem. These filters belong to the class of approaches where all densities in ((2), (3), and (4)) are assumed to be Gaussian. An appealing advantage of this approximation is that the functional recursion in ((2), (3), and (4)) reduces to an algebraic recursion, where only means and covariances have to be calculated.

*4.2. Extended Kalman Filter.* In the EKF, the nonlinear functions $f(\mathbf{x}(k-1))$ and $\mathbf{h}(\mathbf{x}(k))$ are approximated with their first-order Taylor series expansion, so that an analytical solution of (2) and (4) is possible. This approach, however, leads to several shortcomings. On the one hand, the EKF may have suboptimal performance or even will diverge, if we have a high degree of nonlinearities in the measurement function. On the other hand, the linearization of the measurement model implies the evaluation of Jacobian matrices, which in some cases may become difficult; for example, consider the case when antenna gain models (cf. (13)) are available only from measurements and, consequently, no closed form expressions for these models exist. In these cases, it is much easier to approximate the models using interpolation than trying to evaluate the corresponding Jacobian matrices. The well-known EKF equations, adopted to the proposed hybrid localization method, are summarized in Algorithm 1 [12].

*4.3. Rao-Blackwellized Unscented Kalman Filter.* While the EKF is based on a simple linear approximation of the nonlinear measurement equation, the unscented Kalman filter (UKF) approximates the multidimensional integrals in (2) and (4) using the (scaled) unscented transformation [26, 27]. In the (scaled) unscented transformation, the multidimensional integrals are approximated using a deterministic sampling procedure. The sampling scheme consists of deterministically choosing a symmetric set of sigma points and weights. These sigma points are then propagated through the true nonlinearity and the corresponding mean and covariances are approximated using a weighted sample mean and covariance. Compared to the EKF, the advantage of the UKF is that no Jacobian matrices have to be evaluated, since the sigma points are transformed through the true nonlinearity. Furthermore, it can be shown that the nonlinear transformed samples capture the mean and covariance accurately to at least the second-order of the Taylor series expansion whereas the EKF only achieves first-order accuracy [27]. Since the noise in the process model and measurement model is assumed to be additive and Gaussian distributed, the dimension of the vector, from which the sigma points are sampled, can be reduced. This technique is also known as Rao-Blackwellization and has the advantage that the quasi-Monte Carlo variance and computational complexity can be reduced [28]. The computational complexity can be further reduced by taking into account that the posterior pdf $p(\mathbf{x}(k-1) \mid \mathbf{Y}(k-1))$ is assumed Gaussian and the process model is linear Gaussian. In this case, the multidimensional integral, given in (2), can be evaluated in closed form, resulting in the well-known Kalman filter update equations. The corresponding RBUKF,

**Initialization**

$\hat{\mathbf{x}}(0 \mid 0) = \mathbb{E}\{\mathbf{x}(0)\}$

$\mathbf{P}(0 \mid 0) = \mathbb{E}\{(\mathbf{x}(0) - \hat{\mathbf{x}}(0 \mid 0))(\mathbf{x}(0) - \hat{\mathbf{x}}(0 \mid 0))^{\top}\}$

**Time Update**

Estimate the predicted state vector and error covariance matrix

$\hat{\mathbf{x}}(k \mid k-1) = \boldsymbol{\Phi}\hat{\mathbf{x}}(k-1 \mid k-1)$,

$\mathbf{P}(k \mid k-1) = \boldsymbol{\Phi}\mathbf{P}(k-1 \mid k-1)\,\boldsymbol{\Phi}^{\top} + \boldsymbol{\Gamma}\mathbf{Q}\boldsymbol{\Gamma}^{\top}$.

**Measurement Update**

Estimate the innovation covariance and cross-covariance matrix

$\mathbf{P}_{\mathbf{yy}}(k \mid k-1) = \mathbf{H}(k)\mathbf{P}(k \mid k-1)\mathbf{H}^{T}(k) + \mathbf{R}$

$\mathbf{P}_{\mathbf{xy}}(k \mid k-1) = \mathbf{P}(k \mid k-1)\mathbf{H}^{T}(k)$.

Estimate the Kalman gain, updated state vector and error covariance matrix

$\mathbf{K}(k) = \mathbf{P}_{\mathbf{xy}}(k \mid k-1)\mathbf{P}_{\mathbf{yy}}^{-1}(k \mid k-1)$,

$\hat{\mathbf{x}}(k \mid k) = \hat{\mathbf{x}}(k \mid k-1) + \mathbf{K}(k)[\mathbf{y}(k) - \mathbf{h}(\hat{\mathbf{x}}(k \mid k-1)) - \boldsymbol{\mu}]$,

$\mathbf{P}(k \mid k) = \mathbf{P}(k \mid k-1) - \mathbf{K}(k)\,\mathbf{P}_{\mathbf{yy}}(k \mid k-1)\mathbf{K}^{\top}(k)$,

where $\mathbf{H}(k)$ denotes the Jacobian matrix of $\mathbf{h}(\mathbf{x}(k))$ evaluated at $\hat{\mathbf{x}}(k \mid k-1)$.

Algorithm 1: Extended Kalman Filter.

adapted to the hybrid localization method, is summarized in Algorithm 2 [13].

*4.4. Modified Cubature Kalman Filter.* In the recently proposed CKF [14], the multidimensional integrals in (2) and (4) are approximated in a different way. Since the conditional pdfs $p(\mathbf{x}(k) \mid \mathbf{Y}(k-1))$ and $p(\mathbf{y}(k) \mid \mathbf{Y}(k-1))$ in (2) and (4) are assumed Gaussian, solving approximately the multidimensional integrals is equivalent to the evaluation of the corresponding means and covariances of $p(\mathbf{x}(k) \mid \mathbf{Y}(k-1))$ and $p(\mathbf{y}(k) \mid \mathbf{Y}(k-1))$. It can be shown that the evaluation of the mean and covariance leads again to multidimensional integrals, but whose integrands are now all of the form *nonlinear function* $\times$ *Gaussian density* [14]. These integrals are then solved using highly efficient numerical integration methods known as cubature rules. As a result, one obtains a set of cubature points and weights, from which the corresponding mean and covariance can be computed without evaluating Jacobian matrices. Due to the fact that (2) can be evaluated in closed form, the computational complexity of the CKF can be further reduced. The modified version of the CKF that is used for the hybrid localization problem is summarized in Algorithm 3. Although the CKF and UKF seem to be very similar, the authors in [14] claim that the cubature approach is more accurate and more principled in mathematical terms than the sigma-point approach used in the UKF. Here, it is worth noting that the RBUKF reduces to the MCKF, when the unknown parameters in the scaled unscented transformation are chosen as $\alpha = 1, \beta = 0$, and $\kappa = 0$ in Algorithm 2.

*4.5. Posterior Cramér-Rao Lower Bound.* After having introduced the different filters for the hybrid localization problem, their performance should be compared to a theoretical bound. In the following, the posterior Cramér-Rao lower bound for the hybrid localization problem is presented that gives the best achievable performance for nonlinear filtering [16, 29]. Let $\hat{\mathbf{x}}(k \mid k)$ be an unbiased estimate of the state vector $\mathbf{x}(k)$. Then, the covariance matrix of the estimation error satisfies the inequality

$$\mathbb{E}\left\{(\hat{\mathbf{x}}(k \mid k) - \mathbf{x}(k))(\hat{\mathbf{x}}(k \mid k) - \mathbf{x}(k))^{\top}\right\} \geq \mathbf{J}^{-1}(k), \quad (21)$$

where $\mathbb{E}\{\cdot\}$ is the expectation with respect to $\mathbf{x}(k)$, $\mathbf{J}(k)$ denotes the filtering information matrix, and its inverse is the PCRLB matrix. The matrix inequality $\mathbf{A} \geq \mathbf{B}$ should be interpreted as the matrix $\mathbf{A} - \mathbf{B}$ being positive semidefinite. The aim is now to calculate $\mathbf{J}(k)$. In [29], an elegant method is presented, where $\mathbf{J}(k)$ can be determined recursively. This recursion, adapted to the hybrid localization problem involving additive Gaussian noise (cf. (5) and (18)) can be written as

$$\mathbf{J}(k) = \left(\boldsymbol{\Gamma}\mathbf{Q}\boldsymbol{\Gamma}^{\top} + \boldsymbol{\Phi}\mathbf{J}^{-1}(k-1)\boldsymbol{\Phi}^{\top}\right)^{-1} + \mathbb{E}\left\{\widetilde{\mathbf{H}}^{\top}(k)\mathbf{R}^{-1}\widetilde{\mathbf{H}}(k)\right\}, \quad (22)$$

where the expectation is with respect to $\mathbf{x}(k)$ and $\widetilde{\mathbf{H}}(k)$ denotes the Jacobian matrix of the nonlinear measurement function $\mathbf{h}(\cdot)$ (cf. (19)) evaluated at the true value of the state $\mathbf{x}(k)$. Since the initial distribution $p(\mathbf{x}(0))$ is assumed to be Gaussian, the recursions are initialized with the information matrix $\mathbf{J}(0) = \mathbf{P}^{-1}(0 \mid 0)$ [16].

*4.6. Computational Complexity.* In this section, the computational complexity of the EKF, RBUKF, and MCKF for the hybrid localization method is investigated in terms of floating-point operations (FLOPs). A FLOP is here defined as one addition, subtraction, multiplication, or division of two floating-point numbers. In Table 1, the computational complexity of some common matrix operations is summarized. Here, it is worth noting that the matrix square root, which is needed to evaluate the set of cubature and sigma points, is computed using Cholesky decomposition, whose complexity grows cubically.

In the EKF as well as in the RBUKF and MCKF, there are certain steps that cannot be measured in FLOPs. In the EKF, for example, one has to evaluate at every time step $k$

Table 1: Computational complexity of some common matrix operations [30].

| Operation | Size | Mult. | Add. | Other |
|---|---|---|---|---|
| $\mathbf{A}+\mathbf{A}$ | $\mathbf{A}\in\mathbb{R}^{n\times m}$ | — | $nm$ | — |
| $\mathbf{A}\cdot\mathbf{B}$ | $\mathbf{A}\in\mathbb{R}^{n\times m},\mathbf{B}\in\mathbb{R}^{m\times l}$ | $lmn$ | $(m-1)ln$ | — |
| $\mathbf{C}^{-1}$ | $\mathbf{C}\in\mathbb{R}^{n\times n}$ | $n^3$ | — | — |
| $\sqrt{\mathbf{C}}$ | $\mathbf{C}\in\mathbb{R}^{n\times n}$ | — | — | $n^3/3+2n^2$ |

the Jacobian matrix $\mathbf{H}(k)$ and the nonlinear function $\mathbf{h}(\cdot)$ (cf. Algorithm 1). In the RBUKF and MCKF, one has to propagate at every time step $2n_x+1$ sigma points and $2n_x$ cubature points through the nonlinear function $\mathbf{h}(\cdot)$ (cf. Algorithms 2 and 3). In the following, the cost of evaluating a certain nonlinear function and Jacobian matrix is neglected. Furthermore, the computation of the weights in the RBUKF, and MCKF as well as the initialization of all three filters can be neglected, since these steps are done only once.

In Table 2, the computational complexity of the different quantities that have to be evaluated in the EKF, RBUKF, and MCKF is presented. Summing up the computational complexity of the different quantities results in the total FLOP complexity of the EKF, RBUKF, and MCKF for one time step which is given by

$$\begin{aligned}
\mathcal{C}_{\mathrm{EKF}}\left(n_x,n_y\right) &= 8n_x^3+n_y^3+6n_x^2n_y+6n_y^2n_x-13n_x^2\\
&\quad -2n_xn_y+9n_x+2n_y,\\
\mathcal{C}_{\mathrm{RBUKF}}\left(n_x,n_y\right) &= \frac{37}{3}n_x^3+n_y^3+6n_x^2n_y+8n_y^2n_x-9n_x^2\\
&\quad +7n_xn_y+4n_y^2+10n_x+5n_y,\\
\mathcal{C}_{\mathrm{MCKF}}\left(n_x,n_y\right) &= \frac{37}{3}n_x^3+n_y^3+6n_x^2n_y+8n_y^2n_x-11n_x^2\\
&\quad +4n_xn_y+3n_y^2+9n_x+2n_y,
\end{aligned}\tag{23}$$

where $n_x$ and $n_y$ denote the dimension of the state and measurement vector, respectively.

## 5. Simulation Results

*5.1. Scenario I.* In the first simulation scenario (Scenario I), it is assumed that a car is equipped with an MT that is capable of providing PR-measured values from GPS and TA, RSS, and GPS reference time uncertainty-measured values from GSM. The car moves with a constant speed of 45 km/h in a dense urban scenario of size 3 km × 3 km as it is shown in Figure 1. The GSM network is composed of $N_{\mathrm{BS}}=7$ BSs, where each BS is equipped with a directional antenna. The BS locations as well as the BS antenna parameters are a priori known. The satellite locations are taken from the real GPS satellite constellation taking into account realistic satellite elevation masks and are assumed to be known. The parameters used in the simulations are summarized in Table 3 and are assumed to be equal for all BSs and all satellites for the sake of simplicity. The following combinations of measured values are investigated:

(i) GSM method: one TA-measured value from the serving BS and a total of seven RSS-measured values from serving and neighbouring BS antennas,

(ii) Hybrid 1 method: measured values of GSM method and, in addition, one PR-measured value from one satellite,

(iii) Hybrid 2 method: measured values of GSM method and, in addition, two PR-measured values from two different satellites.

Here, it is worth noting that the case when more than two PR-measured values are available has been investigated in [12]. For simplicity, the serving BS is assumed to be the BS located at $[750\,\mathrm{m},1000\,\mathrm{m}]^\top$. Here, it is worth noting that the serving BS has been placed very close to the MT trajectory in order to better illustrate how the nonlinearity, inherent in the TA- and RSS-measured values, influences the performance of the different filters. The PR-, TA-, and RSS-measured values are updated every $T_{\mathrm{s}}=0.48\,\mathrm{s}$, which corresponds to the reporting period of measured values in GSM networks. The performance of the proposed algorithms for the hybrid localization method is evaluated in terms of the root mean square error (RMSE) determined from $N_{\mathrm{MC}}=500$ Monte Carlo trials [16]. For each Monte Carlo trial, the MT trajectory is generated using (5) with process noise parameters as given in Table 3 and initial state vector $\mathbf{x}(0)=[-200\,\mathrm{m},8.84\,\mathrm{m/s},-200\,\mathrm{m},8.84\,\mathrm{m/s},0\,\mathrm{m},0\,\mathrm{m}]^\top$. For the simulations, the initial error covariance matrix of the three filters is set to $\mathbf{P}(0\mid 0)=\mathrm{diag}((200\,\mathrm{m})^2,(10\,\mathrm{m/s})^2,(200\,\mathrm{m})^2,(10\,\mathrm{m/s})^2,(300\,\mathrm{km})^2/3,(10\,\mathrm{m})^2/3)$, and the initial state vector $\hat{\mathbf{x}}(0\mid 0)$ is obtained from random initialization [20]. The covariance matrix $\mathbf{Q}$ for the three filters, which is a design parameter, is chosen to be $\mathbf{Q}=\mathrm{diag}(100\cdot\mathbf{Q}_{cv},10\cdot\mathbf{Q}_{\delta t})$, in order to account for possible MT maneuvers and receiver clock uncertainties. The measurement covariance matrix $\mathbf{R}$ for the simulations and the filters is assumed to be the same.

*5.2. Scenario II.* The second simulation scenario (Scenario II) investigates the tracking performance of the three different filters for a more general and realistic scenario. It is assumed that a car is equipped with an MT that is capable of providing PR-measured values from GPS and TA, RSS from GSM. Here, it is worth noting that the results for taking into account the GPS reference time uncertainty measurements are very similar to those of Scenario I and, thus, are not further elaborated. The car moves clockwise on a trapezoidal route, divided into 4 sections, in an urban scenario of size 5 km × 5 km as it is shown in Figure 2. In each section, the car moves with a different velocity in order to reflect a more realistic car movement as depicted in Figure 3. The GSM network is composed of $N_{\mathrm{BS}}=12$ BSs, where each BS is equipped with three directional antennas. The BS and satellite locations as well as the BS antenna parameters are assumed a priori known. The combination of measurements investigated and the parameters used in the simulations is the same as in Scenario I. The serving BS is assumed to be the

**Initialization**

$\hat{\mathbf{x}}(0 \mid 0) = \mathbb{E}\{\mathbf{x}(0)\}$

$\mathbf{P}(0 \mid 0) = \mathbb{E}\{(\mathbf{x}(0) - \hat{\mathbf{x}}(0 \mid 0))(\mathbf{x}(0) - \hat{\mathbf{x}}(0 \mid 0))^\top\}$

**Time Update**

Estimate the predicted state vector and error covariance matrix

$\hat{\mathbf{x}}(k \mid k-1) = \mathbf{\Phi}\, \hat{\mathbf{x}}(k-1 \mid k-1)$

$\mathbf{P}(k \mid k-1) = \mathbf{\Phi}\, \mathbf{P}(k-1 \mid k-1)\, \mathbf{\Phi}^\top + \mathbf{\Gamma}\, \mathbf{Q}\, \mathbf{\Gamma}^\top$

**Measurement Update**

Evaluate the sigma points ($i = 1, \ldots, n_x$)

$\mathcal{X}_0(k \mid k-1) = \hat{\mathbf{x}}(k \mid k-1),$

$\mathcal{X}_i(k \mid k-1) = \hat{\mathbf{x}}(k \mid k-1) + (\sqrt{(n_x + \lambda)\mathbf{P}(k \mid k-1)})_i,$

$\mathcal{X}_{n_x+i}(k \mid k-1) = \hat{\mathbf{x}}(k \mid k-1) - (\sqrt{(n_x + \lambda)\mathbf{P}(k \mid k-1)})_i.$

Evaluate the weights ($i = 1, \ldots, 2n_x$)

$$W_0^{(\mathrm{m})} = \frac{\lambda}{n_x + \lambda}, \quad W_0^{(\mathrm{c})} = \frac{\lambda}{n_x + \lambda} + (1 - \alpha^2 + \beta),$$

$$W_i^{(\mathrm{m})} = W_i^{(\mathrm{c})} = \frac{1}{2(n_x + \lambda)}.$$

Evaluate the propagated sigma points ($i = 0, \ldots, 2n_x$)

$\mathcal{Y}_i(k \mid k-1) = \mathbf{h}(\mathcal{X}_i(k \mid k-1)).$

Estimate the predicted measurement

$\hat{\mathbf{y}}(k \mid k-1) = \sum_{i=0}^{2n_x} W_i^{(\mathrm{m})}\, \mathcal{Y}_i(k \mid k-1).$

Estimate the innovation covariance and cross-covariance matrix ($i = 0, \ldots, 2n_x$)

$\widetilde{\mathcal{X}}_i(k \mid k-1) = \mathcal{X}_i(k \mid k-1) - \hat{\mathbf{x}}(k \mid k-1),$

$\widetilde{\mathcal{Y}}_i(k \mid k-1) = \mathcal{Y}_i(k \mid k-1) - \hat{\mathbf{y}}(k \mid k-1),$

$\mathbf{P}_{\mathbf{yy}}(k \mid k-1) = \sum_{i=0}^{2n_x} W_i^{(\mathrm{c})}\, \widetilde{\mathcal{Y}}_i(k \mid k-1)\, \widetilde{\mathcal{Y}}_i^\top(k \mid k-1) + \mathbf{R},$

$\mathbf{P}_{\mathbf{xy}}(k \mid k-1) = \sum_{i=0}^{2n_x} W_i^{(\mathrm{c})}\, \widetilde{\mathcal{X}}_i(k \mid k-1)\, \widetilde{\mathcal{Y}}_i^\top(k \mid k-1).$

Estimate the Kalman gain, updated state vector and error covariance matrix

$\mathbf{K}(k) = \mathbf{P}_{\mathbf{xy}}(k \mid k-1)\, \mathbf{P}_{\mathbf{yy}}^{-1}(k \mid k-1),$

$\hat{\mathbf{x}}(k \mid k) = \hat{\mathbf{x}}(k \mid k-1) + \mathbf{K}(k)[\mathbf{y}(k) - \hat{\mathbf{y}}(k \mid k-1) - \boldsymbol{\mu}],$

$\mathbf{P}(k \mid k) = \mathbf{P}(k \mid k-1) - \mathbf{K}(k)\mathbf{P}_{\mathbf{yy}}(k \mid k-1)\mathbf{K}^\top(k),$

where $n_x$ is the dimension of state vector, $\lambda = \alpha^2(n_x + \kappa) - n_x$ is a scaling parameter, $\alpha$ determines the spread of the sigma points, $\kappa$ is a secondary scaling parameter and $\beta$ is a weight parameter. $(\mathbf{A})_i$ denotes the $i$th column of the matrix $\mathbf{A}$

Algorithm 2: Rao-Blackwellized Unscented Kalman Filter.

Table 2: Computational complexity of the EKF, RBUKF, and MCKF. The dimension of the state vector is given by $n_x$ and the dimension of the measurement vector is given by $n_y$. $\mathcal{X}(k \mid k-1)$ denotes the matrix composed of sigma/cubature point vectors.

| Quantity | Complexity | | |
|---|---|---|---|
| | EKF | RBUKF | MCKF |
| $\hat{\mathbf{x}}(k \mid k-1)$ | $2n_x^2 - n_x$ | $2n_x^2 - n_x$ | $2n_x^2 - n_x$ |
| $\mathbf{P}(k \mid k-1)$ | $8n_x^3 - 15n_x^2 + 10n_x$ | $8n_x^3 - 15n_x^2 + 10n_x$ | $8n_x^3 - 15n_x^2 + 10n_x$ |
| $\boldsymbol{\mathcal{X}}(k \mid k-1)$ | — | $13n_x^3/3 + 2n_x^2$ | $13n_x^3/3 + 2n_x^2$ |
| $\hat{\mathbf{y}}(k \mid k-1)$ | — | $2n_xn_y + 2n_y$ | $2n_xn_y$ |
| $\mathbf{P}_{\mathbf{yy}}(k \mid k-1)$ | $2n_y^2n_x + 2n_x^2n_y - n_xn_y$ | $4n_y^2n_x + 2n_xn_y + 4n_y^2 + n_y$ | $4n_y^2n_x + 3n_y^2$ |
| $\mathbf{P}_{\mathbf{xy}}(k \mid k-1)$ | $2n_x^2n_y - n_xn_y$ | $4n_x^2n_y + 3n_xn_y + 2n_x^2 + n_x$ | $4n_x^2n_y + 2n_xn_y$ |
| $\mathbf{K}(k)$ | $n_y^3 + 2n_y^2n_x - n_xn_y$ | $n_y^3 + 2n_y^2n_x - n_xn_y$ | $n_y^3 + 2n_y^2n_x - n_xn_y$ |
| $\hat{\mathbf{x}}(k \mid k)$ | $2n_xn_y + 2n_y$ | $2n_xn_y + 2n_y$ | $2n_xn_y + 2n_y$ |
| $\mathbf{P}(k \mid k)$ | $2n_y^2n_x + 2n_x^2n_y - n_xn_y$ | $2n_y^2n_x + 2n_x^2n_y - n_xn_y$ | $2n_y^2n_x + 2n_x^2n_y - n_xn_y$ |

BS antenna providing the largest RSS-measured value. The performance of the proposed algorithms is evaluated from $N_{\mathrm{MC}} = 500$ Monte Carlo trials. For each Monte Carlo trial, the MT trajectory is generated based on Figure 3 and initial state vector $\mathbf{x}(0) = [500\,\mathrm{m}, 8\,\mathrm{m/s}, 1500\,\mathrm{m}, 0\,\mathrm{m/s}, 0\,\mathrm{m}, 0\,\mathrm{m}]^\top$. For the simulations, the initial state vector $\hat{\mathbf{x}}(0 \mid 0)$ is obtained from random initialization and the initial error covariance matrix of the three filters is set to $\mathbf{P}(0 \mid 0) = \mathrm{diag}((200\,\mathrm{m})^2, (10\,\mathrm{m/s})^2, (200\,\mathrm{m})^2, (10\,\mathrm{m/s})^2, (300\,\mathrm{km})^2/3, (10\,\mathrm{m})^2/3)$. The covariance matrix $\mathbf{Q}$ and the measurement covariance matrix $\mathbf{R}$ for the three filters are chosen as in Scenario I.

**Initialization**

$\hat{\mathbf{x}}(0 \mid 0) = \mathbb{E}\{\mathbf{x}(0)\}$

$\mathbf{P}(0 \mid 0) = \mathbb{E}\{(\mathbf{x}(0) - \hat{\mathbf{x}}(0 \mid 0))(\mathbf{x}(0) - \hat{\mathbf{x}}(0 \mid 0))^{\top}\}$

**Time Update**

Estimate the predicted state vector and error covariance matrix

$\hat{\mathbf{x}}(k \mid k-1) = \boldsymbol{\Phi}\, \hat{\mathbf{x}}(k-1 \mid k-1)$,

$\mathbf{P}(k \mid k-1) = \boldsymbol{\Phi}\, \mathbf{P}(k-1 \mid k-1)\boldsymbol{\Phi}^{\top} + \boldsymbol{\Gamma}\, \mathbf{Q}\, \boldsymbol{\Gamma}^{\top}$.

**Measurement Update**

Evaluate the cubature points ($i = 1, \ldots, 2n_x$)

$\mathbf{P}(k \mid k-1) = \mathbf{S}(k \mid k-1)\mathbf{S}^{\top}(k \mid k-1)$,

$\boldsymbol{\Xi} = \sqrt{n_x} \cdot [\, \mathbf{I}_{n_x}, -\mathbf{I}_{n_x}]$,

$\mathcal{X}_i(k \mid k-1) = \hat{\mathbf{x}}(k \mid k-1) + \mathbf{S}(k \mid k-1)\, \boldsymbol{\xi}_i$.

Evaluate the weights ($i = 1, \ldots, 2n_x$)

$W_i^{(\mathrm{m})} = W_i^{(\mathrm{c})} = 1/(2n_x)$.

Evaluate the propagated cubature points ($i = 1, \ldots, 2n_x$)

$\mathcal{Y}_i(k \mid k-1) = \mathbf{h}(\mathcal{X}_i(k \mid k-1))$.

Estimate the predicted measurement

$\hat{\mathbf{y}}(k \mid k-1) \sum_{i=1}^{2n_x} W_i^{(\mathrm{m})}\, \mathcal{Y}_i(k \mid k-1)$

Estimate the innovation covariance and cross-covariance matrix

$\mathbf{P}_{\mathbf{yy}}(k \mid k-1) = \sum_{i=1}^{2n_x} W_i^{(\mathrm{c})}\, \mathcal{Y}_i(k \mid k-1)\mathcal{Y}_i^{\top}(k \mid k-1) - \hat{\mathbf{y}}(k \mid k-1)\hat{\mathbf{y}}^{\top}(k \mid k-1) + \mathbf{R}$,

$\mathbf{P}_{\mathbf{xy}}(k \mid k-1) = \sum_{i=1}^{2n_x} W_i^{(\mathrm{c})}\, \mathcal{X}_i(k \mid k-1)\, \mathcal{Y}_i^{\top}(k \mid k-1) - \hat{\mathbf{x}}(k \mid k-1)\hat{\mathbf{y}}^{\top}(k \mid k-1)$

Estimate the Kalman gain, updated state vector and error covariance matrix

$\mathbf{K}(k) = \mathbf{P}_{\mathbf{xy}}(k \mid k-1)\, \mathbf{P}_{\mathbf{yy}}^{-1}(k \mid k-1)$,

$\hat{\mathbf{x}}(k \mid k) = \hat{\mathbf{x}}(k \mid k-1) + \mathbf{K}(k)[\mathbf{y}(k) - \hat{\mathbf{y}}(k \mid k-1) - \boldsymbol{\mu}]$,

$\mathbf{P}(k \mid k) = \mathbf{P}(k \mid k-1) - \mathbf{K}(k)\, \mathbf{P}_{\mathbf{yy}}(k \mid k-1)\, \mathbf{K}^{\top}(k)$.

where $\boldsymbol{\xi}_i$ denotes the $i$th column vector of the matrix $\boldsymbol{\Xi}$.

Algorithm 3: Modified Cubature Kalman Filter.

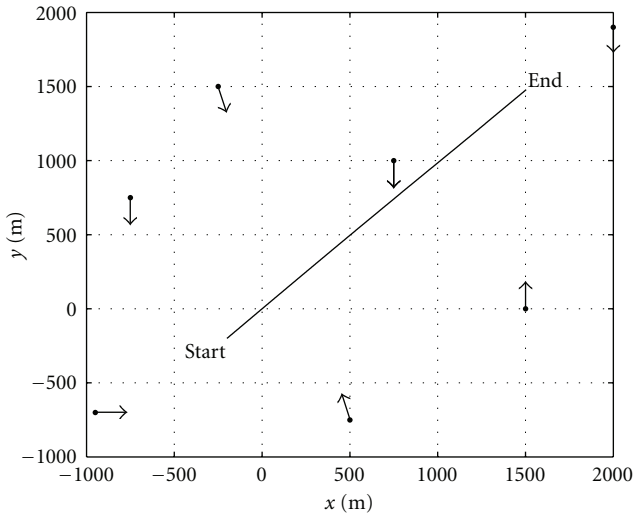


Figure 1: Simulation Scenario I with $N_{\mathrm{BS}} = 7$ BSs (•). The arrows (→) indicate the BS antenna boresight direction.

Table 3: Simulation parameters.

| Parameter | Value | Parameter | Value |
|---|---|---|---|
| $A$ in dB | 132.8 | $\sigma_x$ in m/s$^2$ | $10^{-2}$ |
| $B$ in dB | 3.8 | $\sigma_y$ in m/s$^2$ | $10^{-2}$ |
| $P_{\mathrm{t}}$ in dBm | 50 | $c_0$ in m/s | $3 \cdot 10^8$ |
| $A_m$ in dB | 20 | $T_{\mathrm{s}}$ in s | 0.48 |
| $\varphi_{3\mathrm{dB}}$ in ° | 60 | $h_0$ | $9.4 \cdot 10^{-20}$ |
| $\sigma_{\mathrm{RSS}}$ in dB | 8 | $h_{-1}$ | $1.8 \cdot 10^{-19}$ |
| $\sigma_{\mathrm{TA}}$ in m | 300 | $h_{-2}$ | $3.8 \cdot 10^{-21}$ |
| $\mu_{\mathrm{TA}}$ in m | 0 | $\alpha$ | $10^{-3}$ |
| $\sigma_{\mathrm{PR}}$ in m | 15 | $\beta$ | 2 |
| $\mu_{\mathrm{PR}}$ in m | 0 | $\kappa$ | 0 |

*5.3. Simulation Results for Scenario I without GPS Reference Time Uncertainty Measurements.* In this section, the simulation results for the case when there are no GPS reference time uncertainty measurements available from the GSM network are presented. In Figure 4, the simulation results for the MT location RMSE in dependence of the time index $k$ for the GSM method are shown. From Figure 4, it can be seen that during the first 200 time steps, the performance of the three filters is approximately the same. However, when the MT is located close to the serving BS, there is a "high degree" of nonlinearity in the TA- and RSS-measured values. In this region, it can be clearly seen that the MCKF outperforms the EKF and RBUKF in terms of RMSE.

In Figures 5 and 6, the MT location RMSE for the Hybrid 1 and Hybrid 2 method for the different filters is shown. Compared to the GSM method, the MT location RMSE can only be marginally improved by the Hybrid 1 method, which additionally takes into account one PR-measured value from GPS. This can be explained by the fact that it is not possible to accurately estimate the unknown MT clock bias with the

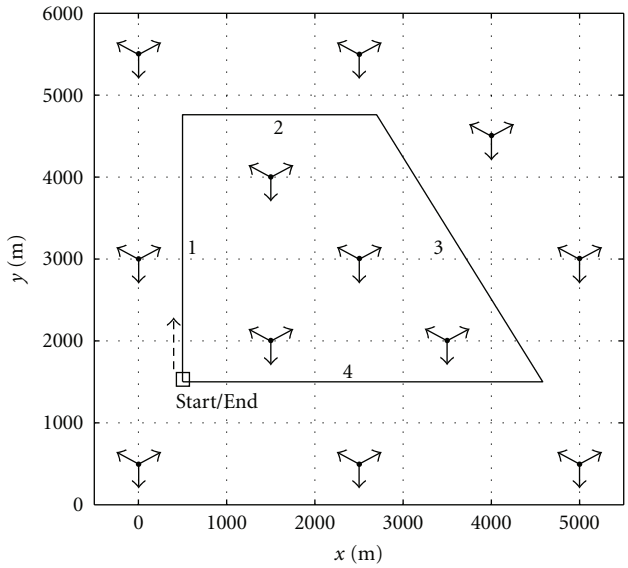


Figure 2: Simulation Scenario II with $N_{BS} = 12$ BSs (•). Each BS is equipped with three directional antennas. The arrows ( → ) indicate the BS antenna boresight direction. The MT starts at $\mathbf{x}_{MT}(0) = [500, 1500]^{\top}$ and moves clockwise on the trapezoidal route.

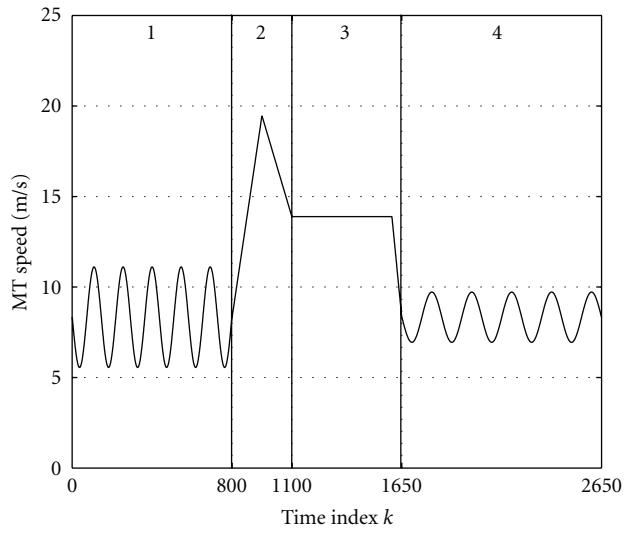


Figure 3: MT speed versus time index $k$ for Scenario II.

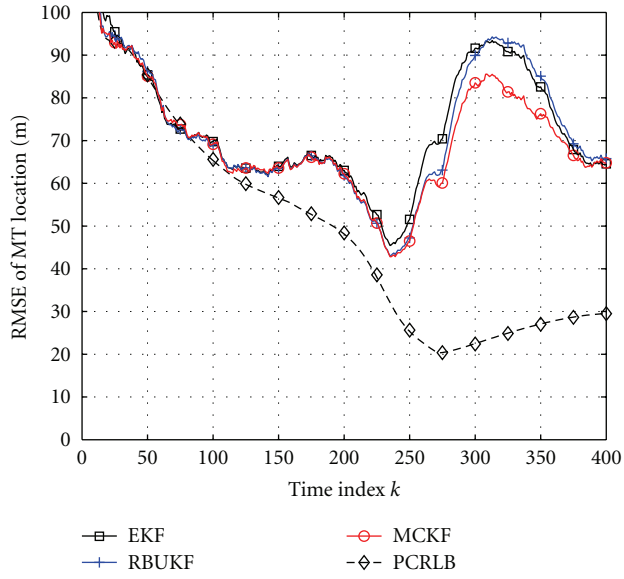


Figure 4: Scenario I: MT location RMSE of the GSM method for the different filters and the corresponding PCRLB.

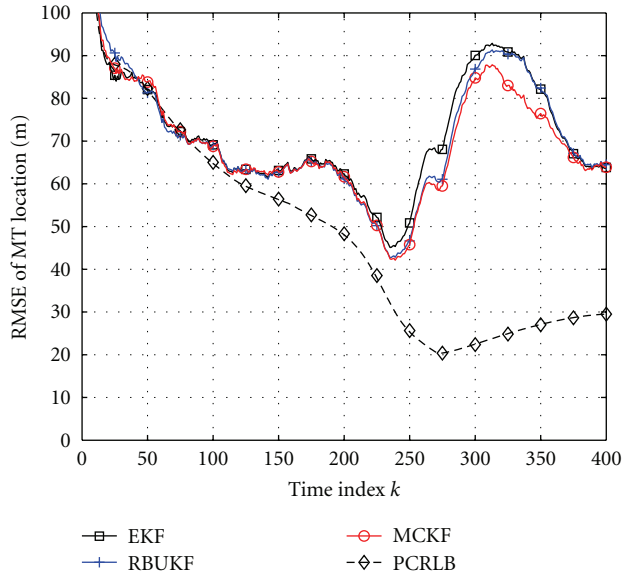


Figure 5: Scenario I: MT location RMSE of the Hybrid 1 method for the different filters and the corresponding PCRLB.

available TA- and RSS-measured values, which is depicted in Figure 7. Furthermore, when looking at the PCRLBs of the GSM and Hybrid 1 method for the MT location, one can conclude that from a theoretical point of view no RMSE improvements are possible, since the PCRLBs practically coincide with each other.

For the Hybrid 2 method (cf. Figure 6) the improvements are significant. Due to the fact that two PR-measured values are available, the filters can much more accurately estimate the MT clock bias (cf. Figure 7) which has a direct impact on the achievable MT location RMSE. However, from Figure 6 it can be also seen that the performance of the three filters is approximately the same. This can be explained by the fact that the two PR-measured values have a larger influence on the MT location estimate of the filters, because these measured values are more accurate than the TA- and RSS-measured values. Since the distances between the MT and the satellites are very large, and the nonlinearity of the PR-measured values is thus "mild", more weight is put on the PR-measured values when the MT location estimates are evaluated in the filters. As a result, the influence of the nonlinearities of the TA- and RSS-measured values is

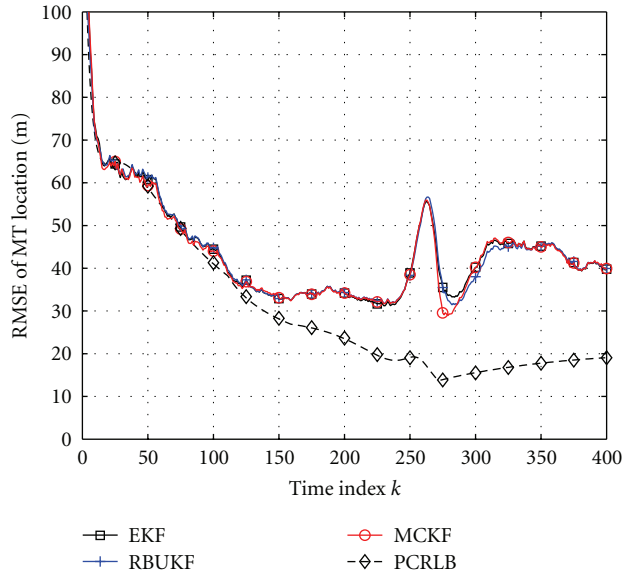


Figure 6: Scenario I: MT location RMSE of the Hybrid 2 method for the different filters and the corresponding PCRLB.

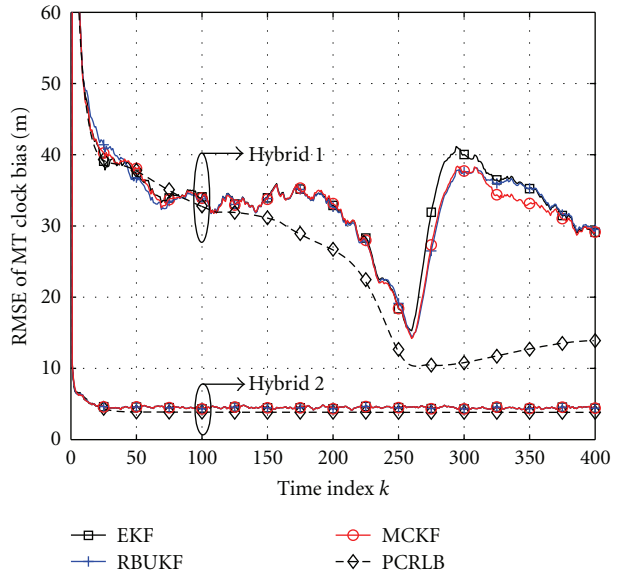


Figure 7: Scenario I: MT clock bias RMSE of the Hybrid 1 and Hybrid 2 method for the different filters and the corresponding PCRLB.

weakened and, thus, for the Hybrid 2 method, the three filters have approximately the same performance. In Table 4, the performance of the EKF is compared to the performance of the RBUKF and MCKF in terms of the RMSE averaged over the whole time period. From Table 4 it can be concluded that for this specific scenario, the MCKF slightly outperforms the RBUKF and EKF in terms of average RMSE.

*5.4. Simulation Results for Scenario I with GPS Reference Time Uncertainty Measurements.* In this section, simulation results for the case when there are GPS reference time uncertainty measurements available from the GSM network are presented. Here, the important question is investigated, what accuracy of the GPS reference time measurements is needed, in order to improve the performance of the MT location RMSE.

In Figure 8, the average MT location RMSE in dependence of the GPS reference time uncertainty standard deviation $\sigma_{\text{RTU}}$ for the different filters are shown. From Figure 8, it can be seen that for the Hybrid 2 method no significant improvements are possible and the performance of the different filters is approximately the same. That is, when two PR-measured values are additionally available, then, the additional evaluation of the GPS reference time information from the GSM network does not help to improve the MT location RMSE of the Hybrid 2 method. However, the improvements for the Hybrid 1 method can be significant, when GPS reference time information is taken into account. For the investigated scenario, the major performance improvements for the Hybrid 1 method can be obtained for values of $\sigma_{\text{RTU}}$ that lie in the range between $10^{-7}$ and $10^{-6}$ seconds. For GPS reference time uncertainty values outside this region, no significant improvements in terms of average MT location RMSE can be achieved. However, for the case when $\sigma_{\text{RTU}} < 10^{-7}$, then, the performance of

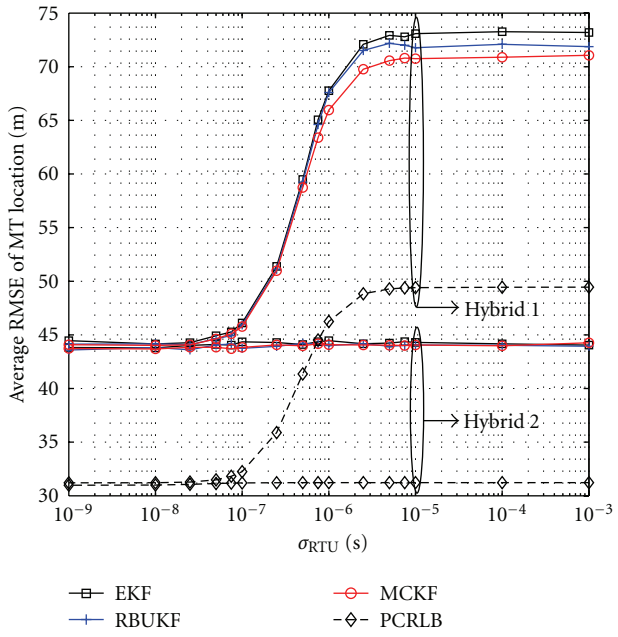


Figure 8: Scenario I: Average MT location RMSE of the Hybrid 1 and Hybrid 2 method for the different filters and the corresponding average PCRLB.

the Hybrid 1 method reaches quickly a lower bound which is approximately equal to the performance of the Hybrid 2 method.

When the different filters are compared with each other, one can clearly see that for large values of $\sigma_{\text{RTU}}$, the MCKF outperforms the RBUKF and EKF. However, when the GPS reference time uncertainty decreases, then, the performance

Table 4: Average RMSE performance of EKF, RBUKF, and MCKF for Scenario I.

| Algorithm | Method | Location in m | Velocity in m/s | Bias in m | Drift in m/s |
|---|---|---|---|---|---|
| EKF [12] | GSM | 73.9 | 3.6 | — | — |
| | Hybrid 1 | 73.0 | 3.4 | 34.2 | 1.9 |
| | Hybrid 2 | 44.3 | 2.7 | 4.6 | 1.2 |
| RBUKF [13] | GSM | 73.8 | 3.6 | — | — |
| | Hybrid 1 | 72.1 | 3.5 | 33.7 | 1.9 |
| | Hybrid 2 | 44.2 | 2.7 | 4.6 | 1.2 |
| MCKF | GSM | 71.5 | 3.6 | — | — |
| | Hybrid 1 | 70.8 | 3.4 | 33.5 | 1.9 |
| | Hybrid 2 | 44.0 | 2.7 | 4.6 | 1.2 |

of the three filters is approximately the same. In Figures 9 and 10, the average RMSEs of the MT clock bias and drift in dependence of the GPS reference time uncertainty standard deviation $\sigma_{\text{RTU}}$ for the different filters are shown. For the Hybrid 1 method, the average bias and drift RMSEs can be gradually decreased for values of $\sigma_{\text{RTU}}$ smaller than $10^{-6}$. For the Hybrid 2 method, this is true for values of $\sigma_{\text{RTU}}$ smaller than $10^{-7}$. From the achieved results one can conclude that the MT location RMSE can be decreased until the MT clock bias RMSE falls below a certain threshold. Beyond this point, the MT location RMSE reaches a lower bound, even though the RMSEs of the MT clock bias and drift states can be further decreased.

In Table 5, the computational complexity in terms of FLOPs for the different filters and methods is presented. From Table 5, it can be seen that for all investigated methods, the EKF has the lowest computational complexity, followed by the MCKF and RBUKF. The complexity reduction of the EKF compared to the RBUKF is about 30%. Using an MCKF rather than an RBUKF results in a complexity reduction of only 4%.

*5.5. Simulation Results for Scenario II.* In this section, the simulation results for Scenario II are presented. In Figures 11, 12, and 13, the MT location RMSE of the GSM, Hybrid 1, and Hybrid 2 method for the three different filters is shown. From these three figures it can be clearly seen that the performance of the three filters is approximately the same. Again, the GSM method provides the worst results in terms of MT location RMSE. The Hybrid 1 method only marginally improves the MT location RMSE at the cost of an increased complexity (cf. Table 5) while the best performance can be achieved by the Hybrid 2 method.

The equal performance of the three filters for the different methods can be explained by the fact that the distances between the BSs and the MT are large and, thus, the impact of the nonlinearities, inherent in the TA and RSS measured values, is small. Compared to the simulation results of Scenario I, there are now several distinct peaks in the MT location RMSE. These peaks that are more pronounced for the GSM and Hybrid 1 method (cf. Figures 11 and 12) result from the geometric constellation of the

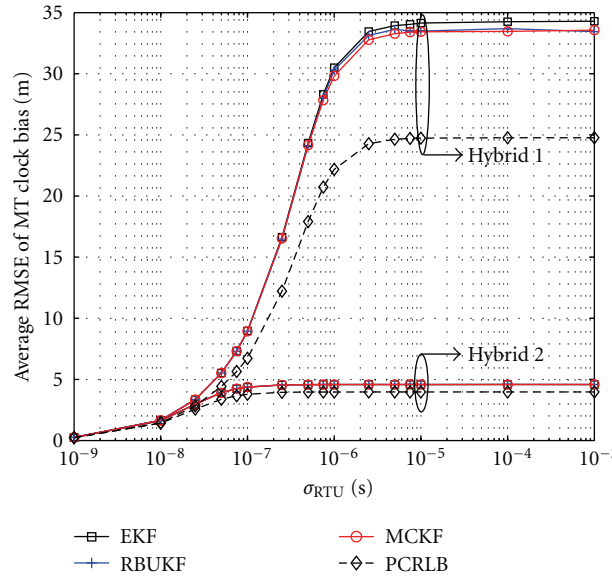


Figure 9: Scenario I: Average MT clock bias RMSE of the Hybrid 1 and Hybrid 2 method for the different filters and the corresponding average PCRLB.

Table 5: Computational complexity in FLOPs of EKF, RBUKF, and MCKF for one time step. Numbers in parentheses denote the FLOP complexity taking into account GPS reference time information.

| Algorithm | Method | Complexity in FLOPs |
|---|---|---|
| EKF | GSM | 3108 |
| | Hybrid 1 | 6813(7974) |
| | Hybrid 2 | 7974(9267) |
| RBUKF | GSM | 4534 |
| | Hybrid 1 | 9708(11230) |
| | Hybrid 2 | 11230(12916) |
| MCKF | GSM | 4314 |
| | Hybrid 1 | 9360(10842) |
| | Hybrid 2 | 10842(12486) |

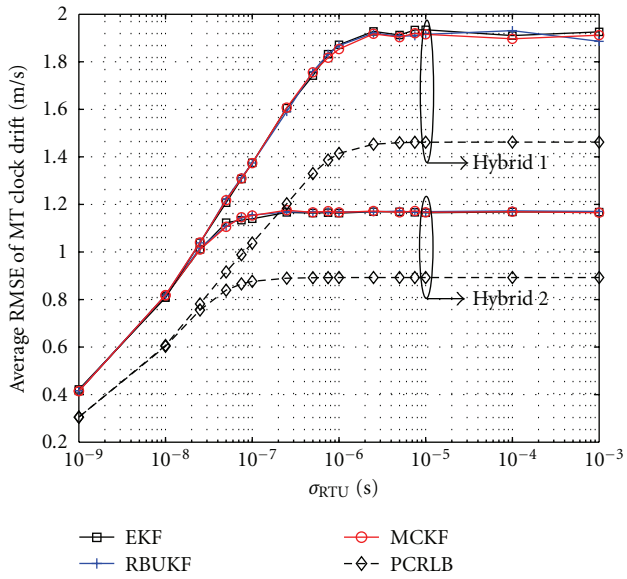


Figure 10: Scenario I: Average MT clock drift RMSE of the Hybrid 1 and Hybrid 2 method for the different filters and the corresponding average PCRLB.

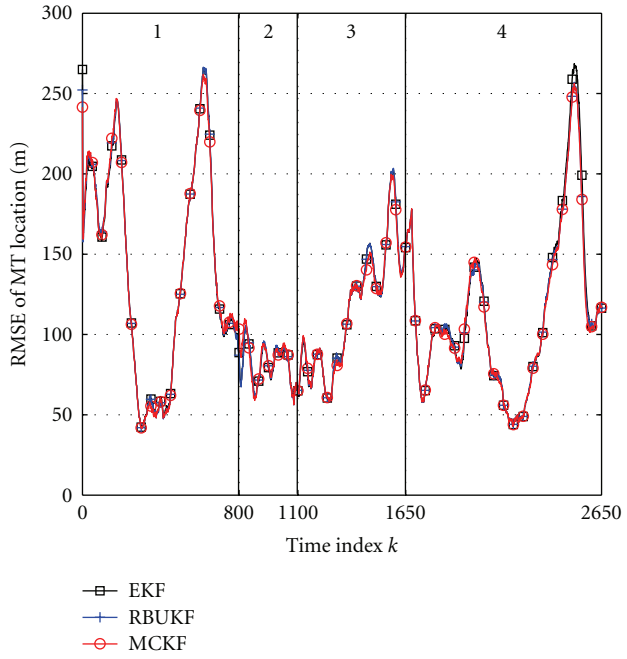


Figure 11: Scenario II: MT location RMSE of the GSM method for the different filters.

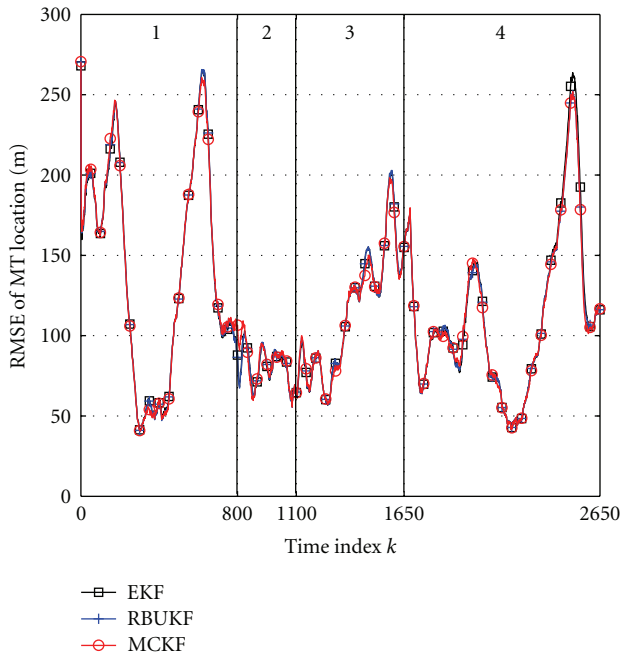


Figure 12: Scenario II: MT location RMSE of the Hybrid 1 method for the different filters.

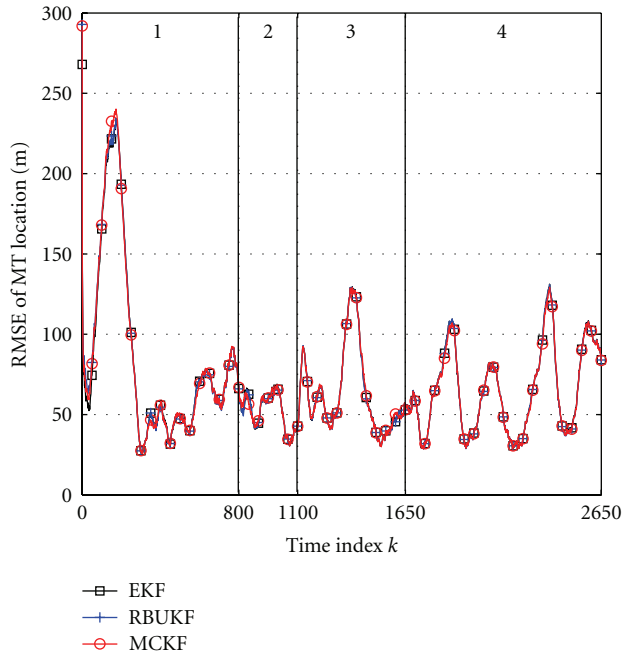


Figure 13: Scenario II: MT location RMSE of the Hybrid 2 method for the different filters.

BSs and satellites relative to the MT. However, for the Hybrid 2 method (cf. Figure 13) the magnitude of the peaks becomes smaller, because additional information from two PR-measured values is processed and more weight is put on the geometric constellation of the satellites relative to the MT. The average RMSE performance of the EKF, RBUKF, and MCKF is summarized in Table 6.

## 6. Experimental Results

In this section, the performance of the proposed hybrid localization method is verified for the different filters with experimental data available from a field trial. The field trial was conducted in an operating GSM network in the city center of a German city, with a test area of approximately

3 km × 3 km. During the field trial, a car equipped with a standard cellular phone is collected every $T_s = 480$ ms RXLEV- (quantized RSS) and TA-measured values from GSM. Here, it is worth noting that in GSM the RXLEV-measured values are available from the serving BS and between one and six strongest RXLEVs from the neighboring BS whereas the TA-measured value is only available from the serving BS. In addition, it should be noted that GPS reference time uncertainty measurements have not been collected during the field trial, so that this issue will not be further elaborated in this section. The GSM network is composed of $N_{BS} = 13$ fixed BSs with known locations. The BSs are equipped with either directional antennas or a single omnidirectional antenna. The antenna boresight directions, equivalent isotropic radiated powers, and half-power beamwidths are a priori known, and the unknown antenna gain patterns are approximated with (13). The remaining parameters of the TA and RSS measurement models (cf. (10) and (14)) are estimated from the available field trial data. Here, it is worth noting that in order to not overfit the different filters for this single trajectory the standard deviations of the TA- and RSS-measured values were chosen to be $\sigma_{RSS}^{(n)} \geq 3$ dB and $\sigma_{TA}^{(n)} \geq 1\,\mu$s. For the path loss model (cf. (12)) the parameters are in the range of $110\,\text{dB} \leq A^{(n)} \leq 150\,\text{dB}$ and $2\,\text{dB} \leq B^{(n)} \leq 5\,\text{dB}$.

For the GPS network, PR-measured values collected from a field trial are not available, so that synthetic PR measurement data have been generated with the parameters given in Table 3. The constellation of the GPS satellites during the field trial is reconstructed by taking true satellite locations from the real satellite constellation, where the satellite locations are assumed a priori known. For simplicity, it is assumed that PR-measured values are available every $T_s = 480$ ms. The satellite's visibility status during the field trial cannot be reproduced subsequently, so that it is assumed that either $N_{SAT} = 1$ or $N_{SAT} = 2$ satellites are visible to the MT. However, this assumption is only made in order to demonstrate the improvements that can be achieved by the proposed hybrid localization algorithm. In reality, the number of visible satellites changes with time, so that there will be situations where GPS (i.e., $N_{SAT} \geq 3$) is available.

In Figure 14, the true MT trajectory together with the trajectories estimated by the EKF, RBUKF, and MCKF for the GSM method of the field trial is shown. Here, the true MT location was obtained from detailed maps and from GPS, where GPS was available. From Figure 14 it can be seen that all three filters can moderately track the MT. In Figure 15, the corresponding MT location error in dependence of the time index $k$ is presented. Here, the MT location error denotes the Euclidean distance between the true and estimated MT location. From Figure 15 it can be seen that the RBUKF marginally outperforms the MCKF and EKF. This rather surprising result can be explained as follows. The MCKF has been derived in a setting where the measurement noise has to be Gaussian distributed [14]. The available field trial measurements, however, are not Gaussian distributed, so that this assumption is explicitly violated. The RBUKF has been derived in a more general setting where the involved densities have to be symmetric, but not necessarily Gaussian.

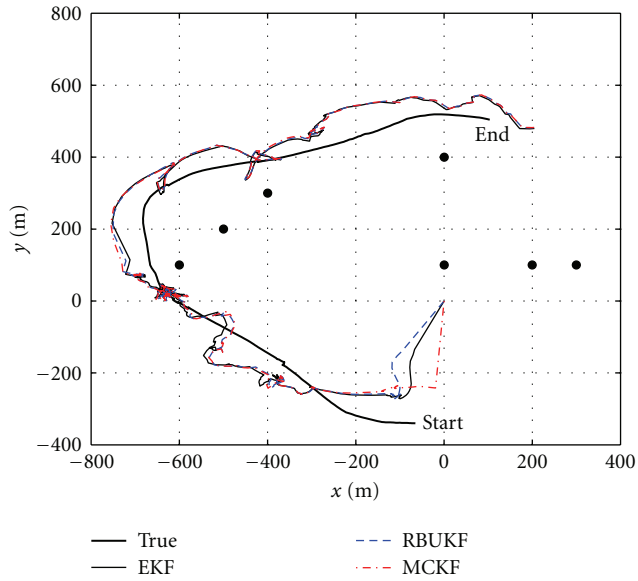


Figure 14: Field trial scenario with true MT trajectory, approximate BS locations (•), and estimated trajectories of the GSM method for the different filters.

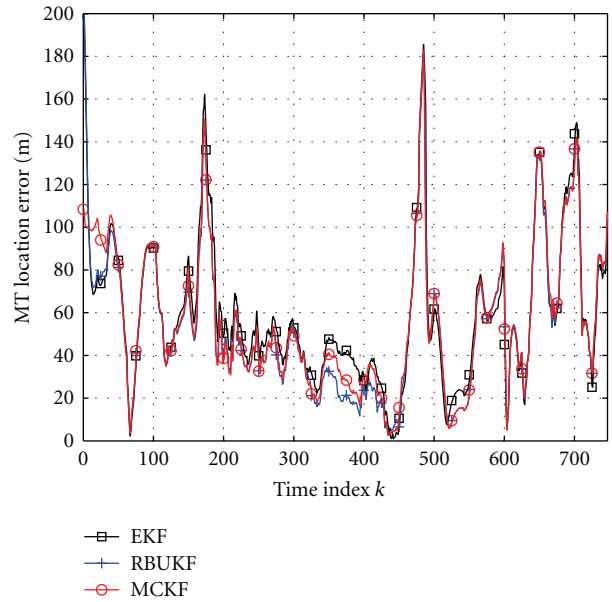


Figure 15: MT location error of the GSM method for the different filters.

As a result, the performance of the RBUKF is slightly better than the performance of the MCKF. The peak values in the MT location error can be explained by the geometric constellation of the BSs relative to the MT location and the change of the MT velocity during the field trial which results in a mismatch to the CV model that is assumed in the filter's process model.

In Figures 16 and 17, the estimated trajectories and the MT location error of the Hybrid 1 method for the different filters is presented. Again, all three filters can track

Table 6: Average RMSE performance of EKF, RBUKF, and MCKF for Scenario II.

| Algorithm | Method | Location in m | Velocity in m/s | Bias in m | Drift in m/s |
|---|---|---|---|---|---|
| EKF [12] | GSM | 119.1 | 4.1 | — | — |
| | Hybrid 1 | 118.4 | 3.9 | 57.1 | 2.0 |
| | Hybrid 2 | 69.9 | 2.8 | 4.5 | 1.1 |
| RBUKF [13] | GSM | 118.8 | 4.1 | — | — |
| | Hybrid 1 | 118.2 | 3.9 | 56.8 | 2.0 |
| | Hybrid 2 | 70.0 | 2.8 | 4.5 | 1.1 |
| MCKF | GSM | 118.5 | 4.1 | — | — |
| | Hybrid 1 | 118.1 | 3.9 | 56.7 | 2.0 |
| | Hybrid 2 | 70.0 | 2.8 | 4.5 | 1.1 |

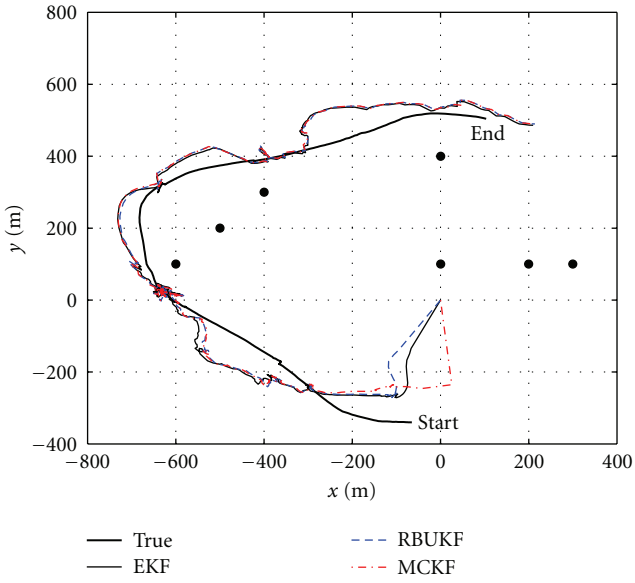


Figure 16: Field trial scenario with true MT trajectory, approximate BS locations (•), and estimated trajectories of the Hybrid 1 method for the different filters.

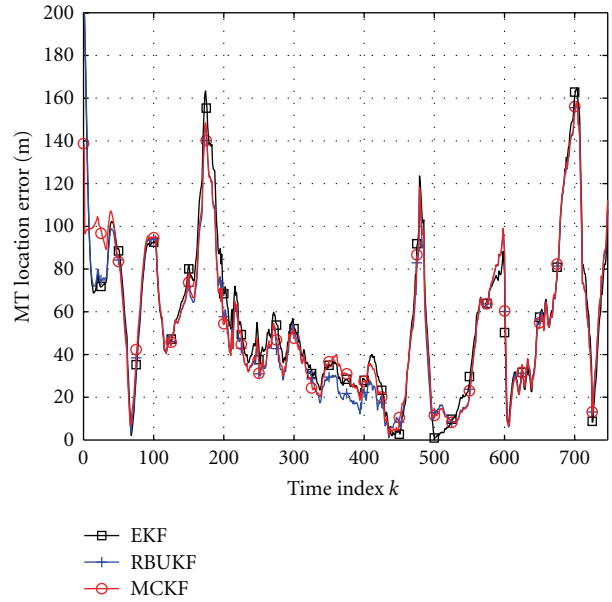


Figure 17: MT location error of the Hybrid 1 method for the different filters.

the MT and the performance of the MT location error is approximately the same. However, compared to the GSM method, the MT location error of the Hybrid 1 method can be slightly improved. In Figures 18 and 19, the filter's estimated trajectories and MT location error of the Hybrid 2 method are shown. It can be clearly seen that, compared to the GSM and Hybrid 1 method, the performance can be significantly improved using the Hybrid 2 method. For the Hybrid 2 method, the MCKF yields the best performance, followed by the RBUKF and EKF.

In Table 7, the average MT location error of the GSM, Hybrid 1, and Hybrid 2 method for the EKF, RBUKF, and MCKF is summarized. It can be seen that for all three filters the GSM method provides the worst performance. The MT location accuracy can be marginally improved with the Hybrid 1 method and significantly improved with the Hybrid 2 method.

Table 7: Average MT location error in meters of EKF, RBUKF, and MCKF for field trial scenario.

| Algorithm | Method | | |
|---|---|---|---|
| | GSM | Hybrid 1 | Hybrid 2 |
| EKF [12] | 59.2 | 55.5 | 43.8 |
| RBUKF | 55.1 | 52.3 | 42.8 |
| MCKF | 56.5 | 53.8 | 41.7 |

## 7. Conclusion

In this paper, the performance and computational complexity of three different MT tracking algorithms, namely, the EKF, RBUKF, and MCKF are investigated that combine TA- and RSS-measured values from GSM and one or two PR measurements from GPS. It has been shown by simulations

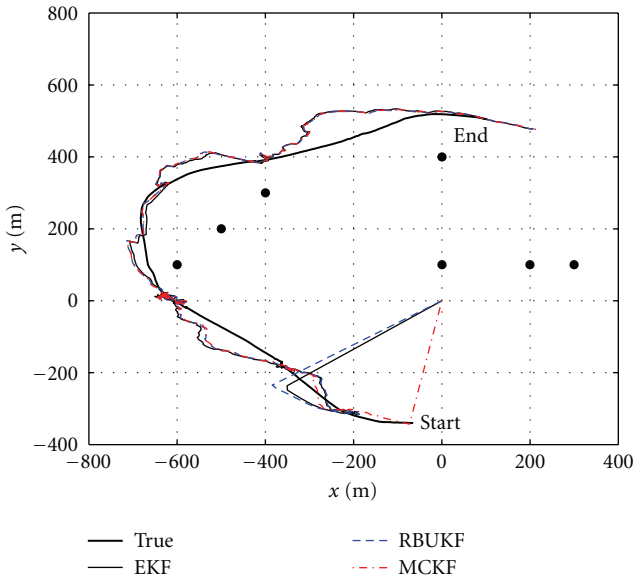


FIGURE 18: Field trial scenario with true MT trajectory, approximate BS locations (•), and estimated trajectories of the Hybrid 2 method for the different filters.

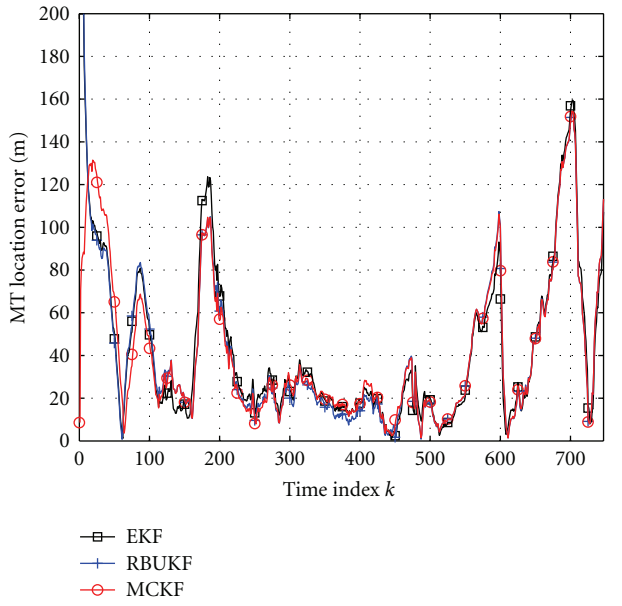


FIGURE 19: MT location error of the Hybrid 2 method for the different filters.

and experiments that, compared to existing GSM-based MT tracking solutions, the location accuracy can be significantly improved by using hybrid GPS/GSM-based MT tracking algorithms, where all three filters have approximately the same performance, and the EKF offers the best trade-off between performance and computational complexity. When GPS reference time is additionally available from the GSM network, then, the hybrid localization method using one PR measurement can be significantly improved. It has been shown by simulations that in this case, it is sufficient to have GPS reference time information available, whose uncertainty lies in the range between $10^{-6}$ to $10^{-7}$ seconds, in order to improve the hybrid localization method.

Although this paper is focused on a specific scenario with measured values from GPS and GSM, the general equations and methodology presented in this paper can be easily adapted to other network configurations and measured values from other systems, for example, universal mobile telecommunications system (UMTS) or wireless local area networks. By additionally considering these measured values in the hybrid localization solution, it is expected that the performance will be further improved.

## References

[1] A. Küpper, *Location-Based Services*, John Wiley & Sons, New York, NY, USA, 1st edition, 2005.

[2] "FCC 99-245: third report and order," Tech. Rep., Federal Communications Commission, Rickey Davis, Ala, USA, October 1999, http://www.fcc.gov/911/enhanced.

[3] F. Gustafsson and F. Gunnarsson, "Mobile positioning using wireless networks," *IEEE Signal Processing Magazine*, vol. 22, no. 4, pp. 41–53, 2005.

[4] G. Sun, J. Chen, W. Guo, and K. J. R. Liu, "Signal processing techniques in network-aided positioning: a survey of state-of-the-art positioning designs," *IEEE Signal Processing Magazine*, vol. 22, no. 4, pp. 12–23, 2005.

[5] P. Misra and P. Enge, *Global Positioning System: Signals, Measurements, and Performance*, Ganga-Jamuna Press, Lincoln, Mass, USA, 2nd edition, 2006.

[6] N. Bourdeau, M. Gibeaux, J. Riba, and F. Sansone, "Hybridised GPS and GSM positioning technology for high performance location based services," in *Proceedings of the IST Mobile & Wireless Communications Summit*, June 2002.

[7] S. Kyriazakos, D. Drakoulis, M. Theologou, and J.-A. Sanchez-P, "Localization of mobile terminals, based on a hybrid satellite-assisted and network-based techniques," in *Proceedings of the IEEE Wireless Communications and Networking Conference (WCNC '00)*, vol. 2, pp. 798–802, September 2000.

[8] S. Soliman, P. Agashe, I. Fernandez, A. Vayanos, P. Gaal, and M. Oljaca, "gpsOne$^{tm}$: a hybrid position location system," in *Proceedings of the 6th IEEE International Symposium on Spread Spectrum Techniques and Applications (ISSSTA '00)*, vol. 1, pp. 330–335, September 2000.

[9] G. Heinrichs, P. Mulassano, and F. Dovis, "A hybrid positioning algorithm for cellular radio networks by using a common RAKE receiver architecture," in *Proceedings of the 15th IEEE International Symposium on Personal, Indoor and Mobile Radio Communications (PIMRC '04)*, vol. 4, pp. 2347–2351, September 2004.

[10] C. Fritsche and A. Klein, "Cramér-Rao lower bounds for hybrid localization of mobile terminals," in *Proceedings of the 5th Workshop on Positioning, Navigation and Communication 2008 (WPNC '08)*, pp. 157–164, March 2008.

[11] C. Mensing, S. Sand, and A. Dammann, "GNSS positioning in critical scenarios: hybrid data fusion with communications signals," in *Proceedings of the IEEE International Conference on Communications Workshop (ICC '09)*, pp. 1–6, Dresden, Germany, March 2009.

[12] C. Fritsche, A. Klein, and D. Würtz, "Hybrid GPS/GSM localization of mobile terminals using the extended Kalman filter," in *Proceedings of the 6th Workshop on Positioning, Navigation and Communication (WPNC '09)*, pp. 189–194, March 2009.

[13] C. Fritsche and A. Klein, "On the performance of hybrid GPS/GSM mobile terminal tracking," in *Proceedings of the IEEE International Conference on Communicationss Workshop on (ICC '09)*, Dresden, Germany, June 2009.

[14] I. Arasaratnam and S. Haykin, "Cubature Kalman filters," *IEEE Transactions on Automatic Control*, vol. 54, no. 6, pp. 1254–1269, 2009.

[15] 3GPP TS 44.031, "Location services LCS; Mobile Station (MS)—Serving Mobile Location Centre (SMLC)—Radio Resource LCS Protocol (RRLP), Version 8.3.0," May 2009.

[16] B. Ristic, S. Arulampalam, and N. Gordon, *Beyond the Kalman Filter: Particle Filters for Tracking Applications*, Artech-House, Boston, Mass, USA, 2004.

[17] A. H. Jazwinski, *Stochastic Processes and Filtering Theory*, vol. 64 of *Mathematics in Science and Engineering*, Academic Press, New York, NY, USA, 1970.

[18] R. E. Kalman, "A new approach to linear filtering and prediction problems," *Transactions of the American Society of Mechanical Engineering-Journal Basic Engineering*, vol. 82, no. 1, pp. 35–45, 1960.

[19] X. Mao, M. Wada, and H. Hashimoto, "Nonlinear GPS models for position estimate using low-cost GPS receiver," in *Proceedings of the IEEE Intelligent Transportation Systems*, vol. 1, pp. 637–642, October 2003.

[20] Y. Bar-Shalom, X. R. Li, and T. Kirubarajan, *Estimation with Applications to Tracking and Navigation*, Wiley-Interscience, New York, NY, USA, 2001.

[21] M. Hata, "Empirical formula for propagation loss in land mobile radio services," *IEEE Transactions on Vehicular Technology*, vol. 29, no. 3, pp. 317–325, 1980.

[22] COST 231, "Digital mobile radio towards future generation systems, final report," 1999.

[23] A. Gelb, et al., Ed., *Applied Optimal Estimation*, MIT Press, Cambridge, Mass, USA, 1974.

[24] G. Welch and G. Bishop, "An introduction to the kalman filter," in *Proceedings of the Annual Conference on Computer Graphics & Interactive Techniques (SIGGRAPH '01)*, ACM Press, Los Angeles, Calif, USA, August 2001.

[25] F. Daum, "Nonlinear filters: beyond the Kalman filter," *IEEE Aerospace and Electronic Systems Magazine*, vol. 20, no. 8, pp. 57–68, 2005.

[26] S. J. Julier, "The scaled unscented transformation," in *Proceedings of the American Control Conference*, vol. 6, pp. 4555–4559, May 2002.

[27] E. A. Wan and R. van der Merwe, "The unscented Kalman filter for nonlinear estimation," in *Proceedings of the Symposium 2000 on Adaptive Systems for Signal Processing, Communication and Control (AS-SPCC '00)*, pp. 153–158, October 2000.

[28] M. Briers, S. Maskell, and R. Wright, "A rao-blackwellised unscented Kalman filter," in *Proceedings of the 6th International Conference of Information Fusion*, vol. 1, pp. 55–61, July 2003.

[29] P. Tichavsky, C. H. Muravchik, and A. Nehorai, "Posterior cramér-rao bounds for discrete-time nonlinear filtering," *IEEE Transactions on Signal Processing*, vol. 46, no. 5, pp. 1386–1396, 1998.

[30] R. Karlsson, T. Schön, and F. Gustafsson, "Complexity analysis of the marginalized particle filter," *IEEE Transactions on Signal Processing*, vol. 53, no. 11, pp. 4408–4411, 2005.

Hindawi Publishing Corporation
International Journal of Navigation and Observation
Volume 2010, Article ID 460860, 11 pages
doi:10.1155/2010/460860

*Research Article*

# Cluster-Based Ranging for Accurate Localization in Wireless Sensor Networks

**Simone Sergi,[1] Fabrizio Pancaldi,[2] and Giorgio M. Vitetta[1]**

[1] *Department of Information Engeneering, University of Modena e Reggio Emilia, Italy*
[2] *Department of Science and Methods for Engeneering, University of Modena e Reggio Emilia, Italy*

Correspondence should be addressed to Giorgio M. Vitetta, giorgio.vitetta@unimore.it

Received 13 November 2009; Revised 21 May 2010; Accepted 1 June 2010

Academic Editor: Ronald Raulefs



A novel ranging technique based on *received signal strength* (RSS) and suitable to indoor scenarios is illustrated. In the proposed technique, multiple power measurements, associated with the signals radiated by a *cluster* of nodes surrounding a given target, are jointly processed to improve the quality of RSS-based estimation of the distance between the target and an anchor. Specific algorithms for the generation of a cluster and for the acquisition of power measurements are described. Simulation results show that, when used in indoor positioning systems, the proposed ranging technique is substantially more accurate than noncooperative strategies. In addition, it allows to concentrate significant processing tasks in a limited number of fixed anchors, so reducing maintenance costs and making it possible to adopt cheap and simple portable wireless nodes.

## 1. Introduction

Wireless sensor networks for accurate localization of people and objects in indoor environments represent a fundamental tool for the provisioning of high-level services in the fields of management and logistics. Despite this, currently the pervasive diffusion of such networks is prevented by their large complexity and maintenance costs. This is mainly due to the fact that, in indoor scenarios, accurate localization in the presence of severe multipath fading usually requires a large number of fixed sensing nodes (called *anchors*) with a known location [1] and the use of complicated signal processing algorithms for distributed distance estimation [2]. It is also important to note that localization algorithms are often designed under the assumption that accurate point-to-point distance measurements between the target node (i.e., that whose location needs to be identified) and a set of anchors are available [3–7]. Unluckily, the first hypothesis can be deemed realistic only when there is a *line of sight* (LOS) path between the given target node and the anchors involved in distance measurements, so that the first echo (i.e., the one with the shortest time of arrival) can be separated from all the following ones, originating from *nonline of sight* (NLOS) paths, via proper signal processing algorithms [8]. However, the accuracy achievable in such measurements reduces noticeably in indoor environments, since, generally speaking, they are characterized by significant obstacles to signal propagation and, frequently, by NLOS links [9].

Recently, an increasing attention has been paid to the use of *ultrawide band* (UWB) transmission techniques [10] for radio localization in indoor scenarios. This interest is motivated by the appreciable time resolution originating from the extremely wide bandwidth of UWB signalling formats [11]. This means that multiple echoes of UWB signals can be accurately resolved by sensing nodes, so that, in principle, the quality of ranging estimation can be substantially improved.

In this work, a new solution to indoor localization based on a UWB wireless sensor network is illustrated. The derivation of the proposed technique relies on the use of low complexity ranging estimation methods based on *received signal strength* (RSS) [2, 12], on some considerations about the statistical properties of UWB channels, and the use of multiple (i.e., of a *cluster* of) transmitting nodes, placed in different points of the considered environment, to refine the distance measurement of a target from a given anchor. These design choices can be motivated as follows: (1) measuring RSS is simple and can be easily accomplished

even by receivers which have not been explicitly designed to perform distance estimation (so avoiding the additional costs of deploying ad hoc hardware); (2) recent studies about statistical modeling of indoor UWB channels (e.g., see [13–15]) provide accurate information about the power decay model and the distribution of multipath components; (3) RSS indirectly exploits the very wide bandwidth of UWB signals, since such signals exhibit little small scale fading when compared to narrowband signals [16]; and (4) the use of multiple low-cost transmitting nodes allows to mitigate the effects of fading, resulting in improved accuracy. As far as the last point is concerned, it is important to note that the adopted solution exploits a sort of *cooperative diversity*, since, in the range measurement procedure, spatially separated nodes cooperate, emitting localization signals, which travel, however, through distinct wireless channels. It is also worth pointing out that, as far as we know, until now statistical modeling of UWB channels has been exploited to improve the overall performance of localization (e.g., see [4, 17]), but not the quality of ranging measurements.

The remaining part of the paper is organized as follow. The use of a cluster of nodes for improving ranging measurements is motivated in detail in Section 2, whereas algorithms for ranging estimation based on RSS and on the use of a cluster of nodes, and methods for cluster generation are derived in Section 3. In Section 4, the problem of acquiring independent RSS measurements is tackled, whereas in Section 5 some simulation results evidencing the enhancement in ranging accuracy provided by the proposed algorithms are analyzed. Finally, Section 6 offers some conclusions.

## 2. Cooperative Ranging Based on a Cluster of Nodes

In a wireless sensor network for indoor localization, the scope of each anchor is estimating its distance from a given target node on the basis of the RSS associated with the digital signal radiated by the node itself. In a static scenario affected by multipath fading, the average power $R$ associated with the useful component of the signal received at a given anchor can be expressed as [18]

$$R = P_0 - (\mathrm{PL} + \mathrm{LSF} + \mathrm{SSF}), \tag{1}$$

where $P_0$ is a *reference power level*, and PL, LSF, and SSF denote the *exponential path loss*, the *large scale fading*, and the *small scale fading* (all expressed in dBm) affecting the communication channel, respectively. In the following an NLOS condition is assumed for signal propagation, so that LSF and SSF can be represented as zero mean random parameters. In particular, LSF is modelled as a zero mean Gaussian random variable whose variance is described, in turn, by a Gaussian distribution characterized by known parameters; such parameters depend on the characteristics of the building, in which signal propagation occurs [14]. In addition, the statistical behavior of SSF is described by a Nakagami distribution with an $m$-factor $m \geq 1/2$ [15]. As far as the path loss PL is concerned, following [14, 15], an exponential power decay is considered; its path gain exponent, however, is modeled as a Gaussian random variable having constant variance and known mean, both depending on the macroscopic characteristics of the considered indoor environment.

In the absence of fading, we have that SFF = LSF = 0 in (1); then, the distance of the target node from a selected anchor can be perfectly estimated from $R$ if the power level $P_0$ and the mathematical model of the PL are completely known. Unluckily, the presence of fading introduces an uncertainty in ranging measurements based on (1). To mitigate fading effects, we propose to exploit, in distance estimation, all the RSSs associated with the digital signals radiated by a spatial *cluster* of nodes, as illustrated in Figure 1. This cluster has the following properties: (a) it consists of a subset of $N$ radiating nodes selected in a pool of $N_T$ nodes; (b) it includes the target node; (c) the signals transmitted by its nodes, as well as the signals transmitted by all the other nodes in the network, are mutually orthogonal in a specific domain (e.g., in the time or in the frequency domain) and can be separated perfectly by the anchor. Then, if $a_n$ denotes the $n$th node of a given cluster $C$ (i.e., $C$ is the set $\{a_n, n = 1, 2, \ldots, N\}$), the average power $R_{\mathrm{av}}$ captured by the anchor is given by (see (1))

$$\begin{aligned} R_{\mathrm{av}} &\triangleq \frac{1}{N}\sum_{n=1}^{N} R_n \\ &= P_0 - \left(\frac{1}{N}\sum_{n=1}^{N}\mathrm{PL}_n + \frac{1}{N}\sum_{n=1}^{N}\mathrm{LSF}_n + \frac{1}{N}\sum_{n=1}^{N}\mathrm{SSF}_n\right), \end{aligned} \tag{2}$$

where $R_n$ denotes the average power received from $a_n$, whereas $\mathrm{PL}_n$, $\mathrm{LSF}_n$, and $\mathrm{SSF}_n$ are the exponential path loss, the large scale fading, and the small scale fading affecting the communication channel between the anchor and $a_n$. The path loss $\mathrm{PL}_n$ can be expressed as

$$\mathrm{PL}_n = \mathrm{PL}_{\mathrm{mean}} + \Delta\mathrm{PL}_n, \tag{3}$$

for $n = 1, 2, \ldots, N$, where $\mathrm{PL}_{\mathrm{mean}}$ represents the average path loss affecting the cluster nodes, whereas $\Delta\mathrm{PL}_n$ denotes the offset of $\mathrm{PL}_n$ from $\mathrm{PL}_{\mathrm{mean}}$. Intuitively, $\mathrm{PL}_{\mathrm{mean}}$ accounts for the loss associated with the separation between the cluster and the anchor, whereas $\Delta\mathrm{PL}_n$ can be related to the displacement of the nodes within the cluster, as shown in Figure 2. It is also worth noting that, generally speaking, the value of the *path loss exponent* depends on the propagation link [14, 15], so that, in principle, it can take on different values for distinct nodes of the same cluster; however, modelling errors concerning this parameter in the evaluation of path loss can be incorporated in the $\{\Delta\mathrm{PL}_n\}$ terms.

Given (3), (2) can be rewritten as

$$R_{\mathrm{av}} = P_0 - \left(\mathrm{PL}_{\mathrm{mean}} + \Delta\mathrm{PL} + \frac{1}{N}\sum_{n=1}^{N}\mathrm{LSF}_n + \frac{1}{N}\sum_{n=1}^{N}\mathrm{SSF}_n\right), \tag{4}$$

where

$$\Delta\mathrm{PL} \triangleq \frac{1}{N}\sum_{n=1}^{N}\Delta\mathrm{PL}(n). \tag{5}$$

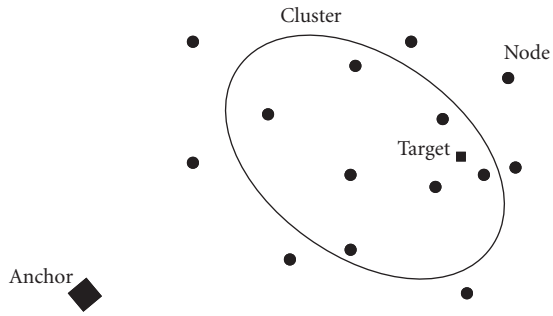


Figure 1: Set-up of the analysed system.

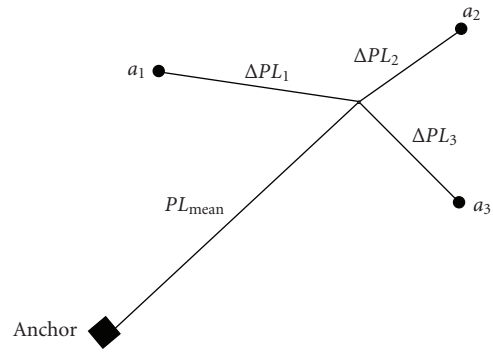


Figure 2: Decomposition of the path loss terms of a cluster of nodes in a common cluster distance-related term ($\text{PL}_{\text{mean}}$) and a set of distance errors ($\Delta\text{PL}_n$).

If ranging estimation of the selected anchor is based on the quantity $R_{\text{av}}$ (2) instead of $R$ (1), a larger accuracy can be achieved thanks to the fading mitigation effect originating from the use of multiple contributions. This can be easily proved if the indoor scenario is characterized by a *rich scattering*, so that the channels between distinct nodes and the selected anchor can be deemed statistically independent. Then, the random variables $\{\text{LSF}_n\}$ and $\{\text{SSF}_n\}$ are mutually independent and, if the radiating nodes are identical and the associated channels are statistically equivalent, can be considered identically distributed. Since the variance of the fading terms $\{\text{LSF}_n\}$ and $\{\text{SSF}_n\}$ is finite, if $N$ is large enough, the central limit theorem [19] can be applied, and each of the terms $\sum_{n=1}^{N} \text{LSF}_n$ and $\sum_{n=1}^{N} \text{SSF}_n$ in (4) can be modelled as zero mean Gaussian random variable with a variance tending to 0 as $N$ increases; in other words, the ranging error component due to multipath fading can be substantially reduced if the number $N$ of (cooperating) cluster nodes is large enough. Note, however, that the achievable accuracy can be limited by the term $\Delta\text{PL}$ (5), representing the residual error due to the spatial spread of the selected cluster. For instance, if the nodes of the cluster are placed in a regular fashion along a circumference and the anchor is placed in its center, the term $\Delta\text{PL}$ will be equal to zero, independently of the distance between the nodes and the anchor, even if this increases to infinity (see the example of Sestion 5.1 for a deeper insight). This means that, in principle, the term $\Delta\text{PL}$ is not minimized if a spatially dense cluster is selected, but if the nodes forming the cluster are enrolled according to a clever strategy.

It is also important to point out that the approach we propose for improving the quality of ranging measurements can provide various practical advantages; some of them are listed below.

(i) If the proposed method can achieve a better accuracy in NLOS conditions then that offered by classic RSS-based ranging techniques, the application level can be simplified, since most of the computational burden is concentrated at lower system layers.

(ii) The employed radio nodes can be extremely simple (and, hence, cheap), since most of signal processing for localization is accomplished by a small number of fixed anchors. In fact, As pointed out in the following, each node is only expected to respond to a query with a certain (and precise) power level.

(iii) System performance can be improved putting *dummy nodes* in the environment; these have the only scope of increasing node density.

The adoption of the proposed solution, however, raises some important technical issues that need to be carefully addressed. In particular, we note that

(i) a proper *strategy* for the generation of a cluster is needed to identify the nodes optimising performance, that is, the overall ranging accuracy,

(ii) the impact of node density over the system performance should be analyzed. In fact, on the one hand, if the cluster covers a small area, the residual error $\Delta\text{PL}$ is negligible with respect to the mean distance (which can be identified as the target distance) associated with $\text{PL}_{\text{mean}}$; however, it is likely that in this situation the fading affecting distinct nodes exhibits a substantial correlation, so that the effectiveness of the proposed strategy can be appreciably affected. On the other hand, if the cluster size is significant, it is not difficult to show that the ranging error due to the fading terms $\{\text{LSF}_n\}$ and $\{\text{SSF}_n\}$ decreases as $1/N^2$ only; the estimation accuracy, however, can get worse because of $\Delta\text{PL}$, that is, of the spread in node locations with respect to cluster center.

The first problem can be solved using proper algorithms, as illustrated in Section 3. Unluckily, the second problem does not lend itself to a simple mathematical analysis. For this reason, its relevance has been assessed via computer simulations; some results are illustrated and commented in Section 5.

## 3. Cluster Selection Strategies

In this Section, two different strategies for the selection of the wireless nodes forming a cluster for a given target node in a *static* indoor scenario are proposed. Then, the problem

of distance estimation based on a set of data acquired from a cluster of nodes is analyzed.

Before analysing the proposed strategies in detail, it is worth noting that any strategy for cluster selection should aim at identifying a group of nodes (in the pool of available ones) in a way that the fading effects in the measurement of $R_{\text{av}}$ (4) are mitigated and that, at the same time, the amplitude of the term $\Delta\text{PL}$ (5) is not enhanced. For this reason, the problem of selecting an optimal cluster $\widehat{C}$ could be formulated as

$$\widehat{C} = \arg\min_{\widetilde{C},N_{\widetilde{C}}} \left| R_{\text{av}}\left(\widetilde{C},N_{\widetilde{C}}\right) - \left(P_0 - \text{PL}_{\text{mean}}\left(\widetilde{C},N_{\widetilde{C}}\right)\right)\right|, \tag{6}$$

where the dependence of $R_{\text{av}}$ and $\text{PL}_{\text{mean}}$ on the trial cluster $\widetilde{C}$ and on its size $N = N_{\widetilde{C}}$ is explicitly indicated. Note that

(i) the cluster optimization procedure expressed by (6) involves not only the selection of a specific set of nodes $\widetilde{C}$, but also that of its size $N_{\widetilde{C}}$. If $N_{\widetilde{C}}$ is large, fading is mitigated, but the effects of the offset $\Delta\text{PL}$ become significant,

(ii) if $N_T$ denotes the overall number of nodes in the environment managed by the anchor, the number of unordered collections of $N_{\widetilde{C}}$ nodes extracted from a set of $N_T$ nodes is given by $\binom{N_T}{N_{\widetilde{C}}} = N_T!/(N_{\widetilde{C}}!(N_T - N_{\widetilde{C}})!)$; this quantity (and, consequently, the computational complexity of the problem (6)) grows quickly as $N_{\widetilde{C}}$ increases.

The last comment motivates the investigation of suboptimal strategies leading to a good accuracy in distance estimation at the price of a reasonable complexity. In the following, Paragraphs we show that such strategies can be developed adopting a heuristic approach to the problem of cluster selection. Our strategies operate in a *centralized fashion*, since cluster selection is accomplished at the anchor. For this reason, in the cluster selection procedure, each involved node is only expected to generate a *signature signal* in response to a radio frequency query from the anchor. In the following, however, we do not tackle the problems of identifying each node (and, in particular, of looking for the target node in the cluster) and of managing the access to a shared radio medium. In fact, we simply assume that the anchor is able to identify each node, exploiting, for instance, an unambiguous identification code wired in the hardware of each node, like in RFID tags [20]. Moreover, the response signal is expected to be transmitted at a certain (and precise) power level, so that active RFIDs [20] could represent a good technical choice in a low-cost node design.

Finally, we note that, as already mentioned in the previous Paragraph, the identification of the optimal cluster $\widehat{C}$ relies on the availability of several *independent* RSS measurements for each node of the trial clusters $\widetilde{C}$; two different strategies for the acquisition of such data are illustrated in Section 4. Here we consider a static scenario, in other wongs we assume that negligible changes occur in the measurement scenario during the interval in which RSS data are acquired. If such an interval is very short, then the solutions we propose can be adopted for portable indoor applications.

*3.1. Cluster Selection Based on the Minimization of a Power Spread.* The first procedure for cluster selection evolves through the following steps:

(1) $N_P$ independent power measurements $\{R_n(m),\ m = 1,2,\ldots,N_P\}$ are acquired for the node $a_n$ (with $n = 1, 2,\ldots,N_T$) reached by a query signal from the anchor;

(2) a trial cluster $\widetilde{C}$, having fixed size $D$ and including the target node, is selected;

(3) for $m = 1,2,\ldots,N_P$ the mean power

$$R_{\widetilde{C}}(m) = \frac{1}{D}\sum_{n\in\Lambda_{\widetilde{C}}} R_n(m) \tag{7}$$

associated with $\widetilde{C}$ is computed (here the set $\Lambda_{\widetilde{C}}$ consists of the $D$ values of $n$ that identify the subset of nodes $\{a_n\}$ forming $\widetilde{C}$);

(4) the "spread" $\sigma_{\widetilde{C}}$ of the set of powers $\{R_{\widetilde{C}}(m),\ m = 1,2,\ldots,N_P\}$ is evaluated as

$$\sigma_{\widetilde{C}}(m) \triangleq \sqrt{\frac{1}{N_P}\sum_{m=1}^{N_P}\left(R_{\widetilde{C}}(m) - \mu_{\widetilde{C}}\right)^2}, \tag{8}$$

where

$$\mu_{\widetilde{C}} \triangleq \frac{1}{N_P}\sum_{m=1}^{N_P} R_{\widetilde{C}}(m); \tag{9}$$

(5) the steps 2–4 are repeated for any possible trial cluster $\widetilde{C}$; at the end of this exhaustive procedure, the cluster $\widehat{C}$ minimizing $\sigma_{\widetilde{C}}$ (8) is selected; in other words, the cluster selection strategy, dubbed *spread minimization* (SM) in the following, can be summarized as

$$\widehat{C} = \arg\min_{\widetilde{C}}\sigma_{\widetilde{C}}. \tag{10}$$

The rationale behind this technique is to search for a cluster such that the power measurements for its nodes exhibit the minimum spread, that is, the smallest sensitivity to fading; in fact, a small spread indicates that the (deterministic and distance-dependent) path loss term prevails over (stochastic) fading terms in the model expressed by (2).

The main drawbacks of the SM strategy are represented by (a) the need of evaluating of a set of $\binom{N_T}{D}$ distinct metrics $\sigma_{\widetilde{C}}$ (8), where $\binom{N_T}{D} = N_T!/(D!(N_T - D)!)$ indicates the number of unordered collections of $D$ distinct elements extracted from a set of $N_T$; (b) the exhaustive search for the minimum over this set. In fact, these tasks entail a substantial

computational burden at the anchor. It is important to point out, however, that the task of cluster selection can be carried out without strict real-time constraints (hence, off line) at the anchor, once the whole measurement process has been completed. Moreover, the anchor can be a fixed device connected to the power network, so that, since it is not limited in the energy and/or size, it can be very powerful.

Finally, it is worth noting that

(i) in principle, the size $D$ of the cluster could be optimized considering progressively larger clusters in our search (10), so that the optimal cluster size $N$ could be identified; however, this approach would make the problem computationally unmanageable for large values of $N_T$;

(ii) a conceptually similar approach has been adopted in [4, 9] to discriminate between LOS and NLOS conditions in a wireless link;

(iii) the performance of the SM strategy is not affected by the presence of correlated shadowing. In fact, in this case, adopting the representation of (3) for the PL, the term $(1/N)\sum_{n=1}^{N} \mathrm{LSF}_n$ in (4) can be rewritten as $\mathrm{LSF}_{\mathrm{mean}} + (1/N)\sum_{n=1}^{N} \Delta\mathrm{LSF}_n$, where $\mathrm{LSF}_{\mathrm{mean}}$ denotes a *bias* due to the above-mentioned phenomenon. Then, it can be shown that the variability of the right hand side of (7) as well as the spread evaluated according to (8) undergo a reduction with respect to the case of uncorrelated LSF terms. For this reason, the nodes affected by correlated shadowing are likely to be included in the cluster, and, since such nodes are also spatially close, the weight of the terms $\Delta$PL and SSF can be appreciably reduced.

*3.2. Cluster Selection Based on the Estimation of a Coarse Distance.* The second procedure for cluster selection is based on the idea of grouping nodes whose distance from the anchor appears to be close to that evaluated for the target node. This strategy consists of the following steps:

(1) $N_P$ independent power measurements $\{R_n(m), m = 1, 2, \ldots, N_P\}$ are acquired by the anchor for the node $a_n$ (with $n = 1, 2, \ldots, N_T$) reached by a query signal from the anchor;

(2) the anchor processes $R_n(m)$, with $m = 1, 2, \ldots, N_P$, to estimate its distance $d_n(m)$ from the node $a_n$, with $n = 1, 2, \ldots, N_T$ (the adopted estimation technique is illustrated in Sestion 3.3);

(3) the *average distance* $d_n$ of the anchor from $a_n$, with $n = 1, 2, \ldots, N_T$, is evaluated as

$$d_n = \frac{1}{N_P}\sum_{m=1}^{N_P} d_n(m); \tag{11}$$

(4) the anchor accomplishes an exhaustive search to identify, in the set of nodes, the $D$ elements whose distance is closer to the average distance $d_{\mathrm{tg}}$ measured for the target node; formally, this strategy for the selection of the optimal cluster $\widehat{C}$ can be expressed, in analogy to (10), as

$$\widehat{C} = \arg\min_{\breve{C}} \sum_{n\in\Lambda_{\breve{C}}} \left| d_n - d_{\mathrm{tg}} \right|. \tag{12}$$

Note, however, that this strategy, called *distance estimation* (DE) in the following, is substantially simpler than that expressed by (10), since it involves a search over a set of $N_T$ nodes, instead of the family of all possible clusters of $D$ nodes.

Finally, it is important to point out that this algorithm does not search for the set of $D$ nodes spatially closer to the target node, but identifies the nodes whose distance is closer to that of the target node $d_{\mathrm{tg}}$. In other words, it selects the nodes closer to a circumference having radius $d_{\mathrm{tg}}$ and the anchor in its center.

*3.3. Target Distance Estimation in the Presence of a Cluster of Nodes.* It is well known that, in free space propagation, the average power $R_x(d)$ (in dBm) captured by a receiver placed at a distance $d$ from a transmitter can be expressed as [15, 18]

$$R_x(d) = P_0 - 10\xi \log\left(\frac{d}{d_0}\right), \tag{13}$$

where $P_0$ represents the power level (in dBm) measured at the so-called *reference distance* $d_0$, whereas $\xi$ is the *path loss exponent*. Note that this expression cannot be exploited as it is for accurately estimating the distance $d$ from a single measurement of average received power, since, as already mentioned in Section 2, the path loss exponent $\xi$ is a random variable. To remove this uncertainty in (13), $\xi$ is replaced by its mean value $\overline{\xi}$ of this parameter in the following. Then, if $R_x(d)$ is known, the distance $d$ can be roughly estimated as

$$d = k \cdot 10^{-R_x(d)/(10\overline{\xi})}, \tag{14}$$

where $k \triangleq d_0 \cdot 10^{-(P_0/10\overline{\xi})}$.

The expression (14) can be certainly exploited for the same target even in the presence of a cluster of nodes. In fact, an estimate $d_{\mathrm{coop}}$ of the distance of the target node from the anchor can be computed as

$$d_{\mathrm{coop}} = k \cdot 10^{-P_{\mathrm{av}}/(10\overline{\xi})}, \tag{15}$$

where

$$P_{\mathrm{av}} \triangleq \frac{1}{NN_P}\sum_{n=1}^{N}\sum_{m=1}^{N_P} R_n(m) \tag{16}$$

regardless the adopted cluster selection strategy.

The proposed distance estimation algorithm benefits from *spatial diversity* [21] and *multiuser diversity* [22], since $N_P$ *independent* power measurements are acquired for each node of a cluster $\widehat{C}$, consisting of $N$ distinct nodes

(i.e., users). It is also worth pointing out that the number $N_P$ of independent measurements that can be acquired from a single node is limited by the availability of independent channel realizations and, consequently, by the characteristics of the considered environment [23]; in addition, the selection of a large value for the cluster size $N$ can lead to a significant residual error $\Delta$PL (see (4)). The joint exploitation of the two forms of diversity allows to mitigate the problem of correlated fading [23] and to improve the overall accuracy of the system.

## 4. Methods to Acquire Independent RSS Measurements

Both the SM and DE algorithms for cluster selection rely on the availability of $N_P$ independent data for each node. In this Section, we illustrate how such data can be acquired. In particular, two methods are proposed below; one is based on the use of an oscillating beam pattern at a fixed anchor, the other one is based on the use of a frequency sweep.

*4.1. Oscillating Beam.* The use of an oscillating beam pattern has been adopted in [23, 24] to generate a sort of "artificial" time diversity in mobile wireless channels. In our scenario, the implementation of this solution requires the anchor to be equipped with an antenna array fed by phase-controlled signals, so that the main lobe of the radiation pattern can be properly steered. Note that, in a rich scattering environment, different transmission lobes can lead to independent multipath propagation and, hence, to independent channel realizations. In particular, [23, 24] evidence that this technique offers the availability of a large number (say, one hundred) of independent channels between two wireless terminals in a static scenario. In our simulations, however, an oscillating beam with 10 distinct angular steps only has been assumed for the reasons illustrated in Section 4.3; this still provides good spatial diversity and, at the same time, does not restrict the significance of the acquired results to a specific propagation environment. Note that (a) when an oscillating beam is used, the index $m$ of $R_n(m)$ (see Sestions 3.1 and 3.2) uniquely identifies the orientation of the radiation beam; (b) the use of an oscillating beam increases the complexity of the fixed anchor, but does not affect that of the mobile devices.

*4.2. Frequency Sweep.* An alternative method to extract independent channel realizations in a static scenario consists of exploiting frequency diversity; in fact, power measurements can be deemed independent if they are collected at multiple frequencies, such that the spacing between adjacent frequencies exceeds the coherence bandwidth of the communication channel [25]. Note that, in this scenario, the index $m$ of $R_n(m)$ uniquely identifies the frequency at which the $m$th power measurement is acquired.

Unluckily, this approach is substantially more complicated than the previous one, since it requires the implementation of mobile nodes with a wideband RF front end.

*4.3. Remarks.* Even if the methods described above can provide a large number of independent power measurements, only a limited number of such measurements are required by the proposed ranging techniques in a rich scattering indoor environment. For instance, in such a scenario, if the angular step of the beam steering is large, the electromagnetic signals captured along different directions are expected to have travelled along paths characterized by different distances; generally speaking, this does not help to improve the accuracy of our ranging procedure. For this reason, it is recommended to acquire a limited number of independent measurements limiting the deviation of the beam steering, so that small scale fading can be averaged out without appreciably influencing the path loss. Similar considerations apply to the case in which the step size in a frequency sweep is large.

## 5. Numerical Results

This section is organized as follows. First, we comment on the relationship between the distribution of cluster nodes and the achievable accuracy in cluster-based ranging. Then, we analyse various numerical results about the ranging accuracy achieved by the proposed strategies in two different scenarios.

*5.1. Spatial Distribution of Cluster Nodes and Ranging Accuracy.* When the distances between distinct nodes of a given cluster are not appreciably smaller than the distance between the cluster center and the fixed anchor, the "spread" error $\Delta$PL is expected to seriously limit the ranging accuracy achievable by a localization system. To understand the relevance of this problem, let us consider a specific cluster $C$, collecting 5 nodes whose structure is illustrated in Figure 3. In this case, it is assumed that the target is the central node and that, for the sake of simplicity, the distance between the nodes $a(1)$ and $a(2)$ ($a(3)$ and $a(4)$) and the anchor is $r_1 = r_2 = r_0 - \epsilon$ ($r_3 = r_4 = r_0 + \epsilon$), where $r_0$ is the distance between the target node and the anchor. If the path loss model (1) characterized by an exponential decay [18] is adopted, the power $R$ received by a transmitter located at a distance $d$ from the anchor is given by

$$R(d) = P_0 - 10\xi\log_{10}(d) + K, \tag{17}$$

where $K$ represents the sum of the LSF and SSF contributions. Then, for the $n$th node (with $n = 0, 1, \ldots, 4$) and considering the availability of a single power measurement for each node (i.e., $N_P = 1$) for the sake of simplicity, the anchor exploits the power measurement

$$R_n = P_0 - 10\xi\log_{10}(r_n) + K_n \tag{18}$$

to compute the mean received power

$$R_{\text{av}} = \frac{1}{5}\sum_{n=0}^{4} R_n = P_0 - \text{PL}_{\text{mean}} + \frac{1}{5}\sum_{n=0}^{4} K_n, \tag{19}$$

where

$$\text{PL}_{\text{mean}} = \frac{10\xi\log_{10}(r_0) + 20\xi\log_{10}(r_1) + 20\xi\log_{10}(r_3)}{5}. \tag{20}$$

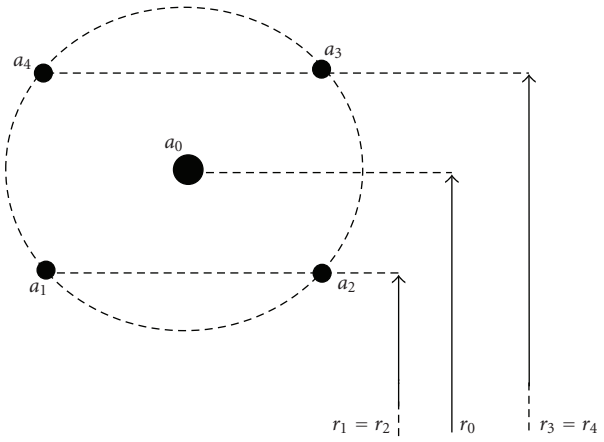


Figure 3: Possible spatial distribution of 5 radiating nodes.

In the last expression, the contribution of the terms $\{K_n\}$ accounts for the fading affecting the nodes; moreover, the path loss $\mathrm{PL}_{\mathrm{mean}}$, depending on the distance between the cluster center and the anchor, can be rewritten as

$$\begin{aligned}\mathrm{PL}_{\mathrm{mean}} &= 10\xi\log_{10}\left(r_0 \cdot r_1^2 \cdot r_3^2\right)^{1/5} \\ &= 10\xi\log_{10}\left(r_0 \cdot (r_0-\epsilon)^2 \cdot (r_0+\epsilon)^2\right)^{1/5} \\ &= 10\xi\log_{10}\left(r_0^5 - 2r_0^3\epsilon^2 + r_0\epsilon^4\right)^{1/5},\end{aligned} \tag{21}$$

to evidence its dependence on the term $\epsilon$. In any application, we have that $\epsilon \neq 0$ (since the nodes belonging to the cluster associated with a given target cluster do not coincide with the target itself), so that a systematic source of error (i.e., a bias) is found in ranging estimation based on node cooperation. Unfortunately, a theoretical analysis of this problem appears unfeasible, since the nodes of a given cluster are not expected to follow a regular distribution in any indoor application. For this reason, the relevance of the irreducible residual error $\Delta\mathrm{PL}$ (related to the presence of $\epsilon$ in the above-mentioned example) is assessed via computer simulation only in the following.

The problem of the effects, on the achievable performance, of the spatial distribution of the nodes forming a cluster around a given target deserves also the following comments. As stated in Section 2, the aim of the anchor in cluster generation according to the proposed algorithms is to search for the nodes that can minimize the ranging error and not for those forming a dense set. Unluckily, in an indoor scenario characterized by rich scattering, an anchor looking for nodes close to a given target tends to discard all those nodes whose transmission is affected by severe fading, since they appear far from the target location. This explains why the proposed techniques for the generation of clusters take advantage of cooperating nodes which are not close to the target node; this is evidenced by Figure 4, illustrating a possible spatial distribution of a node population and of the cluster nodes selected for a given target.

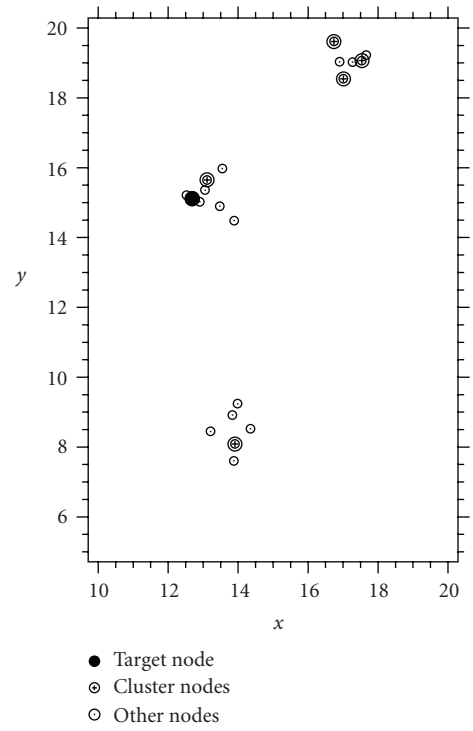


Figure 4: Example of spatial node distribution and of a cluster of nodes selected for ranging.

*5.2. Ranging Accuracy.* The performance offered by the proposed ranging technique has been assessed resorting to computer simulations. In all the simulations, the UWB indoor channel model adopted in [14, 15] has been used. This model is characterized by (a) an exponential path loss (see [14, equation (12)]) with a Gaussian distributed path gain exponent; (b) a lognormal large-scale fading (see [14, equation (14)]) with zero mean and random variance (a Gaussian distribution is adopted); (c) a Nakagami small-scale fading with the $m$-factor equal to 1/2 (see [15, equation (19)]). All the parameters characterizing this channel model are summarized in [14, Table II]; note that in our simulations, NLOS channel models have been used, when not differently stated.

Two different bidimensional scenarios have been considered for the cluster structure. The first scenario (dubbed *scenario* #1 in the following) is characterized by a uniform distribution of nodes and aims at modelling a rich scattering environment in an indoor industrial/commercial open space. In this case, the anchor is placed at a fixed distance of 20 m from the centre of an area having a square shape with a side $S$ ranging from 3 cm to 12 m; 20 nodes are uniformly distributed in such an area, and one is randomly selected as the target. The second scenario (called *scenario* #2 in the following) is more suitable to modelling a residential indoor environment (e.g., an office or an hospital) and is characterized by (a) an anchor placed at a fixed distance of 20 m from the centre of a square region having fixed side equal to 12 m; (b) 20 nodes divided in 3 groups (for instance, each group could consist of the nodes located in a

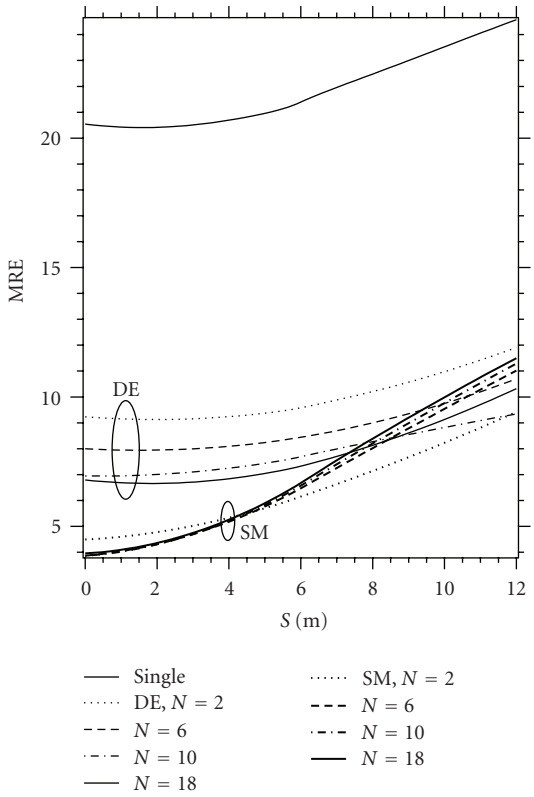


Figure 5: Comparison between the MRE provided by the proposed ranging techniques and by a traditional RSS-based technique in the presence of uniformly distributed nodes and NLOS propagation.

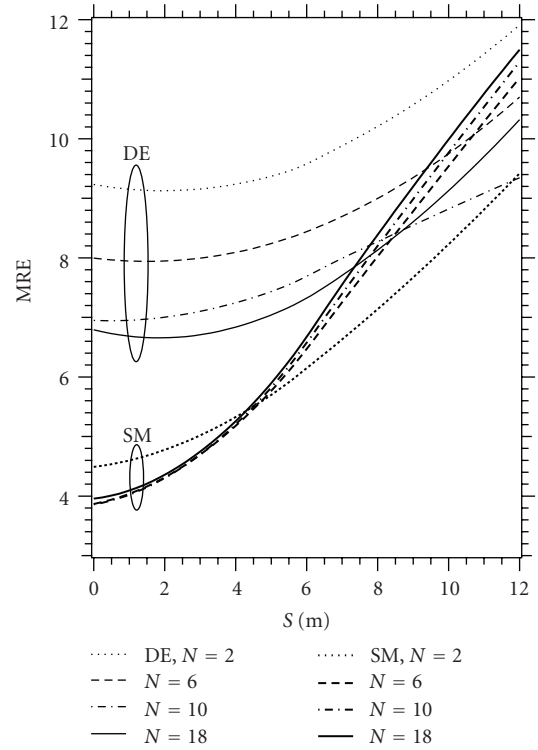


Figure 6: MRE provided by the SM and the DE algorithms in the presence of uniformly distributed nodes and NLOS propagation.

different room of the same floor in an indoor environment); (c) the centre of each group is randomly placed within the square region of fixed side and the coordinates of the group nodes are Gaussian distributed around it (the variance of this distribution is properly adjusted to ensure that the side $G$ of the square area containing the group ranges from about 2 cm to 6 m). The target is selected randomly among the nodes. Note that, for both the scenarios, the anchor is always out of the area over which the nodes are distributed.

System performance is assessed in terms of *mean ranging error* (MRE), defined as the difference between the estimated distance of the target from the anchor and the true distance of the target from the anchor averaged over 500 distinct trials of the ranging procedure. In addition, in the following simulation results, when not differently stated, it is assumed that 10 independent channel realizations are available for each node; we deem this hypothesis realistic, independently of the specific scenario (see Sestion 4.1).

Figure 5 compares the MRE, versus the spatial size $S$ of the area in which the nodes are distributed, of the proposed strategy (using DE or SM for the generation of clusters) with that of a standard single node RSS technique for ranging [12] in scenario #1. These results show that the former strategy substantially outperforms the latter one, characterized by an MRE comparable to the distance of the target node. The improvement offered by an increase in the number of nodes forming the cluster is evidenced by Figure 6, referring to the case of the DE and SM techniques only. For instance, if the DE method is adopted, the MRE is limited to about 9 m, 8 m, and 7 m with clusters made of $N = 2$, 6, and 10 nodes, respectively, note that, when a cluster includes more than 10 nodes, the residual error $\Delta$PL can lead to a slight performance degradation. The SM algorithm allows to achieve even better accuracies than the DE; in fact, when $N = 2$ nodes form the cluster, the MRE is approximately equal to 4.5 m, whereas the minimum error is reduced to about 4 m if $N$ is increased to 6. These results also evidence that SM technique is more sensitive to node density than the DE, which does not appreciably depend on the size of the environment. In fact, if the scenario is densely populated, the SM method outperforms the DE one, whereas the accuracy is comparable when the node distribution is more sparse or even worse when $N > 6$. This result can be related to the different rationales behind these two techniques and, in particular, to the fact that the SM aims at mitigating fading effects independently of the residual errors $\{\Delta\text{PL}_n\}$, whereas the DE minimizes the differences in distance measurements, so coping with all the sources of error (residual errors $\{\Delta\text{PL}_n\}$ and fading) indistinctly.

Similar comments can be expressed for the results shown in Figure 7, referring to scenario #2. Note that, despite the substantial difference between the test scenarios, the performance enhancement provided by the proposed techniques is similar to that achieved in scenario #1.

Our methods have been also tested in the presence of quasi-LOS propagation conditions, assuming the node

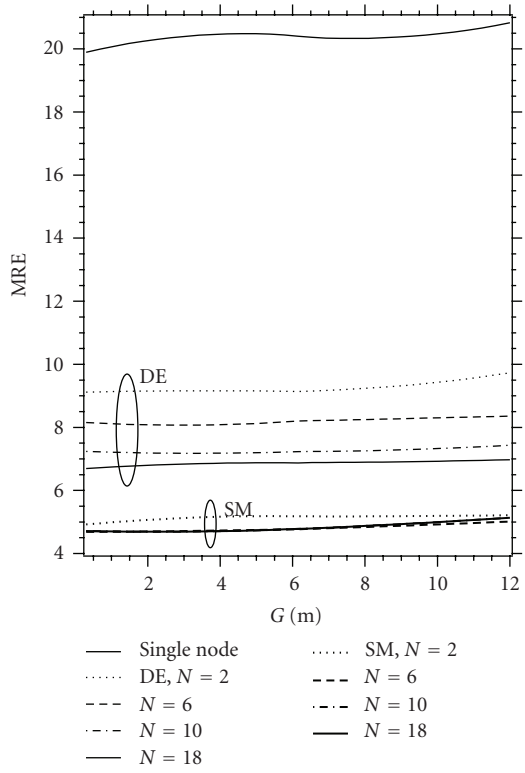


Figure 7: Comparison between the MRE provided by the proposed ranging techniques and by a traditional RSS-based technique in the presence of a clustered node distribution and NLOS propagation.

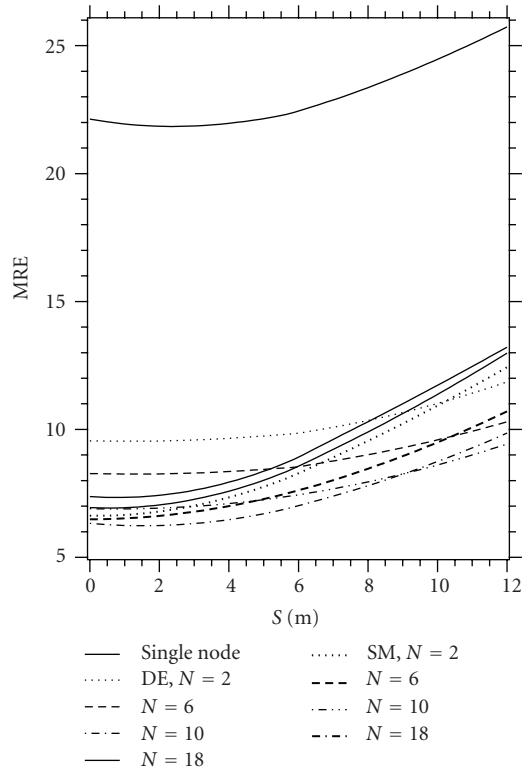


Figure 8: Comparison between the MRE offered by the proposed ranging techniques and by a traditional RSS-based technique in the presence of uniformly distributed nodes and quasi-LOS propagation.

arrangement of scenario #1. Some numerical results are illustrated in Figure 8 and show that the performance of the SM algorithm is slightly better than that of the DE (even if the gap is smaller than that of the NLOS scenario), and that the performance gain offered by DE algorithm over standard RSS techniques is similar in quasi-LOS and NLOS conditions. This is due to the fact that in quasi-LOS channels, the MRE is mainly due to the terms $\{\Delta PL_n\}$ (rather than to fading), whose effects are not accounted for by the SM algorithm.

The sensitivity of the MRE with respect to $N_P$ (i.e., to the number of available independent power measurements for each node) is evidenced by Figure 9, whose results have been obtained for $N_P = 5$. Note that, on the one hand, the reduction in the available diversity appreciably worsens the performance of the DE algorithm (the MRE can increase up to 2-3 m for a small cluster). On the other hand, the performance of the SM algorithm, relying on both spatial and multiuser diversity, is not substantially affected.

Finally, it is important to point out that

(i) the proposed strategies outperform the standard single node ranging techniques because they can rely on the RSS measurements of all the nodes populating the environment. In fact, clusterization can be viewed as the selection of the "most convenient data" to perform ranging for a given node,

(ii) the ranging accuracy provided by the SM and the DE algorithms depends on the overall number of nodes in the environment rather than on their density; in fact these algorithms cooperatively exploit nodes which can be placed far away from the target node, as already discussed in the previous Paragraph,

(iii) further simulations, whose results are not presented here for space limitations, have been run to assess the achievable performance when the generation of clusters is based on a distributed procedure, carried out by the nodes themselves. Our results have evidenced that, since severe fading can lead to uncorrelated channels among the nodes and between the nodes and the anchor, distributed node selection does not provide a substantial improvement, even with the respect to the case of nodes randomly selected by an anchor.

## 6. Conclusions

In this paper, a novel ranging technique based on RSS and suitable to indoor scenarios affected by severe multipath fading has been presented. The technique improves the quality of RSS-based estimation: (a) exploiting the signals radiated by a cluster of nodes; (b) averaging over multiple independent power measurements for each node of the

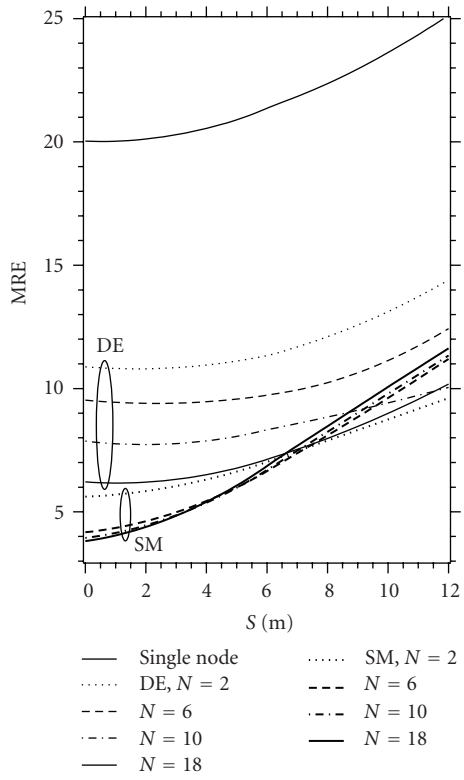


Figure 9: Comparison between the MRE offered by the proposed ranging techniques and by a traditional RSS-based technique in the presence of uniformly distributed nodes and NLOS propagation; $N_P = 5$ independent channel realizations are assumed for each node.

cluster. Specific algorithms for the generation of clusters and for the acquisition of power measurements have been illustrated.

Numerical results have evidenced that the proposed ranging technique is substantially more accurate than traditional strategies in specific scenarios. In addition, thanks to the centralized nature of the algorithms for cluster generation, it allows to move the complexity of an indoor positioning system to a limited number of fixed anchors, so reducing its maintenance costs and making possible to adopt cheap and simple portable wireless nodes. Finally, it is worth mentioning that in poorly populated areas, good performance results can be still achieved if the node density is artificially increased using multiple dummy devices in the environment.

## Acknowledgments

The authors wish to acknowledge the activity of the Network of Excellence in Wireless COMmunications (NEWCOM++, contract no. 216715), supported by the European Commission and that has motivated this work. The authors would like also to thank the anonymous reviewers for their comments which have been extremely helpful in improving the quality of the paper.

## References

[1] http://www.ubisense.net.

[2] N. Patwari, J. N. Ash, S. Kyperountas, A. O. Hero III, R. L. Moses, and N. S. Correal, "Locating the nodes: cooperative localization in wireless sensor networks," *IEEE Signal Processing Magazine*, vol. 22, no. 4, pp. 54–69, 2005.

[3] T. Roos, P. Myllymaki, and H. Tirri, "A statistical modeling approach to location estimation," *IEEE Transactions on Mobile Computing*, vol. 1, no. 1, pp. 59–69, 2002.

[4] N. A. Alsindi, K. Pahlavan, B. Alavi, and X. Li, "A novel cooperative localization algorithm for indoor sensor networks," in *Proceedings of the IEEE 17th International Symposium on Personal, Indoor and Mobile Radio Communications (PIMRC '06)*, pp. 1–6, Helsinki, Finland, September 2006.

[5] N. Patwari, A. O. Hero III, M. Perkins, N. S. Correal, and R. J. O'Dea, "Relative location estimation in wireless sensor networks," *IEEE Transactions on Signal Processing*, vol. 51, no. 8, pp. 2137–2148, 2003.

[6] J.-C. Chen, Y.-C. Wang, C.-S. Maa, and J.-T. Chen, "Network-side mobile position location using factor graphs," *IEEE Transactions on Wireless Communications*, vol. 5, no. 10, pp. 2696–2704, 2006.

[7] M. Castillo-Effen, W. A. Moreno, M. A. Labrador, and K. P. Valavanis, "Adapting sequential Monte-Carlo estimation to cooperative localization in wireless sensor networks," in *Proceedings of the IEEE International Conference on Mobile Ad Hoc and Sensor Sysetems (MASS '06)*, pp. 656–661, Vancouver, Canada, October 2006.

[8] J. Borras, P. Hatrack, and N. B. Mandayam, "Decision theoretic framework for NLOS identification," in *Proceedings of the 48th IEEE Vehicular Technology Conference (VTC '98)*, vol. 2, pp. 1583–1587, May 1998.

[9] X. Li, K. Pahlavan, D. Ramsburg, and R. Passmore, "Phase I Final Report: Innovative Methods for Geolocation and Communication with UWB Mobile Radio," Internal Report for DARPA, May 2004.

[10] S. Gezici, Z. Tian, G. B. Giannakis et al., "Localization via ultra-wideband radios: a look at positioning aspects of future sensor networks," *IEEE Signal Processing Magazine*, vol. 22, no. 4, pp. 70–84, 2005.

[11] I. Oppermann, M. Hämäläinen, and J. Iinatti, *UWB: Theory and Applications*, John Wiley & Sons, New York, NY, USA, 2004.

[12] T. Gigl, G. J. M. Janssen, V. Dizdarević, K. Witrisal, and Z. Irahhauten, "Analysis of a UWB indoor positioning system based on received signal strength," in *Proceedings of the 4th Workshop on Positioning, Navigation and Communication (WPNC '07)*, pp. 97–101, March 2007.

[13] L. J. Greenstein, S. S. Ghassemzadeh, S.-C. Hong, and V. Tarokh, "Comparison study of UWB indoor channel models," *IEEE Transactions on Wireless Communications*, vol. 6, no. 1, pp. 128–135, 2007.

[14] A. F. Molisch, "Ultrawideband propagation channels-theory, measurement, and modeling," *IEEE Transactions on Vehicular Technology*, vol. 54, no. 5, pp. 1528–1545, 2005.

[15] A. F. Molisch, D. Cassioli, and C. C. Chong, "A comprehensive standardized model for ultrawideband propagation channels," *IEEE Transactions on Antennas and Propagation*, vol. 54, no. 11, pp. 3151–3166, 2006.

[16] J. Romme and B. Kull, "On the relation between bandwidth and robustness of indoor UWB communication," in *Proceedings of the IEEE Conference on Ultra Wideband Systems and Technologies*, pp. 255–259, November 2003.

[17] N. A. Alsindi, K. Pahlavan, and B. Alavi, "An error propagation aware algorithm for precise cooperative indoor localization," in *Proceedings of the Military Communications Conference (MILCOM '06)*, pp. 1–7, Washington, DC, USA, October 2006.

[18] T. S. Rappaport, *Wireless Communications: Principles and Practice*, Prentice Hall, Upper Saddle River, NJ, USA, 2nd edition, 2002.

[19] A. Papoulis and S. U. Pillai, *Probability, Random Variables and Stochastic Processes*, McGraw-Hill, New York, NY, USA, 4th edition, 2001.

[20] P. Krishna and D. Husak, "RFID infrastructure," *IEEE Communications Magazine*, vol. 45, no. 9, pp. 4–10, 2007.

[21] S. N. Diggavi, N. Al-Dhahir, A. Stamoulis, and A. R. Calderbank, "Great expectations: the value of spatial diversity in wireless networks," *Proceedings of the IEEE*, vol. 92, no. 2, pp. 219–270, 2004.

[22] A. Nosratinia, T. E. Hunter, and A. Hedayat, "Cooperative communication in wireless networks," *IEEE Communications Magazine*, vol. 42, no. 10, pp. 74–80, 2004.

[23] S. A. Zekavat and C. R. Nassar, "Transmit diversity via oscillating-beam-pattern adaptive antennas: an evaluation using geometric-based stochastic circular-scenario channel modeling," *IEEE Transactions on Wireless Communications*, vol. 3, no. 4, pp. 1134–1141, 2004.

[24] S. A. Zekavat, C. R. Nassar, and S. Shattil, "Smart antenna spatial sweeping for combined directionality and transmit diversity," *Journal of Communications and Networks*, vol. 2, no. 4, pp. 325–330, 2000.

[25] J. G. Proakis, *Digital Communications*, Mcgraw Hill Series in Electrical and Computer Engineering, McGraw-Hill, New York, NY, USA, 4th edition, 2001.

Hindawi Publishing Corporation
International Journal of Navigation and Observation
Volume 2010, Article ID 105723, 12 pages
doi:10.1155/2010/105723

*Research Article*

# Underlay Cognitive Radio with Full or Partial Channel Quality Information

**Na Yi, Yi Ma, and Rahim Tafazolli**

*C.C.S.R., University of Surrey, Guildford GU2 7XH, UK*

Correspondence should be addressed to Yi Ma, y.ma@surrey.ac.uk

Received 11 November 2009; Accepted 1 June 2010

Academic Editor: Ronald Raulefs



Underlay cognitive radios (UCRs) allow a secondary user to enter a primary user's spectrum through intelligent utilization of multiuser channel quality information (CQI) and sharing of codebook. The aim of this work is to study two-user Gaussian UCR systems by assuming the full or partial knowledge of multiuser CQI. Key contribution of this work is motivated by the fact that the full knowledge of multiuser CQI is not always available. We first establish a location-aided UCR model where the secondary user is assumed to have partial CQI about the secondary-transmitter to primary-receiver link as well as full CQI about the other links. Then, new UCR approaches are proposed and carefully analyzed in terms of the secondary user's achievable rate, denoted by $C_2$, the capacity penalty to primary user, denoted by $\Delta C_1$, and capacity outage probability. Numerical examples are provided to visually compare the performance of UCRs with full knowledge of multiuser CQI and the proposed approaches with partial knowledge of multiuser CQI.

## 1. Introduction

Cognitive radios convey a dynamic and flexible spectrum allocation policy that allows a secondary user to access a primary user's spectrum through exploitation of advanced air-interface techniques and intelligent utilization of multiuser side information such as user activity, channel quality information (CQI), message, codebook, and location information, and so forth. A good tutorial about cognitive radios can be found in [1], focused on the signal-processing perspective, and in [2], focused on the information-theoretic perspective. One group of cognitive radios is known as the interweave paradigm, where a secondary user can opportunistically enter temporary spectrum holes and white spaces existing in both licensed or unlicensed radio spectrum [3]. Fast and reliable spectrum sensing techniques are the key to the success of interweave cognitive radios. The other group of cognitive radios includes overlay and underlay paradigms, where the secondary user and the primary user form a cognitive interference channel (e.g., [4–6]). Specifically, the overlay cognitive user is able to sense the primary user's message, and then employs advanced coding schemes such as the Gel'fand-Pinsker code [7] or the dirty-paper code [8] for interference precancellation. In the underlay paradigm, the secondary user enters the primary spectrum only when its activity will not cause considerable interference or capacity penalty to the primary user. Measure of interference requires knowledge about multiuser CQI. The focus of this paper is on the two-user Gaussian underlay cognitive radios (UCR).

Figure 1 illustrates an example of two-user UCR system accommodating one primary transmitter (Tx1) and receiver (Rx1) pair in System number 1 and one secondary transmitter (Tx2) and receiver (Rx2) pair in System number 2. The block diagram of this UCR system is depicted in Figure 2(a). In the flat-Gaussian scenario, this UCR system can be described as the following linear model (this is a well-recognized model in the literature [8–12] where both users are assumed to employ simple random codes. Although rate-splitting codes have been recently introduced to cognitive radio channels, the focus of this paper will be on this simple system model)

$$Y_1 = a_{11}X_1 + a_{21}X_2 + V_1, \tag{1}$$

$$Y_2 = a_{12}X_1 + a_{22}X_2 + V_2, \tag{2}$$

where $X_i$ stands for the signal sent by the transmitter Tx$i$ with power $P_i$ and rate $R_i$, $Y_j$ for the signal received at the receiver Rx$j$, $a_{ij}$ for the channel coefficient of the Tx$i$-Rx$j$ link, $V$ for the Gaussian noise with zero mean and variance $N_o$. This linear model shows that the UCR system is a special case of interference channels presented in [9, 10], but the interference term $(a_{21}X_2)$ in (1) must not cause considerable capacity penalty to the primary user. According to the multiuser decoding capability, we can divide the UCR system into the following four groups. Detailed introduction about these four modes can be found in Sections 3–6, respectively.

(1) *Individual Decoding.* Both the primary user and the secondary user always deal with the mutual interference as noise in their decoding process.

(2) *Secondary-User Side Multiuser Decoding (SSMD).* The secondary user optimally deals with the interference term $(a_{12}X_1)$ in its decoding process. But, the primary user always deals with the interference term $(a_{21}X_2)$ as noise.

(3) *Primary-User Side Multiuser Decoding (PSMD).* The primary user optimally deals with the interference term $(a_{21}X_2)$ in its decoding process. But, the secondary user always deals with the interference term $(a_{12}X_1)$ as noise.

(4) *Two Sides Multiuser Decoding (TSMD).* Both the primary user and the secondary user perform an optimal treatment about the corresponding interference term in their decoding process.

Key physical layer issues this work seeks to address are mainly in two folds:

*Issue 1.* Provided full knowledge about multiuser CQI, what is the fundamental relationship between the secondary user's achievable rate, denoted by $C_2$, and capacity penalty to the primary user, denoted by $\Delta C_1$? What are criteria for Tx2 to perform efficient power allocation? Those questions require an answer for various UCR modes.

*Issue 2.* In many practical environments, having full knowledge of CQI about all links of the UCR system is not a suitable assumption. What are more suitable assumptions in practice? What is the efficient UCR strategy under new assumptions? What is the secondary user's achievable rate? Those questions require a satisfactory answer.

The primary objective of this work is to partially answer the above questions through a study from the information-theoretic viewpoint. In order to focus on the major technical issues, the following assumptions are made throughout this paper.

(A1) We consider a two-user UCR system accommodating one primary transmitter-receiver pair and one secondary transmitter-receiver pair. This assumption can be easily assured by introducing orthogonal multiple-access schemes such as TDMA or FDMA to multiuser systems.

(A2) Users in the system are synchronized in both the time and frequency. Although the time-frequency synchronization is a challenge in practice, we would argue that the achievable rate produced under this assumption can be regarded as an upper bound of the practical performance.

(A3) Both receivers employ maximum-likelihood (ML) detector/decoder to offer the optimum decoding performance.

Contribution towards this work includes the following

(1) The first work is to answer those questions listed in *Issue 1*. Provided full knowledge of multiuser CQI, the fundamental relationship between $C_2$ and $\Delta C_1$ is investigated for four UCR groups. Criteria for efficient power allocation at Tx2 are established. The produced results are the key to new UCR strategies proposed for the case with partial knowledge of the multiuser CQI.

(2) As a starting point of the work towards *Issue 2*, we study modeling of UCR systems in the absence of full knowledge of multiuser CQI. After a careful justification, we establish an UCR system model, where the secondary user is assumed to have partial knowledge of CQI about the Tx2-Rx1 link, and have full knowledge of CQI about the other links. Location-aided UCR is employed as an example to support our justification.

(3) We propose new spectrum-access approaches for various UCR groups by assuming the availability of p.d.f. of CQI about the Tx2-Rx1 link. Power allocation criteria are carefully investigated in terms of $C_2$, $\Delta C_1$, and capacity outage probability. (In practice, the performance of power allocation will be influenced by air-interfaces and synchronization errors. The results presented in this paper are to provide an information-theoretic guidance to practical designs.) Assuming the channel to be Rayleigh, numerical results are provided to visually show the performance of UCRs with full knowledge of multiuser CQI and the proposed approaches with partial knowledge of multiuser CQI.

The rest of this paper is organized as follows. Section 2 offers a brief review about capacity theorem of Gaussian interference channel (GIC) and relates it to the UCR system. Moreover, modeling about the UCR system with partial knowledge of multiuser CQI is also presented. Technical contributions towards four UCR groups are presented in Sections 3–6, respectively. Section 7 draws the conclusion.

## 2. System Model and Preparation

This section first presents capacity theorem about two-user GIC and its relationship with the UCR system, and then

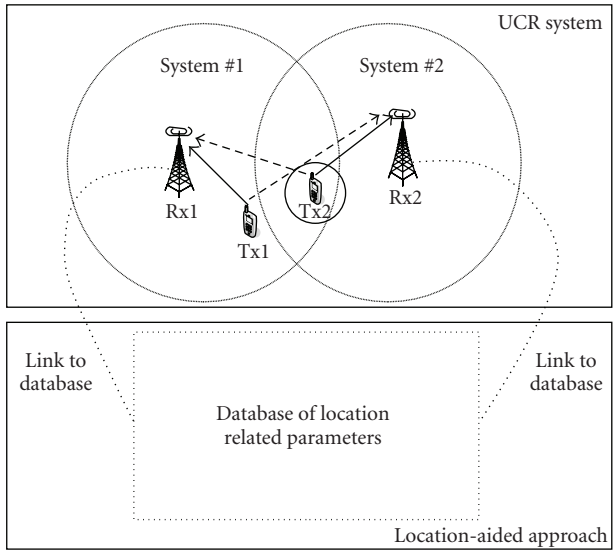


Figure 1: Illustration of an example about the two-user UCR system and a location-aided approach.

presents modeling of the UCR system with partial knowledge of the multiuser CQI.

*2.1. Two-User UCR with Full Multiuser CQI.* The UCR system is a special case of interference channels. The information-theoretic research towards interference channels started from Carleial's work published in [9]. Although lots of research efforts have been paid in the last 30 years, capacity region of interference channels has been found only for the case of strong interference [13]. To the best of our knowledge, the state-of-the-art capacity bound of two-user GIC has recently been reported in [11, 12]. Next, we provide a brief review about capacity theorem of two-user GIC, which offers the theoretical support to our further investigation about the two-user UCR system.

*2.1.1. Two-User GIC with Strong Interference.* In the linear model (1)–(2), the case of strong interference denotes the scenario $|a_{12}| \geq |a_{11}|$ and $|a_{21}| \geq |a_{22}|$ [10]. In this case, the two-user GIC is in fact a compound Gaussian multiple-access channel (MAC), whose capacity region is known as the following union [14]:

$$\bigcup \begin{pmatrix} R_1 < \mathcal{C}[\gamma_{11}], R_2 < \mathcal{C}[\gamma_{22}] \\ R_1 + R_2 < min(\mathcal{C}[\gamma_{21} + \gamma_{11}], \mathcal{C}[\gamma_{12} + \gamma_{22}]) \end{pmatrix}, \quad (3)$$

where $\gamma_{ij} \triangleq (P_i|a_{ij}|^2)/(N_o)$ denotes the instantaneous signal-to-noise ratio (SNR) and $\mathcal{C}[x] \triangleq \log_2(1+x)$. Provided (3) and the assumption that users share their codebook, each receiver can reliably recover the message sent by Tx1 and Tx2, respectively.

*2.1.2. Two-User GIC with Weak or Mixed Interference.* This scenario includes cases other than the case of strong interference. The closed form of capacity region is unknown to this date. A lookup table (but incomplete) about the channel capacity with respect to various channel conditions has been reported in [12]. Alternatively, we can divide the two-user GIC into the following three groups with respect to the way of dealing with the interference. The following result is adequate for us to investigate the two-user Gaussian UCR system.

*Group I.* Each receiver can reliably decode the message sent by Tx1 and Tx2, respectively. The achievable rate region, denoted by $\mathcal{R}^{\mathbf{I}}$, is (3).

*Group II.* Each receiver can only decode the message sent by its corresponding transmitter. The interference will be regarded as noise. The achievablerate region, denoted by $\mathcal{R}^{\mathbf{II}}$, is (see [9])

$$\mathcal{R}^{\mathbf{II}} = \bigcup \begin{pmatrix} R_1 < \mathcal{C}\left[\dfrac{\gamma_{11}}{\gamma_{21}+1}\right] \\ R_2 < \mathcal{C}\left[\dfrac{\gamma_{22}}{\gamma_{12}+1}\right] \end{pmatrix}. \quad (4)$$

*Group III.* One receiver can decode the message sent by both transmitters, and the other can only decode the message sent by its corresponding transmitter. In this group, the achievable rate region, denoted by $\mathcal{R}^{\mathbf{III}}$, is (see [12])

$$\mathcal{R}^{\mathbf{III}} = \bigcup \begin{pmatrix} R_j < \mathcal{C}\left[\dfrac{\gamma_{jj}}{\gamma_{ij}+1}\right] \\ R_i < \mathcal{C}\left[\gamma_{ii} + \gamma_{ji}\right] - R_j \\ R_i < \mathcal{C}[\gamma_{ii}] \end{pmatrix}, \quad i \neq j. \quad (5)$$

Provided $\gamma_{ij}$, $_{i,j=1,2}$, we can obtain the maximum sum-rate, $\max(R_1 + R_2)$, through a comparison between $\mathcal{R}^{\mathbf{I}}$, $\mathcal{R}^{\mathbf{II}}$, and $\mathcal{R}^{\mathbf{III}}$.

*2.1.3. Two-User Gaussian UCR.* The UCR system is modeled as an interference channel where the primary user wants to keep its interference-free capacity. But in many cases, the secondary user will cause capacity penalty $\Delta C_1$ to the primary user. Hence, the primary user's capacity is expressible as [5]

$$C_1 = \mathcal{C}[\gamma_{11}] - \Delta C_1 \quad (6)$$

and the secondary user's achievable rate is (see [12])

$$C_2 = \max(R_1 + R_2) - C_1. \quad (7)$$

Define

$$\Delta C_1 \triangleq \rho \mathcal{C}[\gamma_{11}], \quad (8)$$

where $\rho$ is a positive coefficient. Equation (6) is expressible as

$$C_1 = (1-\rho)\mathcal{C}[\gamma_{11}]. \quad (9)$$

In order to keep the capacity penalty to be reasonably small, we usually let $\rho \ll 1$.

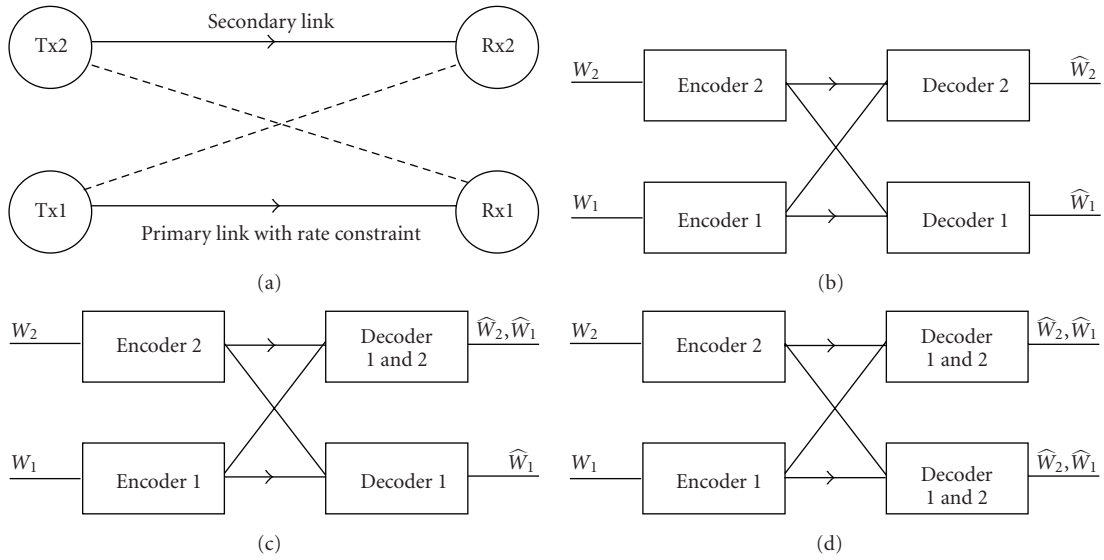


Figure 2: Block diagram of various UCR modes: (a) two-user UCR channel, (b) the individual mode, (c) the CSMD mode, and (d) the TSMD mode.

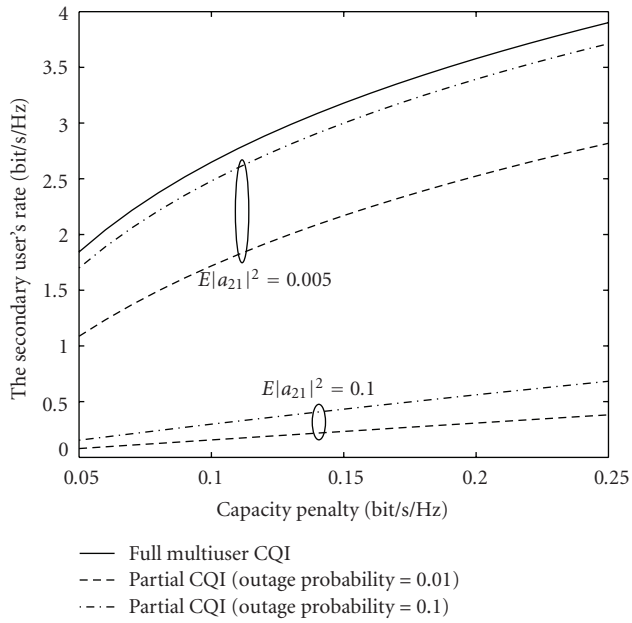


Figure 3: An example of capacity results for the individual decoding mode. The secondary user's achievable rate versus capacity penalty to the primary user.

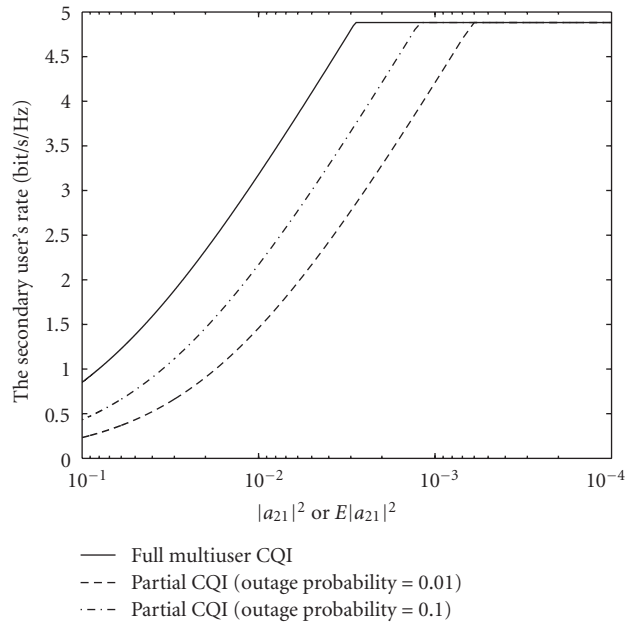


Figure 4: An example of capacity results for the individual decoding mode. The secondary user's achievable rate versus the channel quality of Tx2-Rx1 link.

*2.2. Two-User UCR with Partial Multiuser CQI.* In practice, the primary transmitter-receiver pair may operate in the frequency-division duplex (FDD) manner, where the transmitter Tx1 periodically sends training sequences to support channel estimation and coherent detection/decode at the receiver Rx1. Rx1 informs Tx1 regarding the CQI of Tx1-Rx1 link through a feedback channel. On the secondary-user side, we assume that Rx2 can communicate with Tx2 through a feedback channel. This feedback channel is orthogonal to the primary user's frequency band and mainly for the purpose of signaling. Based on the above system description, we provide the following justification of assumptions about the knowledge of CQI:

(i) The secondary receiver Rx2 listens to the conversation between Tx1 and Rx1. Then, Rx2 can estimate the CQI of Tx1-Rx2 link.

(ii) We assume that Rx1 employs a simple common codebook such as repetition code to perform the

feedback of CQI. Then, Rx2 can obtain the CQI about Tx1-Rx1 link through sensing of the primary user's feedback channel.

(iii) At the beginning of cognitive communication, Rx2 requests Tx2 to send a training sequence over the primary spectrum. This offers the knowledge of CQI about the Tx2-Rx2 link, but introduces a short burst of interference to the primary user. We argue that this burst of interference will not cause considerable performance loss to the primary user.

(iv) Rx1 may estimate the CQI of Tx2-Rx1 link if appropriate, but does not show this information in its feedback channel due to an upper-layer protocol. In this case, Rx2 cannot know the CQI of Tx2-Rx1 link. Then, our assumption is that the secondary user knows the p.d.f. of CQI about the Tx2-Rx1 link. This assumption is suitable for a scenario such as where the secondary user has the location information about itself and the primary user. The secondary user can access a well-designed and maintained database, which records the p.d.f. of CQI between two locations. Figure 1 illustrates an example of location-aided UCR system, where Rx1 and Rx2 are fixed network nodes such as base-stations or access points, and Tx1 and Tx2 are mobile stations. The database has a lookup table about the p.d.f. of CQI between each fixed network node and a certain area such as the black circle with solid line. Provided the location of Tx2, Rx2 knows which circle Tx2 is currently in, and thus can look up the database to find out the p.d.f. of CQI about the Tx2-Rx1 link. Recently, how to design and maintain the location-related database is becoming an important research topic. However, it is out of the scope of this paper. Further information about location estimation and location-related database can be found in European ICT WHERE [15].

As a summary, when we investigate the UCR strategy with partial multiuser CQI, the following assumptions are made in addition to (A1)–(A3):

(A4) Rx2 has full knowledge of CQI about the Tx1-Rx1 link, the Tx1-Rx2 link, and the Tx2-Rx2 link, but only knows p.d.f. of CQI about the Tx2-Rx1 link, denoted by $p(|a_{21}|^2)$ as well as the mean $E(|a_{21}|^2)$.

(A5) Rx2 determines the secondary user's power and transmission rate, and then informs Tx2 through the feedback channel.

## 3. The Individual Decoding Mode

Figure 2(b) depicts the individual decoding mode where each receiver only wants to decode the message sent by its corresponding transmitter, and deals with the corresponding interference as noise. This mode is suitable for the following cognitive radio scenarios:

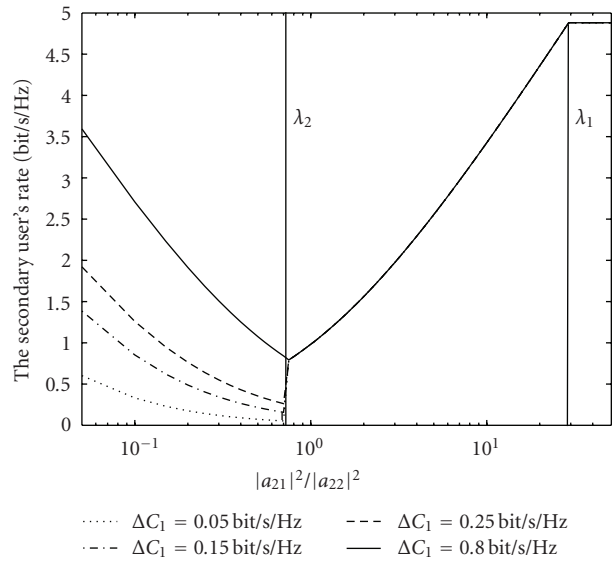


Figure 5: An example of capacity results for the PSMD mode with full multiuser CQI.

(i) Both the primary user and secondary user employ their private codebook;

(ii) Even if both users employ a common codebook, each receiver cannot decode the other user's message due to reasons such as channel conditions and upper layer protocols.

In this situation, the UCR system can be regarded as a simple collection of individual links. This mode has recently received an intensive investigation in both the basic and system-level research, for example, in [16, 17].

*3.1. Capacity Results with Full Knowledge of CQI.* This simple mode is already mature in terms of capacity results. The channel capacity for both users is given by (4). The capacity penalty $\Delta C_1$ is calculated as

$$\Delta C_1 = \mathcal{C}[\gamma_{11}] - \mathcal{C}\left[\frac{\gamma_{11}}{\gamma_{21}+1}\right]. \tag{10}$$

Equations (4) and (10) show a known result that increasing the secondary user's power $P_2$ will increase both $C_2$ and $\Delta C_1$. Applying (8) into (10), we can relate $P_2$ to the capacity-penalty coefficient $\rho$ as

$$P_2 = \frac{1}{|a_{21}|^2}\left(\frac{\gamma_{11}}{(1+\gamma_{11})^{(1-\rho)}-1}-1\right). \tag{11}$$

Given a coefficient $\rho$, the secondary user's power should be no larger than (11). Otherwise, the primary user would suffer capacity outage.

*Remark 1.* A remarkable issue is that $\Delta C_1$ in (10) is a monotonically decreasing function of $\gamma_{11}$ due to the partial derivative $(\partial \Delta C_1)/(\partial \gamma_{11}) < 0$. This means that the primary user operating at a high-SNR scenario is less sensitive to the

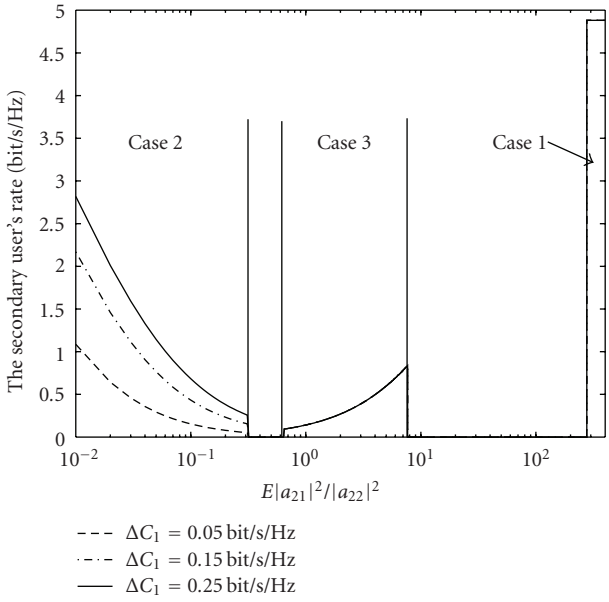


Figure 6: An example of capacity results for the PSMD mode with partial multiuser CQI.

interference. Considering a high-SNR scenario that fulfills the conditions (C1) $\gamma_{11} \gg 1$, and (C2) $\gamma_{11} \gg \gamma_{21}$, (10) approximates to

$$\Delta C_1 \approx \mathcal{C}[\gamma_{21}]. \tag{12}$$

Plugging (8) into (12) leads to

$$P_2 \approx \frac{N_o}{|a_{21}|^2}\left((1+\gamma_{11})^{\rho}-1\right). \tag{13}$$

This simplified result can be utilized to allocate the secondary user's power when the primary user operates in the high-SNR range.

*3.2. The UCR Strategy with Partial Multiuser CQI.* Section 3.1 shows that, provided the power $P_2$, the secondary user can employ (4) to configure its transmission rate. However, using (11) or (13) to configure $P_2$ requires the knowledge about $|a_{21}|^2$, which is supposed to be unknown in some situations. Next, we propose a new power-allocation criterion based on the assumption (A4).

*Criterion 1.* The power $P_2$ should be appropriately configured so that the capacity-outage probability of primary user is not larger than a given threshold $\mathcal{O}_t$.

Based on Criterion 1, the power-allocation strategy can be summarized into the following two steps.

*Step 1.* Outage probability to the primary user is a function of the SNR mean of Tx2-Rx1 link denoted by $\overline{\gamma}_{21} = (P_2 E(|a_{21}|^2))/(N_o)$. Motivated by this fact, the secondary user can first calculate the outage probability for a given $p(|a_{21}|^2)$, and then determine a threshold $\overline{\gamma}_t$ corresponding to $\mathcal{O}_t$.

*Step 2.* The secondary user can access the primary spectrum for the condition $\overline{\gamma}_{21} \le \overline{\gamma}_t$. The maximum of $P_2$ is therefore given by

$$\max(P_2) = \frac{\overline{\gamma}_t N_o}{E\left(|a_{21}|^2\right)}. \tag{14}$$

The secondary user's transmission rate can be calculated by applying (14) into (4). Next, we will use a numerical example to introduce about how to determine the threshold $\overline{\gamma}_t$, and to show the performance in this example.

*3.3. Numerical Example.* Define an instantaneous SNR threshold $\gamma_t$ as

$$\gamma_t \triangleq \frac{\gamma_{11}}{(1+\gamma_{11})^{(1-\rho)}-1} - 1. \tag{15}$$

Equation (11) indicates that the secondary user will cause capacity outage to the primary user when $\gamma_{21} > \gamma_t$. Assume the p.d.f. $p(|a_{21}|)$ to be Rayleigh as an example. The probability for the event $(\gamma_{21} > \gamma_t)$ to happen can be calculated as [18]

$$\Pr(\gamma_{21} > \gamma_t) = \exp\left(-\frac{\gamma_t}{\overline{\gamma}_{21}}\right) \le \exp\left(-\frac{\gamma_t}{\overline{\gamma}_t}\right), \tag{16}$$

where $\Pr(\cdot)$ denotes the probability. According to Criterion 1, the threshold $\overline{\gamma}_t$ should be carefully chosen to fulfill the following condition:

$$\exp\left(-\frac{\gamma_t}{\overline{\gamma}_t}\right) \le \mathcal{O}_t. \tag{17}$$

We apply the definition of $\gamma_t$ (15) in (17) and obtain

$$\overline{\gamma}_t = \frac{(1+\gamma_{11})^{(1-\rho)}-1-\gamma_{11}}{\left((1+\gamma_{11})^{(1-\rho)}-1\right)\ln(\mathcal{O}_t)}. \tag{18}$$

Moreover, when the primary user fulfills the high-SNR condition (C1)-(C2), we can use (13) to define

$$\gamma_t \triangleq (1+\gamma_{11})^{\rho} - 1. \tag{19}$$

Applying (19) into (17) results in

$$\overline{\gamma}_t = \frac{1-(1+\gamma_{11})^{\rho}}{\ln(\mathcal{O}_t)}. \tag{20}$$

Based on the above analytical results, we use a visual example to exhibit the performance. In this example, the UCR system is configured as $|a_{11}| = 1$, $|a_{22}| = 1$, $|a_{12}| = 0.1$. The primary user's power-to-noise ratio is $P_1/N_o = 16$ dB. The secondary user's power-to-noise ratio is also limited by 16 dB. This ratio is one of typical configurations for high-data-rate systems. For the scenario with full multiuser CQI, we set $|a_{21}| = 0.1$. Figure 3 illustrates the secondary user's achievable rate (see (4)) against the capacity penalty $\Delta C_1$ (see (10)) for cases with full or partial multiuser CQI. It is observed that the secondary user's achievable rate generally

increases with the pay of capacity penalty to the primary user. Moreover, in the scenario with partial multiuser CQI, the secondary user shows increased achievable rate for the case of larger outage probability, for example, $\mathcal{O}_t = 0.1$ or smaller $E(|a_{21}|^2)$, for example, $E(|a_{21}|^2 = 0.005)$. Figure 4 illustrates the secondary user's achievable rate with respect to the channel quality of Tx2-Rx1 link ($\Delta C_1 = 0.15$ bit/sec/Hz). It shows that the UCR approach with partial CQI offers the same performance as the UCR with full CQI when the Tx2-Rx1 channel is deep faded.

## 4. The SSMD Mode

Figure 2(c) depicts the SSMD mode where each receiver wants to decode the message sent by its corresponding transmitter. The secondary receiver Rx2 will decode the primary user's message if appropriate. The primary receiver Rx1 always deals with the interference term ($a_{21}X_2$) as noise. This mode is suitable for the following cognitive radio scenario:

(i) The secondary user knows the primary user's codebook, and thus has a chance to decode the primary user's message. This is possible if the primary user is either using a common codebook or broadcasting its own codebook to support, for example, user cooperation. On the other hand, the primary user may be not aware of the existence of secondary user, or does not know the secondary user's private codebook.

In this situation, the receiver Rx2 can reliably decode the primary user's message only for the channel condition $|a_{12}| \geq |a_{11}|$, otherwise the SSMD mode reduces to the individual decoding mode presented in Section 3. (Multiuser information theory about the interference channel shows that Rx2 can decode the signal $X_1$ if the rate of $X_1$ is not larger than the achievable rate of Tx1-Rx2 link. However, the UCR channel requires the rate of $X_1$ to be constrained only by the achievable rate of Tx1-Rx1 link. In the case of weak interference, the Tx1-Rx1 link offers larger achievable rate than the Tx1-Rx2 link. Rx2 cannot decode $X_1$ if the rate of $X_1$ is larger than the achievable rate of Tx1-Rx2 link.) Therefore, the focus of SSMD mode is on the case $|a_{12}| \geq |a_{11}|$.

*4.1. Capacity Results with Full Multiuser CQI.* Suppose the channel condition $|a_{12}| \geq |a_{11}|$. The transmission rate for both users is given in (5) by setting $i = 2$ and $j = 1$. More precisely, the capacity penalty $\Delta C_1$ is (10), and the secondary user's achievable rate is expressible as

$$C_2 = \min(\mathcal{C}[\gamma_{12} + \gamma_{22}] - (1-\rho)\mathcal{C}[\gamma_{11}], \mathcal{C}[\gamma_{22}]). \quad (21)$$

This result is subject to the power constraint of $P_2$ given in (11).

*Remark 2.* For the high-SNR conditions (C1), (C2) and the case $|a_{12}| \geq |a_{11}|$, we can apply (10) and (12) into (21) to obtain

$$\begin{aligned} C_2 &= \min(\mathcal{C}[\gamma_{12} + \gamma_{22}] - \mathcal{C}[\gamma_{11}] + \Delta C_1, \mathcal{C}[\gamma_{22}]) \\ &\approx \min\left(\log_2\left(\frac{\gamma_{12} + \gamma_{22}}{\gamma_{11}}\right) + \mathcal{C}[\gamma_{21}], \mathcal{C}[\gamma_{22}]\right) \end{aligned} \quad (22)$$

and the transmit power $P_2$ is limited by (13). Next, we will use the above capacity results to investigate the UCR strategy with partial multiuser CQI.

*4.2. The UCR Strategy with Partial Multiuser CQI.* Major difference between the SSMD mode and the individual decoding mode is that the secondary user has improved achievable rate due to the availability of primary user's codebook. However, on the primary user's side, there is no difference between these two modes. The spectrum access and power allocation strategy for the SSMD mode should also obey Criterion 1 so as to fulfill the requirement of outage probability. Therefore, the UCR strategy for SSMD mode is the same as that for the individual mode, and the transmit-power $P_2$ is limited by (14). The secondary user's transmission rate is restricted by the result produced by applying (14) in (21).

Apart from (21), numerical results for the SSMD mode is the same as those for the individual decoding mode. Moreover, (21) is also a well-known result in the domain of multiuser information theory. Therefore, we do not provide a numerical example for this mode.

## 5. The PSMD Mode

This mode is referred to as a scenario where the secondary user does not know the primary user's codebook, but share its own codebook through upper-layer protocols. In this case, the primary user has a chance to decode the secondary user's message, and thus has the potential to cancel the interference caused by the secondary user. On the other hand, the secondary user has to deal with the interference term ($a_{12}X_1$) as noise.

*5.1. Capacity Results with Full Multiuser CQI.* In order to ensure reliable communication of the Tx2-Rx2 pair, the secondary user's transmission rate is restricted by the second formula in (4). On the other hand, Section 2.1 Group III shows that the primary user can reliably decode the secondary user's message only when

$$R_2 \leq \mathcal{C}[\gamma_{21} + \gamma_{11}] - C_1, \quad (23)$$

where $C_1$ is given by (9). Moreover, the primary user's capacity should fulfill the following condition:

$$C_1 \geq \mathcal{C}\left[\frac{\gamma_{11}}{\gamma_{21} + 1}\right], \quad (24)$$

where the interference term ($a_{21}X_2$) in (1) is treated as noise.

**Theorem 1.** *Suppose* $|a_{21}| \neq 0$ *and* $\rho = 0$*, the secondary user's achievable rate is*

$$R_2 \leq \mathcal{C}\left[\frac{\gamma_{22}}{\gamma_{12}+1}\right], \tag{25}$$

*for the channel condition*

$$\frac{|a_{21}|^2}{|a_{22}|^2} > \frac{\gamma_{11}+1}{\gamma_{12}+1} \triangleq \lambda_1, \tag{26}$$

*otherwise*

$$R_2 \leq \mathcal{C}[\gamma_{21}+\gamma_{11}] - \mathcal{C}[\gamma_{11}]. \tag{27}$$

*Proof.* For the case of $\rho = 0$, the results (4) and (23) show that the secondary user's transmission rate should fulfill

$$R_2 \leq \min\left(\mathcal{C}\left[\frac{\gamma_{22}}{\gamma_{12}+1}\right], \mathcal{C}[\gamma_{21}+\gamma_{11}] - \mathcal{C}[\gamma_{11}]\right), \tag{28}$$

otherwise, either the primary user or the secondary user cannot perform reliable communication. Then, it is straightforward to justify that the right-hand term in (25) is smaller than the right-hand term in (27) only for the channel condition (26) to be satisfied. This theorem is therefore proved. □

Theorem 1 gives the secondary user's achievable rate subject to zero capacity-penalty to the primary user. It can be observed that $R_2$ would be almost zero if the channel gain $|a_{21}|$ is deep fade. This result is inconsistent with the original idea of UCR which takes advantage of the case $|a_{21}| \approx 0$. In other words, it is not wise to always target on zero capacity-penalty to the primary user. Below provides two criteria to handle the issue of capacity penalty.

*Criterion 2.* The pay of capacity penalty offers improvement of the sum rate of UCR, that is, $\max(R_1 + R_2)$.

*Criterion 3.* The capacity penalty is tolerable to the primary user, for example, $\rho \ll 1$.

**Theorem 2.** *Suppose the following channel condition:*

$$\frac{|a_{21}|^2}{|a_{22}|^2} < \frac{1}{\gamma_{12}+1} \triangleq \lambda_2; \tag{29}$$

*the secondary user's achievable rate is* (25) *subject to the power constraint* (11).

*Proof.* The result (23) indicates that the pay of capacity penalty will not improve $\max(R_1 + R_2)$ if the primary user wants to reliably decode the secondary user's message. Hence, the only case to have an improved $\max(R_1 + R_2)$ is to deal with the interference term $(a_{21}X_2)$ as noise, for which $R_2$ is only limited by (25). Moreover, the following inequality has to be satisfied so as to fulfill Criterion 2:

$$\mathcal{C}\left[\frac{\gamma_{11}}{\gamma_{21}+1}\right] + \mathcal{C}\left[\frac{\gamma_{22}}{\gamma_{12}+1}\right] > C[\gamma_{11}+\gamma_{21}]. \tag{30}$$

Solving (30) leads to the channel condition (29). In order to fulfill Criterion 3, the transmit power $P_2$ should be limited by (11). This theorem is therefore proved. □

According to Theorems 1 and 2, we can conclude the following results:

(1) For the channel condition (26), Tx2 can talk to Rx2 at a rate (25) without causing capacity penalty to the primary user. The transmit power $P_2$ is limited by the secondary user's local power constraint.

(2) For the channel condition (29), Tx2 can talk to Rx2 at a rate (25). The transmit power $P_2$ is limited by (11) to keep the capacity penalty $\Delta C_1$ under an acceptable level.

(3) For channel conditions other than (26) and (29), Tx2 can talk to Rx2 at a rate (27) without causing capacity penalty to the primary user. The transmit power $P_2$ is limited by the secondary user's local power constraint.

*5.2. The UCR Strategy with Partial Multiuser CQI.* Section 5.1 shows that the spectrum access and power-allocation strategy for the PSMD mode requires the full knowledge of $|a_{21}|$. Here, we present a new UCR strategy under the assumption (A4). The main idea is summarized as follows.

Define a threshold of probability denoted by $\epsilon$. Based on Theorems 1 and 2, the secondary user will access the primary spectrum for the following three cases.

*Case 1.* Suppose

$$\Pr\left(\frac{|a_{21}|^2}{|a_{22}|^2} > \lambda_1\right) > \epsilon, \tag{31}$$

the secondary user will enter the primary spectrum at a rate (25) with $P_2$ limited by its local power constraint. In this case, the primary user does not have a capacity penalty, but suffers capacity outage with the probability $(1 - \epsilon)$.

*Case 2.* Suppose

$$\Pr\left(\frac{|a_{21}|^2}{|a_{22}|^2} < \lambda_2\right) > \epsilon, \tag{32}$$

the secondary user's transmission rate is also (25). In this case, the primary user deals with the interference as noise, and thus has the capacity penalty (10). Moreover, the secondary user's power $P_2$ should be carefully configured in terms of capacity penalty and outage probability to the primary user. This issue will receive further investigation by employing a numerical example.

*Case 3.* Suppose

$$\Pr\left(\lambda_2 \leq \frac{|a_{21}|^2}{|a_{22}|^2} \leq \lambda_1\right) > \epsilon. \tag{33}$$

Theorem 1 shows that the secondary user can talk at a rate (27). Unfortunately, the secondary user does not know $|a_{21}|$, and thus cannot straightforwardly employ (27) to determine its achievable rate. In this case, we propose to use the

following formula produced by replacing the term $\gamma_{21}$ with $(P_2\mathcal{L})/(N_o)$ in (27)

$$R_2 \le \mathcal{C}\left[\frac{P_2\mathcal{L}}{N_o} + \gamma_{11}\right] - \mathcal{C}[\gamma_{11}], \tag{34}$$

where $\mathcal{L} \in (|a_{22}|^2\lambda_2, |a_{22}|^2\lambda_1)$ is a scaling factor. This case will be further investigated through a numerical example.

Finally, for cases other than (31)–(33), the secondary user will not enter the primary spectrum.

*5.3. Numerical Example.* Equations (31)–(33) show that the proposed UCR strategy is based on the statistical relationship between $|a_{21}|$ and $|a_{22}|$. Considering $|a_{21}|$ to be Rayleigh as a numerical example, we investigate the performance of the proposed approach.

*Case 1.* The key issue of this case is to find out the relationship between $E(|a_{21}|^2)$ and the threshold of outage probability $\mathcal{O}_t$, and then to link this relationship to the spectrum-access strategy. The following result is derived for this issue.

**Corollary 1.** *Given a threshold of the primary user's outage probability $\mathcal{O}_t$, the condition for* (31) *to be satisfied is*

$$E\left(|a_{21}|^2\right) > \frac{\lambda_1|a_{22}|^2}{\ln(1/(1-\mathcal{O}_t))}. \tag{35}$$

*Proof.* We first rewrite (31) into

$$\Pr(\gamma_{21} > \gamma_{22}\lambda_1) > \epsilon. \tag{36}$$

Using the result derived in [18], (36) becomes

$$\exp\left(-\frac{\gamma_{22}\lambda_1}{\overline{\gamma}_{21}}\right) > \epsilon. \tag{37}$$

Given a threshold of outage probability $\mathcal{O}_t$, the probability $\epsilon$ should fulfill $\epsilon \ge (1-\mathcal{O}_t)$. Applying this result in (37), we can easily obtain (35) by solving the inequality. □

*Case 2.* The key issue of this case is to find out the relationship between $\overline{\gamma}_{21}$ and the primary user's capacity penalty and outage probability. The derived result is summarized as below, which offers a criterion to configure the power $P_2$.

**Corollary 2.** *Given a probability $\epsilon$ and a threshold of outage probability $\mathcal{O}_t$, the condition for the secondary user to operate in Case 2 is*

$$\overline{\gamma}_{21} \le \min\left(\frac{\lambda_2\gamma_{22}}{\ln(1/(1-\epsilon))}, \overline{\gamma}_t\right), \tag{38}$$

*where $\overline{\gamma}_t$ is given by* (18).

*Proof.* The first criterion for the secondary user to operate in Case 2 is (32). Following the derivation in [18], we can easily justify that (32) is equivalent to

$$\overline{\gamma}_{21} \le \frac{\lambda_2\gamma_{22}}{\ln(1/(1-\epsilon))}. \tag{39}$$

Moreover, provided the condition (32), the primary user will always deal with the interference as noise. The SNR-mean $\overline{\gamma}_{21}$ should fulfill the condition (14) to ensure the primary user's outage probability under the threshold $\mathcal{O}_t$. Then, $\overline{\gamma}_{21}$ should simultaneously fulfill the conditions (39) and (14), which leads to the result (38). □

Once $\overline{\gamma}_{21}$ is determined by employing (38), we can calculate maximum of the secondary user's power as $\max(P_2) = (38)/(E(|a_{21}|^2))$.

*Case 3.* This case includes three issues: (1) to find the relationship between $E(|a_{21}|^2)$ and $\epsilon$ by solving (33); (2) to determine the scaling factor $\mathcal{L}$ in (34); (3) provided the condition (33), Theorem 1 shows that the secondary user will suffer capacity outage for the case of $|a_{21}|^2 > \lambda_1|a_{22}|^2$. Then, we should calculate the outage probability to the secondary user. Note that, in Case 3, the primary user does not suffer capacity outage.

**Corollary 3.** *Given a probability $\epsilon$, a necessary condition for* (33) *to be satisfied is*

$$\gamma_{11} < \epsilon^{-\gamma_{11}} - 1. \tag{40}$$

*Proof.* See the appendix. □

Usually, the probability $\epsilon$ is expected to be sufficiently large, for example, $\epsilon > 90\%$. In this situation, we can use (40) to obtain $\gamma_{11} > 15$ dB. It means a necessary condition for Case 3 to happen is that the primary user operates in a high-SNR range. Provided the condition (40), the secondary user can employ (A.1) to relate $E(|a_{21}|^2)$ to $\epsilon$.

Using the scaling factor $\mathcal{L}$ in (34) will result in capacity outage to the secondary user with the outage probability

$$\Pr\left(\mathcal{L} \le |a_{21}|^2\right) = 1 - \exp\left(-(\mathcal{L})/\left(E\left(|a_{21}|^2\right)\right)\right). \tag{41}$$

If this outage probability is required to be no larger than a threshold $\mathcal{O}_1$, we can obtain

$$\mathcal{L} \le \ln\left(\frac{1}{1-\mathcal{O}_1}\right)E\left(|a_{21}|^2\right). \tag{42}$$

This is one criterion to determine $\mathcal{L}$. Moreover, $\mathcal{L}$ is also limited by the range given in (34). Applying that range in (42) results in

$$E\left(|a_{21}|^2\right) \ge \frac{|a_{22}|^2\lambda_2}{\ln(1/(1-\mathcal{O}_1))}. \tag{43}$$

Then, we can conclude the following result.

**Corollary 4.** *Given the threshold of outage probability $\mathcal{O}_1$, a necessary condition for Case 3 to happen is* (43).

Corollaries 3 and 4 provide an answer to the first two issues of Case 3. The last issue to concern is the probability $\Pr(|a_{21}|^2 > \lambda_1|a_{22}|^2)$ subject to the condition (33). The result is summarized as follows.

**Corollary 5.** *Provided the condition* (33)*, the probability for the event* $(|a_{21}|^2 > \lambda_1|a_{22}|^2)$ *to happen is smaller than* $(1)/(\gamma_{11}+1)$.

*Proof*. The probability for the event $(|a_{21}|^2 > \lambda_1|a_{22}|^2)$ to happen is given in (37), which can be represented into

$$\Pr\left(|a_{21}|^2 > \lambda_1|a_{22}|^2\right) = \exp\left(-\frac{|a_{22}|^2\lambda_1}{E\left(|a_{21}|^2\right)}\right). \quad (44)$$

Provided the condition (33), (A.2) gives the maximum of $E(|a_{21}|^2)$. Since (44) is an increasing function of $E(|a_{21}|^2)$, we can apply (A.2) into (44) and obtain

$$\Pr\left(|a_{21}|^2 > \lambda_1|a_{22}|^2\right) \le \exp\left(\frac{\ln(\lambda_2/\lambda_1)}{1-\lambda_2/\lambda_1}\right) \quad (45)$$

$$\le \exp\left(\frac{-\ln(\gamma_{11}+1)}{1-(1/\gamma_{11}+1)}\right). \quad (46)$$

The discussion about Corollary 3 shows that $\gamma_{11} \gg 1$ is the necessary condition for Case 3. Therefore, the right hand of (46) approximates to $(1)/(\gamma_{11}+1)$. □

According to Corollaries 3–5, we summarize Case 3 as follows.

*Step 1.* Utilize (40) and Corollary 5 to verify whether $\gamma_{11}$ fulfills the required condition. if true, go to Step 2.

*Step 2.* Utilize (43) and (A.2) to verify whether $E(|a_{21}|^2)$ is in the appropriate range; if true, go to Step 3;

*Step 3.* Utilize (42) to determine $\mathcal{L}$, and apply it in (34).

Next, we use a visual example to exhibit the performance. The system configuration is the same as the setup in Section 3.3. For the scenario with full multiuser CQI, Figure 5 shows the secondary user's achievable rate as a function of the ratio $|a_{21}|^2/|a_{22}|^2$. Calculation of the achievable rate follows the conclusion in Section 5.1. For the scenario with partial multiuser CQI, Figure 6 shows the secondary user's achievable rate as a function of the ratio $E(|a_{21}|^2)/|a_{22}|^2$. Calculation of the achievable rate follows the results presented in Corollaries 1–4 by setting the outage probability $\mathcal{O}_t = \mathcal{O}_1 = 10\%$ and the probability $\epsilon = 90\%$. It is observed that Case 1 will happen only for the condition $E(|a_{21}|^2)/|a_{22}|^2 > 300$, which often does not hold in practice. Case 3 requires the primary user to operate at a SNR larger than 15 dB (see Corollary 3). However, in this case, the secondary user cannot gain more than 1 bit/sec/Hz at $P_2/N_o = 16$ dB. Finally, Case 2 shows a comparable performance with the corresponding scenario $(|a_{21}|^2/|a_{22}|^2 < \lambda_2)$ in Figure 5.

## 6. The TSMD Mode

Figure 2(d) depicts the TSMD mode where each user knows the other's codebook. Then, each user has the chance to decode the other user's message so as to cancel the interference.

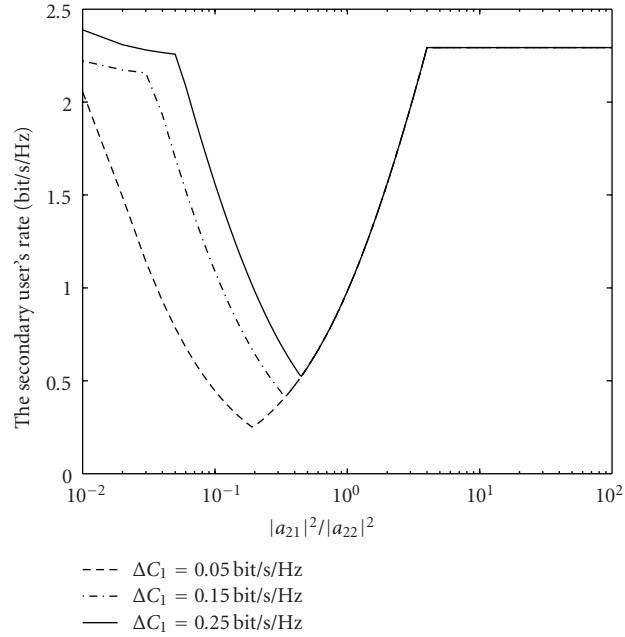


Figure 7: An example of capacity results for the TSMD mode with full multiuser CQI.

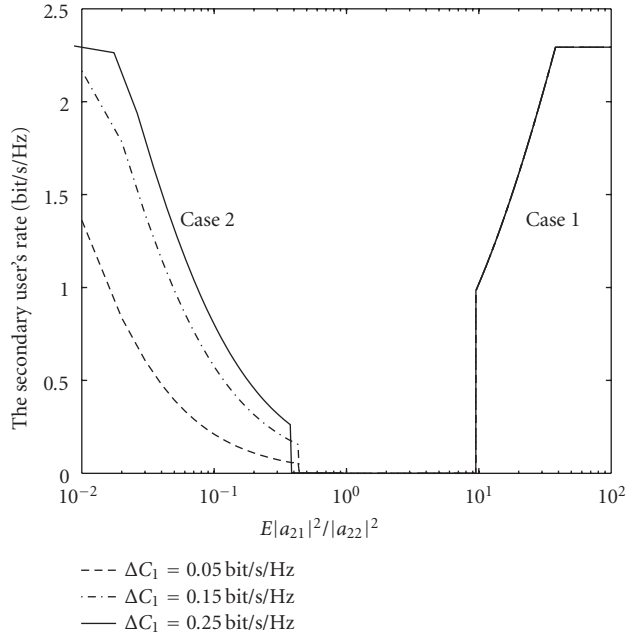


Figure 8: An example of capacity results for the TSMD mode with partial multiuser CQI.

*6.1. Capacity Results with Full Multiuser CQI.* Capacity theorem about two-user GIC channel [11] has told us that the secondary user cannot reliably decode the primary user's message for the channel condition $|a_{12}| < |a_{11}|$. Hence, for the case of $|a_{12}| < |a_{11}|$, the TSMD mode reduces to a special example of the PSMD mode.

For the channel condition $|a_{12}| \ge |a_{11}|$ and $|a_{21}| \ge |a_{22}|$, the TSMD system becomes a compound multiple-access

channel [10] whose capacity region is given by (3). In this case, the primary user does not need to pay capacity penalty, and thus the secondary user's capacity is

$$C_2 = \min(\mathcal{C}[\gamma_{21} + \gamma_{11}], \mathcal{C}[\gamma_{12} + \gamma_{22}]) - \mathcal{C}[\gamma_{11}]. \quad (47)$$

The transmit power $P_2$ is limited only by the local power constraint.

For the channel condition $|a_{12}| \geq |a_{11}|$ and $|a_{21}| < |a_{22}|$, the secondary user can access the primary spectrum without causing capacity penalty to the primary user. In this case, each user will decode the other's message for interference cancelation, and thus the secondary user's transmission rate is (47). Due to $|a_{21}| < |a_{22}|$, we can easily justify that (47) equals to (27). If the primary user deals with the interference as noise, the TSMD mode reduces to the SSMD mode. Then, the secondary user's transmission rate is (21), and the transmit power $P_2$ is limited by (11). According to *Criteria 2&3*, the secondary user's achievable rate for the channel condition $|a_{12}| \geq |a_{11}|$ and $|a_{21}| < |a_{22}|$ is

$$R_2 < \max((21), (27)). \quad (48)$$

*6.2. The UCR Strategy with Partial Multiuser CQI.* It has been shown in Section 6.1 that the TSMD mode reduces to the PSMD mode for the channel condition $|a_{12}| < |a_{11}|$. Therefore, the UCR strategy here is proposed only for the condition $|a_{12}| \geq |a_{11}|$.

*Case 1.* Suppose

$$\Pr\left(|a_{21}|^2 \geq |a_{22}|^2\right) > \epsilon, \quad (49)$$

the secondary user will access the primary spectrum at the transmission rate

$$R_2 \leq \min\left(\mathcal{C}\left[\frac{P_2\mathcal{L}}{N_o} + \gamma_{11}\right], \mathcal{C}[\gamma_{12} + \gamma_{22}]\right) - \mathcal{C}[\gamma_{11}]. \quad (50)$$

Equation(50) is produced by replacing the term $\gamma_{21}$ in (47) with $(P_2\mathcal{L})/(N_o)$ where $\mathcal{L} > |a_{22}|^2$.

*Case 2.* Suppose

$$\Pr\left(|a_{21}|^2 < |a_{22}|^2\right) > \epsilon, \quad (51)$$

the UCR strategy is described as the following steps.

*Step 1.* Utilize (14) to determine $\max(P_2)$ with respect to a given capacity penalty $\Delta C_1$.

*Step 2.* Calculate the following result which is produced by replacing $P_2$ in (21) with (14)

$$C_2^{(21)} = \min\left(\mathcal{C}\left[\gamma_{12} + \frac{\max(P_2)|a_{22}|^2}{N_o}\right] - (1-\rho)\mathcal{C}[\gamma_{11}], \mathcal{C}\left[\frac{\max(P_2)|a_{22}|^2}{N_o}\right]\right). \quad (52)$$

*Step 3.* Calculate the following result which is produced by replacing the term $\gamma_{21}$ in (27) with $(P_2\mathcal{L})/(N_o)$ $(\mathcal{L} < |a_{22}|^2)$

$$C_2^{(27)} = \mathcal{C}\left[\frac{P_2\mathcal{L}}{N_o} + \gamma_{11}\right] - \mathcal{C}[\gamma_{11}]. \quad (53)$$

*Step 4.* Determine the secondary user's transmission rate via $R_2 \leq \max(C_2^{(21)}, C_2^{(27)})$.

*6.3. Numerical Example.* Considering $|a_{21}|$ to be Rayleigh distributed, we derive the following results for Case 1 and Case 2, respectively.

**Corollary 6.** *A sufficient condition for Case 1 to happen is*

$$E\left(|a_{21}|^2\right) \geq \frac{|a_{22}|^2}{\ln(1/\epsilon)}, \quad E\left(|a_{21}|^2\right) \geq \frac{\mathcal{L}}{\ln(1/\epsilon)}. \quad (54)$$

*Proof.* Equation (54) can be straightforwardly obtained through calculation of (49) and $\Pr(\mathcal{L} \leq |a_{21}|^2) \leq \epsilon$. □

**Corollary 7.** *A sufficient condition for Case 2 to happen is*

$$E\left(|a_{21}|^2\right) \leq \frac{|a_{22}|^2}{\ln(1/1-\epsilon)}, \quad E\left(|a_{21}|^2\right) \geq \frac{\mathcal{L}}{\ln(1/\epsilon)}. \quad (55)$$

*Proof.* (55) can be straightforwardly obtained through calculation of (51) and $\Pr(\mathcal{L} \leq |a_{21}|^2) \leq \epsilon$. Figures 7 and 8 show a visual example for scenarios with full or partial multiuser CQI, respectively. The system configuration is almost the same as the setup in Section 3.3, but we set $|a_{12}|^2 = 4$ to fulfill the condition $|a_{12}| > |a_{11}|$. For the scenario with partial multiuser CQI, we set $\mathcal{O}_t = 10\%$ and $\epsilon = 90\%$ as an example. It is observed that Case 1– Case 2 in Figure 8 offers comparable performance with the corresponding scenario in Figure 7. □

## 7. Conclusion

In this paper, we have investigated two-user Gaussian UCR systems by assuming the availability of full multiuser CQI or partial multiuser CQI. Provided full multiuser CQI, we have studied the fundamental relationship between the secondary user's achievable rate $C_2$ and capacity penalty to the primary user $\Delta C_1$ in four carefully classified UCR modes. For the scenario with partial multiuser CQI, we first established a new physical-layer model through exploitation of the location-aided approach. Then, new spectrum access and power allocation strategies have been investigated in terms of $C_2$, $\Delta C_1$, and capacity outage probability. Numerical examples are provided to show the performance of the UCR with full multiuser CQI and the proposed approach with partial multiuser CQI.

## Appendix

## Proof of Corollary 3

For the Rayleigh distribution, we can calculate

$$\begin{aligned}\Pr\left(\lambda_2 \le \frac{|a_{21}|^2}{|a_{22}|^2} \le \lambda_1\right) &= \exp\left(-\frac{\gamma_{22}\lambda_2}{\overline{\gamma}_{21}}\right) - \exp\left(-\frac{\gamma_{22}\lambda_1}{\overline{\gamma}_{21}}\right) \\ &\triangleq f\left(\overline{\gamma}_{21}\right).\end{aligned} \tag{A.1}$$

Using the first derivative of $f(\overline{\gamma}_{21})$ with respect to $\overline{\gamma}_{21}$, we can find that $f(\overline{\gamma}_{21})$ is an increasing function of $\overline{\gamma}_{21}$ for the condition

$$\overline{\gamma}_{21} \le \frac{\gamma_{22}(\lambda_1 - \lambda_2)}{\ln(\lambda_1/\lambda_2)} \tag{A.2}$$

and otherwise a decreasing function. Hence, we have

$$\begin{aligned}\max\left(f\left(\overline{\gamma}_{21}\right)\right) &= f\left(\overline{\gamma}_{21} = \frac{\gamma_{22}(\lambda_1 - \lambda_2)}{\ln(\lambda_1/\lambda_2)}\right) \\ &= \exp\left(-\frac{\ln(\gamma_{11}+1)}{\gamma_{11}}\right)\left(\frac{\gamma_{11}}{\gamma_{11}+1}\right).\end{aligned} \tag{A.3}$$

A necessary condition for (33) to be satisfied is $\max(f(\overline{\gamma}_{21})) > \epsilon$. Due to $(\gamma_{11})/(\gamma_{11}+1) < 1$, it is necessary to have the following condition to be satisfied

$$\exp\left(-\frac{\ln(\gamma_{11}+1)}{\gamma_{11}}\right) > \epsilon. \tag{A.4}$$

Solving this inequality leads to (40).

## Acknowledgments

The authors would like to thank the editor, Dr. Ronald Raulefs, and anonymous reviewers for their extremely constructive and supportive comments. This work has been performed in the framework of the ICT project ICT-217033 WHERE, which is partly funded by the European Union.

## References

[1] Q. Zhao and B. M. Sadler, "A survey of dynamic spectrum access," *IEEE Signal Processing Magazine*, vol. 24, no. 3, pp. 79–89, 2007.

[2] A. Goldsmith, S. A. Jafar, I. Maric, and S. Srinivasa, "Breaking spectrum gridlock with cognitive radios: an information theoretic perspective," *Proceedings of the IEEE*, vol. 97, no. 5, pp. 894–914, 2009.

[3] J. Mitola III and G. Q. Maguire Jr., "Cognitive radio: making software radios more personal," *IEEE Personal Communications*, vol. 6, no. 4, pp. 13–18, 1999.

[4] I. Marić, R. D. Yates, and G. Kramer, "Capacity of interference channels with partial transmitter cooperation," *IEEE Transactions on Information Theory*, vol. 53, no. 10, pp. 3536–3548, 2007.

[5] N. Devroye, P. Mitran, and V. Tarokh, "Achievable rates in cognitive radio channels," *IEEE Transactions on Information Theory*, vol. 52, no. 5, pp. 1813–1827, 2006.

[6] W. Wu, S. Vishwanath, and A. Arapostathis, "Capacity of a class of cognitive radio channels: interference channels with degraded message sets," *IEEE Transactions on Information Theory*, vol. 53, no. 11, pp. 4391–4399, 2007.

[7] S. I. Gel'fand and M. S. Pinsker, "Coding for channel with random parameters," *Problems of Control and Information Theory*, vol. 9, no. 1, pp. 19–31, 1980.

[8] M. H. M. Costa, "Writing on dirty paper," *IEEE Transactions on Information Theory*, vol. IT-29, no. 3, pp. 439–441, 1983.

[9] A. B. Carleial, "Interference channels," *IEEE Transactions on Information Theory*, vol. IT-24, no. 1, pp. 60–70, 1978.

[10] H. Sato, "The capacity of gaussian interferene channel under strong interference," *IEEE Transactions on Information Theory*, vol. IT-27, no. 6, pp. 786–788, 1981.

[11] G. Kramer, "Outer bounds on the capacity of Gaussian interference channels," *IEEE Transactions on Information Theory*, vol. 50, no. 3, pp. 581–586, 2004.

[12] X. Shang, G. Kramer, and B. Chen, "A new outer bound and the noisy-interference sum-rate capacity for Gaussian interference channels," *IEEE Transactions on Information Theory*, vol. 55, no. 2, pp. 689–699, 2009.

[13] M. H. M. Costa and A. A. El Gamal, "The capacity region of the discrete memoryless interference channel with strong interference," *IEEE Transactions on Information Theory*, vol. IT-33, no. 5, pp. 710–711, 1987.

[14] T. M. Cover and J. A. Thomas, *Element of Information Theory*, John Wiley & Sons, New York, NY, USA, 2nd edition, 2006.

[15] EU-ICT FP7 WHERE Project, http://www.ict-where.eu/.

[16] Y. Xing, C. N. Mathur, M. A. Haleem, R. Chandramouli, and K. P. Subbalakshmi, "Dynamic spectrum access with QoS and interference temperature constraints," *IEEE Transactions on Mobile Computing*, vol. 6, no. 4, pp. 423–432, 2007.

[17] A. T. Hoang and Y.-C. Liang, "A two-phase channel and power allocation scheme for cognitive radio networks," in *Proceedings of the IEEE 17th International Symposium on Personal, Indoor and Mobile Radio Communications (PIMRC '06)*, Helsinki, Finland, September 2006.

[18] M. K. Simon and M.-S. Alouini, *Digital Communication over Fading Channel*, John Wiley & Sons, Canada, 2nd edition, 2005.